Nanoporous and Nanostructured Materials for Energy Storage and Sensor Applications

A DISSERTATION
SUBMITTED TO THE FACULTY OF THE GRADUATE SCHOOL
OF THE UNIVERSITY OF MINNESOTA
BY

Anh D. Vu

IN PARTIAL FULFILLMENT OF THE REQUIREMENTS
FOR THE DEGREE OF
DOCTOR OF PHILOSOPHY

Andreas Stein, Advisor

March 2013

© Anh Vu 2013

Acknowledgements

I would like to thank the following individuals for the support and the help they have provided:

Professor Andreas Stein, my research advisor for all the support, encouragement, and trust throughout the course of my graduate studies. He has been and always be my inspiration scientist and human decency.

Professor William Smyrl for the collaboration on the supercapacitor projects. I am grateful for his valuation discussion and generous access to all electrochemical instruments in his lab.

Professor Philippe Buhlmann for the collaboration on the sensor and supercapacitor projects.

Current and former Stein group members for their contribution and valuable input to my work: Dr. Nicholas Denny, Dr. Fan Li, Dr. Won Cheol Yoo, Dr. Matthew Dubay, Ms. Melissa Fierke, Mr. David Josephson, Mr. Yuqang Qian, Mr. Nicholas Petkovich, Mr. Stephen Rudisill, and Mr. Benjamin Wilson. I also want to thank former undergraduate students John Phillipe, Xiao Jie, and Rajac for working with me.

My parents, my family, and my friends for all of the love, sacrifices, and support that they have given me so freely in my life.

My wife, Anh Nguyen, and my daughter, Phuong Vu, for being supportive and patient. I am deeply in debt for the sacrifices that they have given me.

DEDICATION

THIS DISSERTATION IS DEDICATED TO MY WIFE **ANH NGUYEN**
AND MY DAUGHTER **PHUONG VU**

Abstract

The major objective of this work is to design nanostructured and nanoporous materials targeting the special needs of the energy storage and sensing fields. Nanostructured and nanoporous materials are increasingly finding applications in many fields, including electrical energy storage and explosive sensing. The advancement of energy storage devices is important to the development of three fields that have strong effects on human society: renewable energy, transportation, and portable devices. More sensitive explosive sensors will help to prevent terrorism activities and boost national security.

Hierarchically porous $LiFePO_4$ (LFP)/C composites were prepared using a surfactant and colloidal crystals as dual templates. The surfactant serves as the template for mesopores and polymeric colloidal spheres serve as the template for macropores. The confinement of the surfactant-LFP-carbon precursor in the colloidal templates is crucial to suppress the fast crystallization of LFP and helps to maintain the ordered structure. The obtained composites with high surface areas and ordered porous structure showed excellent rate performance when used as cathode materials for LIBs, which will allow them to be used as a power source for EVs and HEVs. The synthesis of $LiFePO_4$ in three dimensionally confined spaces within the colloidal template resulted in the formation of spherical particles. Densely packed $LiFePO_4$ spheres in a carbon matrix were obtained by spin-casting the LFP-carbon precursor on a quartz substrate and then pyrolyzing it. The product showed high capacity and could be charged /discharged with very little capacity fading over many cycles.

Three-dimensionally ordered mesoporous carbons were prepared from nano-sized silica sphere colloidal crystal templates. These materials with very high surface areas and ordered porous structure showed high capacitance and excellent rate capability when used as electrodes for supercapacitors.

Mesoporous silica thin films of different morphologies, including disordered (wormlike), 2D-hexagonal, 3D-hexagonal, and cubic structure, were prepared. The films were then doped or bridged with fluorescence compounds and used as sensors for nitroaromatic compounds. The sensor performance depended on both the film structure and the mode of fluorophore attachment. The best films showed high quenching rates and were

stable during long time storage. The films can potentially be incorporated in portable sensing devices. (351 words)

Table of Contents

List of Tables

List of Figures

Symbols and Abbreviations

°C	degrees Celsius
3DOm	three-dimensionally ordered mesoporous
3DOM	three-dimensionally ordered macroporous
Å	angstrom
AAO	anodic aluminum oxide
ABTS 4.0	Arbin battery-testing system
AMPD	2,2'-azobis(2-methyl propionamidine) dihydrochloride
BET	Brunauer Emmett Teller adsorption isotherm equation
BJH	Barrett, Joyner, and Halenda
CCT	colloidal crystal templating
CPs	conjugated polymers
CTAOH/Br	cetyltrimethylammonium hydroxide/bromide
CV	cyclic voltammetry
DCM	dichloro methane
DNB	1,3-dinitrobenzene
DNT	2,4-dinitrotoluene
DSC	differential scanning calorimetry
ED	electron diffraction
EDLC	electrical double layer capacitor
EIS	electrochemical impedance spectroscopy
EISA	evaporation-induced self-assembly
EMI-TFSI	1-ethyl-3-methylimidazolium bis(trifluoromethylsulfonyl)imide
EtOH	ethanol
EVs	electric vehicles
FCC	face-centered cubic
fcc	face-centered cubic
FE-SEM	field emission scanning electron microscopy
FFT	fast Fourier Transform
g	gram

h	hour
hcp	hexagonally close packed
HEVs	hybrid electric vehicles
LATP	$Li_{1.5}Al_{0.5}Ti_{1.5}(PO_4)_3$ (LATP)
LFP	lithium iron phosphate
LIB	lithium ion batteries
LUMOs	lowest unoccupied molecular orbitals
mg	milli gram
mL	milliliter
µm	micrometers
MMA	methyl methacrylate
NACs	nitroaromatic compounds
NB	nitrobenzene
nm	nanometer
NMR	nuclear magnetic resonance
P/P0	relative pressure
PEO	polyethylene oxide
PF	phenol formaldehyde
PHEV	plug-in hybrid electric vehicles
PMMA	poly(methylmethacrylate)
PPO	polypropylene oxide
PS	polystyrene
PS-b-PEO	polystyrene-*b*-polyethylene
PTFE	polytetrafluoroethylene
PXRD	powder X-ray diffraction
QSDFT	quenched solid density functional theory
RF	resorcinol formaldehyde
RT	room temperature
s	second
SAXS	small-angle X-ray scattering
SDAs	structure directing agents

SEM	scanning electron microscopy
SOHIO	Standard Oil Company of Ohio
SWNT	single-walled carbon nanotubes
t	time
TEA BF4	tetraethylammonium tetrafluoroborate
TEM	transmission electron microscopy
TEOS	tetraethylorthosilicate
TG	thermogravimetric
THF	tetrahydrofuran
TKHPP	1,3,6,8-tetrakis(4-hydroxyphenyl)pyrene
TKMPP	-1,3,6,8-tetrakis(4-methoxyphenyl)pyrene
TKSPP	1,3,6,8-tetrakis[4-(3-triethoxysilylpropylaminocarbonyloxy)phenyl]pyrene
TMOS	tetramethylammonium hydroxide
wt%	weight percent
XRD	X-ray diffraction
λ	wavelength

CHAPTER 1.

An Introduction to Nanostructured and Nanoporous Materials and Their Applications in Energy Storage and Sensing

Outline

Reproduced in part with permission from ref. 42.
Copyright © 2012 Willey-VCH

1.1 Electrical Energy Storage

Electrical energy storage is unarguably a great challenge in the 21st century. The advancement of electrical energy storage devices is urgently needed to support the development of renewable energy sources.[1] Green, sustainable energy sources have been attracting intense interest in response to the ever-increasing energy demands due to population explosion and economic development, which have long been supported with limited fossil fuels. Solar, wind, hydroelectric, and geothermal power are the most promising alternative energy sources. These resources are widely available but variable in time and diffuse in space, so they require efficient energy storage methods to guarantee the availability of energy when needed. Electrical energy is an ideal form of energy for storage, as it can be efficiently transmitted over long distances to generate work at the demand points. Electrical energy is also considered greener than fossil fuels and chemical energy, because it can be stored and used without gaseous exhausts. The gaseous emissions from burning fossil fuels are known to cause environmental pollution and the greenhouse effect.

In efforts to reduce CO_2 emissions from vehicles, plug-in hybrid electric vehicles (PHEV) and electric vehicles (EVs) have been attracting intense interest recently. The vehicles require light weight, high energy density, and high power density electrical storage devices that can store more charge and operate at higher rates than all of the currently available technologies.[2,3]

The portable device market, which has been prosperous since the introduction of lithium ion batteries (LIB), also needs power sources with smaller sizes and higher energy densities. This is crucial in today's information-rich mobile society, where miniaturized but powerful devices are preferred. The advancement of electrical energy storage devices will clearly benefit the development of the three fields that have strong effects on human society: renewable energy, transportation, and portable devices.[4]

Electricity can be stored in electrical energy-storage devices such as batteries and supercapacitors. The two devices share many structural similarities but are quite different

in their performance. Batteries are able to store a large amount of energy but suffer from slow power delivery, whereas supercapacitors can provide high specific power but can only store a limited amount of energy.[5] The differences between them are due to the mechanism by which charge is stored and delivered in these systems. Batteries store charge in the bulk material, whereas supercapacitors store charge only on the electrode surfaces via ion adsorption (electrical double layer capacitor (EDLC)) or fast redox reactions (pseudo-capacitor). In this thesis, lithium ion batteries (LIB) and EDLC are topics of interest, and the subsequent discussion will focus on these systems. Supercapacitors can quickly release stored energy simply by replacing the surface-adsorbed ions with counter ions from the electrolyte. On the other hand, the charge transfer process in a battery is usually coupled with structural changes of the cathode and the anode materials, which is much slower than the ion adsorption/desorption steps in supercapacitors. The performance of current batteries and supercapacitors is shown in the Ragone plot of energy density vs. power density together with the performance of conventional capacitors and fuel cells (Figure 1.1).

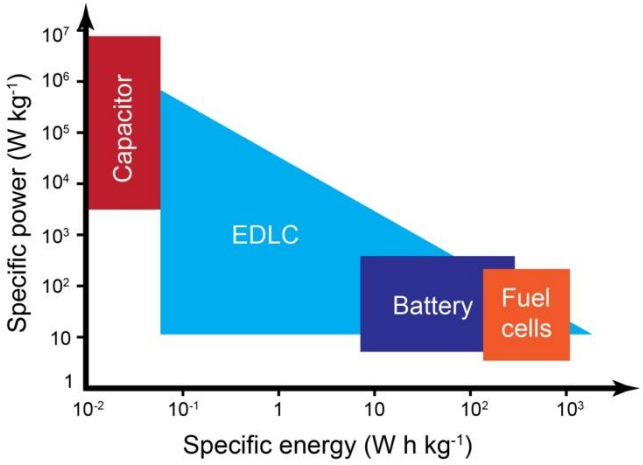

Figure 1.1 Comparison of specific power and specific energy of electrical energy storage devices.

According to Figure 1.1, power densities need to be improved for batteries and energy densities for supercapacitors to meet future requirements. Unfortunately, these needs are not achievable with conventional micron-size electrode materials, which have reached their performance limits and have shown few significant breakthroughs over the last decade. As the performance of these electrochemical energy storage devices ultimately depends on materials properties, numerous efforts have been devoted to investigating new

electrode materials. In recent years, nanostructured materials have attracted great interest because of their unusual mechanical, optical, and electrical properties that are not found in the counterparts made from micron-size particles.[6-8] These novel properties were resulted from confining the dimensions of the materials and from the enhanced surface-to-volume ratio of the nano particles. In this thesis, several nanostructured cathode materials for lithium-ion battery and nanoporous carbons for EDLC will be investigated. Related to these discussions, Chapters 2, 3, and 4 will be devoted to nanostructured cathode materials for LIBs with high rate capabilities. Chapter 5 is the study of hierarchical porous carbons with ordered mesopores (8-40 nm) and microporous walls as high energy density and high power density electrode materials for supercapacitors. However, before addressing specific electrochemical systems, this chapter aims to cover some basic background information on LIBs and EDLCs, the current active trends of research in the electrical energy storage field, and how nanostructured and nanoporous materials can help to achieve the goals in these fields.

1.1.1 Lithium-ion Batteries

Since they were first commercialized about twenty years ago, rechargeable lithium-ion batteries (LIBs) have become ubiquitous power sources for portable devices used in a wide range of consumer, health, and military applications. They are now beginning to enter the market in the transportation sector, and for load leveling and large-scale storage of electrical energy from alternative power sources, such as wind and solar energy. Batteries based on the Li^+/Li redox couple are attractive for high voltage and high capacity applications, lithium being the most electropositive metal (-3.04 V vs. a standard hydrogen electrode) and having a very low atomic mass. Over two decades of development, cell capacities have slowly improved, but the main components, including cathode and anode materials, have not changed significantly. A typical modern LIB cell consists of a cathode made from a lithium-intercalated layered oxide (e.g., $LiCoO_2$, $LiNi_xCo_{1-x}O_2$, or $LiNi_xMn_yCo_{1-x-y}O_2$) and a graphite anode with an organic electrolyte. The battery operates following a "rocking chair" concept with an initial charging step, during which lithium ions are extracted from $LiMO_2$ (M = Co, Ni, Mn) and intercalate into graphite, and a subsequent discharging step, during which lithium ions deintercalate from the graphite particles and

are reintroduced into the layered $Li_{1-x}MO_2$ structure.[9] Both electrodes are composed of micrometer-sized active particles, mixed with conductive carbon particles to lower the electrical resistance of the electrodes, and held together by a binder phase. Each cell can be discharged and recharged for many cycles, as long as the cathode and anode do not undergo significant structural changes.

Numerous applications are now putting increased demands on electrical energy storage devices, calling for higher specific capacities and faster rate performance.[3] These requirements are particularly important for electric vehicles (EVs) and plug-in hybrid electric vehicles (HEVs), where energy storage devices must supply sufficient power to accelerate a vehicle quickly and recover energy during braking. Future portable devices with smaller sizes but more powerful performance will need batteries with much higher energy densities that currently available LIB technologies based on graphite anodes and $LiCoO_2$ or $LiMn_2O_4$ cathodes would not be able to supply. In transportation applications, shorter recharge times would increase the consumer acceptance rate of EV and HEV technology. Improved energy densities and rate performance are also required for devices storing charge from renewable energy sources, such as solar and wind energy, which are seasonal and intermittent.

For LIBs, nanostructured electrodes have many advantages compared to micron-size electrode materials, some of which are listed below:

- Short path lengths for electronic transport and Li^+ diffusion permitting operation with low electronic/ionic conductivity and high power
- Higher electrode/electrolyte contact area leading to higher rate performance
- Allow new reactions that are not possible with bulk materials
- Better accommodation for volume changes during the cycling, especially useful for alloy anodes (Sn, SnO_2, and Si)

High cost, slow rate performance, and safety are the three biggest obstructions that prevent current LIB technology from being applied in PHEV and EV fields. Considering the fast advancements of nanotechnology in understanding properties and methods to fabricate nanosized objects, nanostructured materials are the golden key to solve these problems. The higher power density of nanostructured electrode materials can be

understood via the equation $\tau_{eq} \sim \frac{l^2}{D}$, where τ_{eq} is the characteristic time for lithium ions to diffuse through an electrode material, l is the diffusion length, and D is the diffusion coefficient.[10] The lithium ion diffusion time, the most important factor for high rate LIBs, can either be reduced by increasing the diffusion coefficient (by synthesizing better Li^+ conductors) or by decreasing the diffusion length (by using electrode components with nanometer dimensions). The latter approach avoids changes in the battery chemistry, has a larger impact on the diffusion time because of the square relationship, and has therefore attracted the attention of many researchers in recent years. It is worth noting that there are also a number of disadvantages of using nano-sized electrode materials. namely, a higher rate of side reactions due to high contacting surface areas between electrode and electrolyte leading to poor cycling, less efficient packing leading to lower volumetric energy density, and more costly and difficult syntheses.

A nanoporous material is a special case of nanostructured materials, in which pores (normally < 100 nm) are deliberately introduced into the bulk materials to obtain systems with nano-sized walls and preferably interconnected pores. Besides the advantages and disadvantages of nanostructured materials, porous materials offer important benefits for electrical energy storage systems, including batteries and supercapacitors. Some of the most important features are listed below:

- Pores provide good access of the electrolyte to the electrode surface.
- The surface area in a porous material is relatively large, thereby facilitating charge transfer across the electrode/electrolyte interface.
- The walls of active material surrounding the pores can be very thin (nanometers to tens of nanometers), reducing path lengths for ion diffusion.
- The small feature sizes permit increased utilization of active material (more utilized volume, deeper cycling), so that specific capacities can be increased, particularly at high charge/discharge rates.
- The walls and pores in a porous electrode can be bicontinuous, thereby providing continuous transport paths through the active phase (walls) and the electrolyte phase (pores).

- Despite the porosity, the volumetric capacity of some porous electrodes may be increased compared to packed nanoparticles.
- The nanosized features in a porous solid are available within a material that has larger dimensions and can therefore be handled and processed more easily than discrete nanoparticles.
- In some cases, less or no binder is needed to hold the active phase together.
- The void spaces separating particles of active material can help to constrain growth of active material during cycling.
- In nanosized particles, irreversible phase transformations that occur in microcrystalline anodes can be suppressed. Such particles are therefore better able to accommodate volume changes due to first order phase changes during cycling.
- It is also possible to synthesize porous composite electrodes in which a supporting structure stabilizes active components with short cycle lives (e.g., components that disintegrate due to large volume changes during cycles).
- Porous composites can incorporate a secondary conductive phase to improve conductivity and high rate capacities of active phases with low intrinsic conductivity. Inclusion of the conductive phase eliminates or reduces the amount of conductive carbon additive needed in the final electrode.

At this point, porous carbon materials are among the most prominent porous electrode materials, being found in capacitors,[11] and different battery systems (lithium-ion, lithium-air, and lithium-sulfur batteries), where they help to enhance the system performance when high power or high current rates are required.[12-14] However, other porous materials, such as metal oxides, metal phosphates, metals, alloys, and composites have been investigated as electrodes, solid electrolytes, or current collector materials over the past years for both capacitor and battery applications.

1.1.2 Supercapacitors

An electrochemical capacitor, also called supercapacitor is able to store a several orders of magnitude higher charge than a conventional capacitor at the electrode/electrolyte

interface, primarily in high surface area carbons. Even though the principle that electrical energy can be stored in a charged capacitor was known since 1745, it was not considered for practical purposes until 1957 in the patent granted to Becker.[15] The reason is the very limited amount of energy that a conventional capacitor consisting of two metal plates can store. Becker, however, built a cell from two porous carbon electrodes immersed in an aqueous electrolyte, which showed capacitance values three to four orders of magnitude higher than conventional capacitors.[16] The high capacitance was attributed to the high surface area of the porous carbon electrodes that are able to store more charge and therefore higher energy content in the double layer at the electrode/electrolyte interface. The cell design was not practical, and it was never commercialized since both electrodes needed to be immersed in a container of electrolyte, which was known to have leaking problems as in a flooded battery. Becker's work was appreciated by researchers at Standard Oil Company of Ohio (SOHIO), to whom the invention of the device in the today's format can be attributed and who pioneered an industry with sales worth several hundred million dollars per year.[17]

EDLC electrodes are usually made of high surface area, well conducting materials such as activated carbons. During the charging process, the anions of electrolytes move toward the positive surface of EDLCs and absorb on the electrode surface, whereas cations are accumulated on the surface of the negative electrode (Figure 1.2). Because the surface charge accumulations do not cause chemical or structural changes of the electrodes, EDLCs usually have extremely long cycle lives (up to 10^6 cycles). The excellent cycle life and reasonably high capacitance have enabled applications of EDLCs in portable electronic devices, memory back-up systems for computers, other electronic devices, and particularly, low emission hybrid electric vehicles (HEVs).[18] However, due to the limited energy density, EDLCs are commonly coupled with primary high-energy batteries or fuel cells to serve as a temporary energy storage device with a high power capability.[18]

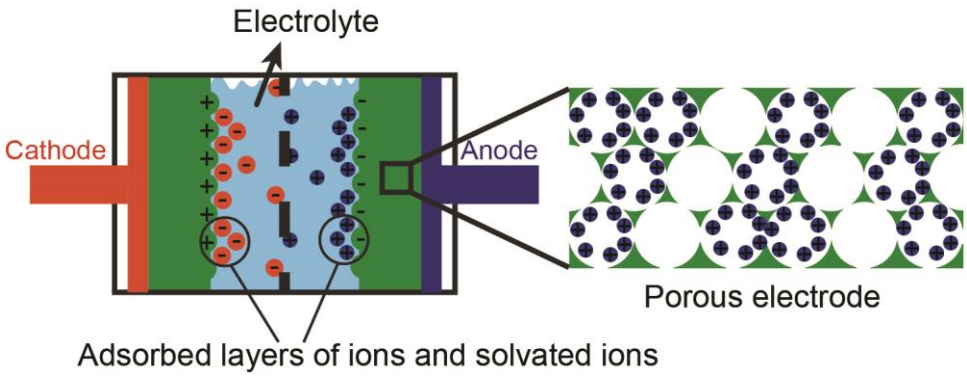

Figure 1.2 Scheme of an EDLC based on porous electrode materials

The capacitance, energy density, and power capacity of the electrode can be calculated using the formulas:

$$C = \frac{\varepsilon_r \varepsilon_0 A}{d} \qquad E = \frac{1}{2} C V^2 \qquad P = \frac{V^2}{4R}$$

where C, E, P are the capacitance, energy, and power of the EDLC respectively, ε_r is the electrolyte dielectric constant, ε_0 is the dielectric constant of the vacuum, d is the effective thickness of the double layer, A is the electrode surface area, V is the working voltage, and R is the resistance of the cell. To increase the capacitance, one can either increase the electrode surface area (replacing metal plates with porous materials) or decrease the effective thickness of the double layer (using electrolyte with smaller ions). This explains why activated carbons with very high surface area, low cost, and reasonably good conductivity have been used predominantly in EDLCs. The energy density and power density of EDLCs can be improved by using electrodes with good conductivity and electrolytes with larger potential windows. In fact, utilizing non-aqueous electrolytes with larger working potentials is a more effective way to improve the performance of EDLCs, since both energy density and power density of EDLCs are exponentially increased with the working potential. Nanostructured electrode materials can benefit the advancement of supercapacitor technologies.[19-22] To improve both energy density and power density, electrode materials with optimized pore size, pore structure, and surface properties are required. This will overcome the limited accessibility of electrolyte into isolated pores and micropores, which is normally found a problematic characteristic of activated carbons. Also, because recent research has revealed anomalously high capacitance values in materials containing mostly sub-nanometer pores,[23-26] it is necessary to develop synthesis

methods with more control over the dispersity of the pores and carry out theoretical studies to have a better understanding of this phenomenon. Nonetheless, microporous materials may have limited power capability because of the limited accessibility of the small pores. In this aspect, hierarchically porous materials with microporous walls and ordered mesoporous system can be a solution.[26,27] The large surface areas from micropores and fast electrolyte accessibility from ordered mesopores will balance between energy capacity and power performance. The research in this direction will be described in Chapter 5 of this thesis with the synthesis of 3DOm carbon with different mesopore sizes.

1.2 Fluorescence Sensors for Nitroaromatic Compounds

Nitroaromatic compounds (NACs) are known to cause environmental pollution and have severe effects on human health.[28] In addition, they are frequently employed as explosives in terrorist activities all around the world. Therefore, detection and quantification of NACs are of great importance in environmental pollution control and clean-up, military operations, and homeland security. Fluorescence sensing is among the most sensitive and cost-effective detection methods, suitable for incorporation in portable devices for on-field testing.[29] The operation of fluorescence-based sensors relies on the quenching of a fluorophore via a photoinduced electron transfer mechanism. In this process, the excited electrons of the fluorophore do not return to the ground state but are transferred to the lowest unoccupied molecular orbitals (LUMOs) of the NAC analytes through non-emitting processes (Figure 1.3).[30] Because NACs are electron-deficient compounds, electron-rich fluorophores are usually used to facilitate the electron transfer process between the fluorophore and the quencher.

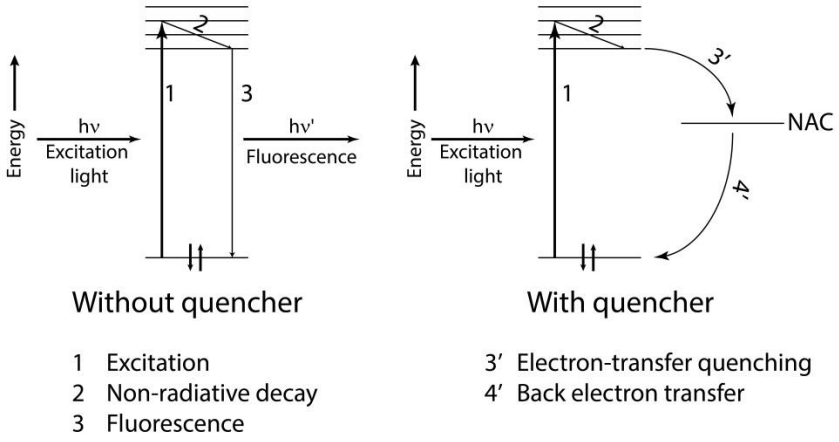

Figure 1.3 General mechanism for the detection of NACs using fluorescent compounds.[37]

To date, most work on fluorescence sensors for NACs has focused on conjugated polymers (CPs), utilizing their ability to amplify the sensing signal in response to interactions with NACs.[31-37] The sensing performance of CP films was found to depend strongly on the thickness and the organization of the polymer chains inside the films.[38] Therefore, porous, thin films of CPs with high analyte diffusivity are preferred. However, photobleaching of thin CP films limits their usable lifetimes. In addition, because of the low quantum yield, relatively thick CP films are usually required to create measurable fluorescence intensity. Limitations of thick CP films include poor molecular organization with weak intermolecular interactions that result in slow sensing times.

Small fluorescence molecules offer another effective way to detect NACs at lower cost and with simpler syntheses compared to CPs. Differences between polymer-based and small-molecule-based detection include the physical mechanism of fluorophore quenching and the absence of excitation migration in the small molecules. However, the greatest advantage of using a small-fluorophore sensor is the ability to incorporate the fluorophore in a matrix that can enhance binding and/or introduce excitation migration. In addition, the matrix can protect the fluorophore from photobleaching and excimer formation.[39-41]

Mesoporous silica is an ideal host for carrying fluorescence compounds because of its large surface area and its excellent thermal, chemical, and mechanical stability. Chapter 6 describes the fabrication of several kinds of mesoporous silica films and their use in a quenching study with DNT in the gas phase. The amphiphilic surfactant P123 was used not only as a template for the formation of mesopores but also to improve the binding of DNT

to the film. Two types of surfactant-free mesoporous silica films were prepared, including fluorophore-impregnated fluorophore-bridged films. The quenching performances of these films were found to depend on both the structures and the components of the films.

1.3 Preparation of Nanostructured and Nanoporous Materials

1.3.1 Nanoporous Materials

Porous materials can be classified based on their pore sizes (micropores < 2 nm, mesopores 2–50 nm, and macropores > 50 nm), their morphologies (ordered and non-ordered), and methods of their synthesis (templated and non-templated). One also distinguishes between "textural" porosity (voids created by the packing of particles), and "true" or "integral" porosity (from pores that are an integral part of a continuous solid framework). The pore sizes in texturally porous materials are usually correlated to particle sizes, whereas in materials with integral porosity they are independent of particle size. In the following discussion of synthetic methods for porous solids, we will emphasize the influence of the synthetic steps on the pore sizes, pore architecture, and dimensions of the walls in the synthesis products, as these parameters influence the electrochemical and optical properties of the materials.[42]

1.3.1.1 Soft Templating of Mesoporous Materials.

Soft templating approaches toward porous electrodes typically involve surfactants as structure directing agents (SDAs). The necessary chemistry has been well developed for silica systems, where surfactants direct the formation of mesoporous silicas with pore diameters covering most of the mesopore size range.[43-48] The pore architecture of surfactant-templated materials can be controlled by the choice of surfactants, solvents, and synthesis conditions. It includes disordered mesopores as well as ordered mesopores with hexagonal, cubic, lamellar, or other symmetries. Syntheses are generally carried out in aqueous solution under hydrothermal or lower temperature conditions. The well-accepted mechanism for the formation of the mesophase under these conditions was proposed by Stucky and co-workers known as cooperative formation mechanism. According to Stucky, the final mesophase is the 3D arrangement with lowest interface energy resulting from the

interactions between silicate species and surfactants. For systems with ionic surfactants, the assembly process is governed by the matching of charge density at the surfactant/inorganic species interfaces. For systems with nonionic surfactants, the assembly process is driven by adsorption and polymerization of silicate species on surfactants, which reduce the polarity and the water content within micelles. The modified micelles then undergo continuous transformations from spheroidal micelles into threadlike micelles. Using *in situ* ^{1}H NMR and TEM, Flodstrom et al. were able to observe the four stages of the formation of mesophases in a system using nonionic surfactants, including the adsorption of silicates on globular micelles, the association of globular micelles into floes, the precipitation of floes, and the micelle-micelle coalescence. It is worth noting that the formation of the final mesophase is susceptible to many factors such as pH, ionic strength, hydrogen bonding, coordination bonds, and covalent bonds. Therefore, in the synthesis of mesoporous silica, all of the possible interactions between surfactants and silicates must be considered and strictly controlled to obtain the targeted phase.

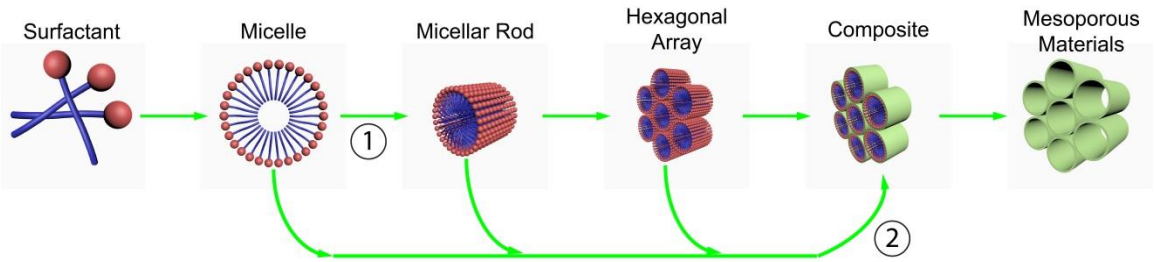

Figure 1.4 Mechanism for the formation of mesophase using surfactants as SDAs. Path 1 involves pre-arranged micelles formed from the surfactants and path 2 involves cooperative interactions between inorganic species and surfactant molecules which influence the formation of the liquid crystal phase. [55]

Alternatively, non-aqueous solvent systems may be used. Particularly for thin film formation, a process called evaporation-induced self-assembly (EISA) is widely employed.[49,50] The syntheses usually start with inorganic precursors with low polymerization degrees in volatile solvents. Upon solvent evaporation, inorganic precursors further hydrolyze and cross-link while surfactants form micelles and then liquid-crystal phases at very high concentration. Inorganic precursors assemble either with the surfactant or around organized surfactant assemblies, forming mesostructured products (Figure 1.4). Removal of the surfactant phase by extraction or calcination produces the

mesoporous material. As described in Chapter 6, mesoporous silicas with different mesostructures (2D-hexagonal, 3D-hexagonal, cubic, and wormlike) were synthesized via the EISA pathway (Figure 1.5 A, B, C, D). The mesoporous silica films were then doped/bridged with several phenyl-substituted pyrene fluorescence compounds. The composite films were used as sensors toward nitroaromatic compounds, which showed excellent quenching rate and high resistance again photobleaching. As shown in Chapter 7, mesoporous carbon spheres were synthesized through a hydrothermal reaction of PF sol in the presence of F127 surfactant (Figure 1.5E). The mesoporous carbon spheres were then used as spacers to keep graphene layers apart and the carbon spheres/graphene composites can be used as supercapacitor materials.

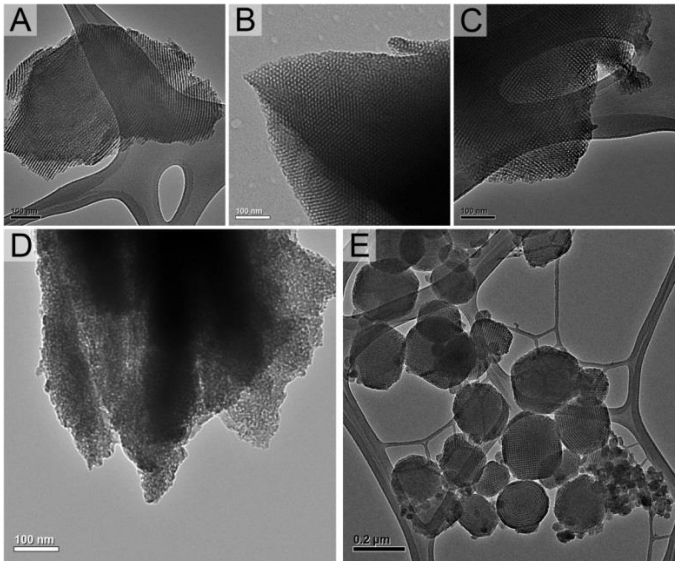

Figure 1.5 TEM images of (A),(B),(C),(D) silica films with 2D-hexagonal, 3D-hexagonal, cubic and wormlike mesopores; (E) mesoporous carbon spheres.

Various soft-templating processes have also been applied to the synthesis of mesoporous carbons, oxides, phosphates, and metals suitable for LIB and EDLC electrodes. Low molecular weight *cationic (*alkyltrimethylammonium)*, anionic (sodium n-ankyl-1-sulfonate), and nonionic (*octaethylene glycol monohexadecyl ether) *surfactants* have been employed to prepare mesoporous materials with relatively small mesopores (2.3–4 nm).[51-58] A broader mesopore size distribution with a larger average mesopore diameter can be obtained (3–7 nm) if a mixture of these cationic surfactants or longer alkyl chain surfactant is used.[55] Mesoporous materials with medium mesopores (3–8 nm) can be obtained when triblock-copolymer Pluronic surfactants are used.[41,42] When these higher molecular weight

triblock-copolymer surfactants are used to prepare mesoporous electrodes, the mesopore size depends on the choice of the polymer surfactant and the particular materials composition. Diblock copolymers of the KLE type (poly(ethylene-*co*-butylene)-*block*-poly(ethylene oxide) diblock copolymer) produce much larger mesopores and thicker walls.[59] Mesoporous hematite Fe_2O_3 films synthesized with a KLE surfactant by the EISA method contained mesopores with diameters of 14–15 nm and walls 10–16 nm thick.[59] In a synthesis of mesoporous titania doped with niobium to increase the electrical conductivity of titania, a KLE surfactant produced disordered mesopores with sizes in the 10–20 nm range.[60] Mesoporous $Li_4Ti_5O_{12}$ (a "zero-strain" anode material) was synthesized by templating with KLE and contained mesopores with an average diameter of ~18 nm and a nanocrystalline framework of phase-pure spinel nanoparticles.[61] In the calcined mesoporous material the nanocrystallites in the walls were 11~15 nm in size. The KLE surfactant has the additional advantage of higher thermal stability than the Pluronic-type surfactants, allowing calcination conditions that result in more complete condensation of the inorganic components.[62] Another amphiphilic diblock surfactant with high thermal stability is polystyrene-*b*-polyethylene (PS-*b*-PEO). This surfactant was employed in the synthesis of mesoporous $NbVO_5$ thin film electrodes with wormlike porous networks whose pore sizes and wall thicknesses could be tuned in the range from 15 to 100 nm, depending on the molecular weight of the surfactant.[62] Partial crystallization of the walls was possible before the pore structure collapsed due to sintering of $NbVO_5$ crystallites.

1.3.1.2 Hard Templating.

Soft templating is a powerful method to prepare mesoporous materials with different compositions and morphologies. However, it is sometimes difficult to obtain ordered mesoporous materials with highly crystalline walls when the crystallization temperatures of the inorganic phase are higher than the temperatures at which surfactants and block copolymers are removed. Without support from the assembled surfactants during crystallization, sintering of crystallites can eventually destroy the mesostructure. For those systems, hard templates can be used whose rigid structures do not change through interactions with a precursor, unlike the situation with soft templates. Hard templates include preformed porous solids, anodic aluminum oxide (AAO) membranes, and

assemblies of colloidal particles, such as silica- or polymer-based colloidal crystals. When hard templates are used, inorganic precursor solutions are infiltrated into the templates, and then the composites are treated at high temperatures. During the heat treatment, the precursor may undergo gelation and crystallization within the support of the template. After the heat treatment, ideally the inorganic framework is strong enough to maintain the porous structure, even when the template is removed. In the following sections, hard templating to syntheses of porous electrodes for LIBs and EDLCs will be discussed. The main focus will be on colloidal crystal templating as the technique is going to be used throughout this thesis. Besides, nanocasting and hard templating in various biological templates and in AAO membranes will be briefly reviewed as they are important methods to prepare electrode materials for LIBs and EDLCs.

1.3.1.2.1 Colloidal crystal templating.

Colloidal crystal templating (CCT) is a versatile method to obtain porous materials with well-ordered, interconnected pores of larger sizes (large mesopores and macropores).[63,64] The general method is described in Figure 1.6. In this method, monodisperse spheres (polymer spheres or silica spheres), are assembled into periodic arrays, so-called colloidal crystals. The void space between spheres is then infiltrated with a precursor solution for the target electrode material. Thermal processing converts the precursor to a solid skeleton that surrounds the templating spheres. Calcination in air above 350 ˚C also removes polymer sphere templates, such as polystyrene (PS) or poly(methylmethacrylate) (PMMA) spheres. If pyrolysis is carried out in an inert atmosphere, polymeric templates and organic precursor components are partially converted into a carbon phase that coats the remaining skeleton. Silica spheres may be removed by etching, e.g., with hydrofluoric acid solution. As in the case of nanocasting from mesoporous silica, the final product of the CCT process is an inverted replica of the original colloidal crystal, i.e., an "inverse opal" or three-dimensionally ordered macroporous (3DOM) or mesoporous (3DOm) solid. The inverse replica typically inherits the face-centered cubic (*fcc*) symmetry of the templating sphere array. The *fcc* macropore array is interconnected through windows where templating spheres were in direct contact (i.e., at twelve points in an ideal and typical structure). As a result, the cubic 3DOM structure is bicontinuous, with a continuous solid phase (the active

electrode material) and a continuous void space suitable for accommodating, for example, an electrolyte solution.

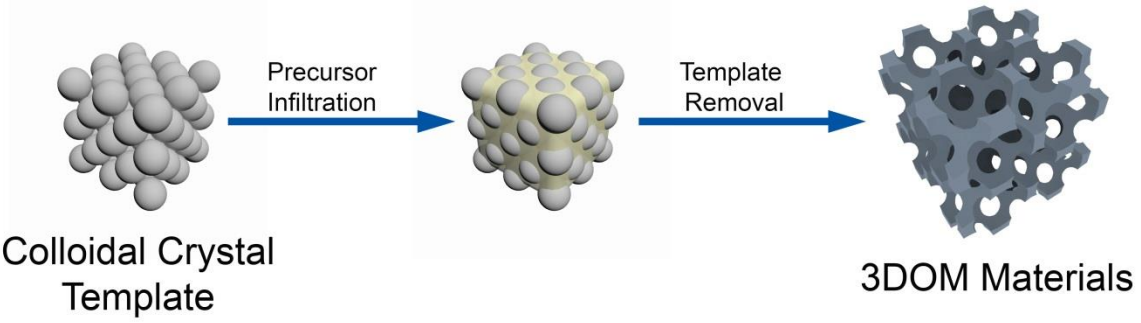

Figure 1.6 General method to prepare 3DOM electrode materials.

The pore sizes can be modified by adjusting the sizes of colloidal polymer spheres or silica spheres. For large mesopores (20–50 nm) and small macropores (50–250 nm), silica spheres are the most suitable templates as they can be prepared in these sizes ranges with relatively low polydispersity. Silica-based colloidal crystal templates are also advantageous for electrode materials that require processing at high temperatures (above ca. 600 ˚C) as the silica matrix limits sintering of grains and minimizes shrinkage of the structure. For the pore size range from ca. 100–2000 nm, polymer spheres are often preferred because they can easily be synthesized in higher yield than uniform silica spheres, also with low polydispersity. Removal of polymeric templates does not require an additional etching step. However, larger shrinkage is observed with polymeric templates, so that the final pore spacing is often 20–40% smaller than the repeat distance between the templating spheres. Although templating spheres with greater polydispersity may also be employed in this type of hard templating, they will not produce periodic structures. Therefore, a high degree of interconnectedness between pores and low pore tortuosity are not guaranteed in those cases.

Besides the pore architecture, an important consideration for porous electrodes is the wall structure. The morphologies of the walls, their crystallinity, and surface texture can be controlled by changing the conditions for template removal. Typically, removing the templates at low temperatures or through etching (solution treatment) yields amorphous walls, whereas removing them at high temperatures produces crystalline samples in many cases. For crystalline 3DOM materials, the macropore walls are composed of interconnected crystallites. The crystallite size depends on the thermal history of the

material. In general, crystallites have dimensions of a few nanometers to a few tens of nanometers and overall wall thicknesses are tens of nanometers, being thinner at the narrow struts and thicker at the vertices (replicas of the octahedral and tetrahedral holes in the fcc colloidal crystal). This provides short diffusion paths for lithium ions through these walls, similar to the situation for discrete nanoparticles, but in a macroscopic material that can be more easily handled than nanoparticles.

Some of the earliest works on 3DOM metal oxide electrode materials were on V_2O_5 and $LiNiO_2$.[65,66] Dunn and coworkers fabricated a 3DOM V_2O_5 aerogel cathode on an indium tin oxide-coated substrate using polystyrene spheres (1 μm in diameter) assembled into an *fcc* array as templates. The 3DOM aerogel-like product contained 800 nm-diameter macropores and ~150 nm-thick mesoporous walls composed of V_2O_5 ribbons with nanometer dimensions. Yan et al. developed templated syntheses for different 3DOM electrode materials, including cathode materials (Shcherbinaite-type V_2O_5 and $LiNiO_2$) and an anode material (Cassiterite-type SnO_2).[67] All the samples showed periodic structures with uniform pores, open windows, and interconnected walls, although, the morphologies of 3DOM SnO_2 and $LiNiO_2$ depended strongly on the calcination temperatures. At higher temperatures, the windows became smaller and the walls became rougher due to grain growth and sintering effects. In the case of $LiNiO_2$, the periodic 3DOM structure was lost when the material was calcined at a temperature of 650 °C or higher, but an interconnected pore structure was still maintained.

Although the general steps of the synthesis of 3DOM electrodes are conceptually simple, details in the precursor chemistry, solvents, and template surface chemistry greatly influence the product structures and properties. A recent example demonstrating the importance of precursor chemistry relates to 3DOM $LiMn_2O_4$.[68] In this system, a templated structure could be obtained from an ethanolic manganese nitrate precursor solution but not from a manganese acetate solution in a water/ethanol mixture. Similar precursor effects had been recognized earlier for general syntheses of 3DOM materials employing salt precursors.[69] Important considerations include the ability of the precursor to wet the template so that the templated is fully infiltrated, the achievable precursor concentration which influences the solid filling fraction, and the thermal decomposition/reaction behavior of the precursor and the template. For polymeric templates, a skeletal structure

must be sufficiently well developed before the template loses its structure. However, even if some structural order is lost due to crystallite growth, the resulting electrode material may still contain open, interconnected pores, as was observed in syntheses of macroporous $LiCoO_2$ powders.[70] In these syntheses, which employed a poly(methylmethacrylate) template and a precursor containing lithium acetate/cobalt acetate mixtures, addition of poly(ethylene glycol) or platinum modifiers permitted control over $LiCoO_2$ grain sizes in the wall skeleton.

Over the last decade, numerous other 3DOM electrodes have been synthesized by colloidal crystal templating, including those composed of the cathode materials $LiMn_2O_4$,[71] $LiFePO_4$,[72] and $FePO_4$,[73] and the anode materials anatase TiO_2,[74-76] $Li_4Ti_5O_{12}$,[77,78] $CoFe_2O_4$,[79] and SnO_2.[80] In addition, a 3DOM solid electrolyte of the composition $Li_{1.5}Al_{0.5}Ti_{1.5}(PO_4)_3$ (LATP) has been synthesized.[81] Variations of colloidal sphere templating with lower dimensionality (2D films) have also been developed to prepare porous electrode structures. A 2D macroporous NiO film was prepared on a stainless steel substrate by first electrophoretically depositing a polystyrene sphere monolayer on the conducting substrate and then anodically electrodepositing nickel oxy-hydroxide.[82] Calcination at 400 ˚C produced the macroporous nickel oxide film that had excellent electronic contact with the metallic substrate, permitting use of this electrode under high rate lithiation conditions.

1.3.1.2.2 Nanocasting.

A particularly versatile methodology for mesoporous electrodes that require high temperature processing is called "nanocasting".[83-87] In the nanocasting process, nanoporous molds with high thermal stability, such as mesoporous silica or mesoporous carbon, are infiltrated with the precursor for the target electrode material. This precursor is then concentrated in the pores via solvent evaporation. Often multiple impregnation steps are necessary to increase filling of the void space in the porous mold.[88,89] Vacuum-assisted impregnation[90] or the application of centrifugal forces[91] can also improve the extent of pore filling and improve the periodicity of the product structure. After thermal processing, the template is removed: silica by extraction with HF or hot NaOH or KOH solutions, carbon by combustion. The product is an inverted replica structure of the original hard template.

Thus, molds with bicontinuous pore/wall structures produce mesoporous replicas, whereas templates with cylindrical mesopores in a 2D hexagonal arrangement produce nanowire arrays, which are interconnected only if the template contains secondary pores between the cylindrical pores.

The most commonly used hard templates for nanocasting of porous electrodes are the mesoporous silica materials KIT-6[92,93] and SBA-15,[94,95] as both are easily synthesized and contain mesopores that are large enough to accommodate precursor fluids for the target electrode. Both of these structure types are templated in acidic media by the triblock copolymer P123. For KIT-6, *n*-butanol is included as a co-structure-directing agent. KIT-6 has a well-ordered cubic mesopore structure with *Ia-3d* symmetry, 4.5–10 nm mesopores (depending on synthesis parameters), and 2–4 nm thick walls (Figure 1.7A). It is important for the nanocasting process that KIT-6 synthesized at hydrothermal treatment temperatures >343 K contains pore channels that are well connected, allowing for complete infiltration of the structure. SBA-15 contains a highly ordered 2D hexagonal mesopore structure with *p6m* symmetry, large pores (4.6–11.4 nm, again depending on synthesis parameters), and thick walls (3.1–6.4 nm) (Figure 1.7C).[45] Because the long PEO chains of the P123 surfactant can be inserted into the silica pore walls, primary mesopores may be connected by secondary tunnels, both micropores and small mesopores. These are responsible for keeping nanowire arrays connected in nanocast replica structures, so that the latter are also mesoporous.

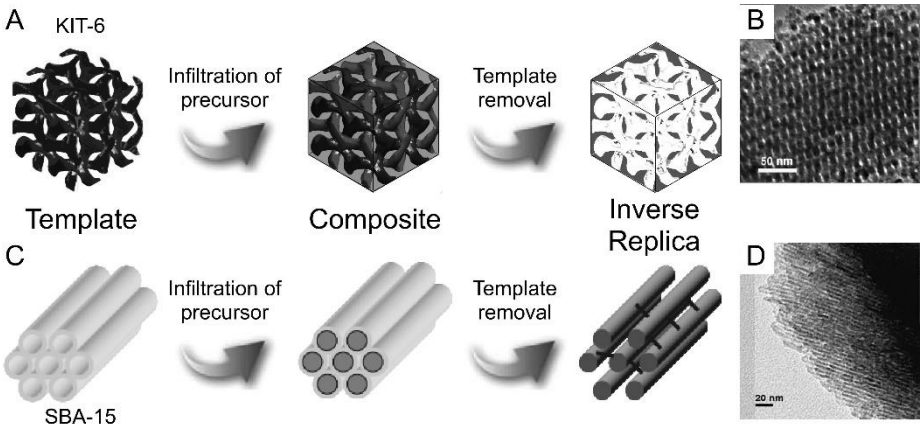

Figure 1.7 Nanocasting of mesoporous electrode materials. (A) A scheme illustrating the nanocasting process in mesoporous silica KIT-6 with a double-gyroid, cubic mesopore structure. The white areas represent mesopores, and the areas shaded in grey represent the silica phase. Dark areas correspond to the

precursor in the composite and to the final solid phase after template removal. (B) TEM image of mesoporous anatase TiO_2, nanocast from KIT-6.[96] (C) The nanocasting process in mesoporous silica SBA-15 with 2D hexagonal mesopore structure.[86] In the final replica, nanowires may be interconnected by small struts resulting from secondary pores. (D) TEM image of mesoporous Si-C nanowire arrays that were nanocast from SBA-15.[97] Reproduced with permission.[86,96,97] Copyright 2010, Wiley-VCH.[86] Copyright 2006, Wiley-VCH.[97] Copyright 2008, American Chemical Society.

Mesoporous electrodes with numerous compositions have been synthesized by hard templating with KIT-6, including the cathode materials β-MnO_2 (tetragonal rutile structure),[98-100] $LiFePO_4$ (olivine structure),[101] and $Li_{1+x}Mn_{2-x}O_4$ (spinel structure),[102] as well as the anode materials Cr_2O_3,[90,103] Co_3O_4,[88,104] anatase TiO_2,[96] rutile TiO_2,[105] NiO,[89], SnO_2,[106] WO_{3-x},[107] and MoO_2.[108] In some of these examples (e.g., SnO_2), nanocasting methods produce mesoporous SnO_2 with higher crystallinity and more ordered mesostructures than soft templating because the hard template protects particles from excessive grain growth by sintering. As discussed later, many of these electrodes demonstrated superior rate capacity compared to corresponding electrodes prepared from bulk particles. The replica structures typically exhibit similar order as the original KIT-6 template and much higher surface areas than bulk particles. Several of the studies pointed out complex pore structures in the products. For example, mesoporous WO_{3-x} templated from KIT-6 exhibited a bimodal mesopore size distribution (4 nm, ~20 nm pores).[107] For mesoporous TiO_2 with ca. 6.5 nm-thick anatase walls, a trimodal pore size distribution was found with peaks at 5 and 11 nm resulting from inverse replication of the silica template and at 50 nm from interparticle voids (Figure 1.7B).[96]

In the context of LIB electrode materials, nanocasting with SBA-15 has been applied to synthesize anatase and rutile TiO_2,[105,109] Cr_2O_3,[90] $LiFePO_4$,[101] Co_3O_4,[88] Si,[97] and SnO_2,[106] where either discrete or connected mesoporous nanowire bundles were observed. As a typical example, the mesoporous nanowires in the case of SnO_2 were composed of aggregated 5–6 nm nanoparticles.[106] A similar structure consisting of packed nanowires was observed for mesoporous MoS_2, nanocast from SBA-15 using phosphomolybdic acid and treatment with H_2S.[110] Although it is usually desirable to remove all of the silica template from the electrode material because silica does not contribute to lithium ion storage and is electronically insulating, residual silica can provide some mechanical

stabilization. For instance, in the case of mesoporous SnO_2 templated from SBA-15 by melt-infiltration of $SnCl_2 \cdot 2H_2O$, a small amount (6 wt%) of residual SiO_2 resulting from incomplete etching was believed to prop up the SnO_2 phase.[111] As a result, the mesoporous SnO_2 was structurally stable up to 700 ˚C.

Instead of using a mesoporous silica as a host, mesoporous carbon can be impregnated with active material without the need to remove this matrix. The carbon scaffold provides a built-in conductive network and facilitates higher charge/discharge rates for the nanocomposite. An example involves a mesoporous carbon nanocomposite with NiO.[91] The CMK-3 mesoporous carbon was itself prepared by nanocasting in mesoporous SBA-15 silica, using a sucrose/sulfuric acid solution as the precursor. Subsequently, CMK-3 was heated in sulfuric acid and then impregnated with an aqueous solution containing nickel nitrate and citric acid. The composite was heated in nitrogen, forming an intimate mixture of mesoporous carbon and ~37 wt% NiO nanoparticles. While the mesopore volume dropped to 10% of its original value, significant micropore volume remained in the nanocomposite.

1.3.1.2.3 Non-templated porous materials.

The main focus of this chapter is on porous electrode materials with well-controlled pore sizes or architectures, which are best achieved by using templating methods. However, numerous template-free methods of obtaining porous electrodes are available, including electrodeposition,[112] ultrasonication,[113] intercalation,[114] hydro- or solvothermal syntheses[115,116] and more. While these tend to produce materials with broader pore size distributions, some of the methods are simpler than those requiring templates, and they can yield materials with features and critical dimensions that benefit the performance of an electrode.

Aerogel syntheses are well suited to produce mesoporous materials. They have been widely applied to vanadium oxide systems. $V_2O_5 \cdot xH_2O$ aerogels are synthesized by sol-gel methods employing supercritical drying, freeze drying, or solvent exchange methods to maintain open pores after solvent removal by minimizing damaging capillary forces.[66,117] The resulting structures are three-dimensional networks of a solid phase surrounded by a continuous, random mesopore or macropore network. In typical vanadia

systems, the solid phase consists of ribbons composed of nanocrystalline nanoparticles (10–50 nm) whose crystalline phase and dimensions can be controlled through subsequent annealing in various atmospheres.[117] In these thermal treatments the atmosphere also determines the oxidation state of the vanadium oxide product. For example, the annealing of $V_2O_5 \cdot xH_2O$ aerogels at 400 ˚C under high vacuum produced the vanadia bronze, VO_2(B); V_6O_{13} was formed under Ar; and in air, the product was V_2O_5.[117] However, sintering during thermal treatment can result in densification of the material and reduce the surface areas and pore volumes. It is possible to incorporate conductive components like single-walled carbon nanotubes (SWNT) during the synthesis of the aerogel.[118] In the case of a vanadia aerogel/SWNT composite, the SWNT formed ca. 10 nm diameter bundles intertwined between 20–30 nm vanadia ribbons. The two phases formed good electrical contact while maintaining sufficient room for electrolyte access.

Several template-free syntheses involving hydrothermal, solvothermal, or simple hydrolysis reactions have been employed to produce mesoporous microspheres. [119] [115] The spherical morphology facilitates higher packing densities in an assembled electrode than individual nanoparticles. In most cases, the microspheres themselves consist of aggregates of nanoparticles either throughout the microsphere or in a shell layer around a hollow core. In either case, textural mesoporosity is present throughout the nanoparticle aggregates.

Carbon-containing precursors may be mixed in with the precursors for the target electrode material to obtain hollow microspheres.[120,121] Depending on experimental conditions, the carbon-containing additives may lead to macroporous structures rather than hollow spheres. In a synthesis of $Li(Ni_{1/3}Co_{1/3}Mn_{1/3})O_2$ from acetate precursors of the metals dissolved in an aqueous solution that also contained resorcinol and formaldehyde, RF polymer was interspersed throughout the electroactive phase.[122] Calcination at 950 ˚C removed the polymer phase, leading to formation of disordered macropores surrounded by 500–1000 nm diameter particles of $Li(Ni_{1/3}Co_{1/3}Mn_{1/3})O_2$. Although not mentioned in the publication, it is possible that the resorcinol-formaldehyde gel component helped achieve compositional homogeneity in this multicomponent electrode material, similar to the role of complexing agents in Pechini-type syntheses.[123] Irregular macropores were also generated in an SnP_2O_7 electrode material where sucrose was added to the reaction mixture before the hydrothermal synthesis.[124]

1.3.1.2.4 Electrode materials with hierarchical porosity.

Hierarchy in pore sizes permits better permeation of an electrolyte through a porous electrode. Secondary mesopores within macropore walls further reduce ion diffusion paths through the electrode. They increase the interfacial area between the electrolyte and the electrode. They also provide a way of hosting active material, an electrically conductive component, or a stabilizing material within the walls of a porous matrix while still maintaining access for the electrolyte phase.

In general, hierarchical macroporous-mesoporous materials can be produced either by the introduction of macropores into mesoporous materials (e.g., by etching) or by the introduction of mesopores into macroporous materials (e.g., by dual templating). Depending on the approach, the distribution of the pores may be random or ordered in the porous substrates. If mass transport is the more important factor, it is preferable to have an ordered, interconnected macropore system with additional mesopores introduced into the walls. This is usually the case when electrolytes with ions having a small diffusion coefficient or viscous solvents are used (ionic liquids or high molecular weight solvents). An ordered, interconnected macropore system with low tortuosity facilitates electrolyte diffusion in and out of the active materials. If mass transport is less important, then the macropores can be randomly distributed in the mesoporous substrate, but now they only function as inner reservoirs supplying electrolyte to the surrounding mesopores.

Several of the structures discussed above possess porosity on multiple length scales if one considers textural mesoporosity between nanocrystals as one of the length scales. However, it is possible to introduce hierarchical porosity with greater control over pore architecture by employing multiple hard and/or soft templates in a synthesis. The procedures are similar to those used to prepare macroporous materials, except for the fact that surfactants, supramolecules, or nanoparticles are added into the precursors before the infiltration of the macropore templates.

3DOM Sn/Ni alloy films with complex hierarchical structure were fabricated by depositing polystyrene spheres within photoresist patterns on a copper substrate, annealing the spheres to stabilize the colloidal crystals, and electroplating a Sn-Ni alloy within the colloidal crystals (Figure 1.8A–C).[125,126] The resulting micro-patterned macroporous Sn-Ni alloy anode exhibited a high areal capacity (i.e., a high capacity per unit area). The areal

discharge capacity increased with the open pore ratio of the photoresist substrate (cylindrical pattern < square pattern < hexagonal pattern). Another interesting example of patterning a potential electrode material with hierarchical porosity involved dip-coating of a TiO_2 precursor/surfactant solution in a lithographically patterned, microstructured photopolymer resin.[127]

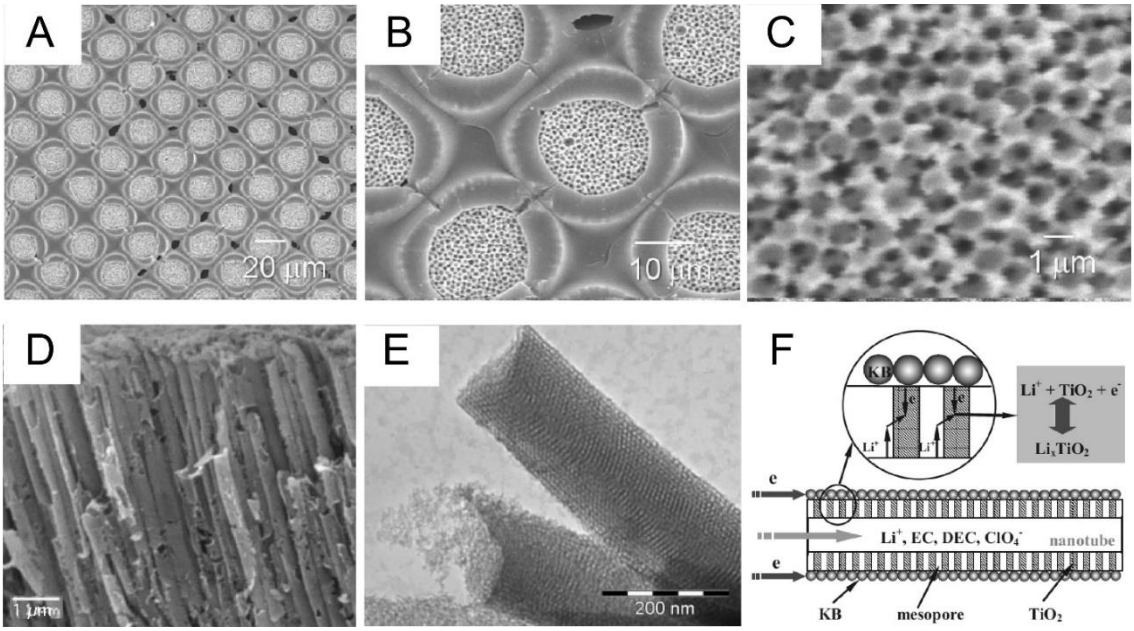

Figure 1.8 Electrode structures with hierarchical porosity. (A)–(C) SEM images of patterned 3DOM Sn-Ni alloy films at various magnifications, showing the lithographic patterns and the colloidal-crystal-templated macropores.4 (D)–(F) Mesoporous titania nanotubes templated in an AAO membrane.[128] (D) SEM image of nanotube array. (E) TEM image showing the hexagonally ordered mesopore structure in the walls of the hollow nanotubes. (F) Schematic diagram of the transport path of lithium ions and electrons in the mesoporous titania nanotubes. Reproduced with permission.[126,128] Copyright 2010, Elsevier Ltd. [128] Copyright 2007, Wiley-VCH.

Templating in anodic aluminum oxide (AAO) films or membrane filters is a well developed technique to prepare nanotube structures,[129] including those of interest for high rate LIBs.[130,131] This type of templating can be combined with surfactant templating to obtain nanotubes containing multiple pore sizes. Titania nanotubes with mesoporous walls were grown within AAO membranes, employing an alkoxide precursor of titanium and the P123 triblock copolymer as the structure-directing agent.[128] Hollow tubes were formed as solvent evaporated due to an affinity between the gel and the hydrophilic alumina walls,

causing the gel to shrink in a direction perpendicular to the pore channels. After calcination, the membrane was removed by dissolution in NaOH solution. Arrays of well-aligned nanotubes (~200 nm outer diameter) formed after treatment in supercritical CO_2 (Figure 7D–F). Without the supercritical drying step, surface tension forces between nanotubes caused the nanotubes to aggregate and entangle. The hierarchical pore structure facilitated the distribution of the electrolyte through ca. 140 nm channels and ~7.5 nm mesopores, leading to excellent high rate performance (150 mAh/g at 240C rate) and good cycle performance.

The most common examples of hierarchical electrode templating with colloidal crystals involve carbon systems, although some oxide materials with hierarchical pore structure, such as Fe_2O_3 have also been fabricated by this approach.[132] Carbon structures can be prepared by nanocasting with hierarchically structured 3DOM/m silica prepared using both surfactants and polymeric colloidal crystals (Figure 1.9A).[133] They can also be synthesized by more direct methods, employing a colloidal crystal template with either a triconstituent precursor (silicon alkoxide, resol, block-copolymer surfactant, Figure 1.9B)[134] or a simpler mixture of phenol-formaldehyde with a block-copolymer surfactant.[135] The last approach avoids the use of caustic chemicals for silica etching and provides some control over the mesopore geometry (2D hexagonal vs. cubic mesopores surrounding macropores) The triconstituent method, on the other hand, produces the largest mesopores and provides a bimodal mesopore size distribution in the carbon skeleton around the macropores. The larger mesopores make the triconstituent-derived or the nanocast monoliths most suitable for preparations of nanocomposite electrodes in which a precursor for active material is imbibed in the carbon host.[136,137] All three of these 3DOM/m carbon materials, when used as monolithic electrodes in a lithium battery, provide improved rate capabilities compared to 3DOM C lacking the templated mesopores.

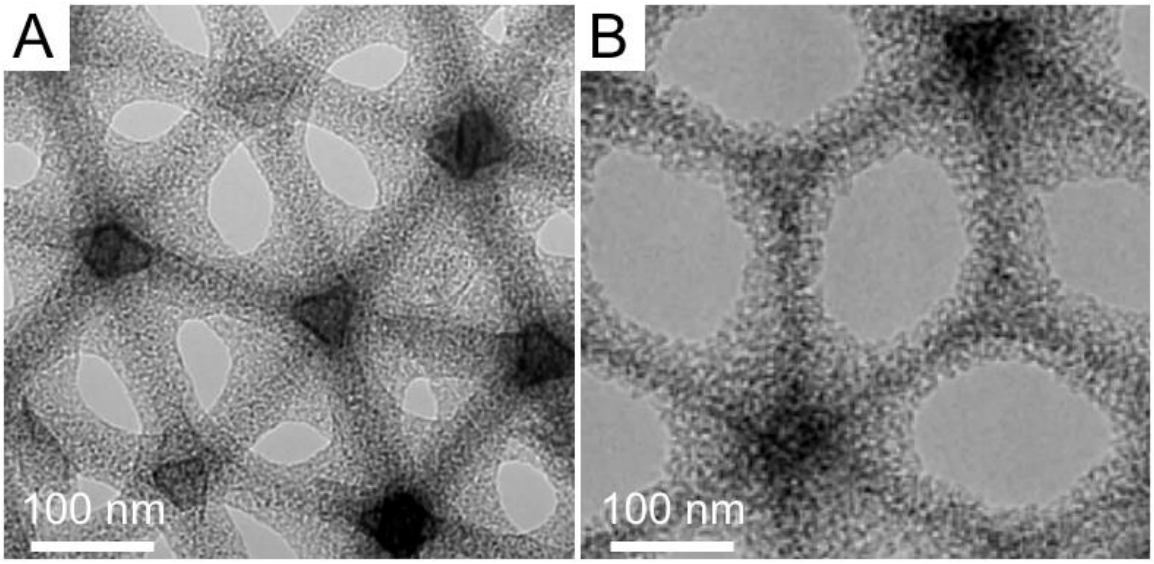

Figure 1.9 TEM images of nanoporous carbon materials with hierarchical pore structure prepared by (A) nanocasting,[133] (B) a triconstituent synthesis.[134] Macropores arise from colloidal crystal templating. Mesopores have wormlike geometries in (A) and (B). Image A reproduced with permission.[133] Copyright 2006, American Chemical Society.

1.4 Summary of Thesis Work

The fabrication of nanostructured and nanoporous materials for energy storage and sensing applications is the basis of this thesis. Chapter 2 describes the preparation of hierarchically porous $LiFePO_4$/C composites by using an amphiphilic surfactant and colloidal crystals as dual templates. The products feature highly ordered macropores and mesoporous walls, in which the $LiFePO_4$ phase is found mainly in the octahedral sites connected by the carbon phase in the tetrahedral site. This special structure results from the confinement of $LiFePO_4$-carbon precursor in the interstitial spaces between the colloidal spheres. The obtained $LiFePO_4$/C composites have very high surface areas and good mass transport. They showed very impressive rate performance when used as cathode materials for LIBs. The results of Chapter 2 are further expanded in Chapter 3, which describes the preparation of sub-micron and micron-sized spherical $LiFePO_4$ particles by confining $LiFePO_4$-carbon precursors in a two dimensional space (i.e., a thin film). The product targets high volumetric energy density LIBs since uniform spherical particles can generally be packed with higher efficiency than randomly shaped particles. The focus of Chapter 4 is on

electrode materials for supercapacitors with high energy and power densities. This could be achieved with hierarchical porous carbons with ordered mesopores and microporous walls. The challenges are not only the preparation of the carbonaceous materials but also the fabrication of nano-sized colloidal templates. As described in this chapter, monodisperse silica spheres with sizes ranging from 8 to 40 nm were successfully prepared and used as templates for the preparation of ordered mesoporous carbons. The hierarchical porous carbon materials were found to outperform commercial activated carbon, as they displayed high capacities and extremely high rate capabilities. Chapter 5 describes the preparation of several ordered mesoporous silica thin films with different structures and their use as host materials for fluorescent compounds. The composite films are then used as sensors to detect nitroaromatic compounds, and showed excellent quenching performance and long-term storage stability.

1.5 References

(1) Yang, Z.; Zhang, J.; Kintner-Meyer, M. C. W.; Lu, X.; Choi, D.; Lemmon, J. P.; Liu, J. *Chem. Rev.* **2011**, *111*, 3577.

(2) Axsen, J.; Kurani, K. S.; Burke, A. *Transport Policy* **2010**, *17*, 173.

(3) Goodenough, J. B.; Kim, Y. *Chem. Mater.* **2010**, *22*, 587.

(4) Tarascon, J. M.; Armand, M. *Nature* **2001**, *414*, 359.

(5) Winter, M.; Brodd, R. J. *Chem. Rev.* **2004**, *104*, 4245.

(6) Rakhi, R. B.; Chen, W.; Cha, D.; Alshareef, H. N. *Advanced Energy Materials* **2012**, *2*, 381.

(7) Myung, S.-T.; Takahashi, N.; Komaba, S.; Yoon, C. S.; Sun, Y.-K.; Amine, K.; Yashiro, H. *Adv. Funct. Mater.* **2011**, *21*, 3231.

(8) Arico, A. S.; Bruce, P.; Scrosati, B.; Tarascon, J.-M.; van Schalkwijk, W. *Nat. Mater.* **2005**, *4*, 366.

(9) Huggins, R. A. 2009.

(10) Levi, M. D.; Aurbach, D. *J. Phys. Chem. B* **1997**, *101*, 4641.

(11) Simon, P.; Gogotsi, Y. *Nat Mater* **2008**, *7*, 845.

(12) Ji, X. L.; Lee, K. T.; Nazar, L. F. *Nat. Mater.* **2009**, *8*, 500.

(13) Lytle, J. C.; Wallace, J. M.; Sassin, M. B.; Barrow, A. J.; Long, J. W.; Dysart, J. L.; Renninger, C. H.; Saunders, M. P.; Brandell, N. L.; Rolison, D. R. *Energ. Environ. Sci.* **2011**, *4*, 1913.

(14) Ren, X.; Zhang, S. S.; Tran, D. T.; Read, J. *J. Mater. Chem.* **2011**, *21*, 10118.

(15) Conway, B. *Electrochemical supercapacitors: scientific fundamentals and technological applications (POD)*; Kluwer Academic/plenum. New York, 1999.

(16) Becker, H. I. In *United State Patent Office*; Company, G. E., Ed.; General Electric Company: USA, 1957; Vol. 2800616.

(17) Miller, J. *Battery+ Energy Storage Technology* **2007**, 61.

(18) Miller, J. R.; Burke, A. F. *The Electrochemical Society Interface* **2008**, *17*, 53.

(19) Zhi, M.; Xiang, C.; Li, J.; Li, M.; Wu, N. *Nanoscale* **2013**, *5*, 72.

(20) Shukla, A. K.; Prem Kumar, T. *Wiley Interdisciplinary Reviews: Energy and Environment* **2013**, *2*, 14.

(21) Zhai, Y.; Dou, Y.; Zhao, D.; Fulvio, P. F.; Mayes, R. T.; Dai, S. *Adv. Mater.* **2011**, *23*, 4828.

(22) Yuan, C. Z.; Gao, B.; Shen, L. F.; Yang, S. D.; Hao, L.; Lu, X. J.; Zhang, F.; Zhang, L. J.; Zhang, X. G. *Nanoscale* **2011**, *3*, 529.

(23) Oschatz, M.; Kockrick, E.; Rose, M.; Borchardt, L.; Klein, N.; Senkovska, I.; Freudenberg, T.; Korenblit, Y.; Yushin, G.; Kaskel, S. *Carbon* **2010**, *48*, 3987.

(24) Portet, C.; Lillo-Rodenas, M. A.; Linares-Solano, A.; Gogotsi, Y. *Phys. Chem. Chem. Phys.* **2009**, *11*, 4943.

(25) Chmiola, J.; Largeot, C.; Taberna, P.-L.; Simon, P.; Gogotsi, Y. *Science* **2010**, *328*, 480.

(26) Rose, M.; Korenblit, Y.; Kockrick, E.; Borchardt, L.; Oschatz, M.; Kaskel, S.; Yushin, G. *Small* **2011**, *7*, 1108.

(27) Liu, H.-J.; Wang, J.; Wang, C.-X.; Xia, Y.-Y. *Advanced Energy Materials* **2011**, *1*, 1101.

(28) Lotufo, G. R.; Farrar, J. D.; Inouye, L. S.; Bridges, T. S.; Ringelberg, D. B. *Environ. Toxicol. Chem.* **2001**, *20*, 1762.

(29) Krausa, M.; Reznev, A. A.; North Atlantic Treaty Organization. Scientific Affairs Division. *Vapour and trace detection of explosives for anti-terrorism purposes*; Kluwer Academic: Dordrecht ; London, 2004.

(30) Caron, T.; Guillemot, M.; Montméat, P.; Veignal, F.; Perraut, F.; Prené, P.; Serein-Spirau, F. *Talanta* **2010**, *81*, 543.

(31) Nguyen, H. H.; Li, X.; Wang, N.; Wang, Z. Y.; Ma, J.; Bock, W. J.; Ma, D. *Macromolecules* **2009**, *42*, 921.

(32) Long, Y.; Chen, H.; Yang, Y.; Wang, H.; Yang, Y.; Li, N.; Li, K.; Pei, J.; Liu, F. *Macromolecules* **2009**, *42*, 6501.

(33) Li, Z.; Dong, Y. Q.; Lam, J. W. Y.; Sun, J.; Qin, A.; Häußler, M.; Dong, Y. P.; Sung, H. H. Y.; Williams, I. D.; Kwok, H. S.; Tang, B. Z. *Adv. Funct. Mater.* **2009**, *19*, 905.

(34) He, G.; Zhang, G.; Lü, F.; Fang, Y. *Chem. Mater.* **2009**, *21*, 1494.

(35) Zhu, D.; He, Q.; Cao, H.; Cheng, J.; Feng, S.; Xu, Y.; Lin, T. *Appl. Phys. Lett.* **2008**, *93*, 261909.

(36) Narayanan, A.; Varnavski, O. P.; Swager, T. M.; Goodson, T. *J. Phys. Chem. C* **2008**, *112*, 881.

(37) Bai, H.; Li, C.; Shi, G. *Sens. Actuators B Chem.* **2008**, *130*, 777.

(38) Wang, Z.; Wang, Z. Y.; Ma, J.; Bock, W. J.; Ma, D. *Polymer* **2010**, *51*, 842.

(39) Angelos, S.; Johansson, E.; Stoddart, J. F.; Zink, J. I. *Adv. Funct. Mater.* **2007**, *17*, 2261.

(40) Hunks, W. J.; Ozin, G. A. *J. Mater. Chem.* **2005**, *15*, 3716.

(41) Germain, M. E.; Knapp, M. J. *Chem. Soc. Rev.* **2009**, *38*, 2543.

(42) Vu, A.; Qian, Y.; Stein, A. *Advanced Energy Materials* **2012**, *2*, 1056.

(43) Di Renzo, F.; Galarneau, A.; Trens, P.; Fajula, F. *Handbook of Porous Solids* **2002**, *3*, 1311.

(44) Hatton, B.; Landskron, K.; Whitnall, W.; Perovic, D.; Ozin, G. A. *Acc Chem Res* **2005**, *38*, 305.

(45) Wan, Y.; Shi, Y.; Zhao, D. *Chemical communications (Cambridge, England)* **2007**, 897.

(46) Kleitz, F. In *Handbook of Heterogeneous Catalysis (2nd Ed.)*; Ertl, G., Ed. 2008; Vol. 1, p 178.

(47) El-Safty, S. A. *J. Porous Mater.* **2011**, *18*, 259.

(48) Edler, K. J. In *Porous Materials*; Bruce, D. W., O'Hare, D., Walton, R. I., Eds.; Wiley: Chichester, 2011, p 69.

(49) Lu, Y.; Ganguli, R.; Drewien, C. A.; Anderson, M. T.; Brinker, C. J.; Gong, W.; Guo, Y.; Soyez, H.; Dunn, B.; Huang, M. H.; Zink, J. I. *Nature* **1997**, *389*, 364.

(50) Grosso, D.; Cagnol, F.; de A. A. Soler-Illia, G. J.; Crepaldi, E. L.; Amenitsch, H.; Brunet-Bruenau, A.; Bourgeois, A.; Sanchez, C. *Adv. Funct. Mater.* **2004**, *14*, 309.

(51) Das, S. K.; Darmakolla, S.; Bhattacharyya, A. J. *J. Mater. Chem.* **2010**, *20*, 1600.

(52) Saravanan, K.; Ananthanarayanan, K.; Balaya, P. *Energy Environ. Sci.* **2010**, *3*, 939.

(53) Wang, D.; Choi, D.; Yang, Z.; Viswanathan, V. V.; Nie, Z.; Wang, C.; Song, Y.; Zhang, J.-G.; Liu, J. *Chem. Mater.* **2008**, *20*, 3435.

(54) S. Zhu, H. Z., T. Miyoshi, M. Hibino, I. Honma, M. Ichihara, *Adv. Mater.* **2004**, *16*, 2012.

(55) Shiva, K.; Asokan, S.; Bhattacharyya, A. J. *Nanoscale* **2011**, *3*, 1501.

(56) Guerra, E. M.; Cestarolli, D. T.; Oliveira, H. P. *J. Sol-Gel Sci. Technol.* **2010**, *54*, 93.

(57) Nara, H.; Fukuhara, Y.; Takai, A.; Komatsu, M.; Mukaibo, H.; Yamauchi, Y.; Momma, T.; Kuroda, K.; Osaka, T. *Chem. Lett.* **2008**, *37*, 142.

(58) Whitehead, A. H.; Elliott, J. M.; Coleman, N. R. B.; Bartlett, P. N.; Attard, G. S.; Owen, J. R. *Proc. Electrochem. Soc.* **1999**, *98-16*, 128.

(59) Brezesinski, K.; Haetge, J.; Wang, J.; Mascotto, S.; Reitz, C.; Rein, A.; Tolbert, S. H.; Perlich, J.; Dunn, B.; Brezesinski, T. *Small* **2011**, *7*, 407.

(60) Wang, Y.; Smarsly, B. M.; Djerdj, I. *Chem. Mater.* **2010**, *22*, 6624.

(61) Haetge, J.; Hartmann, P.; Brezesinski, K.; Janek, J.; Brezesinski, T. *Chem. Mater.* **2011**, *23*, 4384.

(62) Krins, N.; Bass, J. D.; Grosso, D.; Henrist, C.; Delaigle, R.; Gaigneaux, E. M.; Cloots, R.; Vertruyen, B. n. d.; Sanchez, C. m. *Chem. Mater.* **2011**, *23*, 4124.

(63) Schroden, R. C.; Stein, A. In *Colloids and Colloid Assemblies: Synthesis, Modification, Organization and Utilization of Colloid Particles*; Caruso, F., Ed.; Wiley-VCH: Weinheim, 2004, p 465.

(64) Stein, A.; Li, F.; Denny, N. R. *Chem. Mater.* **2008**, *20*, 649.

(65) Sakamoto, J. S.; Dunn, B. *J. Mater. Chem.* **2002**, *12*, 2859.

(66) Dong, W.; Sakamoto, J. S.; Dunn, B. *Sci. Tech. Adv. Mater.* **2003**, *4*, 3.

(67) Yan, H.; Sokolov, S.; Lytle, J. C.; Stein, A.; Zhang, F.; Smyrl, W. H. *J. Electrochem. Soc.* **2003**, *150*, A1102.

(68) Tonti, D.; Torralvo, M. J.; Enciso, E.; Sobrados, I.; Sanz, J. *Chem. Mater.* **2008**, *20*, 4783.

(69) Yan, H.; Blanford, C. F.; Holland, B. T.; Smyrl, W. H.; Stein, A. *Chem. Mater.* **2000**, *12*, 1134.

(70) Ergang, N. S.; Lytle, J. C.; Yan, H.; Stein, A. *J. Electrochem. Soc.* **2005**, *152*, A1989.

(71) Eftekhari, A. *Solid State Ionics* **2003**, *161*, 41.

(72) Doherty, C. M.; Caruso, R. A.; Smarsly, B. M.; Drummond, C. J. *Chem. Mater.* **2009**, *21*, 2895.

(73) Cui, W.; Liu, H.; Wang, C.; Xia, Y. *Electrochem. Commun.* **2008**, *10*, 1587.

(74) Kavan, L.; Zukalova, M.; Kalbac, M.; Graetzel, M. *J. Electrochem. Soc.* **2004**, *151*, A1301.

(75) Yamada, H.; Yamato, T.; Moriguchi, I.; Kudo, T. *Solid State Ionics* **2004**, *175*, 195.

(76) Bing, Z.; Yuan, Y.; Wang, Y.; Fu, Z.-W. *Electrochem. Solid-State Lett.* **2006**, *9*, A101.

(77) Jusic, A. *Lijecnicki vjesnik* **1992**, *114*, 166.

(78) Woo, S.-W.; Dokko, K.; Kanamura, K. *Electrochim. Acta* **2007**, *53*, 79.

(79) Li, Z. H.; Zhao, T. P.; Zhan, X. Y.; Gao, D. S.; Xiao, Q. Z.; Lei, G. T. *Electrochim. Acta* **2010**, *55*, 4594.

(80) Lytle, J. C.; Yan, H.; Ergang, N.; Smyrl, W. H.; Stein, A. *J. Mater. Chem.* **2004**, *14*, 1616.

(81) Kotobuki, M.; Isshiki, Y.; Munakata, H.; Kanamura, K. *Electrochim. Acta* **2010**, *55*, 6892.

(82) Wu, M.-S.; Lin, Y.-P. *Electrochim. Acta* **2011**, *56*, 2068.

(83) Sommer, R.; Schaller, H. *Molecular & general genetics : MGG* **1979**, *168*, 331.

(84) Polarz, S.; Antonietti, M. *Chem. Commun.* **2002**, 2593.

(85) Yang, H.; Zhao, D. *J. Mater. Chem.* **2005**.

(86) Lu, a.-H.; Schüth, F. *Adv. Mater.* **2006**, *18*, 1793.

(87) Lu, A.-H.; Zhao, D.; Wan, Y. *Nanocasting - A Versatile Strategy for Creating Nanostructured Porous Materials*; RSC Publishing: Cambridge, UK, 2009.

(88) Wang, G.; Liu, H.; Horvat, J.; Wang, B.; Qiao, S.; Park, J.; Ahn, H. *Chem. Eur. J.* **2010**, *16*, 11020.

(89) Liu, H.; Wang, G.; Liu, J.; Qiao, S.; Ahn, H. *J. Mater. Chem.* **2011**, *21*, 3046.

(90) Liu, H.; Du, X.; Xing, X.; Wang, G.; Qiao, S. Z. *Chemical communications (Cambridge, England)* **2012**, *48*, 865.

(91) Cheng, M.-Y.; Hwang, B.-J. *J. Power Sources* **2010**, *195*, 4977.

(92) Kleitz, F.; Choi, S. H.; Ryoo, R. *Chemical communications (Cambridge, England)* **2003**, 2136.

(93) Kim, T.-W.; Kleitz, F.; Paul, B.; Ryoo, R. *J. Am. Chem. Soc.* **2005**, *127*, 7601.

(94) Zhao, D.; Feng, J.; Huo, Q.; Melosh, N.; Fredrickson, G. H.; Chmelka, B. F.; Stucky, G. D. *Science* **1998**, *279*, 548.

(95) Zhao, D.; Huo, Q.; Feng, J.; Chmelka, B. F.; Stucky, G. D. *J. Am. Chem. Soc.* **1998**, *120*, 6024.

(96) Ren, Y.; Hardwick, L. J.; Bruce, P. G. *Angew. Chem. Int. Ed.* **2010**, *49*, 2570.

(97) Kim, H.; Cho, J. *Nano Lett.* **2008**, *8*, 3688.

(98) Luo, J.-Y.; Zhang, J.-J.; Xia, Y.-Y. *Chem. Mater.* **2006**, *18*, 5618.

(99) Jiao, F.; Bruce, P. G. *Adv. Mater.* **2007**, *19*, 657.

(100) Ren, Y.; Armstrong, A. R.; Jiao, F.; Bruce, P. G. *J. Am. Chem. Soc.* **2009**, *132*, 996.

(101) Lim, S.; Yoon, C. S.; Cho, J. *Chem. Mater.* **2008**, *20*, 4560.

(102) Feng Jiao, J. B., Adrian H. Hill, Peter G. Bruce, *Angew. Chem. Int. Ed.* **2008**, *47*, 9711.

(103) Dupont, L.; Laruelle, S.; Grugeon, S.; Dickinson, C.; Zhou, W.; Tarascon, J. M. *J. Power Sources* **2008**, *175*, 502.

(104) Shaju, K. M.; Jiao, F.; Debart, A.; Bruce, P. G. *Phys. Chem. Chem. Phys.* **2007**, *9*, 1837.

(105) Yue, W.; Xu, X.; Irvine, J. T. S.; Attidekou, P. S.; Liu, C.; He, H.; Zhao, D.; Zhou, W. *Chem. Mater.* **2009**, *21*, 2540.

(106) Kim, H.; Cho, J. *J. Mater. Chem.* **2008**, *18*, 771.

(107) Yoon, S.; Jo, C.; Noh, S. Y.; Lee, C. W.; Song, J. H.; Lee, J. *Phys Chem Chem Phys* **2011**, *13*, 11060.

(108) Shi, Y.; Guo, B.; Corr, S. A.; Shi, Q.; Hu, Y.-S.; Heier, K. R.; Chen, L.; Seshadri, R.; Stucky, G. D. *Nano Lett.* **2009**, *9*, 4215.

(109) Yue, W.; Randorn, C.; Attidekou, P. S.; Su, Z.; Irvine, J. T. S.; Zhou, W. *Adv. Funct. Mater.* **2009**, *19*, 2826.

(110) Fang, X.; Yu, X.; Liao, S.; Shi, Y.; Hu, Y.-S.; Wang, Z.; Stucky, G. D.; Chen, L. *Micropor. Mesopor. Mater.* **2012**, *151*, 418.

(111) Shon, J. K.; Kim, H.; Kong, S. S.; Hwang, S. H.; Han, T. H.; Kim, J. M.; Pak, C.; Doo, S.; Chang, H. *J. Mater. Chem.* **2009**, *19*, 6727.

(112) Ke, F.-S.; Huang, L.; Wei, H.-B.; Cai, J.-S.; Fan, X.-Y.; Yang, F.-Z.; Sun, S.-G. *J. Power Sources* **2007**, *170*, 450.

(113) Kim, J. M.; Huh, Y. S.; Han, Y.-K.; Cho, M. S.; Kim, H. J. *Electrochem. Comm.* **2012**, *14*, 32.

(114) Ha, H.-W.; Kim, T. W.; Choy, J.-H.; Hwang, S.-J. *J. Phys. Chem. C* **2009**, *113*, 21941.

(115) Lee, K.-H.; Song, S.-W. *ACS. Appl. Mater. Interfaces* **2011**, *3*, 3697.

(116) Qu, B.; Zhang, M.; Lei, D.; Zeng, Y.; Chen, Y.; Chen, L.; Li, Q.; Wang, Y.; Wang, T. *Nanoscale* **2011**, *3*, 3646.

(117) Li, H.; He, P.; Wang, Y.; Hosono, E.; Zhou, H. *J. Mater. Chem.* **2011**, *21*, 10999.

(118) Sakamoto, J. S.; Dunn, B. *J. Electrochem. Soc.* **2002**, *149*, A26.

(119) Wang, J.; Zhou, Y.; Hu, Y.; O'Hayre, R.; Shao, Z. *J. Phys. Chem. C* **2011**, *115*, 2529.

(120) Zhang, F.; Zhang, Y.; Song, S.; Zhang, H. *J. Power Sources* **2011**, *196*, 8618.

(121) Demir-Cakan, R.; Hu, Y.-S.; Antonietti, M.; Maier, J.; Titirici, M.-M. *Chem. Mater.* **2008**, *20*, 1227.

(122) Shaju, K. M.; Bruce, P. G. *Adv. Mater.* **2006**, *18*, 2330.

(123) Pechini, M. P. *U. S. Patent* **1967**, No. 3.

(124) Li, Y.; Li, J. *J. Phys. Chem. C* **2008**, *112*, 14216.

(125) Kotobuki, M.; Okada, N.; Kanamura, K. *Chem. Commun.* **2011**, *47*, 6144.

(126) Woo, S.-W.; Okada, N.; Kotobuki, M.; Sasajima, K.; Munakata, H.; Kajihara, K.; Kanamura, K. *Electrochim. Acta* **2010**, *55*, 8030.

(127) Heinroth, F.; Münzer, S.; Feldhoff, A.; Passinger, S.; Cheng, W.; Reinhardt, C.; Chichkov, B.; Behrens, P. *Journal of Materials Science* **2009**, *44*, 6490.

(128) Wang, K.; Wei, M.; Morris, M. A.; Zhou, H.; Holmes, J. D. *Adv. Mater.* **2007**, *19*, 3016.

(129) Martin, C. R. *Science* **1994**, *266*, 1961.

(130) Li, N.; Martin, C. R. *J. Electrochem. Soc.* **2001**, *148*, A164.

(131) Sides, C. R.; Croce, F.; Young, V. Y.; Martin, C. R.; Scrosati, B. *Electrochem. Solid-St. Lett.* **2005**, *8*, A484.

(132) Zhang, R.; Dai, H.; Du, Y.; Zhang, L.; Deng, J.; Xia, Y.; Zhao, Z.; Meng, X.; Liu, Y. *Inorg. Chem.* **2011**, *50*, 2534.

(133) Wang, Z.; Li, F.; Ergang, N. S.; Stein, A. *Chem. Mater.* **2006**, *18*, 5543.

(134) Wang, Z.; Stein, A. *Chem. Mater.* **2008**, *20*, 1029.

(135) Wang, Z.; Kiesel, E. R.; Stein, A. *J. Mater. Chem.* **2008**, *18*, 2194.

(136) Wang, Z.; Li, F.; Ergang, N. S.; Stein, A. *Carbon* **2008**, *46*, 1702.

(137) Wang, Z.; Fierke, M. A.; Stein, A. *J. Electrochem. Soc.* **2008**, *155(9)*, A658.

CHAPTER 2

3DOM/m $LiFePO_4$/C Composites as Cathode Materials for High Rate Performance Lithium Ion Batteries

Outline

Reproduced in part with permission from ref. 40.

Copyright © 2011 American Chemical Society

2.1 Introduction

In recent years, much research on cathode materials for lithium ion batteries has focused on $LiFePO_4$, because it has several advantageous features for large volume energy storage applications, e.g., in electric vehicles (EVs) and hybrid electric vehicles (HEVs).[1] Currently, most lithium ion batteries designed for portable devices use cathodes based on $LiCoO_2$, but this material is relatively expensive and toxic compared to several alternative cathode materials and presents safety concerns when the electrode is overcharged, especially at high temperatures.[2,3] Overcharging causes the collapse of the $LiCoO_2$ structure, which is accompanied by evolution of oxygen and the potential for an explosion.[4,5] These drawbacks can be mitigated to some degree by using mixed metal oxides ($LiNi_xCo_{1-x}O_2$ and $LiMn_xNi_yCo_{1-x-y}O_2$), but the high cost and environmental effects of Co-based cathodes remain unavoidable. Unlike $LiCoO_2$, olivine $LiFePO_4$ and other phosphate-based cathodes have strong P-O covalent bonds, which stabilize the structure, preventing abrupt oxygen evolution.[1] Because of the relative abundance of iron ores, iron-based cathodes are less costly than Co-containing electrodes. Furthermore, olivine $LiFePO_4$ has a reasonably high theoretical capacity (170 mA h g^{-1}) with almost no capacity fading even after a few hundred cycles. However, the low electronic conductivity (10^{-9} to 10^{-10} S cm^{-1}),[6] and slow one-dimensional lithium diffusion limit the high rate performance of olivine $LiFePO_4$.

To overcome the low electronic conductivity, $LiFePO_4$ particles are usually coated with conductive agents (carbon, polymers, RuO_2, or others) or doped with supervalent cations.[7-9] Chung et al. found that the conductivity of olivine $LiFePO_4$ doped with Mg^{2+}, Al^{3+}, Ti^{4+}, Zr^{4+}, Nb^{5+}, or W^{6+} was improved by up to eight orders of magnitude.[6] Recently, Kang and Ceder synthesized nano-sized $LiFePO_4$ coated with a thin layer of lithium phosphate, which acted as a Li^+ reservoir to direct Li^+ into the *b* and *c* directions of the unit cell, enhancing the diffusion of Li^+ in the particles.[8] This cathode construction could be cycled at rates as high as 400C (i.e., charged and recharged within a few seconds), which would be sufficient for EV and HEV applications. However, it has still not been resolved, whether the high rate performance was due to carbon residues from an organic source or due to the formation of other conductive phases, such as FeP, Fe_2P. Huang et al.[10] prepared a $LiFePO_4$/C

composite by mixing a $LiFePO_4$ precursor with a carbon gel, which inhibited the growth of $LiFePO_4$ particles when treated at high temperature and acted as an electronic conductive matrix in the final composite, giving the material high capacity and good life cycles (158 mA h g^{-1} at C/5 and 120 mA h g^{-1} at 5C rate). Konarova et al.[11] prepared $LiFePO_4$/C composites with different amounts of carbon by ultrasonic spray pyrolysis followed by heat treatment and found that with 1.87 wt% of carbon, the composite exhibited capacities of 140 mA h g^{-1} at C/10 and 84 mA h g^{-1} at 5C.

The slow lithium diffusion can be addressed by decreasing particle dimensions to the nanometer scale to reduce diffusion paths.[12-14] However, the surface chemistry of nanoparticles is more complex than that of their micrometer-sized analogues, and factors such as the interconnectivity of particles, formation of a solid electrolyte interphase (SEI) layer, nucleation and aggregation of particles during cycling strongly affect the performance of the electrode. Gaberscek et al.[15] reported that at a lower rate (<1C), the rate-limiting step depended on active particle sizes, while at higher rates, the rate-determining step depended on how the particles were wired. Therefore, a method to synthesize well-wired $LiFePO_4$ nanoparticles would be interesting for high rate batteries.

Porous materials have been investigated as electrode materials for high rate lithium ion batteries due to their nanometer-sized features and high surface areas, which increase the ion-exchange rates between electrolyte and active material.[16-22] To-date, much of the work on porous electrodes, particularly mesoporous ones, has focused on anode materials such as C, Sn, SnO_2, TiO_2, and their composites, the mesostructures of which are fairly well understood, and which have found applications in various fields including catalysis, separation and adsorption.[19,22-27] In contrast, work on mesoporous cathodes, mostly metal oxides and metal phosphates, has been more limited until recently. The main reason for this is that the electrochemical performance of cathodes tends to be better when these are highly crystalline; higher crystallinity requires higher temperature syntheses, which tend to produce large grains that are incompatible with maintaining ordered mesopore structures.[28-30]

Driven by the needs of the HEV market, a few recent studies have addressed porous cathodes, including cathodes with hierarchical porosity.[15,31-33] Doherty et al.[34,35] prepared macroporous and mesoporous $LiFePO_4$ using poly(methyl methacrylate) (PMMA)

colloidal crystal and surfactant templates which showed that the rate performance of mesoporous $LiFePO_4$ is better than that of macroporous $LiFePO_4$, confirming the importance of a high surface area for improving rate capability. High surface area $LiFePO_4$ could also be obtained by using a mesoporous support. Wang et al.[36] prepared $LiFePO_4$/C composites based on the mesoporous carbon CMK-13, while Doherty et al.[37] prepared $LiFePO_4$ inside hierarchically porous carbon synthesized from a porous silica template. They obtained materials with capacities as high as 118 mA h g^{-1} at 10C for the material built around the CMK-13 support and 124 mA h g^{-1} at 5C when the hierarchical carbon support was used. However, these approaches required separate synthesis steps for the formation of the carbon host and the $LiFePO_4$/carbon composite phase and careful control during infiltration of the inorganic precursor to ensure high loadings of the active phase.

Here we synthesized $LiFePO_4$/carbon composites with hierarchical porosity by a multiconstituent synthesis,[38,39] in which all components (precursors for carbon and $LiFePO_4$ together with surfactant templates) were infiltrated into a colloidal crystal template together.[40] Additional heat treatment was applied to improve the cross-linking and polymerization of the precursor so that a robust, interconnected framework was formed that surrounded the colloidal spheres. Slow ramping rates and multi-step temperature programs were used to transform the precursor into a solid and remove the template. This procedure yielded an inverse opal or three dimensionally ordered macroporous and meso-/microporous (3DOM/m)[41] structure of the target materials. The synthesis of 3DOM/m $LiFePO_4$/C composites is outlined in Figure 2.1. For colloidal spheres with 400–500 nm diameters, structures were typically characterized by 300–400 nm pores connected by 50–100 nm windows and 20–50 nm thick walls. The surfactant templates were intended to introduce additional mesopores into the walls. The built-in carbon phase was intimately mixed with the electrochemically active $LiFePO_4$ phase, effectively wiring $LiFePO_4$ particles together in a long-range ordered network. In this configuration, carbon bridges enhanced the conductivity of the system and helped to maintain the porous structure during cycling. Compared to conventional coating methods, in which micrometer-sized $LiFePO_4$ particles are covered with thin layers of carbon, the connectivity in the 3DOM/m $LiFePO_4$/C composite materials is better defined, surface areas are larger, and particle sizes

of the cathode phase are smaller. Therefore less polarization and improved rate performance are expected.

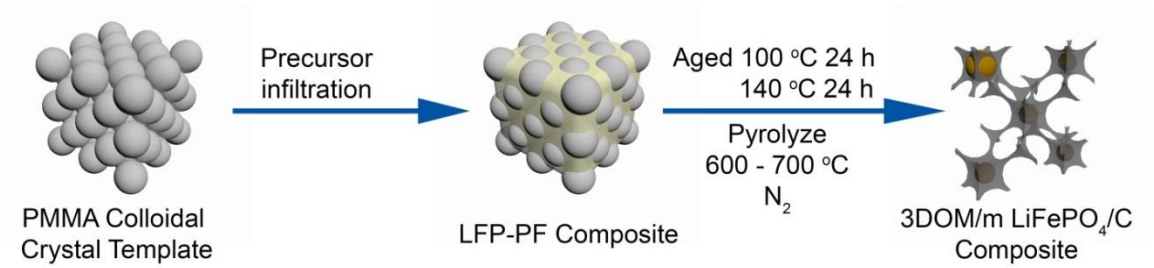

Figure 2.1 Synthesis scheme for 3DOM/m $LiFePO_4$/C composite

2.2 Experimental Section

2.2.1 Materials.

The chemicals used in this study were obtained from the following sources: methyl methacrylate (MMA) monomer (99%), 2,2'-azobis(2-methyl propionamidine) dihydrochloride (AMPD) initiator (97%), concentrated aqueous H_3PO_4 solution (85 wt%) from Aldrich; lithium perchlorate (99.0%), ethylene carbonate (>99.0%), dimethyl carbonate (>99.0%) from Fluka; $FeCl_2 \cdot 4H_2O$ (98%), LiCl (99.5%), phenol (ACS reagent) and formaldehyde solution (37% aqueous solution) from Fisher Scientific; Pluronic F127 from BASF; hydrochloric acid (37%) from Malinckrodt Chemicals; and sodium carbonate (anhydrous, 99.7%) from J.T. Baker. Deionized water was purified to a resistance higher than 18 MΩ.

2.2.2 Poly(phenol formaldehyde) (PF) sol preparation.

Prepolymerized PF sol was prepared following an established method.[42] Briefly, phenol (61 g) was melted at 50 °C in a 500 mL round bottom flask using an oil bath. Under constant stirring, 13.6 g NaOH aqueous solution (20 wt %) was added slowly to the melted liquid over a period of 15 minutes. After that, 110.4 g aqueous formaldehyde solution (37 wt %) was added dropwise into the mixture. The solution was stirred at 500 rpm and heated at 70 °C for 1 h to increase the polymerization rate. The product was neutralized with 30 mL HCl (0.6 M), filtered to remove NaCl, and water was removed by vacuum evaporation

at 50 °C overnight. The dried product was dissolved in 80 g ethanol to obtain the PF-sol, which was stored under refrigeration.

2.2.3 PMMA sphere synthesis and assembly of colloidal crystal.

Polymeric colloidal crystal templates composed of 400 ± 10 nm diameter PMMA spheres were synthesized using an emulsifier-free emulsion polymerization.[43] MMA monomer (400 mL) and deionized water (1600 mL) were added to a 3 L five-neck, round-bottom flask. The monomer solution was heated to 70 °C before the addition of initiator. During heating, the solution was stirred and purged with nitrogen gas. When the temperature fluctuation was less than 0.2 °C, 1.50 g of the initiator, 2,2'-azobis(2-methylpropionamidine) dihydrochloride dissolved in 25 mL of deionized water was added to the flask. The solution turned milky white as MMA began to polymerize, forming a colloidal suspension. When the reaction had finished, the milky solution was filtered through glass wool to remove large agglomerates from the monodisperse sphere suspension. Subsequently, the PMMA sphere suspension was poured into a crystallization dish and was allowed to sediment. Opalescent PMMA colloidal crystals were obtained after the spheres settled and water was removed. The material was then broken with a spatula into small pieces, and pieces with an approximate size of $1\times1\times0.4$ cm^3 were used as the templates. PMMA sphere sizes were determined from scanning electron microscopy (SEM) images, taking averages and standard deviations over ca. 200 spheres.

2.2.4 3DOM/m $LiFePO_4$ preparation.

3DOM/m $LiFePO_4$/C composites were prepared by a dual templating method, in which the nonionic surfactant F127 (the poly(ethylene oxide)-poly(propylene oxide)-poly(ethylene oxide) triblock copolymer $PEO_{106}PPO_{70}PEO_{106}$) and PMMA colloidal crystals were intended as templates for mesopores and macropores, respectively. All syntheses were carried out according to the following procedure: PF-sol (2 g) was mixed with 2 g aqueous HCl (0.2 M) in a 20 mL vial and stirred for 15 min. F127 surfactant (1 g) was then added and stirred until a clear solution was obtained. $FeCl_2$ (1.988 g) and LiCl (0.435 g) were mixed and ground in a mortar, then transferred to the solution. At this point, the color of the solution changed from light yellow to green. The vial was placed in a larger

glass bottle under flowing nitrogen to avoid the oxidation of Fe^{2+}. The mixture was vigorously stirred until all the salts were dissolved (usually 3–4 h, add 0.5 ml ethanol if the solution is too viscous), then concentrated H_3PO_4 (0.011 mol) was slowly added to the solution, and the mixture was stirred overnight. The order of addition of each component was crucial to maintain a clear, homogeneous precursor solution before and during infiltration into the PMMA templates. In addition, the F127 surfactant was required to prevent immediate complexation of Fe^{2+} with phenol groups in the PF-sol, which prevented penetration of the colloidal templates. With F127, the precursor was stable as a homogeneous solution for 24 h in air and up to 48 h in a nitrogen atmosphere. For template infiltration, several pieces of PMMA colloidal crystal templates were placed upright in a 20 mL vial, and the precursor solution was slowly added until the template pieces were partially immersed. The templates were infiltrated as a result of capillary forces. After 4 h, the infiltrated pieces were removed from the solution, gently touched with KimWipes^{TM} paper tissue to wick away excess liquid, and then placed in a vacuum chamber for 30 min at room temperature. A second infiltration step was carried out following the same procedure. The samples were then placed in a vial that had been purged with nitrogen. The sealed vial was heated at 100 °C for 24 h, then at 140 °C for 24 h to increase the amount of cross-linking and to strengthen the composite. The aged composite samples were polished with 600 grit sand paper to remove nontemplated $LiFePO_4$ from the surface before pyrolysis. 3DOM/m $LiFePO_4$/C composites were obtained by pyrolyzing the thermally-cured composite under flowing N_2 (0.8 L min^{-1}) at 350 °C for 5 h and then at 600, 700, or 800 °C for another 10 h with a heating rate of 1 °C min^{-1}.

2.2.5 Product Characterization

All samples were ground into fine powder before structural analyses. Product crystallinities and phase purities were determined by powder X-ray diffraction (XRD) using a PANalytical X-Pert PRO MPD X-ray diffractometer equipped with a cobalt source and an X-Celerator detector. Data were collected from 10° to 85° 2θ, at a step size of 0.017° and a rate of 20.7 s/step. Average crystallite sizes were estimated by Rietveld refinement using X'pert HighScore Plus 2.0a software. Instrumental broadening was corrected using a LaB_6 standard. Small-angle X-ray scattering (SAXS) data were acquired on a Rigaku RU-

200BVH 2D SAXS instrument using a 12 kW-rotating anode with a Cu source and a Siemens Hi-Star multi-wire area detector. Raman spectroscopy was performed with a Witec Alpha300R confocal raman microscope using 514.5 nm incident radiation at the lowest possible potential to minimize beam damage of the sample. Scanning electron microscopy (SEM) was carried out with a JEOL-6700 microscope operating at 5 kV with emission currents ranging from 2 to 10 μA. Transmission electron microscopy (TEM) was carried out with Technai T12 microscope operating at 120 kV with emission currents ranging from 7 to 12 μA. Thermogravimetric (TG) analysis and differential scanning calorimetry (DSC) were performed on a Netzsch model STA 409 instrument to determine a suitable temperature program for the precursor transformation (flowing nitrogen atmosphere) and to determine the carbon content in the final products (flowing air atmosphere), using a heating rate of 5 °C min^{-1} to a final temperature of 900 °C. Nitrogen-sorption measurements were performed on a Micromeritics ASAP 2000 gas sorptometer. Samples were degassed to 0.003 mmHg for 12 h at 60 °C. Specific surface areas were calculated by the Brunauer Emmett Teller (BET) method, and pore sizes and volumes were estimated from pore size distribution curves from the adsorption branches of the isotherms.

2.2.6 Electrochemical Tests.

All electrochemical tests were carried out using an Arbin battery-testing system (ABTS 4.0). Galvanostatic charge–discharge measurements were performed with a three-electrode cell, in which a 3DOM/m $LiFePO_4$/C monolith was used as the working electrode, and Li metal as the counter and reference electrodes. The cell was constructed by sandwiching a monolithic $LiFePO_4$/C sample and lithium foil separated by two Celgard films between two glass slides. The cell was then placed in a three-neck, round-bottom glass flask containing an electrolyte solution composed of 1.0 M $LiClO_4$ in a mixture of ethylene carbonate and dimethyl carbonate (1:1 vol:vol). The cell was constructed in a dry room with <1% relative humidity. For cycling experiments, constant currents were applied and the voltages were restricted to a window of 2.0–4.2 V with 5 min rest periods between each step. All potential values are reported vs. Li/Li^+, and specific capacities are reported per gram of $LiFePO_4$.

The electronic conductivity of the composites was measured at room temperature via the 4-probe van der Pauw method using a Solartron SI 1287 electrochemical interface.[44] The samples were connected to copper wires at four points A, B, C, D using silver paste. Constant currents were applied through two points A and B, while voltages were measured between two points C and D. The samples were then rotated to apply current through B and C and measure voltages between A and D. Two sets of data were linearly fitted to calculate R_{ABCD} and R_{BCAD}, which were used to calculate conductivity through the van der Pauw equation.

2.3 Results and Discussion

2.3.1 PMMA Colloidal Crystal Synthesis

Spherical, uniform PMMA (400±10 nm) was successfully synthesized by emulsifier-free emulsion polymerization (Figure 2.2). The spheres were then packed by gravity sedimentation over a period of one month. The opalescence of the template under room light confirms the high order of the packed spheres. The SEM image in Figure 2.2B shows that these spheres are well packed into a face-centered cubic structure (FCC), in which each sphere is in contact with six other spheres in a particular (111) plane and three other spheres in the planes above and below this plane. The contacting points are where the windows connecting pore system in the final material are formed, which are critical for mass transport and ionic transport of the cathode materials. The well-ordered, packed PMMA colloidal crystals were then broken into 0.5×0.5×0.2 cm^3 fragments and used as templates for the synthesis of 3DOM/m $LiFePO_4$/C composites.

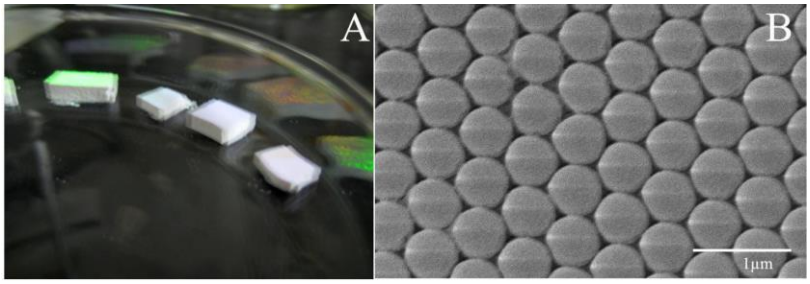

Figure 2.2 A) Photograph of PMMA templates with opalescence indicating high order of spheres in the templates; B) SEM image of PMMA spheres with diameters of about 434±10 nm.

2.3.2 Thermal Stability of PMMA-LFP Precursor-PF Composite

For high rate batteries, crystalline cathode materials are preferred to provide fast ionic transport.[45] However, in surfactant-templated syntheses, extensive crystallization is usually deleterious to the mesostructure. An ideal high-rate cathode material would have a structure with interconnected pores and thin crystalline walls of active material, which can be obtained by adding supporting agents (e.g. C, Si) and by controlling crystallization.[46,47] Suitable additives for mesoporous cathode materials should be able to strengthen the mesostructure and also be electronically conductive to enhance the rate performance of the electrodes. In this work, polymer-derived carbon was selected as an integral component in the composite cathode because it can readily form mesoporous structures and has good electrical conductivity.

TG-DSC analysis of the thermally cured PMMA/precursor composite was carried out under a nitrogen atmosphere to find a suitable temperature program for obtaining a $LiFePO_4$/C composite phase. The TG curve (Figure 2.3) shows three major mass loss steps. The first mass loss starting at 70 °C is associated with an endothermic peak in the DSC trace due to evaporation of ethanol. The surfactant and PMMA decomposed between 250 and 300 °C with endothermic DSC peaks at 263 and 294 °C. The third mass loss step between 300 and 425 °C is related to condensation of the walls and crystallization of $LiFePO_4$. According to the DSC data, the crystallization step occurred mainly in the temperature range from 400–425 °C, giving rise to an exotherm peaking at 409 °C. Removal of the surfactant and PMMA templates before this step would result in the loss of the supporting and confining scaffold for the inorganic phase, rendering grain growth during the crystallization process less controllable. It would therefore seem beneficial to treat the precursor first at temperatures below 250–300 °C to harden the inorganic skeleton, while it is still supported by the organic templates, and only then to treat the sample at higher temperatures (600–800 °C) to remove the templates and to induce further crystallization of the active $LiFePO_4$ phase. Contrary to our expectations, however, only powdered samples were obtained if the precursor were pretreated at 300 °C or below. Only precursors treated at temperatures higher than 325 °C formed monolithic samples. It appears that an important factor for the formation of monolithic 3DOM/m $LiFePO_4$/C composites is the slow ramping rate causing slow removal of the template (PMMA and

surfactant), and the 5 h treatment at an intermediate temperature right below the crystallization temperature, which strengthens the composite framework most effectively before the sample is heated above the crystallization temperature. On the basis of this information, all samples were aged first at 100 °C and then at 140 °C to enhance polymerization of the phenol formaldehyde phase. Pyrolysis was then carried out following programs with a lower temperature pretreatment step at 350 °C for 5 h and a higher temperature step at 600, 700, or 800 °C for 10 h.

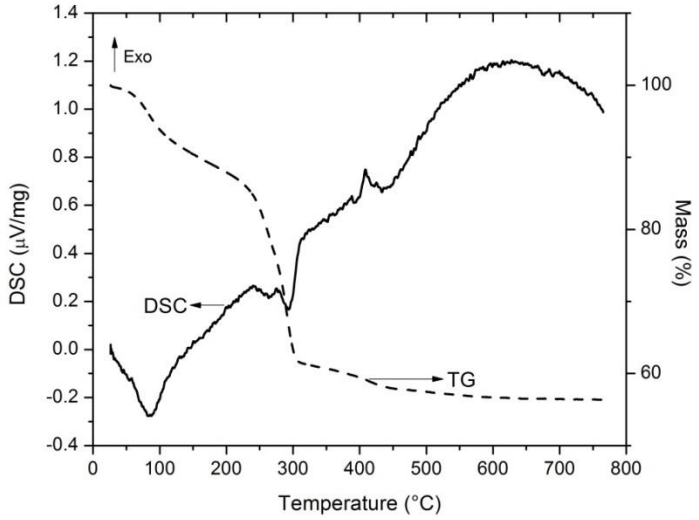

Figure 2.3 TG-DSC data for the cured $LiFePO_4$-PF-F127-PMMA composite obtained in a nitrogen atmosphere.

2.3.3 Structural Characterization of 3DOM/m $LiFePO_4$/C Composites

2.3.3.1 Phase Analysis (XRD, Raman, TGA-DSC Characterization)

Powder X-ray diffraction was used to investigate the crystallinity and phase purity of the $LiFePO_4$/C composites. Figure 2.4 shows the wide-angle X-ray diffraction patterns of samples pyrolyzed at different temperatures. In the temperature range from 600 to 800 °C, olivine $LiFePO_4$ was the only crystalline phase present. All of the sample peaks were indexed to the orthorhombic $LiFePO_4$ phase (Pnmb) with average lattice constants, a = 6.01 Å, b = 10.34 Å, c = 4.70 Å, and a unit-cell volume of 292 $Å^3$. A broad background peak between 18° and 32° 2θ, observed in all three patterns, originated from the nongraphitic carbon component. Other impurities such as FeP, Fe_3C, and Fe_2P, which are often found in $LiFePO_4$ samples formed in the presence of the reducing agent carbon, were

not present or only present in such small quantities that they were undetectable by XRD. Such impurities are well known for improving electronic conductivity but worsening rate performance of $LiFePO_4$.[48] Crystal sizes of $LiFePO_4$ in these samples were estimated by whole pattern fitting using Rietveld refinement. Because carbon was present as glassy carbon and therefore did not contribute any sharp peaks, all refinements were carried out for a single phase of $LiFePO_4$ using the Pnmb unit cell above. The calculated average crystallite sizes are summarized in Table 1. Crystallite sizes of $LiFePO_4$ in all three composite samples were small ($\leq$ 68 nm), providing short diffusion paths for Li ions. They increased from 42 to 68 nm as the pyrolysis temperature increased from 600 to 800 °C. The small crystal sizes can be in part attributed to the isolation of particles by the carbon phase, as well as the PMMA spheres (before template combustion) or the macrovoid space (after combustion) which minimizes direct contact between particles and limits mass transport of the solid phase.

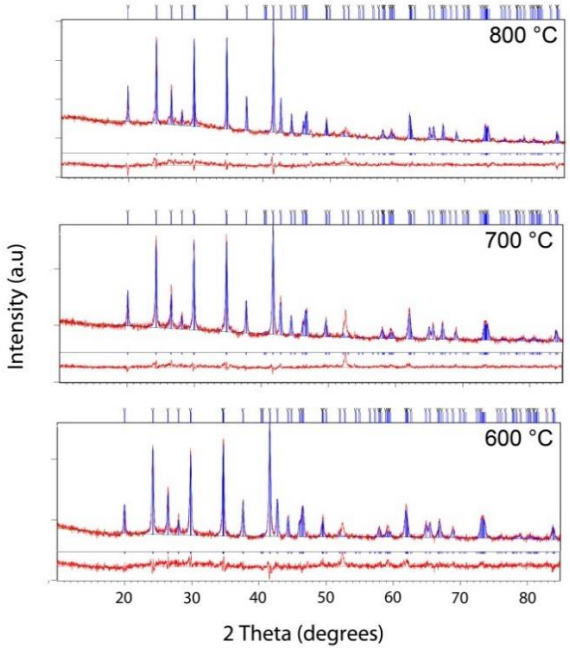

Figure 2.4 X-ray diffraction patterns of $LiFePO_4$/C composites prepared by pyrolyzing precursors at 600, 700, and 800 °C for 10 h under nitrogen. The experimental patterns match the published line pattern for the olivine phase of $LiFePO_4$ (PDF # 00-40-1499, blue lines). Rietveld refinements are shown using a unit cell with Pnmb symmetry. The experimental patterns and difference patterns are shown in red, the calculated patterns in blue. The peak at 52.4° 2θ originates from the Al sample holder.

Table 2.1. Rietveld refinement data of samples pyrolyzed at 600, 700, and 800 °C.

Temperature (°C)	600	700	800
a (Å)	6.0108(4)	6.0122(5)	6.0064(3)
b (Å)	10.3378(8)	10.3387(8)	10.3300(5)
c (Å)	4.6974(4)	4.6969(4)	4.6917(3)
Unit-cell volume ($Å^3$)	291.9	292.0	291.1
Crystallite size (nm)	41.9	47.6	68.2
R profile	3.56	3.3	3.23
Weighted R profile	4.57	4.32	4.08
Goodness of fit	1.68	1.94	2.08

The carbon content of the 3DOM/m $LiFePO_4$/C composites was determined by TG-DSC analysis in air. For the sample synthesized at 600 °C, a mass loss of 30 wt% overlapped with a broad exothermic peak in the DSC trace (Figure 2.5A) between 350 and 550 °C and corresponds to the carbon component in the composite. The carbon content was slightly lower for samples synthesized at 700 and 800 °C (27 and 22 wt%, respectively) (Figure 2.5B and 2.5C), indicating that the carbon content was weakly affected by the pyrolysis temperature in this range. The carbon phase was further characterized by Raman spectroscopy. The Raman spectrum of 3DOM/m $LiFePO_4$/C shows two prominent peaks associated with sp^2 carbon (G-band, 1597 cm^{-1}) and sp^3 carbon (D-band, 1351 cm^{-1}) (Figure 2.5D). The G-band originates from the in-plane bond-stretching motion of pairs of sp^2 carbon atoms, while the D-band involves a breathing mode of A_{1g} symmetry, which is only active in the presence of disorder.[49] The G peak shifts from 1581 cm^{-1} in graphite to 1597 cm^{-1} in $LiFePO_4$/C composite, which indicates that carbon in the composite is nanocrystalline graphite. The size domain can be estimated using the equation $\frac{I_D}{I_G} = \frac{C(\lambda)}{L_a}$, where I_D, I_G are the intensities of the disordered peak and the graphitic peak, respectively, $C(\lambda = 515.5\ nm) = 4.4$ nm, λ is the wavelength of the laser used in the Raman spectrometer, and L_a is the cluster diameter of nanocrystalline graphite.[49] The broad peaks contain additional contributions from sp^3 carbon sites present in amorphous carbonaceous materials.[50] Therefore simply fitting the spectrum with two peaks does not give an accurate

value of I_D/I_G. In order to interpret the Raman features, the spectrum was instead deconvoluted with four Gaussian peaks situated at 1190, 1351, 1518, and 1597 cm^{-1}, where the additional bands at 1190 and 1518 cm^{-1} are associated with sp^3 carbon vibrations. On the basis of the fitted intensity ratios of the D and G peaks ($I_D/I_G \sim 0.88$), one can estimate the crystallite size in the direction of graphitic planes to be approximately 5 nm.[49,51]

The difference patterns from the Rietveld refinements (Figure 2.4) correspond mostly to the carbon phase. Judging from the low intensity and breadth of the peaks at 38.2° 2θ (002) and at 24.0° 2θ (101) in the difference patterns, the extent of well-stacked graphitic layers perpendicular to the planes is also small. Similar features in Raman spectra and XRD patterns are typically observed for porous glassy carbon anode materials for lithium ion batteries made from resorcinol formaldehyde (RF) or phenol formaldehyde (PF) precursors.[52,53] Although the conductivity of such carbon materials is lower than that of graphite (ca. 0.1–0.3 S cm^{-1} for 3DOM/m carbon materials),[54] it is many orders of magnitude higher than that of $LiFePO_4$. The built-in carbon can enhance the electronic conductivity of the composite and help to improve rate performance of the cathode material.

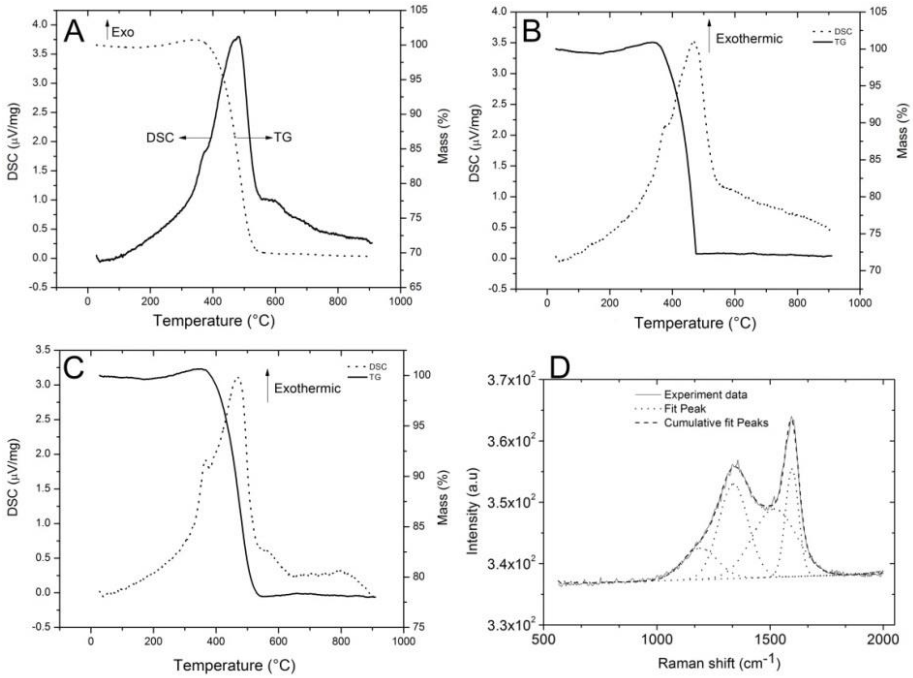

Figure 2.5 A, B, and C are TG-DSC traces (obtained in air) of 3DOM/m $LiFePO_4$/C composites pyrolyzed at 600, 700, and 800 °C respectively. (D) Raman spectrum of the sample pyrolyzed at 600 °C.

2.3.3.2 Effect of Pyrolysis Temperatures on The Morphologies of 3DOM/m $LiFePO_4$/C Composites

The morphologies of the 3DOM/m $LiFePO_4$/C composites pyrolyzed at different temperatures were studied using field emission scanning electron microscopy (FE-SEM). Images A and B in Figure 2.6 show cross-sections of a sample pyrolyzed at 600 °C. More than 90% of this sample has a well-ordered, interconnected macropore structure, in which the walls follow the curvature of the original colloidal crystal template. The texture of the wall provides a first indication of additional porosity (see below). The average macropore and window diameters of the sample pyrolyzed at 600 °C are 285 ± 10 nm and 90 ± 8 nm, respectively. As is typical for samples prepared from polymeric colloidal crystal templates, the macropore values are smaller than the diameters of the 400 nm PMMA templating spheres, due to shrinkage of the structure during thermal processing. The open, interconnected pore system in the 3DOM structure facilitates penetration of an electrolyte, and the large accessible surface of the material can enhance the exchange of Li^+ between the electrolyte and the electrode. The 3DOM structure is also well maintained for a sample pyrolyzed at 700 °C for 10 h. However, the walls are more strut-like, resulting in larger windows between interconnecting pores. After a higher temperature treatment at 800 °C for 10 h, a similar strut-like structure is observed. At this temperature, the 3DOM structure has undergone some distortion in a few regions, but an interconnected pore system is still preserved.

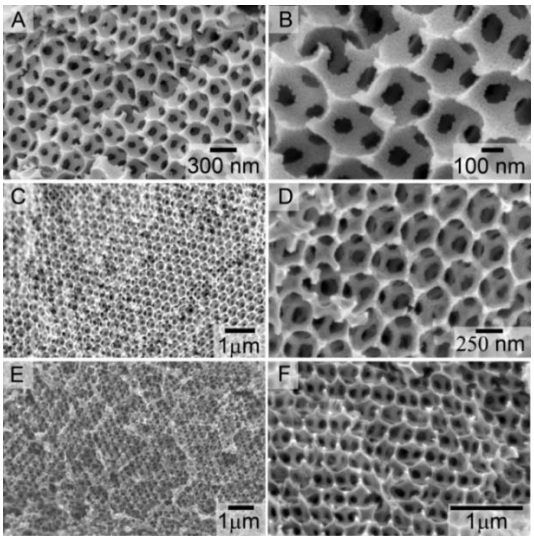

Figure 2.6 SEM images of samples pyrolyzed at 600 °C (A and B), 700 °C (C and D), and 800 °C (E and F) for 10 h under nitrogen.

The morphologies of the 3DOM/m $LiFePO_4$/C composites were further analyzed by TEM. At lower magnifications, all samples showed features of the periodic macropore structure (Figure 2.7). The 3DOM structure is the inverse replica of the fcc colloidal crystal template. It can therefore be described as a network of interconnected octahedral and tetrahedral sites (replicas of the octahedral and tetrahedral holes in the close-packed template), with twice as many tetrahedral sites as octahedral sites. Interestingly, the curvature is different for the replicas of tetrahedral and octahedral sites in the materials pyrolyzed at 600 °C. Although in an ideal inverse opal structure, both should be concave, in the 3DOM/m $LiFePO_4$/C materials, only the tetrahedral regions are concave and the octahedral cubes are slightly convex, almost spherical. Furthermore, the octahedral replica sites appear significantly darker than the tetrahedral bridges. These features were observed for three different samples prepared at 600 °C in most areas of each sample (ca. 90%) (Figure 2.7). In part, the contrast differences can be attributed to a greater thickness of the octahedral regions. However, another cause is likely to be an uneven distribution of $LiFePO_4$ in the composite phases. In TEM, the iron-rich regions would produce greater contrast than the carbon-rich phase with lower electron density. Based on the observed contrast differences and curvature differences, we propose that the octahedral sites are richer in $LiFePO_4$ (which is more prone to sintering than carbon) and the tetrahedral and thinner bridging regions are richer in carbon. Unfortunately the resolution for elemental analysis in our TEM is insufficient to confirm this. Selected-area electron diffraction patterns (insets in Figure 2.8) show strong dot patterns characteristic of crystalline $LiFePO_4$, in agreement with XRD data, but they also represent the whole area viewed in the TEM image that contained both octahedral and tetrahedral replica units. The micro-phase separation is probably caused by a favorable crystallization energy for $LiFePO_4$ compared to the interaction energy that stabilizes the inorganic ($LiFePO_4$)–organic (carbon) interface. In terms of site preference, both $LiFePO_4$ and carbon should occupy octahedral sites (the bigger sites and lower surface-to-volume fraction) to lower their surface energy, but the contribution for the system from $LiFePO_4$ is greater because it is present in larger amounts (70 wt%). The structure of the sample pyrolyzed at 600 °C can therefore be described approximately as $LiFePO_4$-rich cubes that are interconnected through tetrahedral mesoporous carbon linkers. For samples treated at 700 and 800 °C, the

features associated with partial phase separation of $LiFePO_4$ and carbon are still present but less pronounced (Figure 2.7). Fewer spherical components are observed in the TEM images and the contrast is more uniform. At these higher temperatures, more efficient diffusion may overcome the surface energy differences.

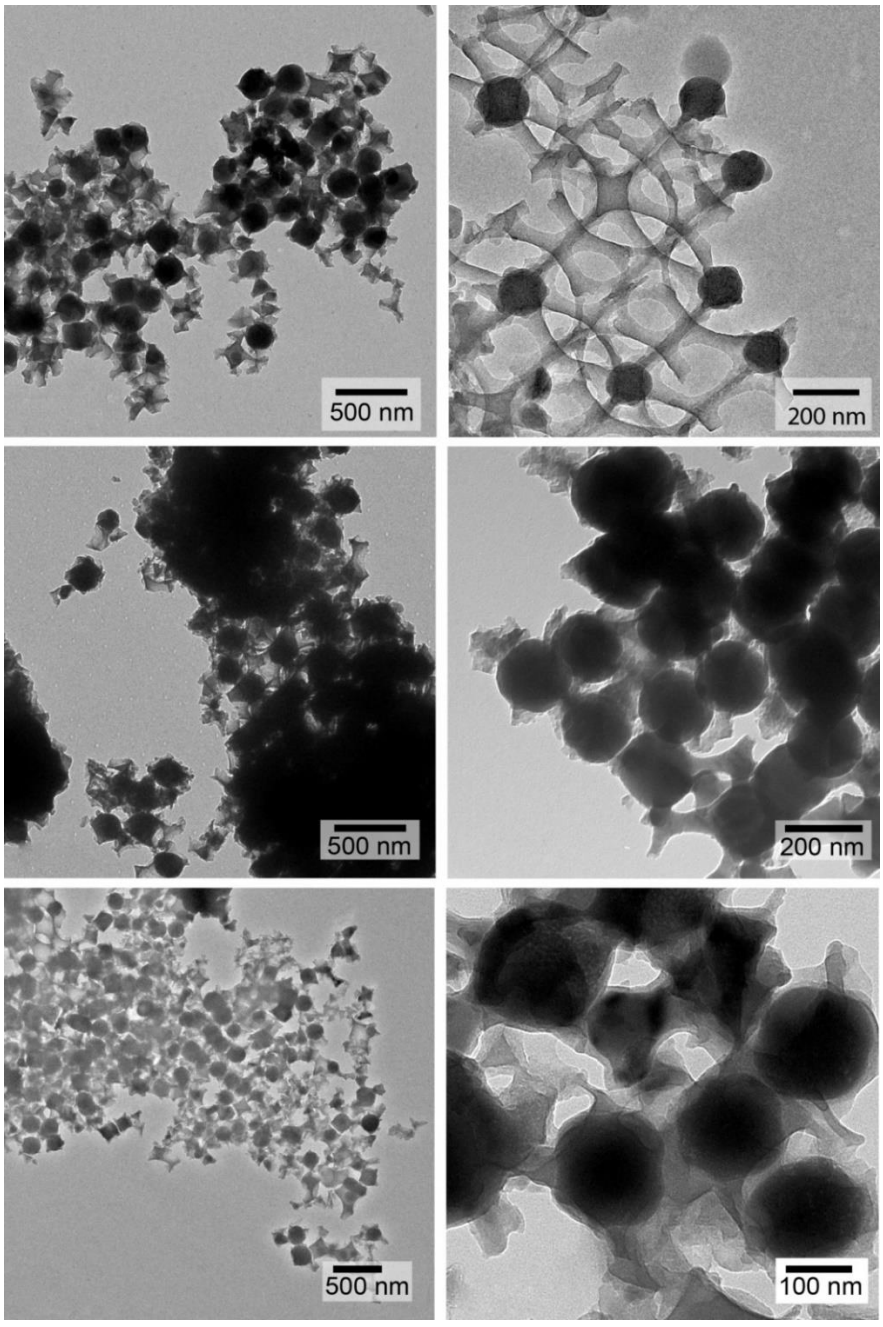

Figure 2.7 TEM images of 3DOM/m $LiFePO_4$/C samples pyrolyzed at 600 ˚C (A, B), 700 ˚C (C, D) and 800 ˚C (E, F) showing contrast between the $LiFePO_4$-rich phase (darker), mainly in octahedral sites, and the carbon rich phase (brighter), mainly in tetrahedral sites

This structure is especially interesting for high-power battery applications, because it may offer several advantages over conventional carbon coatings. First, lithium diffusion paths are limited by the small crystallite size and the size of the octahedral replica features, in which the longest possible pathway is less than about 180 nm. Moreover, these sizes are tunable by altering the size of the PMMA template spheres. With conventional carbon coatings, $LiFePO_4$ particle growth is unrestricted, and typical particle sizes are a few micrometers, even if individual crystalline domains may be as small as a few tens of nanometers. If these continuous crystalline domains are correctly directed, i.e., in the [010] direction, the diffusion path lengths double or triple, approaching the overall particle size. Finally, in the 3DOM/m composite, $LiFePO_4$ nanoparticles are efficiently wired by carbon, forming networks that are hundreds of micrometers in size.

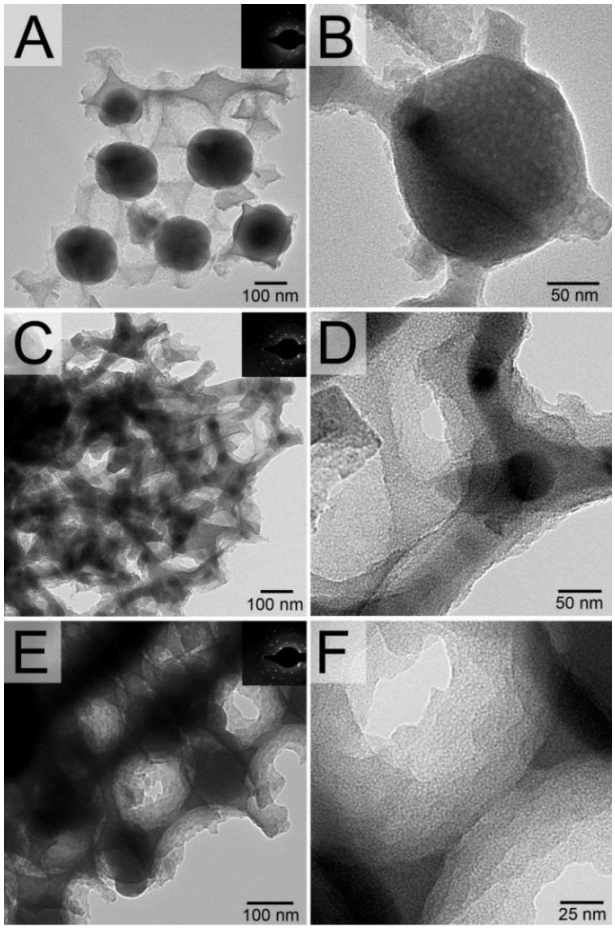

Figure 2.8 TEM images of 3DOM/m $LiFePO_4$/C samples pyrolyzed at 600 (A and B), 700 (C and D) and 800 °C (E and F). Insets in images (A), (C), and (E) are SAED patterns for the corresponding sample regions, confirming the crystalline nature of $LiFePO_4$ in the composites.

The TEM images also show features that may be associated with micro- or mesoporosity. In the structural components linking tetrahedral replicas, disordered texture is visible, with spacings between ca. 1.5 and 4 nm. Larger circular features with sizes varying from 3 to 15 nm are visible in the darker octahedral replica regions of the sample pyrolyzed at 600 °C. The SAXS pattern for this sample shows a single weak peak at 0.4° 2θ corresponding to a spacing of 22 nm (Figure 6A) which may be associated with the bigger pores observed in the darker spherical regions (Figure 2.7 and Figure 2.8B). While a SAXS pattern of 3DOM/m C[18] synthesized from PF and F127 precursors shows two weak peaks between 0.7° and 3° 2θ, none of the SAXS patterns of $LiFePO_4$/C composites pyrolyzed at different temperatures showed any peaks in this range, consistent with the low degree of mesopore order observed by TEM (Figures 2.9 and Figure 2.10). The introduction of $LiFePO_4$ to the PF/F127 precursor mixture changed the interaction between the surfactant and the polymeric precursor, resulting in smaller and more disordered mesopores.

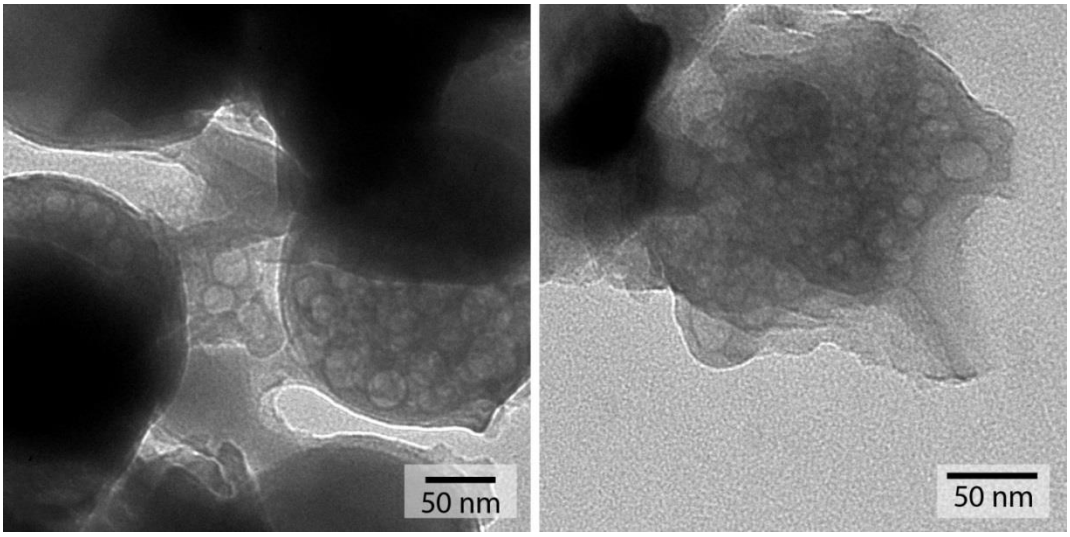

Figure 2.9 TEM images of a 3DOM/m $LiFePO_4$/C composite pyrolyzed at 600 °C, showing larger pores (13–20 nm) that may be associated with the weak peak at 0.4° 2θ in the SAXS pattern (Figure 2.10A).

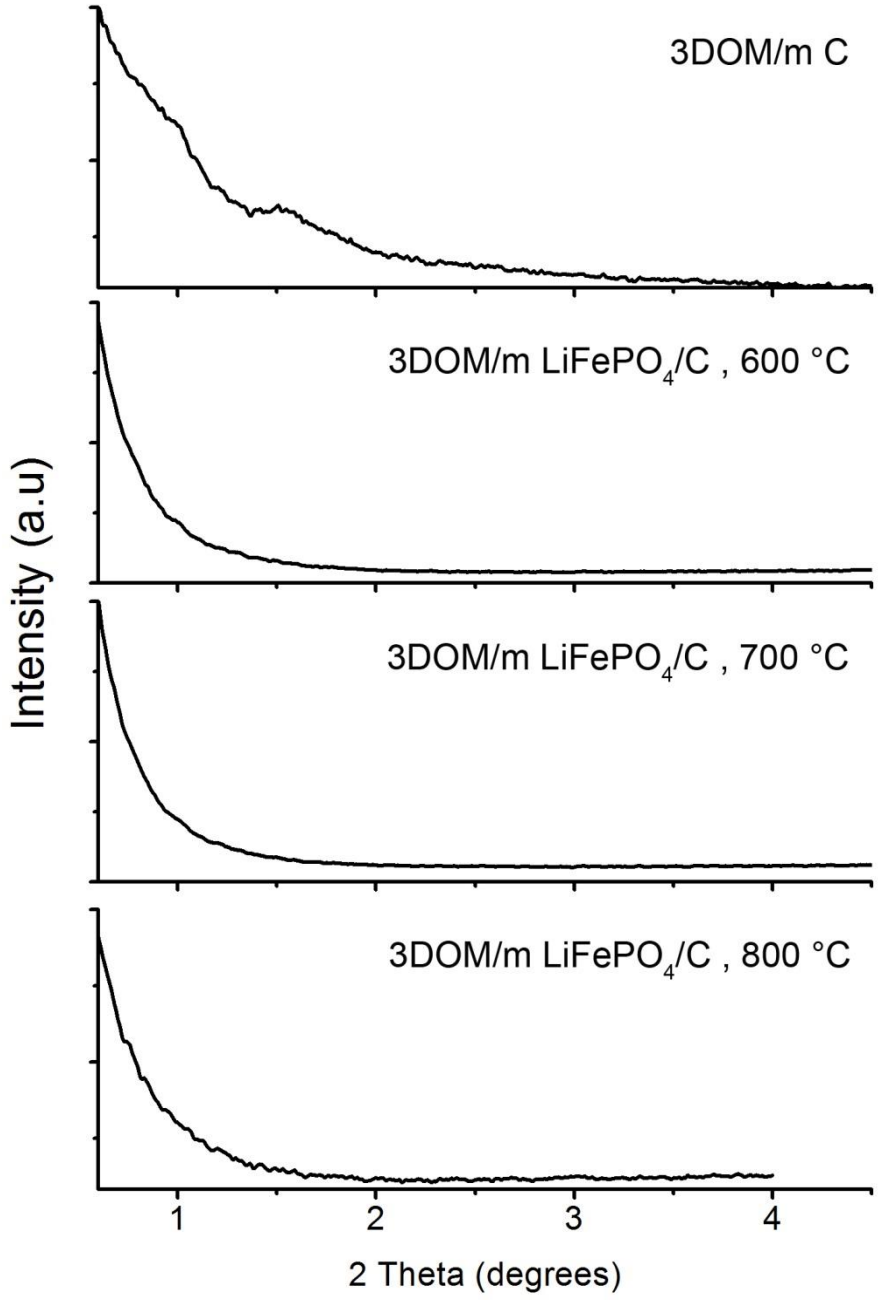

Figure 2.10 SAXS patterns of 3DOM/m C and 3DOM/m $LiFePO_4$/C composites pyrolyzed at the indicated temperatures.

To further examine the textural properties of the 3DOM/m $LiFePO_4$/C composites as a function of pyrolysis temperature, nitrogen adsorption-desorption measurements were performed. All isotherms feature a hysteresis loop between 0.5 and 0.95 P/P_0 typical for mesoporous structures (Figure 2.11B). However, the hysteresis loops are relatively narrow, characteristic for a pore size range near the border between mesopores (>2 nm) and

micropores (<2 nm). Except for a small peak at 2.7 nm, the pore size distribution curves derived from the adsorption isotherms show no features that can be associated with templated mesopores (Figure 2.8C). In fact, for the sample pyrolyzed at 600 °C, which has the highest surface area (200 $m^2 g^{-1}$, see Table 2), the largest fraction of this surface area and more than half of the pore volume is due to micropores. For samples pyrolyzed at higher temperatures, the surface areas decrease as high temperature treatment caused contraction, mainly of the micropores. Surface areas of 123 $m^2 g^{-1}$ and 86 $m^2 g^{-1}$ were obtained for samples pyrolyzed at 700 °C and 800 °C, respectively. In other dual templating syntheses of carbon-based materials with hierarchical porosity, mesopores tend to be larger even when the same surfactant (F127) is used. In a direct dual templating synthesis of 3DOM/m C uniform mesopores with diameters of 2.8 nm were formed[53], and in a triconstituent synthesis of 3DOM/m C-SiO_2, mesopores were ca. 5.2 nm in diameter.[55] In the current synthesis, the additional inorganic precursor components appear to have prevented the formation of well-formed micellar arrays. However, the obtained surface areas were still much higher than those of nonporous analogues, which are typically in the range of a few $m^2 g^{-1}$.

Table 2.2 Dependence of textural properties of 3DOM/m $LiFePO_4$/C on synthesis temperature.

Pyrolysis temperature (°C)	BET surface area ($m^2 g^{-1}$)	Micropore area ($m^2 g^{-1}$)	V_{pore} ($cm^3 g^{-1}$)[a]	$V_{micropore}$ (%)	Crystallite size (nm)[b]
600	200	157	0.13	55	41.9
700	123	90	0.12	36	47.6
800	86	61	0.08	34	68.2

[a] Single-point total pore volume at $P/P_0 = 0.983$. [b] Crystallite sizes for the $LiFePO_4$ phases in the composites were determined by Rietveld refinement of the powder XRD patterns.

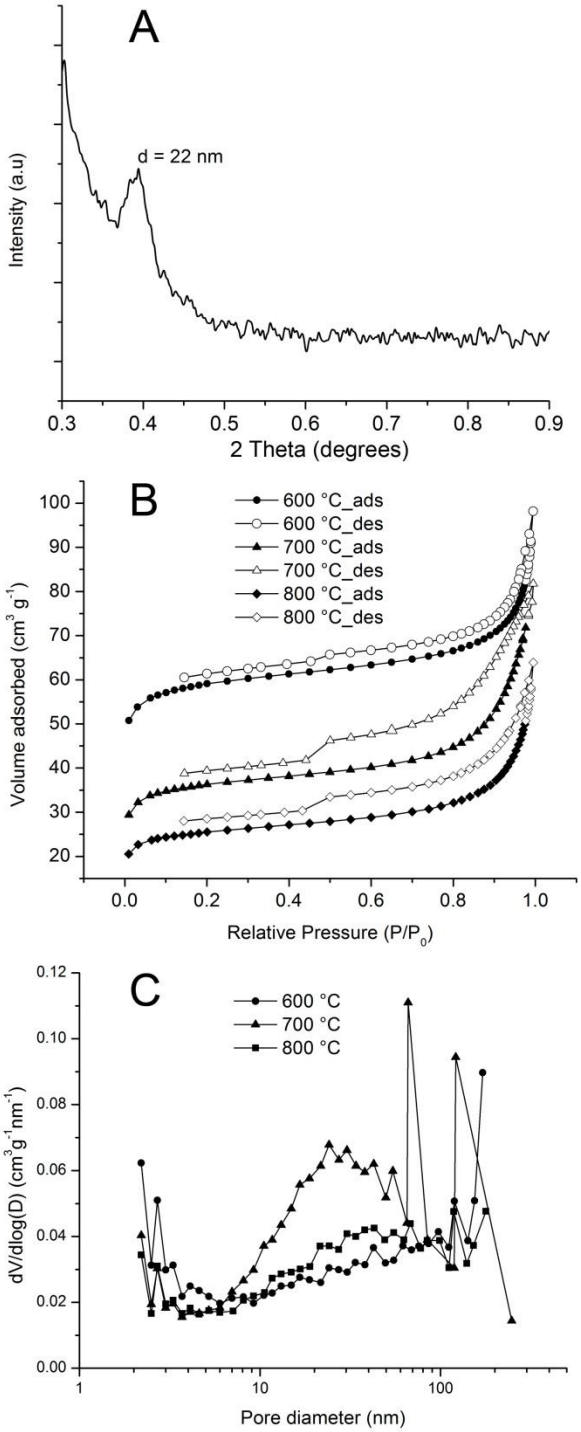

Figure 2.11 (A) SAXS pattern of 3DOM/m $LiFePO_4$/C treated at 600 °C, (B) Isotherms of 3DOM/m $LiFePO_4$/C samples pyrolyzed at 600, 700, and 800 °C, and (C) the corresponding pore size distributions.

2.3.4 Electrochemical Characterization of 3DOM/m $LiFePO_4$/C Composites

Electrochemical tests were carried out in a three-electrode cell on the sample pyrolyzed at 600 °C, because this sample exhibits the highest surface area, smallest crystallite size, yet high crystallinity, which are potentially useful features for high rate battery applications. Because of the monolithic nature of the electrode, no carbon black additive or binder were needed, which would lower the capacity of the cell. The cell was cycled at different rates from C/5 to 16 C in the potential range between 2.0 and 4.2 V vs. Li^+/Li. In this potential range, the contribution of carbon to lithium uptake is negligible.[54,56] At a slow rate (C/5), the discharge curve is characterized by a plateau at 3.39 V, which corresponds to the reaction $LiFePO_4 \rightarrow Li^+ + FePO_4 + e^-$. The electrode capacity is 150 mA h g^{-1} (based on the mass of $LiFePO_4$), which is 89% of the theoretical capacity. At higher rates, the capacity decreases but remains as high as 123 mA h g^{-1} at 1 C, 103 mA h g^{-1} at 4 C, 78 mA h g^{-1} at 8 C, and 64 mA h g^{-1} at 16 C rate (Figure 2.12). The good performance is attributed to the presence of the conductive carbon phase that embeds and connects the $LiFePO_4$ nanoparticles and to the high surface area of the composite that facilitates ionic transport across the interfaces. The electronic conductivity of the composite pyrolyzed at 600 °C is 0.14 S cm^{-1}, i.e., much higher than that of bulk $LiFePO_4$ (10^{-9}–10^{-10} S cm^{-1}). In our tests, the monolithic $LiFePO_4$/C composite was able to support current densities as high as 2720 mA g^{-1} (at 16 C rate).

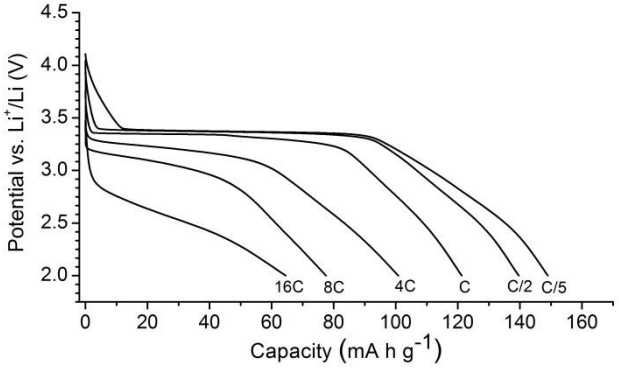

Figure 2.12 Discharge profile at different C rates for the 3DOM/m $LiFePO_4$/C composite sample pyrolyzed at 600 °C.

Figure 2.13 shows the capacity of the cell cycled at different rates for the first 5 cycles at each rate. The cell capacity keeps stable, even at a rate as high as 16C, at which the cell is fully charged or discharged within 4 minutes. It is worth noting that as the current density

is later reduced again to C/5, the capacity returns to its original value, which indicates that the electrode material remained stable. This stability is attributed to the interconnected macropore system that assists mass transport and the built-in carbon component which improves the mechanical stability of the composite. Both features give the composite the stability to withstand the stresses caused by the phase change from $LiFePO_4$ to $FePO_4$, and by the infiltration of electrolyte into the composite.

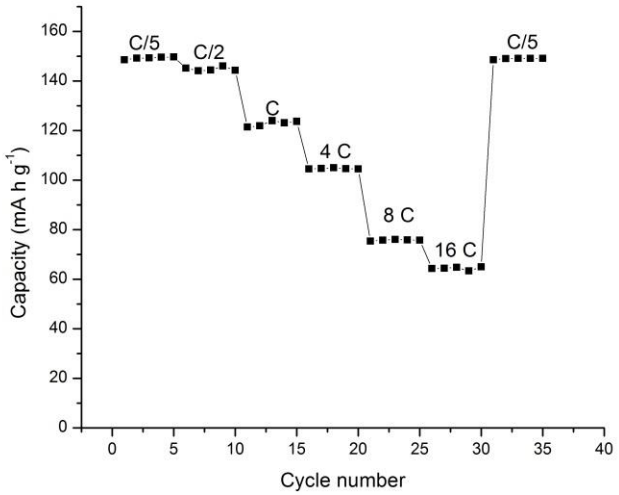

Figure 2.13 Capacity of the 3DOM/m $LiFePO_4$/C composite sample pyrolyzed at 600 °C and cycled for 5 cycles each at different rates.

The composite was cycled at rate of 4C over 70 cycles and at 8 C over 100 cycles to test the capacity retention at high rates (Figure 2.14). The data demonstrate the excellent capacity retention at both rates with coulombic efficiencies almost approaching 100%.

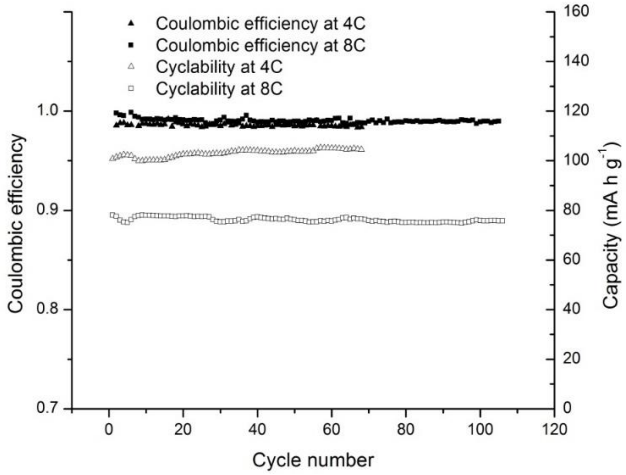

Figure 2.14 Capacity retention and coulombic efficiency of $LiFePO_4$/C composite pyrolyzed at 600 °C when cycled at 4C and 8C rates.

2.4 Conclusion

The combination of colloidal crystal templating with surfactant templating provides an efficient synthetic method for forming $LiFePO_4$/C composites with high capacities for lithiation (150 mA h g^{-1} at C/5, 78 mA h g^{-1} at 8C, and 64 mA h g^{-1} at 16C rate) and excellent capacity retention at high rates. The colloidal crystal templating approach maintains small particle sizes and easy access for electrolyte and lithium ions to the active cathode phase through an interconnected macropore system. Although the secondary pore structure introduced by the surfactant template was not as well defined as in related dual templating syntheses of pure 3DOM/m C or mixed 3DOM/m C-SiO_2 materials, the additional micropores and small mesopores provided the composites with surface areas as high as 200 m^2 g^{-1}. Another role of the surfactant was to act as a compatibilizer for the complex precursor mixture.

In composite samples pyrolyzed at 600 °C, carbon and $LiFePO_4$ selectively occupy different locations in the inverse opal structure. The resulting structure can therefore be described as a network of cubic $LiFePO_4$-rich nanoparticles wired together by tetrapodal mesoporous carbon-rich particles. This special structure gives the electrode greater structural stability so that millimeter-sized monolithic porous electrodes could be formed, and it provides improved conductivity to support high currents. The materials are therefore of interest as cathodes for high-rate lithium-ion batteries. Although the macropore space contributes to nonactive volume, such volume may be utilized to accommodate additional active material, for example in a 3D-interpenetrating, nanostructured battery.[52,57] The concepts of micro phase-separation and site preference found for the 3DOM/m $LiFePO_4$/C composite may also apply to other templated electrode systems containing multiple components, in which active material may be embedded and wired together in an electronically more conductive phase.

2.5 References

(1) Padhi, A. K.; Nanjundaswamy, K. S.; Goodenough, J. B. *J. Electrochem. Soc.* **1997**, *144*, 1188.

(2) Tarascon, J. M.; Armand, M. *Nature* **2001**, *414*, 359.

(3) Manthiram, A. *J. Phys. Chem. Lett.* **2011**, 176.

(4) Nishimura, S.-I.; Kobayashi, G.; Ohoyama, K.; Kanno, R.; Yashima, M.; Yamada, A. *Nat. Mater.* **2008**, *7*, 707.

(5) Huggins, R. A. 2009.

(6) Chung, S.-Y.; Bloking, J. T.; Chiang, Y.-M. *Nat. Mater.* **2002**, *1*, 123.

(7) Meethong, N.; Kao, Y.-H.; Speakman, S. A.; Chiang, Y.-M. *Adv. Funct. Mater.* **2009**, *19*, 1060.

(8) Kang, B.; Ceder, G. *Nature* **2009**, *458*, 190.

(9) Hu, Y.-S.; Guo, Y.-G.; Dominko, R.; Gaberscek, M.; Jamnik, J.; Maier, J. *Adv. Mater.* **2007**, *19*, 1963

(10) Huang, H.; Yin, S. C.; Nazar, L. F. *Electrochem. Solid-State Lett.* **2001**, *4*, A170.

(11) Konarova, M.; Taniguchi, I. *Mater. Res. Bull.* **2008**, *43*, 3305.

(12) Murugan, A. V.; Muraliganth, T.; Ferreira, P. J.; Manthiram, A. *Inorg. Chem.* **2009**, *48*, 946.

(13) Kim, M. G.; Cho, J. *Adv. Funct. Mater.* **2009**, *19*, 1497.

(14) Muraliganth, T.; Murugan, A. V.; Manthiram, A. *J. Mater. Chem.* **2008**, *18*, 5661.

(15) Gaberscek, M.; Kuzma, M.; Jamnik, J. *Phys. Chem. Chem. Phys.* **2007**, *9*, 1815.

(16) Long, J. W.; Sassin, M. B.; Fischer, A. E.; Rolison, D. R.; Mansour, A. N.; Johnson, V. S.; Stallworth, P. E.; Greenbaum, S. G. *J. Phys. Chem. C* **2009**, *113*, 17595.

(17) Baxter, J.; Bian, Z.; Chen, G.; Danielson, D.; Dresselhaus, M. S.; Fedorov, A. G.; Fisher, T. S.; Jones, C. W.; Maginn, E.; Kortshagen, U.; Manthiram, A.; Nozik, A.; Rolison, D. R.; Sands, T.; Shi, L.; Sholl, D.; Wu, Y. *Energy Environ. Sci.* **2009**, *2*, 559.

(18) Wang, Z.; Kiesel, E. R.; Stein, A. *J. Mater. Chem.* **2008**, *18*, 2194.

(19) Wang, Z.; Fierke, M. A.; Stein, A. *J. Electrochem. Soc.* **2008**, *155(9)*, A658.

(20) Woo, S.-W.; Dokko, K.; Nakano, H.; Kanamura, K. *J. Mater. Chem.* **2008**, *18*, 1674.

(21) Su, F.; Zeng, J.; Bai, P.; Lv, L.; Guo, P.-Z.; Sun, H.; Li, H. L.; Yu, J.; Lee, J. Y.; Zhao, X. S. *Ind. Eng. Chem. Res.* **2007**, *46*, 9097.

(22) Lu, A.-H.; Schmidt, W.; Spliethoff, B.; Schuth, F. *Adv. Mater.* **2003**, *15*, 1602

(23) Fan, J.; Wang, T.; Yu, C.; Tu, B.; Jiang, Z.; Zhao, D. *Adv. Mater.* **2004**, *16*, 1432

(24) Zhang, W.-M.; Hu, J.-S.; Guo, Y.-G.; Zheng, S.-F.; Zhong, L.-S.; Song, W.-G.; Wan, L.-J. *Adv. Mater.* **2008**, *20*, 1160.

(25) Wang, Z. Y.; Ergang, N. S.; Al-Daous, M. A.; Stein, A. *Chem. Mater.* **2005**, *17*, 6805.

(26) Cao, F. F.; Wu, X. L.; Xin, S.; Guo, Y. G.; Wan, L. J. *J. Phys. Chem. C* **2010**, *114*, 10308.

(27) Tirado, J. L.; Santamaría, R.; Ortiz, G. F.; Menéndez, R.; Lavela, P.; Jiménez-Mateos, J. M.; Gómez García, F. J.; Concheso, A.; Alcántara, R. *Carbon* **2007**, *45*, 1396.

(28) Monnier, A.; Schuth, F.; Huo, Q.; Kumar, D.; Margolese, D.; Maxwell, R. S.; Stucky, G. D.; Krishnamurty, M.; Petroff, P.; Firouzi, A.; Janicke, M.; Chmelka, B. F. *Science* **1993**, *261*, 1299.

(29) Yang, P.; Zhao, D.; Margolese, D. I.; Chmelka, B. F.; Stucky, G. D. *Chem. Mater.* **1999**, *11*, 2813.

(30) Yang, P.; Zhao, D.; Margolese, D. I.; Chmelka, B. F.; Stucky, G. D. *Nature* **1998**, *396*, 152.

(31) Dominko, R.; Bele, M.; Goupil, J.-M.; Gaberscek, M.; Hanzel, D.; Arcon, I.; Jamnik, J. *Chem. Mater.* **2007**, *19*, 2960.

(32) Lim, S.; Yoon, C. S.; Cho, J. *Chem. Mater.* **2008**, *20*, 4560.

(33) Luo, J.-y.; Wang, Y.-g.; Xiong, H.-m.; Xia, Y.-y. *Chem. Mater.* **2007**, *19*, 4791.

(34) Doherty, C. M.; Caruso, R. A.; Smarsly, B. M.; Drummond, C. J. *Chem. Mater.* **2009**, *21*, 2895.

(35) Doherty, C. M.; Caruso, R. A.; Drummond, C. J. *Energy Environ. Sci.* **2010**, *3*, 813.

(36) Wang, G.; Liu, H.; Liu, J.; Qiao, S.; Lu, G. M.; Munro, P.; Ahn, H. *Adv. Mater.* **2010**, *22*, 4944.

(37) Doherty, C. M.; Caruso, R. A.; Smarsly, B. M.; Adelhelm, P.; Drummond, C. J. *Chem. Mater.* **2009**, *21*, 5300.

(38) Liu, R.; Shi, Y.; Wan, Y.; Meng, Y.; Zhang, F.; Gu, D.; Chen, Z.; Tu, B.; Zhao, D. *J. Am. Chem. Soc.* **2006**, *128*, 11652.

(39) Kang, Y.-S.; Lee, H. I.; Zhang, Y.; Han, Y. J.; Yie, J. E.; Stucky, G. D.; Kim, J. M. *Chem. Commun.* **2004**, 1524.

(40) Vu, A.; Stein, A. *Chem. Mater.* **2011**, *23*, 3237.

(41) Li, F.; Wang, Z.; Ergang, N. S.; Fyfe, C. A.; Stein, A. *Langmuir* **2007**, *23*, 3996.

(42) Meng, Y.; Gu, D.; Zhang, F.; Shi, Y.; Yang, H.; Li, Z.; Yu, C.; Tu, B.; Zhao, D. *Angew. Chem. Int. Ed.* **2005**, *44*, 7053.

(43) Schroden, R. C.; Al-Daous, M.; Sokolov, S.; Melde, B. J.; Lytle, J. C.; Stein, A.; Carbajo, M. C.; Fernández, J. T.; Rodríguez, E. E. *J. Mater. Chem.* **2002**, *12*, 3261.

(44) Van Der Pauw, L. J. *Philips Tech. Rev.* **1958/59**, *20*, 220.

(45) Ellis, B. L.; Makahnouk, W. R. M.; Makimura, Y.; Toghill, K.; Nazar, L. F. *Nat. Mater.* **2007**, *6*, 749.

(46) Dong, A.; Ren, N.; Tang, Y.; Wang, Y.; Zhang, Y.; Hua, W.; Gao, Z. *J. Am. Chem. Soc.* **2003**, *125*, 4976.

(47) Li, D.; Zhou, H.; Honma, I. *Nat. Mater.* **2004**, *3*, 65.

(48) Song, M.-S.; Kim, D.-Y.; Kang, Y.-M.; Kim, Y.-I.; Lee, J.-Y.; Kwon, H.-S. *J. Power Sources* **2008**, *180*, 546.

(49) Ferrari, A. C.; Robertson, J. *Phys. Rev. B* **2000**, *61*, 14095.

(50) Doeff, M. M.; Hu, Y.; McLarnon, F.; Kostecki, R. *Electrochem. Solid-State Lett.* **2003**, *6*, A207.

(51) Tuinstra, F.; Koenig, J. L. *J. Chem. Phys.* **1970**, *53*, 1126.

(52) Ergang, N. S.; Fierke, M. A.; Wang, Z.; Smyrl, W. H.; Stein, A. *J. Electrochem. Soc.* **2007**, *154*, A1135.

(53) Wang, Z.; Li, F.; Ergang, N. S.; Stein, A. *Chem. Mater.* **2006**, *18*, 5543.

(54) Wang, Z.; Li, F.; Ergang, N. S.; Stein, A. *ECS Trans.* **2008**, *6*, 199.

(55) Wang, Z.; Stein, A. *Chem. Mater.* **2008**, *20*, 1029.

(56) J.R.Dahn *Phys. Rev. B* **1991**, *44*, 9170.

(57) Ergang, N. S.; Lytle, J. C.; Lee, K. T.; Oh, S. M.; Smyrl, W. H.; Stein, A. *Adv. Mater.* **2006**, *18*, 1750.

CHAPTER 3

Lithium Iron Phosphate Spheres as Cathode Materials for High Power Lithium Ion Batteries

Outline

3.1 Introduction

Its low cost, environmental compatibility, and intrinsic thermal safety have placed lithium iron phosphate ($LiFePO_4$ or LFP) among the most promising cathode materials for LIBs targeting the hybrid electric vehicle (HEV) and electric vehicle (EV) markets.[1-3] However, the intrinsic low electronic and ionic conductivities of bulk LFP particles have restricted their rate performance, which is critical for HEV and EV power sources.[4-7] The electronic conductivity of LFP can be improved by coating it with carbon or a metallic conductive layer.[8-10] The ionic conductivity can be boosted by doping with isovalent ions and by nanostructuring the bulk particles into nanosized particles.[11] The rate performance of LFP electrodes can be also improved by using nanoporous electrodes, because the interfacial area between a nanoporous electrode and the electrolyte is greatly increased. Combinations of nanostructuring and conductive coatings would increase the electronic conductivity and ionic conductivity simultaneously. As described in Chapter 2, 3DOM/m $LiFePO_4$ composites with high surface areas, well-ordered structure, and good electronic conductivity have shown extremely good rate performance (84 mA h g^{-1} at 5C rate).[12] Hierarchically porous $LiFePO_4$ and $LiFePO_4$/C composites have been reported with extremely high rate performances.[13-15] The biggest disadvantage of using porous electrode materials is their low volumetric energy density, which will be addressed in this chapter.

The volumetric energy density of a battery is an important factor for electronic devices where the available space for the power source is limited, such as in portable devices. An electrode composed of nanoparticles generally has good electrochemical performance but low volumetric energy density as the nanoparticles are poorly packed. The volumetric energy density of an electrode depends strongly on its tap density, which is a macroscopic property that is affected by the morphology and the size of the bulk particles. In most cases, micrometer-sized particles have higher tap densities but worse electrochemical performances than those of nanometer dimensions. For particles of similar size, the shape of the particles has a strong effect on tap density. Electrodes made of spherical particles normally have higher tap densities than those composed of irregular particles, as the spherical particles can be packed with higher efficiency. One way to overcome the dilemma of increasing the electrochemical performance but worsening the tap density is to fabricate

micron-sized particles with nanometer-sized features, which are accessible to the electrolyte. Hollow-sphere $LiFePO_4$, and porous $LiFePO_4$ microspheres have been fabricated for LIBs, and showed both high rate performance and high volumetric energy densities.[16-18]

Carbon coatings are known not only to boost the electronic conductivity of LFP particle but also limit the growth of LFP particles at high temperature.[13,19-24] In the synthesis of 3DOM/m $LiFePO_4$/C composites, the precursor was confined in the octahedral and tetrahedral sites of the FCC structure created from the packing of 400 nm PMMA spheres, which resulted in the formation of a network of spherical $LiFePO_4$ particles that were connected through carbon matrix.[12] The spheres themselves are composed of nanoparticles with nanopores, which can be used as the cathode materials without the need of carbon matrix. This cathode material would have higher volumetric energy density and should preserve the high rate performance of the original composite as long as the nano-features remain after the carbon removal step. It seems that in the colloidal crystal template synthesis, the special interactions between $LiFePO_4$ precursor, PF sol, and surfactant inside the confined spaces (the octahedral and tetrahedral sites) resulted in the formation of nano-spherical $LiFePO_4$ particles. We therefore wondered if this would also be true for different types of confinement where growth is limited to only two dimensions such as in thin films. In this chapter, we describe syntheses of nano-spherical $Li_3Fe_2(PO_4)_3$ and $LiFePO_4$/C composites whose morphologies were influenced through the interplay between LFP precursor, PF sol, and amphiphilic surfactant inside confinement. $Li_3Fe_2(PO_4)_3$ was synthesized by burning 3DOM/m $LiFePO_4$ composites in air to remove the carbon phase. Spherical $LiFePO_4$ particles embedded in a carbon matrix were synthesized by first spin-coating the precursor containing LFP-precursor, PF sol, and F127 in ethanol onto a quartz substrate and then pyrolyzing the aged composites for 4–6 h under nitrogen at different temperatures. These syntheses are outlined in Figure 3.1 below.

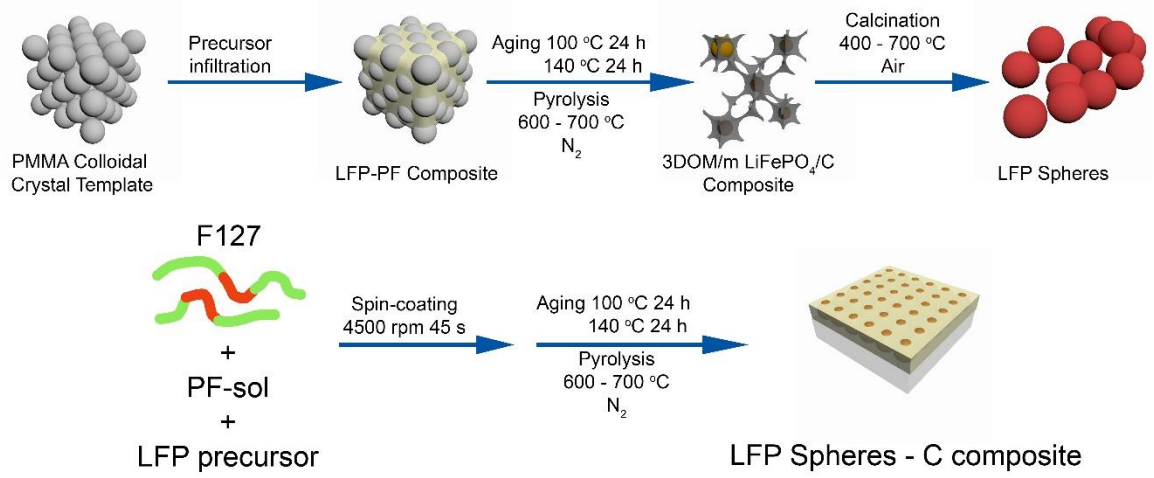

Figure 3.1 Synthesis schemes of LFP spheres and LFP sphere–C composites.

3.2 Experimental Section

3.2.1 Materials.

The chemicals used in this study were obtained from the following sources: methyl methacrylate (MMA) monomer (99%), 2,2'-azobis(2-methyl propionamidine) dihydrochloride (AMPD) initiator (97%), concentrated aqueous H_3PO_4 solution (85 wt%), N-methyl-2-pyrrolidone (NMP) battery quality electrolyte (99.5%), polyvinylidene fluoride (PVdF), lithium foil, and Ketjenblack from Aldrich; lithium perchlorate (99.0%), ethylene carbonate (>99.0%), dimethyl carbonate (>99.0%) from Fluka; $FeCl_2 \cdot 4H_2O$ (98%), LiCl (99.5%), phenol (ACS reagent) and formaldehyde solution (37% aqueous solution) from Fisher Scientific; Pluronic F127 from BASF; hydrochloric acid (37%) from Malinckrodt Chemicals; and sodium carbonate (anhydrous, 99.7%) from J.T. Baker. Deionized water was purified to a resistance higher than 18 MΩ.

3.2.2 3DOM/m $LiFePO_4$ preparation.

3DOM/m $LiFePO_4$/C composites were prepared by a dual templating method, in which the nonionic surfactant F127 (the poly(ethylene oxide)-poly(propylene oxide)-poly(ethylene oxide) triblock copolymer $PEO_{106}PPO_{70}PEO_{106}$) and PMMA colloidal crystals were intended as templates for mesopores and macropores, respectively. The detailed synthesis was described in section 2.2.4 of Chapter 2.

3.2.3 Preparation of $Li_3Fe_2(PO_4)_3$ nanospheres.

$Li_3Fe_2(PO_4)_3$ nanospheres were prepared by calcining 3DOM/m $LiFePO_4$ composites in air at 400, 600, and 700 °C for 5 h with a heating rate of 1 °C min^{-1}. The original 3DOM/m $LiFePO_4$ composite was pyrolyzed at 600 °C, which resulted in the formation of spherical $LiFePO_4$ connected by a carbon matrix.

3.2.4 Preparation of $LiFePO_4$/C composite nanospheres.

Nanospherical $LiFePO_4$ was prepared by spin-coating LFP/C precursors on a quartz substrate at 4500 rpm for 45 s. Two different precursors with different amounts of PF sol were used. PF-sol (2 g or 1 g 50 wt% in ethanol) was mixed with 2 g aqueous HCl (0.2 M) in a 20 mL vial and stirred for 15 min. F127 surfactant (1 g) was then added and stirred until a clear solution was obtained. $FeCl_2$ (1.988 g) and LiCl (0.435 g) were mixed and ground in a mortar, then transferred to the solution. At this point, the color of the solution changed from light yellow to green. The vial was placed in a larger glass bottle under flowing nitrogen to avoid the oxidation of Fe^{2+}. The mixture was vigorously stirred until all the salts were dissolved (usually 3–4 h). If the solution became too viscous for stirring, 0.5 mL ethanol was added. Then concentrated H_3PO_4 (0.011 mol) was slowly added to the solution, and the mixture was stirred overnight before being used for spin-coating. The spin-coated film was aged at 100 °C for 24 h, then at 140 °C for 24 h to increase the cross-linking of the polymer. The aged film was then stripped from the substrate and pyrolyzed at 600 or 700 °C for 5 h with a heating rate of 1 °C min^{-1} under nitrogen.

3.2.5 Product characterization.

All samples were ground into a fine powder before structural analyses. Product crystallinities and phase purities were determined by powder X-ray diffraction (XRD) using a PANalytical X-Pert PRO MPD X-ray diffractometer equipped with a cobalt source and an X-Celerator detector. Data were collected from 10° to 85° 2θ, at a step size of 0.017° and a rate of 20.7 s/step. Average crystallite sizes were estimated by Rietveld refinement using X'pert HighScore Plus 2.0a software. Instrumental broadening was corrected using a LaB_6 standard. Small-angle X-ray scattering (SAXS) data were acquired on a Rigaku RU-200BVH 2D SAXS instrument using a 12 kW-rotating anode with a Cu source and a

Siemens Hi-Star multi-wire area detector. Raman spectroscopy was performed with a Witec Alpha300R confocal Raman microscope using 514.5 nm incident radiation at the lowest possible potential to minimize beam damage of the sample. Scanning electron microscopy (SEM) was carried out with a JEOL-6700 microscope operating at 5 kV with emission currents ranging from 2 to 10 μA. Transmission electron microscopy (TEM) was carried out with a Technai T12 microscope operating at 120 kV with emission currents ranging from 7 to 12 μA. Thermogravimetric analysis (TGA) and differential scanning calorimetry (DSC) were performed on a Netzsch model STA 409 instrument to determine a suitable temperature program for the precursor transformation (flowing nitrogen atmosphere) and to determine the carbon content in the final products (flowing air atmosphere), using a heating rate of 5 °C min^{-1} to a final temperature of 900 °C

3.2.6 Electrochemical tests.

All electrochemical tests were carried out using an Arbin battery-testing system (ABTS 4.0). Galvanostatic charge–discharge measurements were performed in a coin cell, in which the spherical LFPs (80 wt%) with 10 wt% carbon black and 10 wt% PVDf in NMP were used as the cathode and Li foil as the anode. The cell was constructed and assembled in a dry room with <1% relative humidity. For cycling experiments, constant currents were applied and the voltages were restricted to a window of 2.0–4.2 V with 5 min rest periods between each step. All potential values are reported vs. Li/Li^+, and specific capacities are reported per gram of active materials.

3.3 Results and Discussion

3.3.1 $Li_3Fe_2(PO_4)_3$ nanospheres

In Chapter 2, we described that 3DOM/m $LiFePO_4$/C composites were constructed by spherical $LiFePO_4$ in octahedral sites connected by mesoporous carbon in tetrahedral sites. To obtain nano-spherical $LiFePO_4$ particles, the carbon phase must be removed. It is desired that the removal of carbon does not affect the $LiFePO_4$ phase. The easiest way to remove carbon is to burn it in air. Phosphate compounds are known to be thermally stable up to 700 °C and were not expected to be affected by the carbon removal step. The TGA

and DSC traces of 3DOM/m $LiFePO_4$/C in air showed that the carbon phase was removed between 350–525 °C (Figure 3.2). The amount of carbon in the sample was calculated from the TGA trace to be 30 wt% of the sample.

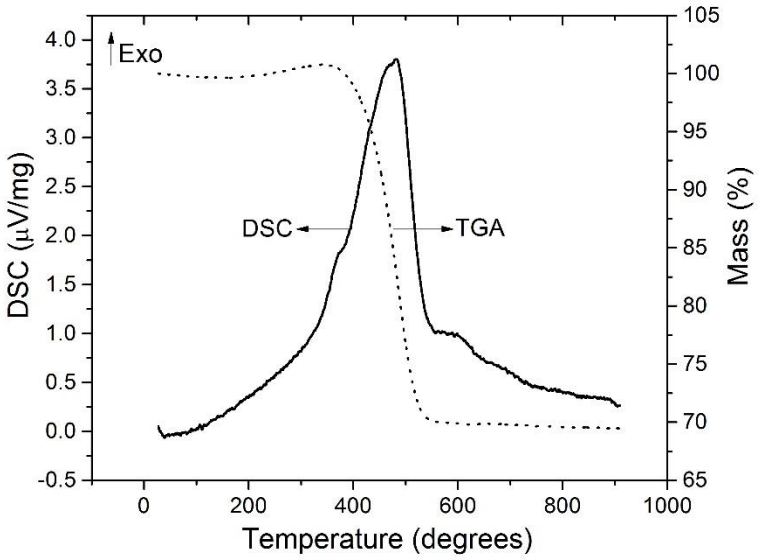

Figure 3.2 TGA and DSC traces (obtained in air) of 3DOM/m $LiFePO_4$/C composites pyrolyzed at 600 ˚C.

It is well known that $LiFePO_4$ will undergo oxidation when heated in air at a temperature higher than 700 °C to give $Li_3Fe_2(PO_4)_3$ and Fe_2O_3, following the reaction:

$$12\ LiFePO_4 + 3\ O_2 \longrightarrow 4\ Li_3Fe_2(PO_4)_3 + 2\ Fe_2O_3$$

However, the XRD patterns of LFP obtained from the calcination of 3DOM/m $LiFePO_4$/C at different temperatures showed that the reaction actually happened at temperatures as low as 400 °C. When treated at 400 °C for 5 h, a dark red powder was obtained which indicated the presence of Fe_2O_3, which was confirmed by XRD of the obtained product. The fact that the reaction happened at lower temperatures can be attributed to the higher reactivity of nanosized $LiFePO_4$ and to the extra heat produced from carbon combustion, which creates local temperatures higher than the temperature set by the furnace. This made it impossible to remove carbon by calcination without affecting the $LiFePO_4$ phase. However, $Li_3Fe_2(PO_4)_3$, the main product of the oxidation reaction is another LFP electroactive phase with a theoretical capacity of 120 mA h g^{-1} and an average discharge voltage of 2.78 V, and it is also an attractive cathode material.[25,26] XRD characterization was used to investigate the products of oxidation of 3DOM/m $LiFePO_4$/C composites in air at 400, 600,

and 700 °C. All XRD patterns showed three crystalline phases, $LiFeP_2O_7$, $Li_3Fe_2(PO_4)_3$, and Fe_2O_3. The fraction of each phase was calculated using the normalized reference intensity ratios (RIR) method since no other phases were detected in the XRD patterns of the calcined 3DOM/m $LiFePO_4$/C composites. For the sample calcined at 400 °C, monoclinic $Li_3Fe_2(PO_4)_3$ contributed to 76% of the molar ratio of the mixture (Figure 3.3). The $LiFeP_2O_7$ crystalline phase was also observed for samples calcined at 600 or 700 °C, although its content became smaller as the calcination temperatures increased (Table 3.1). It is possible that the oxidation reaction of 3DOM/m $LiFePO_4$/C composites in air is a two-step reaction. First, $LiFePO_4$ undergoes a conversion to $LiFeP_2O_7$, then $LiFeP_2O_7$ is oxidized to $Li_3Fe_2(PO_4)_3$ and Fe_2O_3. In addition, the second reaction is endothermic, so that more $LiFeP_2O_7$ is oxidized at higher temperatures.

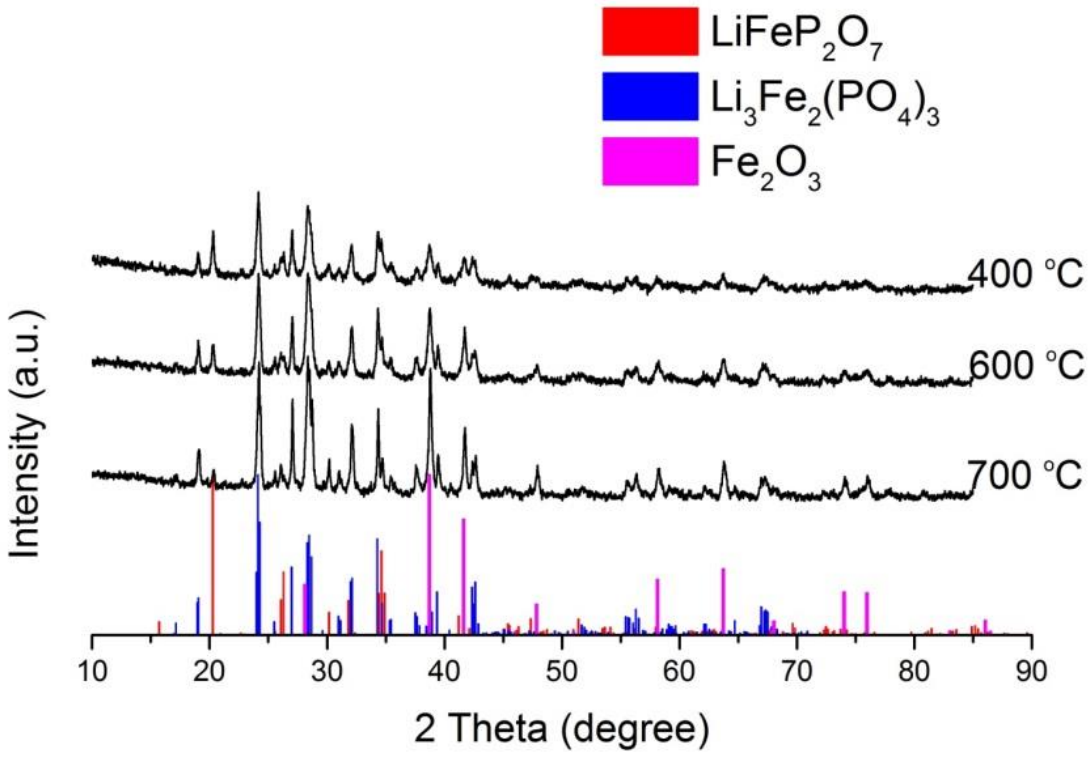

Figure 3.3 XRD pattern of calcined 3DOM/m $LiFePO_4$/C composites at 400, 600 and 700 °C showing $LiFeP_2O_7$, $Li_3Fe_2(PO_4)_3$, and Fe_2O_3 crystalline phases.

Table 3.1 XRD semi-quantitative analysis for $LiFeP_2O_7$, $Li_3Fe_2(PO_4)_3$, and Fe_2O_3 content based on their reference intensity rations (RIRs).

	400 °C	**600 °C**	**700 °C**
Fe_2O_3 (%)	6	9	11
$LiFeP_2O_7$ (%)	18	11	9
$Li_3Fe_2(PO_4)_3$ (%)	76	80	80

The effect of calcination temperature on morphologies of $Li_3Fe_2(PO_4)_3$ was investigated using SEM and TEM. Figure 3.4A shows a TEM image of the spherical $LiFePO_4$ phase in the carbon matrix before calcination and Figure 3.4B an image of $Li_3Fe_2(PO_4)_3$ particles after calcination at 400 °C. When calcined at 400 °C, the sizes of the obtained $Li_3Fe_2(PO_4)_3$ spheres were smaller than the sizes of spherical $LiFePO_4$ in the carbon matrix, which may be attributed to loss of the carbon component and collapse of the porous structure. The sizes of these dense, crystalline spheres range from 132 nm to 155 nm, thereby creating short diffusion paths for lithium ions. In addition, the spheres are quite monodisperse, which ensures a high packing efficiency and high volumetric capacity of the electrode materials. For samples calcined at 600 and 700 °C, the sizes of isolated particles are smaller than the sizes of particles calcined at 400 °C, which indicates further condensation of the spheres at higher temperatures. In these samples, big particles formed from the aggregation of smaller particles were also observed. These aggregated particles are more noticeable in the sample calcined at 700 °C (Figure 3.4E). The selected-area diffraction patterns of samples calcined at 400 and 600 °C (insets in Figure 3.4B and 3.4C) feature bright dots, which confirm the crystalline nature of these materials. The highly crystalline nature of these samples was also confirmed by lattice fringes shown in an image with higher magnification (Figure 3.4F).

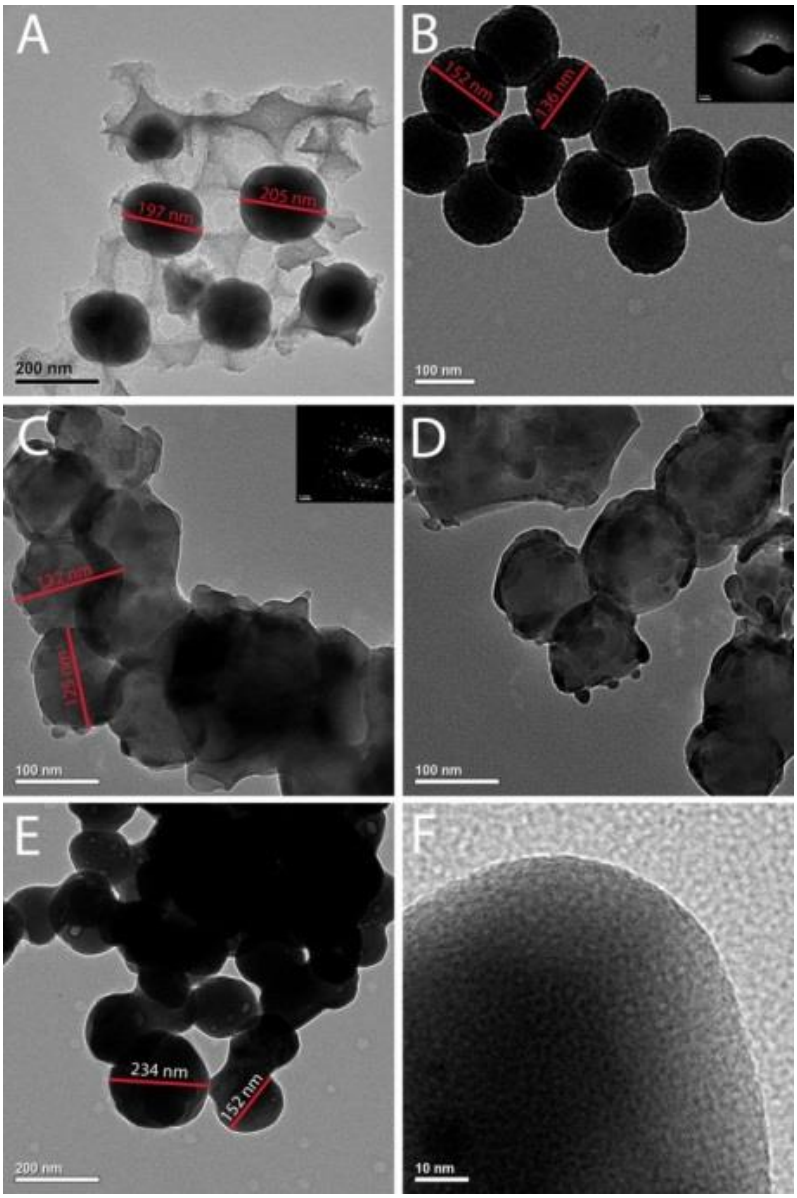

Figure 3.4 TEM images of (A) 3DOM/m $LiFePO_4$/C composite; B, (C and D), and (E and F)) are $Li_3Fe_2(PO_4)_3$ obtained from the calcination of 3DOM/m $LiFePO_4$/C composite at 400, 600, and 700 °C respectively. The insets in figure (B) and (C) are electron diffractions patterns of the TEM images showing crystallinity of these samples.

The morphologies of spherical $Li_3Fe_2(PO_4)_3$ particles were further investigated by SEM. All the SEM images of samples calcined at 600 and 700 °C show evidence for the aggregation of spherical particles into elongated particles. The aggregation was more prominent in the sample calcined at 700 °C. These samples also feature small pores between particles, which can enhance the mass transport of electrolyte inside the material.

The elongated particles formed from the aggregation of 2–3 spherical particles, consistent with observations in the TEM images (Figure 3.4 C and D).

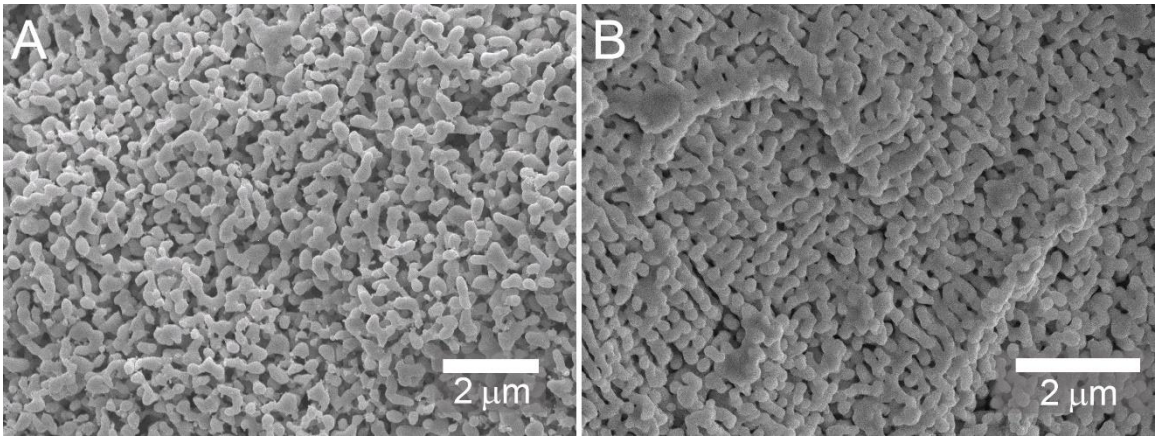

Figure 3.5 SEM images of (A) $Li_3Fe_2(PO_4)_3$ calcined at 600 °C; (B) $Li_3Fe_2(PO_4)_3$ calcined at 700 °C, showing that spherical particles have sintered into longer particles.

3.3.2 $LiFePO_4$/C Nanosphere Composites

Spherical $LiFePO_4$ is of great interest for high volumetric energy density LIBs. The spherical shape was achievable by confining PF sol-LFP precursor in the interstitial sites of an FCC close-packed array of colloidal PMMA spheres. The sizes of the $LiFePO_4$ spheres were found to depend on the volume of the interstitial sites and on the sizes of the colloidal spheres. The colloidal crystal provides the three dimensional confinement. In the following part, we will try to investigate if it is possible to achieve spherical shape of $LiFePO_4$ in two dimensional confinement such as in a thin film configuration.

Because two different precursors with different amounts of PF-sol were used, the samples were named after the amount of PF in the precursors. For instance, the sample made from the precursor containing 1 g PF and 2g PF and pyrolyzed at 600 °C will be named as PF_600_1 and PF_600_2 respectively. The different amounts of PF in the precursors were expected to produce products with different contents of carbon. The TG traces for samples pyrolyzed at 600 °C showed that the carbon content for samples made from 1 g PF and 2 g PF precursors was 15 and 28 wt%, respectively (Figure 3.6).

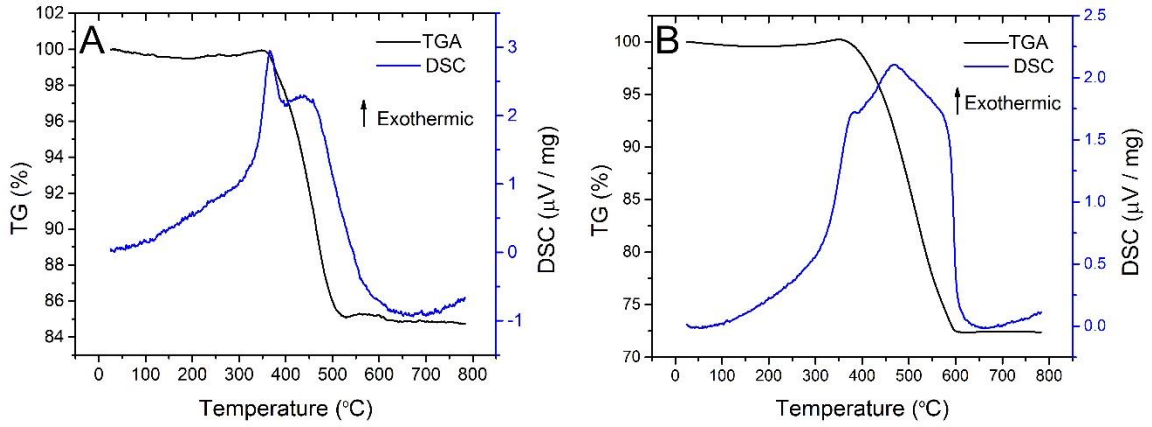

Figure 3.6 TGA-DSC traces in air of samples made from (A) 1 g PF and (B) 2 g PF precursor.

The crystallinity of samples pyrolyzed at different temperatures was investigated using XRD. All samples produced a pattern of $LiFePO_4$ (ICCD#00-40-1499) as the only crystalline phase; other crystalline impurities were not present or in such small quantities that they could not be detected by XRD. For the sample with the higher content of PF sol precursor (2 g), the background between 8 and 30° 2Θ was higher than the background for the sample with a lower content of PF precursor (1 g), which is attributed to a higher content of amorphous carbon in the final products.

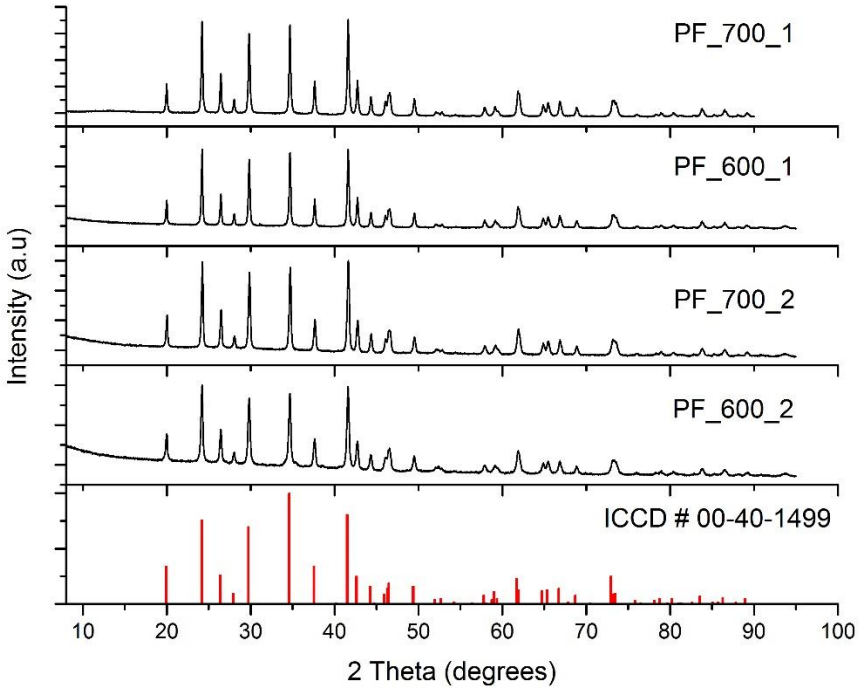

Figure 3.7 XRD pattern of LFP/C composites showing $LiFePO_4$ patterns (ICCD#00-40-1499).

In the synthesis of spherical $LiFePO_4$ embedded in a carbon film, after spin-coating and aging at 100 and then at 140 °C, both precursors formed very homogeneous films (Figure 3.8A). It was important to process the film by annealing immediately after spin coating, otherwise micron-sized, spherical iron-rich particles formed within the polymeric network. Figure 3.8 B is the image of a film that was left at room temperature for 48 h before performing the annealing steps at 100 and 140 °C. It appears that the mobility of iron species in the pre-polymerized solution is high and they have strong affinity to each other, resulting in aggregation. The heat treatment accelerates the cross-linking of the pre-polymerized PF sol. Once a stable network is formed, it can prevent aggregation more effectively as iron ions are now strongly bonded to phenol groups in the rigid network. A dark precipitate resulting from the chelation between phenol groups in PF sol and iron ions was observed for the precursor solution after being left for 2–3 days at room temperature. The chelation happened quicker if F127 was not added to the solution. However, complexation leading to the formation of a precipitate in the solution is not desired as it makes it impossible to cast homogeneous thin films.

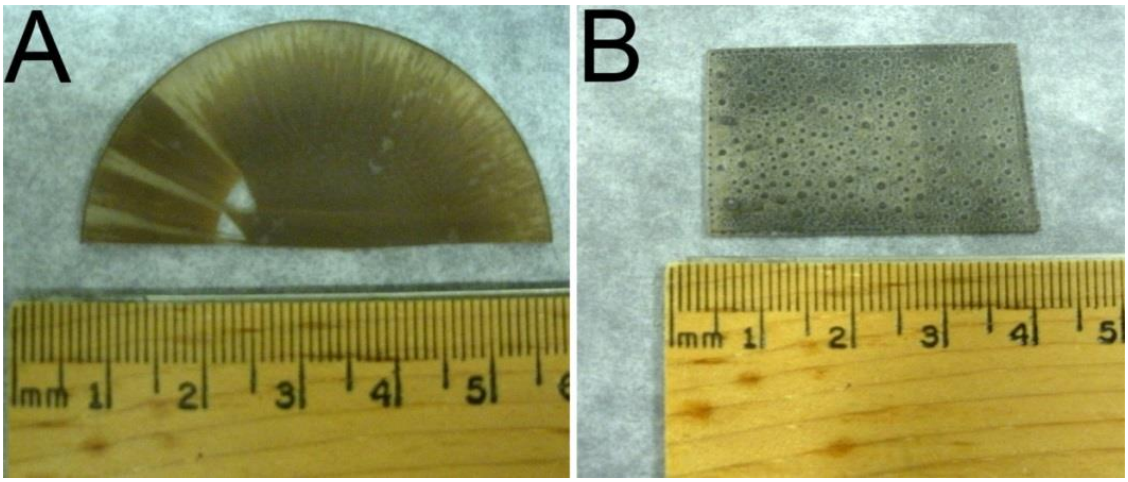

Figure 3.8 Images of $LiFePO_4$/C thin film composite (A) annealed at 100 °C then at 140 °C immediately after spin-coating; (B) an unannealed film left in the atmosphere for 48 h.

Film morphologies of all samples were characterized using SEM and TEM. The film thicknesses were estimated from cross-sections of SEM images and were approximately 1 and 2 μm for samples prepared from 1 g and 2 g PF precursor, respectively (Figure 3.9). The thicker films resulted from the higher viscosity of the precursor containing more PF.

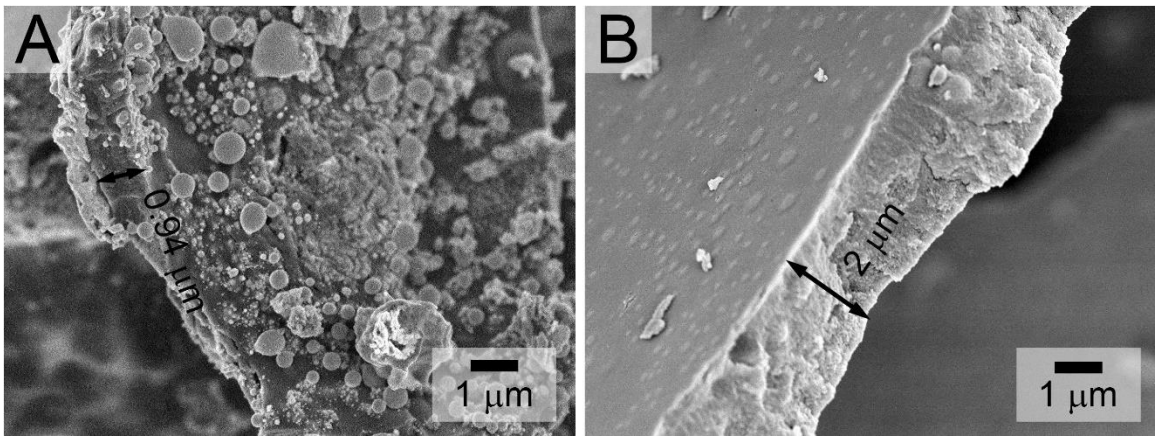

Figure 3.9 SEM images of (A) PF_600_1 and (B) PF_600_2 $LiFePO_4$/C films that were used to estimate the film thickness.

The morphologies of $LiFePO_4$/C samples were found to depend on both compositions and pyrolysis temperatures. For samples with lower carbon content, submicron to micron-sized spheres were found that protruded from the surfaces (Figure 3.10A, 3.10 C), whereas the surfaces of samples with higher carbon content were smoother and contained smaller spheres (Figure 3.11A, and 3.11C). In addition, the spheres inside the film are much smaller than the spheres found on the surface of the film. The reason is the higher mobility of iron species on the surface compared to the ones inside the film, where they are restricted by the rigid polymer network. It is interesting that inside the films, smaller $LiFePO_4$ particles were found to be embedded in the carbon matrix. This carbon network effectively connects the $LiFePO_4$ particles, providing short, conductive paths for electrons. Higher pyrolysis temperatures created bigger spheres and more rugged film surfaces even though the carbon phase seemed not to be affected by the temperature.

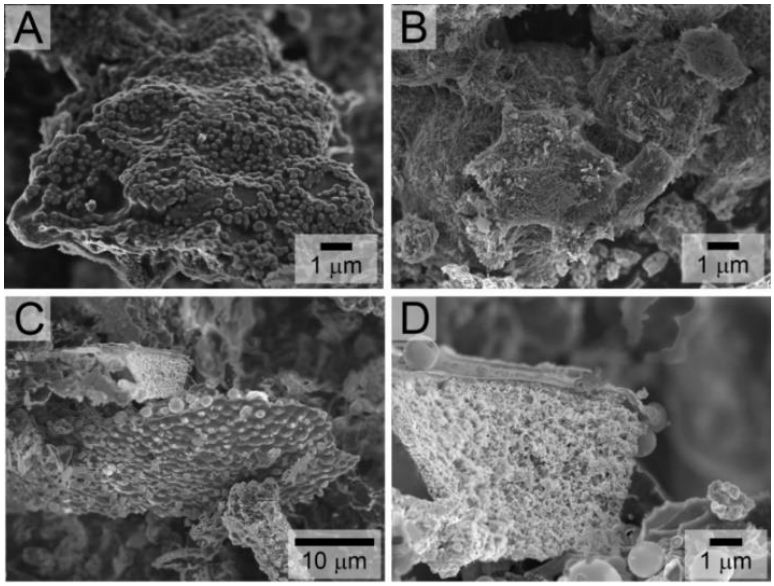

Figure 3.10 SEM images of (A) and (B) PF_600_1; (C) and (D) PF_700_1 showing microspheres protruding from the films and a carbon network.

For samples with higher carbon content, the film surface was smoother with fewer big spherical $LiFePO_4$ particles found outside of the carbon film (Figure 3.11). Yet the cross section of the film still showed sub-micron spheres (Figure 3.11B), particularly at the higher temperature (Figure 3.11D).

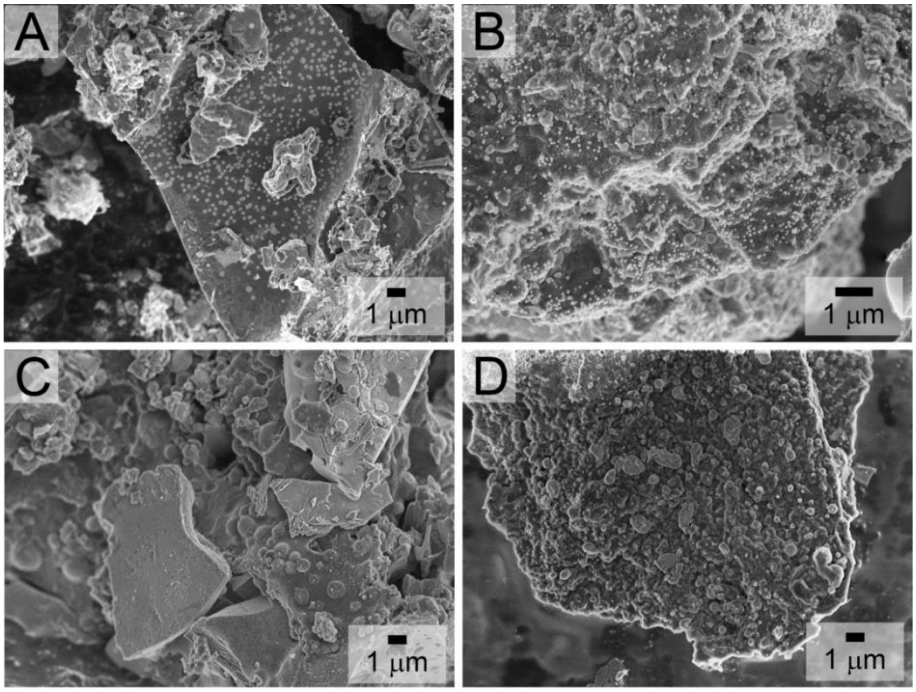

Figure 3.11 SEM images of (A) and (B) PF_600_2; (C) and (D) PF 700_2 showing a smoother film surface with fewer microspheres protruding from the films.

The carbon phase was characterized by Raman spectroscopy. The Raman spectrum of the $LiFePO_4$/C film shows two prominent peaks associated with sp^2 carbon (G-band, 1606 cm^{-1}) and sp^3 carbon (D-band, 1351 cm^{-1}) (Figure 3.12). The G-band originates from the in-plane bond-stretching motion of pairs of sp^2 carbon atoms, while the D-band involves a breathing mode of A_{1g} symmetry, which is only active in the presence of disorder.[27] The G peak shifts from 1581 cm^{-1} in graphite to 1606 cm^{-1} in the $LiFePO_4$/C film, which indicates that carbon in the composite is nanocrystalline graphite. The size domain can be estimated using the equation $\frac{I_D}{I_G} = \frac{C(\lambda)}{L_a}$, where I_D, I_G are the intensities of the disordered peak and the graphitic peak, respectively, $C(\lambda = 515.5\ nm) = 4.4\ nm$, λ is the wavelength of the laser used in the Raman spectrometer, and L_a is the cluster diameter of nanocrystalline graphite.[27] The broad peaks contain additional contributions from sp^3 carbon sites present in amorphous carbonaceous materials.[28] Therefore simply fitting the spectrum with two peaks does not give an accurate value of I_D/I_G. In order to interpret the Raman features, the spectrum was instead deconvoluted with four Gaussian peaks situated at 1190, 1351, 1518, and 1606 cm^{-1}, where the additional bands at 1190 and 1518 cm^{-1} are associated with sp^3 carbon vibrations. On the basis of the fitted intensity ratios of the D and G peaks, one can estimate the crystallite size in the direction of graphitic planes.[27,29] Figure 3.11 showed the fitted curves and the calculated graphitic size domains of all LFP/C films. It is interesting that the crystalline sizes are actually decreased with the increase of pyrolysis temperature. In general, carbon with larger graphitic domain has better conductivity. It is likely that the electronic conductivity of LFP/C films pyrolyzed at lower temperatures is higher than those of samples pyrolyzed at higher temperatures. Sevilla et.al investigated the effect of pyrolysis temperatures on the crystalline size and the electronic conductivity of iron-catalyzed graphitic carbons.[30] The result showed that the sample pyrolyzed at 500 °C has higher electronic conductivity than samples pyrolyzed at 550 and 600 °C, while only amorphous carbon with very low electronic conductivity was obtained when the sample was pyrolyzed at 800 °C.

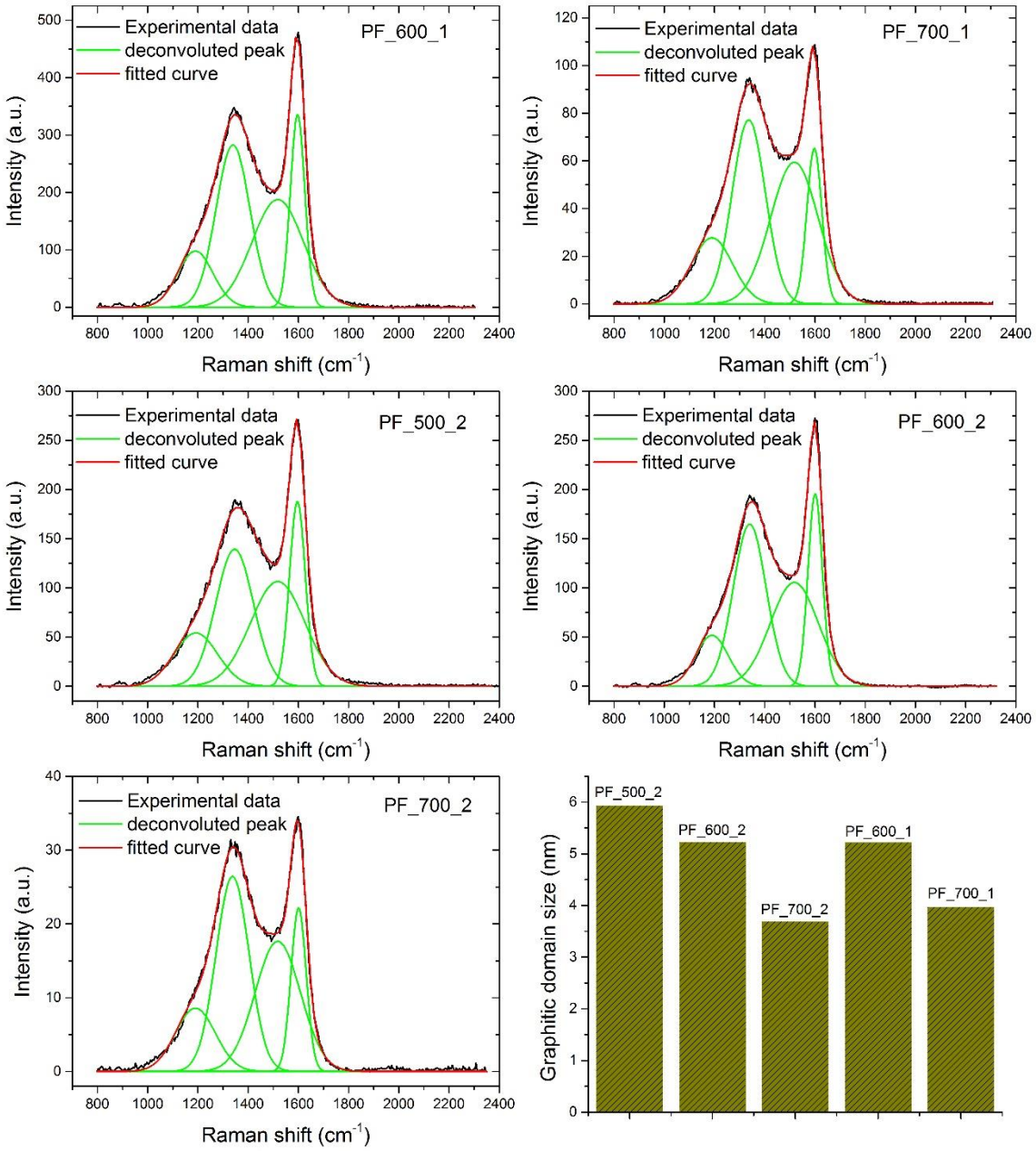

Figure 3.12 Raman spectra of LFP/C films used to estimate the graphitic domain size of the carbon phase.

TEM images of the sample prepared from 2 g PF sol and pyrolyzed at 600 °C showed packed spherical $LiFePO_4$ particles inside a thin film with the sphere sizes were less than 200 nm (Figure 3.13). Many nanocrystalline $LiFePO_4$ particles smaller than 8 nm were observed inside the carbon matrix. The HRTEM image in Figure 3.14B clearly shows the lattice fringes of crystalline $LiFePO_4$ particles, which are different from the surrounding amorphous carbon phase. TEM images of PF_700_2 also showed the presence of spherical

LFP particles embedded in carbon matrix with the particle sizes ranging from 10 to 150 nm (Figure 3.14C and 3.14D). To summarize the structural information from SEM and TEM analyses, the 1–2 μm thick, spin-coated films were composed of nanospheres smaller than 350 nm, packed inside a fibrous carbon-containing matrix. On the surface of the films, spheres with sizes ranging from 0.7 to 1.5 μm were present. The carbon phase itself contains many randomly distributed nanocrystalline $LiFePO_4$ particles smaller than 10 nm.

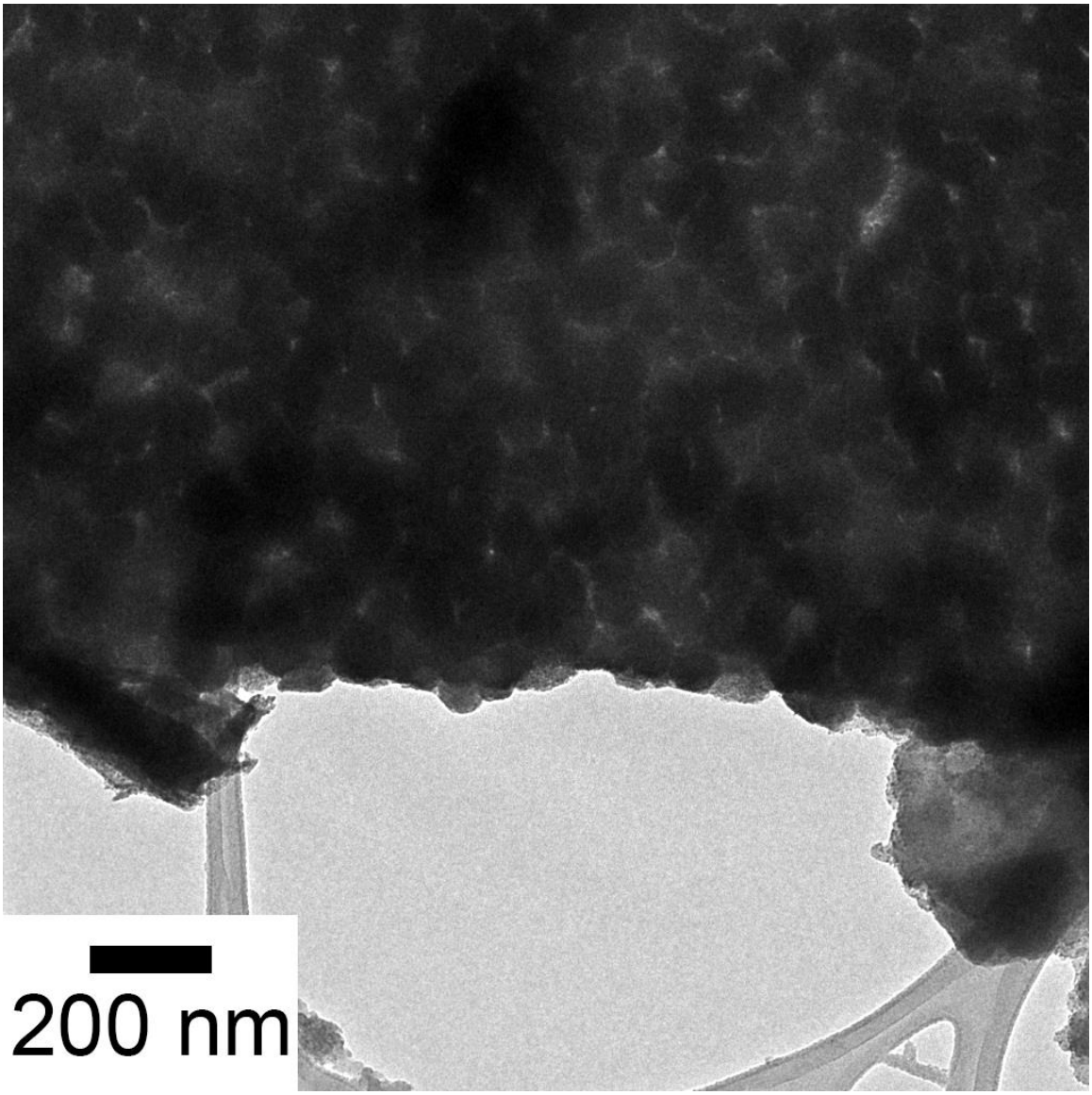

Figure 3.13 TEM images of $LiFePO_4$/C composite thin film pyrolyzed at 600 °C under nitrogen.

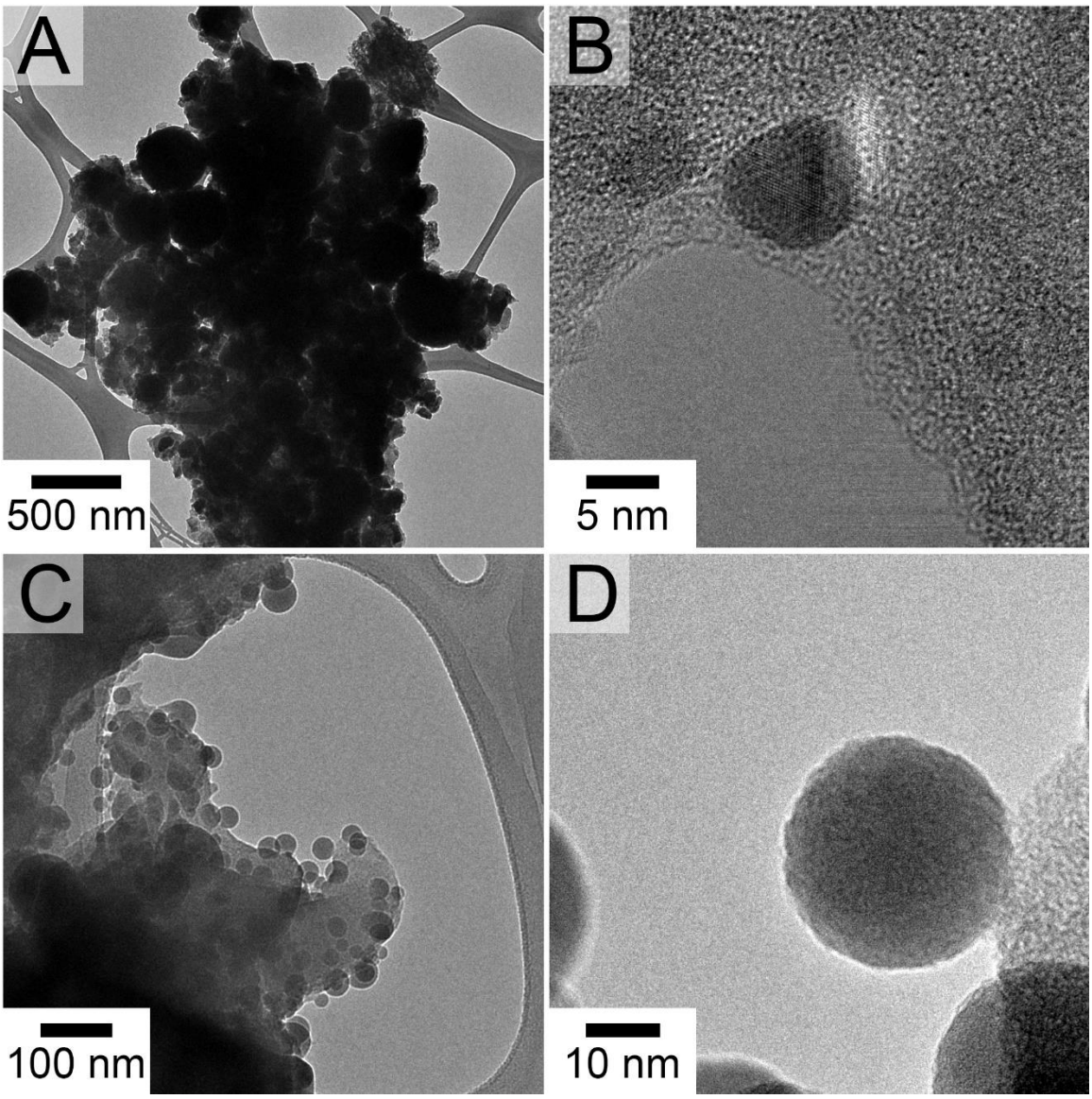

Figure 3.14. TEM images of $LiFePO_4$/C composite thin film made from 2 g PF precursor and pyrolyzed at A and B) 600 °C, and C and D) 700 °C under nitrogen.

3.4 Electrochemical Tests

3.4.1 $Li_3Fe_2(PO_4)_3$ Nanospheres

The discharge profile of a sample calcined at 600 °C shows two plateaus at 2.4 and 2.7 V (Figure 3.15A), which are characteristic for the discharge profile of $Li_3Fe_2(PO_4)_3$.[31,32] At slow rates (C/2), the specific discharge capacities for the samples calcined at 600 °C and

700 °C are 100 and 50 mA h g^{-1}, respectively. It is interesting that the capacity of the sample calcined at 600 °C is much higher than the capacity of the sample calcined at 700 °C even though the two samples showed similar morphology and crystallinity. The capacity of the sample calcined at 600 °C is about 83% of the theoretical capacity, which is very promising for using this material for LIB cathodes. At different rates varying from C/2 to 2.5C, the capacity of the sample calcined at 600 °C was retained while the capacity of sample calcined at 700 °C continuously decreased. This may be attributed to the loss of surface area and the higher degree of aggregation of the sample calcined at 700 ˚C.

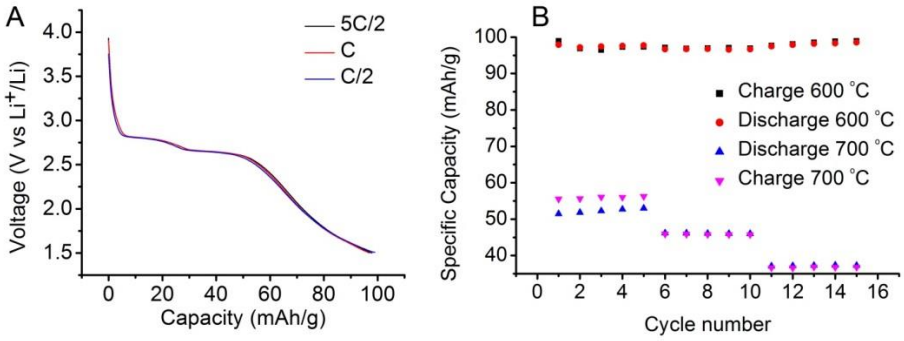

Figure 3.15 (A) discharge profile of $Li_3Fe_2(PO_4)_3$ calcined at 600 °C; (B) cyclability of $Li_3Fe_2(PO_4)_3$ at different rates.

3.4.2 Spherical $LiFePO_4$/C Composites

Electrochemical tests were performed with coin cells of spherical $LiFePO_4$/C composites. The cells were tested at different rates, ranging from C/2 to 16 C for many cycles. The discharge profiles of all samples showed the characteristic plateau of $LiFePO_4$ at 3.4 V. The two samples PF_600_1 and PF_700_1 with the lower carbon content showed similar performance. At a slow rate (C/2), both samples were able to deliver about 120 mA h g^{-1}, and at higher rate (4C) their discharge capacities were about 65 mA h g^{-1} (Figure 3.16). However, if we take a closer look at the discharge profiles of these samples, they are quite different. The sample pyrolyzed at 700 °C has more of its capacity delivered at 3.4 V, whereas a large portion of the capacity of the sample pyrolyzed at 600 °C is delivered at a lower potential. This means that even though both materials have the same lithium capacity, the sample pyrolyzed at 700 °C has a higher energy density than the sample pyrolyzed at 600 °C. The plateau at 3.4 V is the characteristic potential for the intercalation

of Li ions into crystal lattice of FePO4 forming $LiFePO_4$. The extraction of lithium ions at lower potential (from 1.8 to 3.4 V) may originate from the removal of interfacial lithium ions at the $LiFePO_4$/carbon interfaces where lithium ions are stored on the ionic conductive side (surface of $FePO_4$/$LiFePO_4$ particles) and electrons are localized on the electronic conductive side (surface of conductive carbon).[33] The interfacial lithium ion storage was also observed in several nanometer-sized transition metal oxides.[34-36] In this regard, $LiFePO_4$/C films pyrolyzed at lower temperature has larger graphitic domain size, which is able to store more lithium in the interfaces and have more of its capacity delivered at lower potential. Both of the samples are able to operate at extremely high rate (16C) and are able to deliver about 25 mA h g^{-1} without fading for 20 cycles.

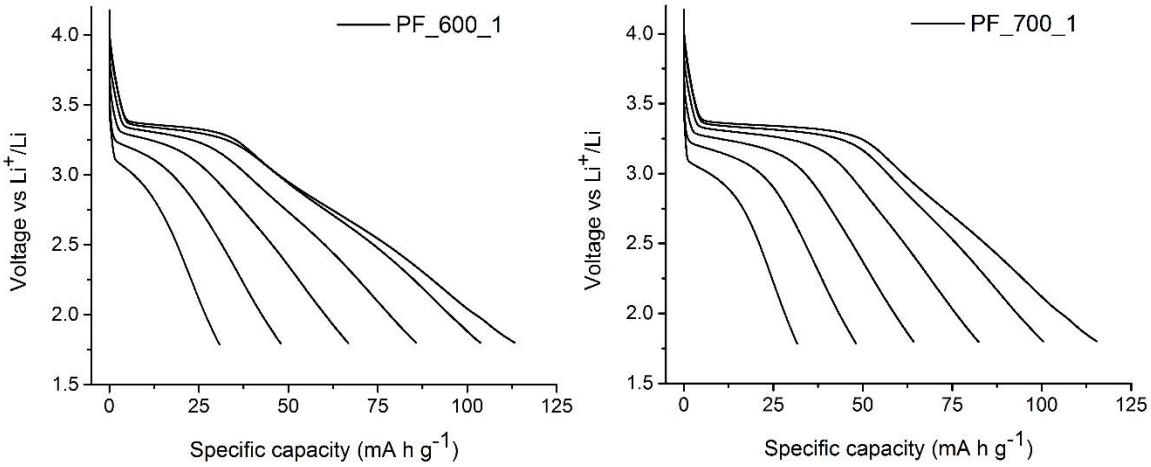

Figure 3.16 Discharge profiles of spherical $LiFePO_4$/C composites prepared from 1 g PF precursor and pyrolyzed at different temperatures.

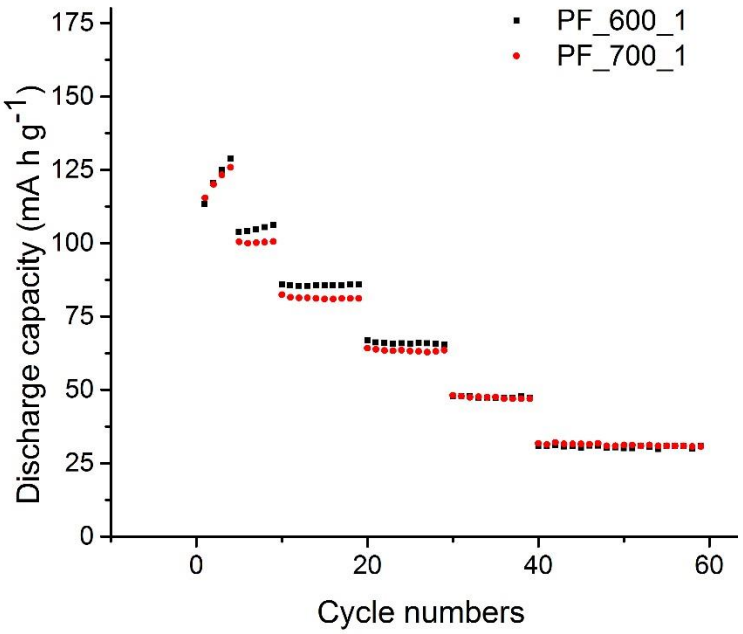

Figure 3.17 Rate performance of spherical $LiFePO_4$/C composites prepared from 1 g PF precursor and pyrolyzed at different temperatures.

The electrochemical performance of the samples with higher contents of carbon was vastly different and strongly depended on the pyrolysis temperature. Samples pyrolyzed at lower temperatures (500 and 600 °C) were able to deliver 130 mA h g^{-1} at C/2 rate while the value for sample pyrolyzed at 700 °C was only 60 mA h g^{-1}. This is quite surprising since the morphologies of the two samples pyrolyzed at 600 and 700 °C were quite similar and no impurity phases were detectable by XRD for the sample pyrolyzed at 700 °C. It is worth noting that only the PF_700_2 sample was not able to maintain the current when cycled at a 16C rate; the other two samples cycled without any problems.

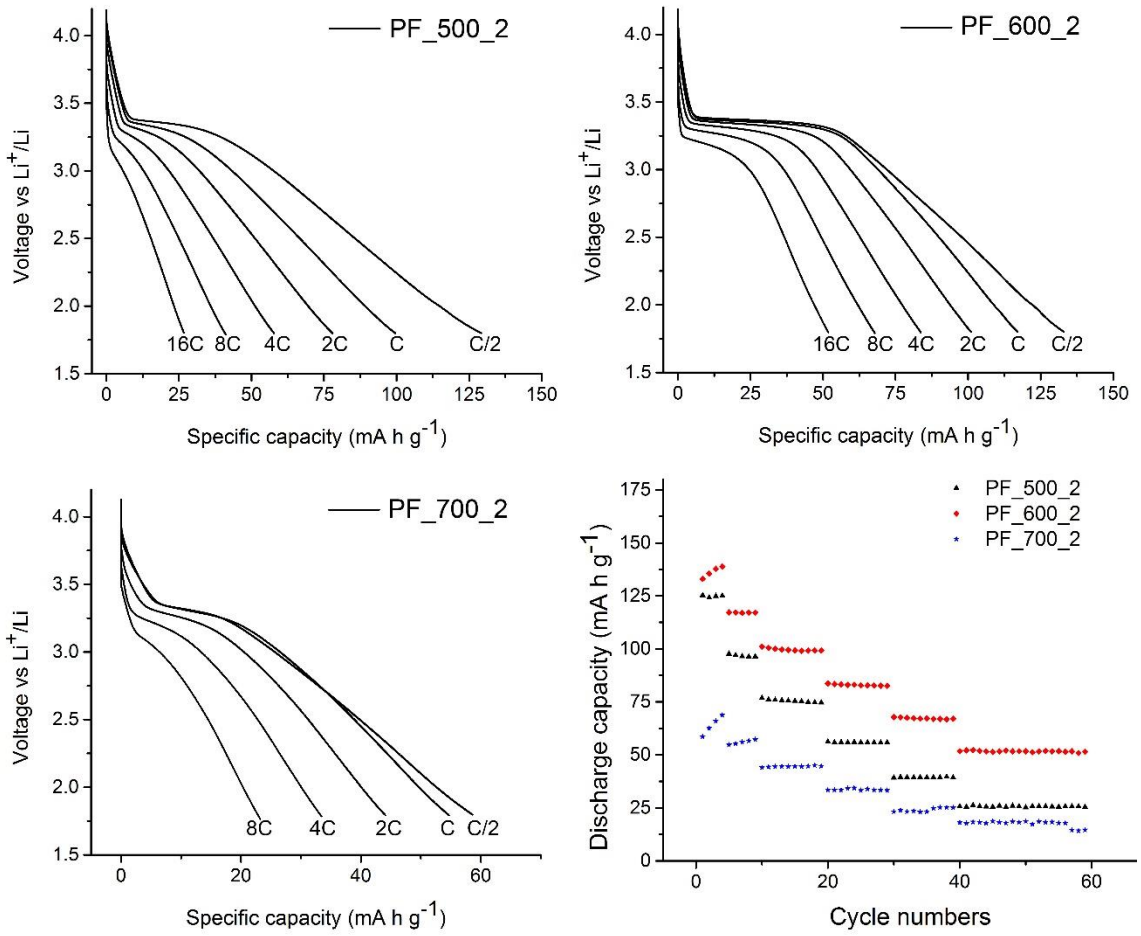

Figure 3.18 Discharge profiles and rate performance of spherical $LiFePO_4$/C composites prepared from 2 g PF precursor and pyrolyzed at different temperatures.

The amount of capacity delivered by the PF_600_2 sample at 3.4 V was higher than that of the PF_500_2 sample, which is also ascribed to the interfacial lithium storage, in which PF_500_2 with larger graphitic domain is able to store more lithium at the $LiFePO_4$/carbon interface. The PF_600_2 sample also had a better rate performance than the PF_500_2, particularly at higher rates. When cycled at a slow rate (C/2), both PF_600_2 and PF_700_2 samples showed increasing capacity over multiple cycles. During each cycle the sample gained about 2–5 mA h g^{-1}, which can be attributed to the presence of big LFP particles on the surface of the films, which need more time for lithium ions to intercalate/deintercalate. This effect disappeared when the sample were cycled at high rates as the capacity contribution from big $LiFePO_4$ particles at these rates are very limited. The PF_600_2 sample showed the best performance of all tested samples with 130 mA h g^{-1} at

C/2 rate and 50 mA h g^{-1} at 16 C rate. The good performance is attributed to the high carbon content and the small size and high crystallinity of the LFP phase that facilitated the diffusion of Li ions and the movement of electrons in the composite.

3.5 Conclusions

LFP cathode materials are of great interest for HEV and EV applications. However, to be useful for portable devices, which require much higher volumetric energy density, morphology control of electrode materials must be considered. Spherical microspheres with nanometer-sized features are of great interest because of their high tap density and good electrode performance. In this chapter, two different spherical LFP materials were described. Nano-spherical $Li_3Fe_2(PO_4)_3$ was obtained from the calcination of 3DOM/m $LiFePO_4$/C composites. The sample calcined at 600 °C showed good electrochemical performance with 100 mA h g^{-1} at 2.5C rate and good cyclability. The capacity was normalized for the actual weight percentage of $Li_3Fe_2(PO_4)_3$ in the sample. The cell capacity did not change when the rate was increased from C/5 to 2.5C, and even at very high rate (2.5C) the capacity was maintained after 50 cycles. However, the disadvantage of this material is the presence of Fe_2O_3 as a non-reactive phase, which decreases its specific capacity.

Spherical $LiFePO_4$/C composites prepared by spin-casting showed very good electrochemical performance. All samples were able to maintain a current when cycled at very high rates (up to 16C). The capacity contribution was closely related to the LFP and carbon phases, and the sample with a carbon phase with higher conductivity had most of its capacity delivered at a higher potential (3.4 V). The best performance was observed for a sample with 72 wt% of $LiFePO_4$ spheres and 28 wt% of carbon pyrolyzed at 600 °C, which delivered 130 mA h g^{-1} at C/2 rate and 100 mA h g^{-1} at 2C rate.

3.6 References

(1) Axsen, J.; Kurani, K. S.; Burke, A. *Transport Policy* **2010**, *17*, 173.

(2) Goodenough, J. B.; Kim, Y. *Chem. Mater.* **2010**, *22*, 587.

(3) Yuan, L.-X.; Wang, Z.-H.; Zhang, W.-X.; Hu, X.-L.; Chen, J.-T.; Huang, Y.-H.; Goodenough, J. B. *Energy Environ. Sci.* **2011**, *4*, 269.

(4) Delacourt, C.; Poizot, P.; Tarascon, J.-M.; Masquelier, C. *Nat Mater* **2005**, *4*, 254.

(5) Delmas, C.; Maccario, M.; Croguennec, L.; Le Cras, F.; Weill, F. *Nat Mater* **2008**, *7*, 665.

(6) Kang, B.; Ceder, G. *Nature* **2009**, *458*, 190.

(7) Nishimura, S.-I.; Kobayashi, G.; Ohoyama, K.; Kanno, R.; Yashima, M.; Yamada, A. *Nat. Mater.* **2008**, *7*, 707.

(8) Chen, Z.; Dahn, J. *J. Electrochem. Soc.* **2002**, *149*, A1184.

(9) Dominko, R.; Bele, M.; Gaberscek, M.; Remskar, M.; Hanzel, D.; Pejovnik, S.; Jamnik, J. *J. Electrochem. Soc.* **2005**, *152*, A607.

(10) Hu, Y. S.; Guo, Y. G.; Dominko, R.; Gaberscek, M.; Jamnik, J.; Maier, J. *Adv. Mater.* **2007**, *19*, 1963.

(11) Chung, S.-Y.; Bloking, J. T.; Chiang, Y.-M. *Nat. Mater.* **2002**, *1*, 123.

(12) Vu, A.; Stein, A. *Chem. Mater.* **2011**, *23*, 3237.

(13) Doherty, C. M.; Caruso, R. A.; Smarsly, B. M.; Adelhelm, P.; Drummond, C. J. *Chem. Mater.* **2009**, *21*, 5300.

(14) Doherty, C. M.; Caruso, R. A.; Smarsly, B. M.; Drummond, C. J. *Chem. Mater.* **2009**, *21*, 2895.

(15) Badot, J. C.; Ligneel, É.; Dubrunfaut, O.; Guyomard, D.; Lestriez, B. *Adv. Funct. Mater.* **2009**, *19*, 2749.

(16) Sun, C.; Rajasekhara, S.; Goodenough, J. B.; Zhou, F. *J. Am. Chem. Soc.* **2011**, *133*, 2132.

(17) Liu, J.; Conry, T. E.; Song, X.; Doeff, M. M.; Richardson, T. J. *Energy Environ. Sci.* **2011**, *4*, 885.

(18) Lee, M. H.; Kim, J. Y.; Song, H. K. *Chem. Commun.* **2010**, *46*, 6795.

(19) Wang, Y.; Hosono, E.; Wang, K.; Zhou, H. *Angew. Chem. Int. Ed.* **2008**, *47*, 7461.

(20) Liu, Y.; Liu, D.; Zhang, Q.; Yu, D.; Liu, J.; Cao, G. *Electrochim. Acta* **2010**, *56*, 2559.

(21) Wang, K.; Cai, R.; Yuan, T.; Yu, X.; Ran, R.; Shao, Z. *Electrochim. Acta* **2009**, *54*, 2861.

(22) Zhi, X.; Liang, G.; Wang, L.; Ou, X.; Gao, L.; Jie, X. *J. Alloys Compd.* **2010**, *503*, 370.

(23) Cho, Y.-D.; Fey, G. T.-K.; Kao, H.-M. *J. Power Sources* **2009**, *189*, 256.

(24) Lin, Y.; Gao, M. X.; Zhu, D.; Liu, Y. F.; Pan, H. G. *J. Power Sources* **2008**, *184*, 444.

(25) Sato, M.; Tajimi, S.; Okawa, H.; Uematsu, K.; Toda, K. *Solid State Ionics* **2002**, *152-153*, 247.

(26) S. Zhu, H. Z., T. Miyoshi, M. Hibino, I. Honma, M. Ichihara, *Adv. Mater.* **2004**, *16*, 2012.

(27) Ferrari, A. C.; Robertson, J. *Phys. Rev. B* **2000**, *61*, 14095.

(28) Doeff, M. M.; Hu, Y.; McLarnon, F.; Kostecki, R. *Electrochem. Solid-State Lett.* **2003**, *6*, A207.

(29) Tuinstra, F.; Koenig, J. L. *J. Chem. Phys.* **1970**, *53*, 1126.

(30) Sevilla, M.; Fuertes, A. B. *Carbon* **2006**, *44*, 468.

(31) Padhi, A. K.; Nanjundaswamy, K. S.; Goodenough, J. B. *J. Electrochem. Soc.* **1997**, *144*, 1188.

(32) Masquelier, C.; Padhi, A. K.; Nanjundaswamy, K. S.; Goodenough, J. B. *J. Solid State Chem.* **1998**, *135*, 228.

(33) Wu, X.-L.; Jiang, L.-Y.; Cao, F.-F.; Guo, Y.-G.; Wan, L.-J. *Adv. Mater.* **2009**, *21*, 2710.

(34) Maier, J. *Nat Mater* **2005**, *4*, 805.

(35) Balaya, P.; Li, H.; Kienle, L.; Maier, J. *Adv. Funct. Mater.* **2003**, *13*, 621.

(36) Jamnik, J.; Maier, J. *Phys. Chem. Chem. Phys.* **2003**, *5*, 5215.

CHAPTER 4

Three Dimensionally Ordered Mesoporous (3DOm) Carbon Materials as Electrodes for Electrical Double-Layer Capacitors

Outline

4.1 Introduction

Electrical double-layer capacitors (EDLCs) are increasingly finding applications in consumer electronics, memory back-up systems, industrial power and energy management due to their high power capability and ultra-long cycle life.[1] The devices can work as alternatives or supplements to batteries in energy storage field, which will support the advancement of the fields such as renewable energy, transportation, and portable devices in the future.[2] For instance, in EVs and HEVs, EDLCs can be used to accelerate vehicles at their startup and regain the energy during braking. The EDLCs can act as an intermediate power source reducing the stress on the battery during high current processes. This combination is more feasible than using EDLCs or LIBs alone in HEVS or EVs because each of them has its own limitations. Batteries are able to store a large amount of energy but suffer from slow power delivery, whereas supercapacitors can provide high specific power but can only store a limited amount of energy. The differences between batteries and supercapacitors are due to the mechanism by which charge is stored and delivered in these systems. Batteries store charge in the bulk material while supercapacitors store charge only on electrode surfaces via ion adsorption. An EDLC can quickly release its stored energy simply by replacing the surface-adsorbed ions with counter ions from the electrolyte. On the other hand, the charge transfer process in a battery is usually coupled with structural changes of the cathode and the anode materials, which is much slower than the ion exchange process at the electrode surface.

The performance of a supercapacitor is described by the following equations:

$$C = \frac{\varepsilon * \varepsilon_0 A}{d} \qquad [4.1]$$

$$E = \frac{1}{2} C U^2 \qquad [4.2]$$

$$P = \frac{U^2}{4R} \qquad [4.3]$$

where C is the capacitance, A the electrode surface area, E the energy density, P the power density, U the working potential, and R the cell resistance. According to these equations,

the energy density and power density can be improved by increasing the electrode surface area, lowering the cell resistance, and using an electrolyte with a higher working potential. To improve the capacitance, traditional planar metal electrodes were replaced with porous carbon electrodes with higher surface area.

In practice, activated carbons with a surface area up to 2000 $m^2 g^{-1}$ and reasonably high electronic conductivity have been widely used for supercapacitor applications.[3-12] The high surface areas are produced by activating carbon using water vapor, carbon dioxide, or KOH at high temperatures. The process usually leads to the formation of carbonaceous materials with wide pore size distributions ranging from sub-nanometer micropores to large macropores.[13] The randomness of pore size distribution and the lack of pore ordering limit access of the electrolyte to the micropores and slow down the mass transport of electrolyte inside the active materials. On the other hand, macropores waste active volume and therefore reduce the energy density of the materials since the large pores only act as an electrolyte reservoir and have little contribution to the total capacitance. Instead, microporous and mesoporous carbons with narrow pore size distribution and controlled pore structures are desired as electrode materials for supercapacitors.

Microporous carbons potentially have the highest capacitance due to their high surface areas. Particularly, some research groups have recently reported on the anomalous high capacitance of materials with sub-nanometer pores.[14-18] Counter to the traditional Helmholtz electrical double layer model for supercapacitor, which assumed that the energy of an EDLC is stored via adsorption of solvated ions on the electrode surface, the solvation shells of ions are partially removed when the ions are inside very small pores.[17] This results in smaller charge separation between the ion and the pore walls (smaller d in equation [1]) leading to an increase in capacitance. However, the accessibility of these sub-nanometer pores is very limited, which can adversely impact the power capability of the materials. It is clear that supercapacitors with both high energy and high power densities must be built on hierarchically porous materials since micropores are needed for high capacitance and mesopores (2 - 50 nm) are necessary for efficient transport of electrolyte into the micropores.[19-27] This is particularly important for systems using organic or ionic liquid electrolytes, which have wider potential windows but smaller diffusion coefficients than aqueous electrolytes. More importantly, these mesopores must be designed in the best way

to facilitate the transport of electrolyte while avoiding significant reduction the volumetric energy density of the materials.

Using non-aqueous electrolytes such as organic electrolytes and ionic liquids with wider working potentials is an effective way to improve the energy density and power density of supercapacitors. These non-aqueous electrolytes can potentially increase the working potential of a supercapacitor cell to 3–4 V, which result in 4–9 times increase of energy and power density as *E* and *P* vary with the square of the potential window (U). To get the same enhancement by increasing the surface area of electrode materials, electrode materials with excluded micropores must be utilized. However, the power capacity of these materials will be definitely very limited and it is not a good choice to trade the power density for the capacitance since their energy densities will never approach the levels of batteries.

This chapter describes the fabrication of carbons with well-ordered, interconnected mesopore structure and microporous walls. The capacitive behavior of these carbons are then studied using an ionic liquid with working potential up to 3.5 V as the electrolyte. The carbon was prepared via a colloidal crystal templating (CCT) method using assembles of monodisperse silica spheres of different sizes ranging from 8 to 40 nm as templates. The CCT offers a versatile method to fabricate nanostructured materials with open, interconnected structure and controlled pore size. In general, the method uses monodisperse spheres (polymer spheres or silica spheres), which are assembled into periodic arrays as templates. The void space between spheres is then infiltrated with a precursor solution for the target electrode material. Thermal processing converts the precursor to a solid skeleton that surrounds the templating spheres. Silica spheres can be removed via treatment with concentrated base solution or hydrofluoric acid. The final product of the CCT process is an inverted replica of the original colloidal crystal, i.e., an "inverse opal" or three-dimensionally ordered macroporous (3DOM) or mesoporous (3DOm) solid. The inverse replica typically inherits the face-centered cubic (fcc) symmetry of the templating sphere array. The fcc macropore array is interconnected through windows where templating spheres were in direct contact (i.e., at twelve points in an ideal and typical structure). Ordered mesoporous carbon samples with pore sizes ranging from 8 to 40 nm, and surface areas as high as 1600 m^2g^{-1} were prepared. The PF carbon showed very high

capacitance, high rate performance, and excellent cyclability, which is suitable to build high energy and high power supercapacitor cells.

4.2 Experimental

4.2.1 Materials.

Resorcinol (99%), phenol (99%), formaldehyde aqueous solution (37 wt%), sodium carbonate, anhydrous ethanol, methanol, tetrahydrofuran, polytetrafluoroethylene (PTFE) 60 wt% dispersion in water, tetraethylorthosilicate (TEOS) (99 %), L-lysine (98 wt%), hydrochloric acid (0.1 M), potassium hydroxide (98 wt%), and the ionic liquid 1-ethyl-3-methylimidazolium bis(trifluoromethylsulfonyl)imide (EMI-TFSI) were purchased from Sigma-Aldrich and used without further purification. Deionized water was purified to a resistance higher than 18 MΩ.

4.2.2 Preparation of Silica spheres.

Silica spheres (8.5–40 nm) were prepared by the hydrolysis of TEOS in the presence of L-lysine at different temperatures. Spheres with diameters >20 nm were synthesized by seed growth from the smaller spheres. In general, L-lysine (70 mg) was dissolved in 70 mL water in a 125 mL polytetrafluoroethylene (PTFE) bottle and stirred for 10 min. TEOS (5.3 g) was added into the L-lysine solution and vigorously stirred at room temperature for 30 min before being transferred into an oil bath and stirred at the designed temperatures for different times, as indicated below.

- The ~10 nm SiO_2 spheres were synthesized by stirring the mixed solution at 500 rpm for 48 h at 70 °C.
- The ~15 nm SiO_2 spheres were synthesized by stirring the mixed solution at 500 rpm for 48 h at 90 °C.
- The ~20 nm SiO_2 spheres were prepared using seeded growth from ~15 nm spheres by adding a total of 5.4 g of TEOS in 5 separate fractions, each 1 h apart.
- The ~40 nm SiO_2 spheres were prepared using seeded growth from ~20 nm spheres by adding a total of TEOS (10.5 g) in three separate fractions, each addition 48 h apart, while stirring at 500 rpm at 90 °C.

The dispersions were then poured into Petri dishes and placed into an oven at 70 °C to allow the spheres to settle and to remove water. The obtained solids were then calcined at 550 ˚C for 6 h in air to remove any organic components and produce silica colloidal crystal templates.

4.2.3 Preparation of 3DOm carbon.

Two different carbon precursors including poly phenolformaldehyde (PF) and poly resorcinolfomaldehyde (RF) were used to prepare PF carbon and RF carbon respectively. The RF precursor was freshly prepared for each batch of carbon, whereas the PF precursor was pre-polymerized at 70 °C for 1 h, then dispersed in THF and kept in a refrigerator as a stock solution.

4.2.3.1 RF precursor.

Resorcinol (3.3 g) and sodium carbonate (0.06 g) were dissolved in 4.5 mL aqueous solution of formaldehyde (37 wt%) and vigorously stirred at RT for 20 min before being infiltrated into the silica colloidal crystal template.

4.2.3.2 PF precursor.

Phenol (61 g) was melted at 50 °C in a 500 mL round-bottom flask. Aqueous formaldehyde solution (200 mL, 37 wt%) was added dropwise into the melted phenol while stirring. After that, the mixture was heated at 70 °C for 1 h to increase the extent of polymerization between phenol and formaldehyde. Water was removed from the mixture by rotary evaporation at 50 °C. The viscous, water-free polymer was then dispersed into THF to obtain a 50 wt% dispersion and kept in the refrigerator before use.

4.2.3.3 Preparation of 3DOm Carbon.

3DOm carbon was prepared by infiltrating carbon precursors into silica colloidal crystal templates for 4 h, then aging the infiltrated composites at designated temperatures (85 °C for RF and 140 °C for PF) for 24 h. The aged composites were then pyrolyzed at 900 °C for 4 h (5 ˚C/min ramping rate) to transform the polymerized PF and RF precursors into carbon. Silica spheres were then etched out by hydrothermal treatment with concentrated KOH (6 M) at 180 °C for 48 h. The obtained carbon was neutralized with

HCl solution (1 M) and washed with copious amounts of water to remove any remaining inorganic salts.

4.2.4 Product Characterization.

Raman spectroscopy was performed with a Witec Alpha300R confocal Raman microscope using 514.5 nm incident radiation at the lowest possible beam power to minimize beam damage of the sample. Scanning electron microscopy (SEM) was carried out with a JEOL-6700 microscope operating at 5 kV with emission currents ranging from 2 to 10 μA. Because of the high conductivity of the carbon, none of these samples were metal coated. Transmission electron microscopy (TEM) was carried out with a Technai T12 microscope operating at 120 kV with emission currents ranging from 7 to 12 μA.

4.2.5 Cell preparation and electrochemical tests.

Carbon was mixed with polytetrafluoroethylene (PTFE) (5 wt%) and extensively ground in a mortar to form a homogeneous mixture. The mixture was rolled into thin films with a pasta-maker, then cut into 1 cm^2 circles and used as electrodes. To prepare electrochemical cells, two carbon electrodes separated by a Cellgard-3501 membrane were pre-wetted with electrolyte and then packed into a two electrode cell. The ionic liquid EMI-TFSI was used as the electrolyte.

Galvanostatic conditions were used to measure the capacitance and to test the cyclability of supercapacitors. For capacitance measurement, the cells were charged and discharged at different rates for 10 to 20 cycles. For cyclability test, the cells were charged and discharged at a current of 10 mA for a few thousand cycles. The capacitance was calculated using the equation: $C = \frac{I*dt}{dV}$ where I is the discharge current, dt is the time for the cell to discharge starting at the voltage determined by the maximum potential (3.5 V) minus the potential due to ohmic drop, and dV is the maximum potential minus the potential due to ohmic drop.

The electrochemical impedance spectroscopy (EIS) tests were carried out using a Solartron 1260 frequency analyze in the frequency range from 10 mHz to 100 kHz with a 20 mV AC amplitude. The gravimetric capacitance, C (F g^{-1}), was calculated according to

$$C = \frac{2}{2\pi f \mathrm{Im}(Z)\mathrm{m}}$$

Where f is the operating frequency (Hz), Im(Z) is the imaginary part of the total device resistance (ohm), and m is the mass of carbon in each electrode (in units of g).

Cyclicvoltammetry (CV) curves was obtained with Solartron 1287 electrochemical station using homemade software. CV curves were scanned at voltage ramp rates from 20 to 100 mV/s. Capacitance values were calculated for the CV curves by dividing the current by the voltage scan rate

$$C = \frac{I}{\frac{dV}{dt}}$$

The reported specific capacitance is the capacitance of the cell normalized to the mass of one electrode.

4.3 Results and Discussion

4.3.1 Preparation of silica spheres and silica templates.

In general, monodisperse colloidal silica spheres readily pack into ordered structures, whereas silica spheres of different sizes assemble into less ordered or even disordered structures. For colloidal crystal templated materials, the pore size is determined by the size of each sphere while the ordered pore structure is inherited from the order of the templates. In this chapter, 3DOm carbon materials templated from silica spheres were used as electrodes in supercapacitors to study the effects of pore size on the capacitance. Therefore, it is critical to use highly monodisperse silica spheres with controllable sizes as templates.

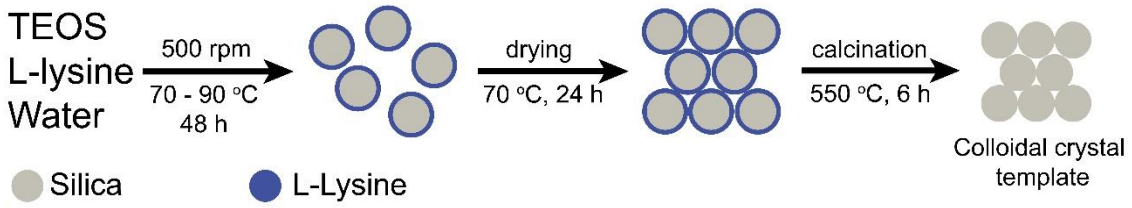

Figure 4.1 Synthesis scheme of the preparation of silica spheres and colloidal crystal templates.

The preparation of periodic arrays of sub-hundred nanometer silica spheres assisted by amino acids was first reported by Takashi and coworkers and is outlined in Figure 4.1.[28] An earlier study showed that the sizes of silica spheres are affected by many factors, such as the concentration of the silica precursor (TEOS), temperature, and stirring rate.[29] In

general, higher initial TEOS concentration, lower stirring rates, and higher temperatures result in bigger spheres. However, to achieve full control over the size of the silica spheres in the range from 8 to 40 nm, a more detailed study on how strongly each factor affects the sphere size had to be carried out.

In direct syntheses of silica spheres, the sizes of the spheres can be controlled with high accuracy by adjusting the hydrolysis temperatures. However, only relatively small spheres can be obtained through this method, as hydrolysis at 90 °C produced only 14.5 nm spheres. Larger spheres must be prepared by a seeded growth method. However, it was observed that the sizes of seeded spheres did not increase linearly with the amount of silica precursor added. The following paragraph will show how the size of the seeded spheres can be calculated for this simple case.

First, the total mass of spheres in the solution is proportional to the mass of TEOS used, which can be described by the following equation:

$$m_{TEOS} \sim \sum m_{spheres} = N * \frac{4}{3}\pi R^3 * d_{sphere} \qquad [4]$$

where m_{TEOS} is the mass of TEOS, N is number of spheres in the solution, R is the average radius of each sphere, and d_{sphere} is the density of each sphere. It is safe to assume that the densities of the seed spheres and the final spheres are the same since they are all formed from the hydrolysis of TEOS at the same temperature and in the presence of extra amount of water. The size of the final spheres is then related to the seed spheres according to the equation:

$$\frac{m_{TEOS(S)}}{m_{TEOS(F)}} = \frac{N_S}{N_F}\frac{d_S}{d_F}\left(\frac{R_S}{R_F}\right)^3 \qquad [5]$$

where S and F refer to seed and final. If the number of spheres does not change ($N_S = N_F$, which means that added TEOS only forms layers outside of the seeded spheres, not any new spheres), the sphere size then varies as the cube root of the mass fraction of the two TEOS precursors that were used to produce the two sphere sizes. However, we found that the actual sphere sizes were bigger than the theoretical values based on the assumption that the numbers of the spheres did not change. This means that the number of spheres actually decreased after new TEOS was added into the solution containing seeded spheres. The decrease, however, was not a constant number but depended on the size of the seed spheres.

To have better control over the size and dispersity of the seeded spheres, it is crucial to know the exact percentage decreasing the number of spheres during the reaction. To do this, we used 14.3 nm silica spheres as the seed and then monitored the sphere size versus the amount of TEOS added. For each addition of TEOS, the solution was stirred for an extra 48 h at 90 °C to make sure that hydrolysis of the newly added TEOS was complete. After that, a small amount of solution was used to prepare a TEM sample, and the sphere size was averaged from the sizes of 200 spheres. Figure 4.2 shows the increase in sphere sizes after adding 10.4 g, 20.8 g, and 31.2 g of TEOS to 14.3 nm seed silica spheres.

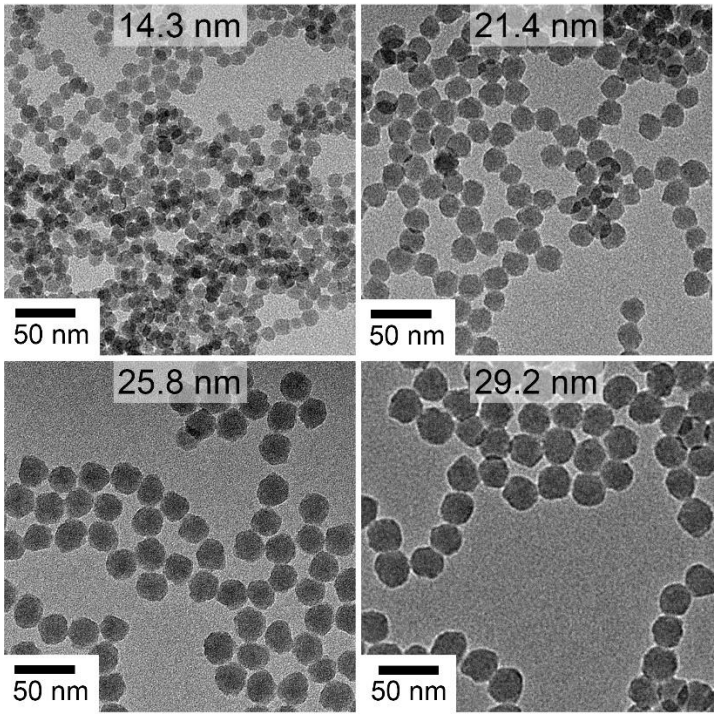

Figure 4.2 TEM images of the silica spheres of different sizes prepared by the seed growth method. The average diameter of the seeds was 14.3 nm. Average product diameters are shown.

The sizes of seed spheres, final spheres and their theoretical sizes after each addition of TEOS are shown in Table 4.1. In all cases, the sizes of the theoretical spheres are smaller than the sizes of the actual ones measured from TEM images. This means the spheres undergo dissolution/reprecipitation processes in solution, in which the dissolution process may be accelerated by collisions between spheres at high stirring rates and long reaction times. The dissolution of spheres should also depend on their sizes because the bigger spheres are more stable and harder to break down than the smaller spheres. The fractions of spheres in solution after 48 h, 96 h, and 144 h stirring estimated using equation [5] are

0.88, 0.96, and 0.99, respectively. This means that 12 % of the 14.3 nm seed spheres were dissolved into solution while the fractions for the 21.4 and 25.8 nm spheres were only 4 % and 1 %, respectively.

Table 4.1 Sizes of silica spheres prepared by the seed growth method.

Seed size (nm)	Theoretical size (nm)	Measured size (nm)
14.3	20.5	21.4±1.3
21.4	25.4	25.8±1.6
25.8	28.8	29.2±1.7

Knowing these percentages, highly monodisperse silica spheres of different sizes ranging from 8 nm to 40 nm were prepared by direct syntheses (Figure 4.3 A and B) and seeded growth (Figure 4.3C, D, E, and F).

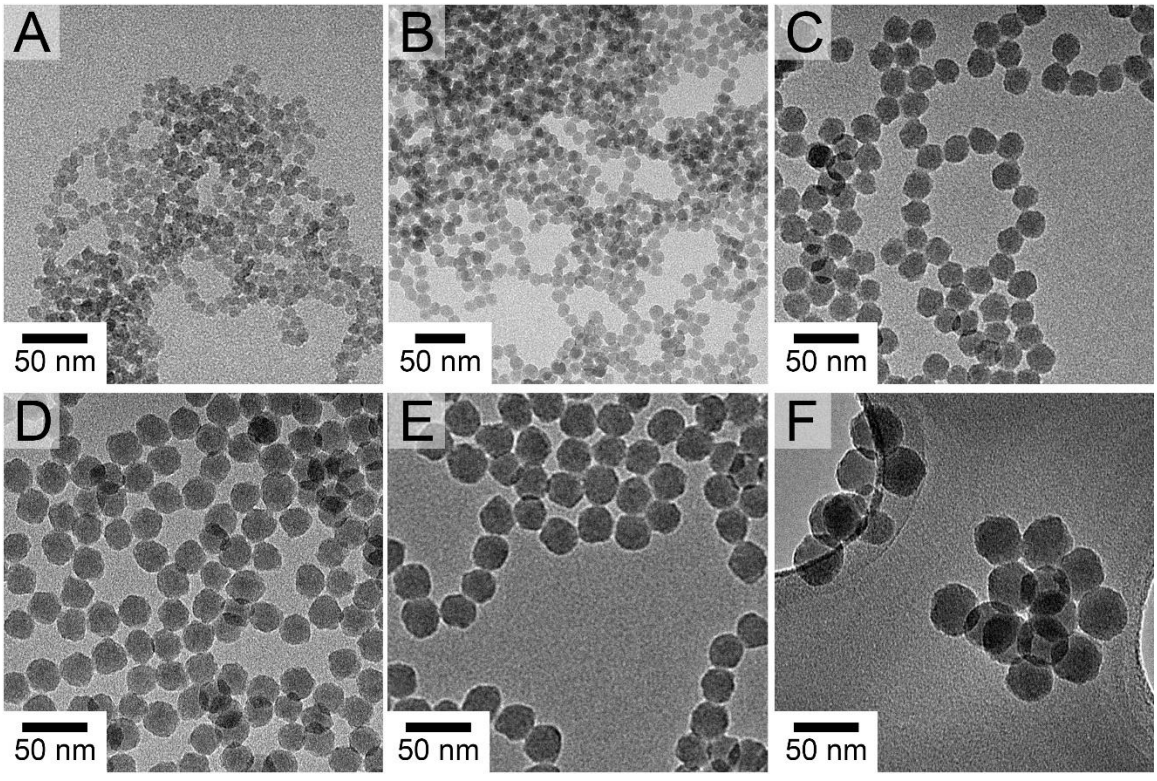

Figure 4.3 (A) 9.5±0.6 nm, (B) 14.3±1nm; (C) 21.4±1.3 nm; (D) 25.8±1.6 nm; (E) 29.2±1.7 nm; (F) 39.5±2 nm SiO_2 spheres. Samples were taken from the solution before calcination.

After evaporation of water, the spheres were packed into ordered face-centered cubic arrays, which can be seen in Figure 4.4. The small spheres (< 10 nm) are usually less monodisperse and therefore harder to be packed into ordered structures. However, the Fast Fourier Transform (FFT) of the TEM images from the 9.5 nm silica spheres still shows a ring pattern with a *d*-spacing of about 9.5 nm. The bigger spheres (25.8 and 39.5 nm) with higher monodispersity are packed into very ordered structures (Figure 4.4B and C). The FFT of the 25.8 nm and 39.5 nm SiO_2 samples showed bright dots from the diffractions of highly ordered SiO_2 arrays.

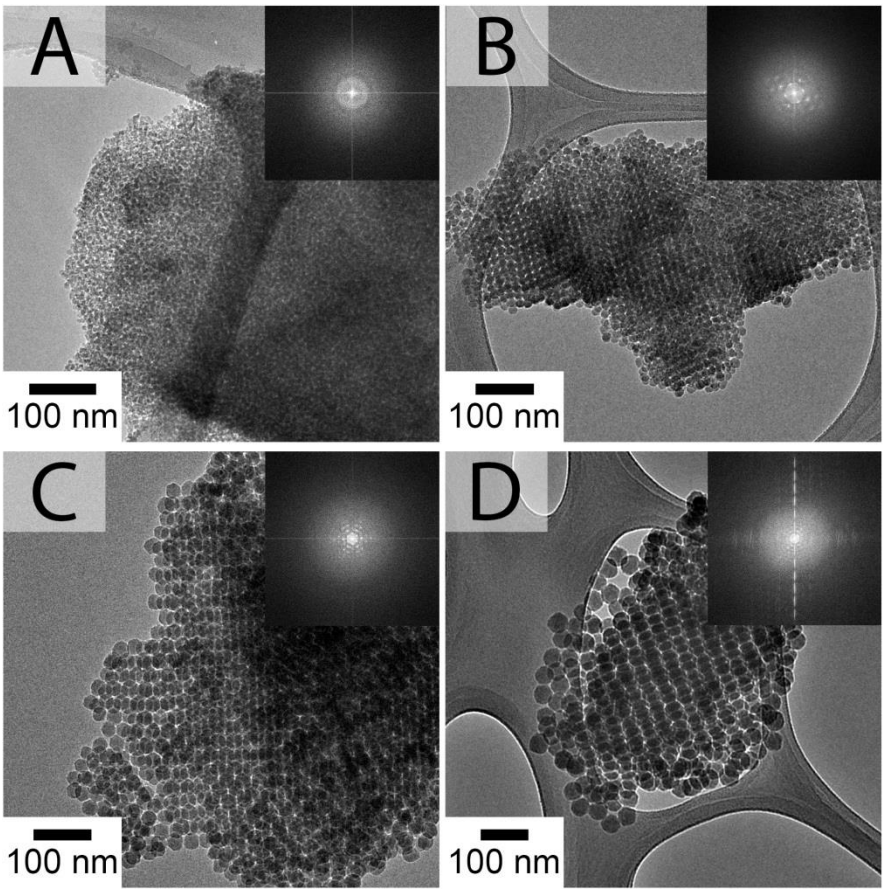

Figure 4.4 TEM images of A) 9.5±0.6 nm; B) 25.8±1.6 nm; C) 29.2±1.7 nm; D) 39.5±2 nm calcined SiO_2 spheres showing ordered structures. D, E, F) FFT of A, B, and C correspondingly.

4.3.2 Preparation of 3DOm carbon.

The orderly packed silica spheres were calcined in air to remove organic components, and were then used as templates to prepare 3DOm carbon. It is worth mentioning that all spheres showed small shrinkage after calcination, which can be ascribed to the loss of

organic components and the further condensation of silica at high temperature. The shrinkage varied from 5 to 10% for spheres of different sizes. The synthesis of 3DOm carbon is outlined in Figure 4.5. First, carbon precursor is infiltrated into the silica template by capillary forces. The composites are then aged at a moderate temperature (100–140 °C) to further polymerize the carbon precursor to strengthen the polymer network surrounding the silica spheres. This step must be done in a closed vial and is necessary to allow most of formaldehyde to react with phenol groups since it is quite volatile and would be lost if the composite were pyrolyzed directly after infiltration. The polymer-silica composite is pyrolyzed at 900 °C to transform the polymer into carbon. The silica template is then etched out using a hot, concentrated KOH solution, creating the porous structure. To study the effects of pore size on the performance of supercapacitor electrodes, four different sphere sizes (9.5±0.6, 21.4±2, 29.2±2, and 39.5±2 nm) were selected to prepare 3DOm carbons. In addition, two different carbon precursors, including poly(resorcinol-formaldehyde) (RF) and poly(phenol-formaldehyde) (PF), were used to prepared carbons. These precursors differ in the number of the phenol group attached to the aromatic ring, and, therefore, produce carbons with different oxygen content and functional groups on the surface. It is known that carbons with a higher content of oxygen usually have lower electronic conductivity.

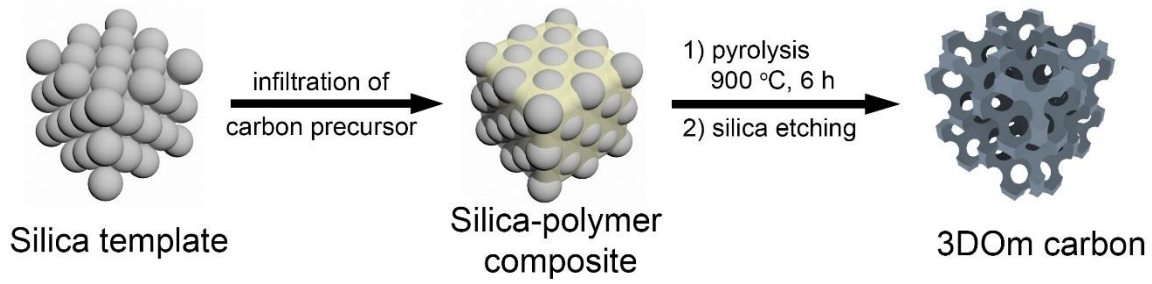

Figure 4.5 Synthesis scheme for 3DOm carbon.

Both precursors were readily infiltrated into silica templates. During the infiltration, bubbles evolved from the templates, which indicated these were well wetted by the carbon precursors. The bubbles surrounding the spheres may block access precursor into the template and slow down the infiltration; therefore they needed to be removed, for example by disturbing the solution with a stirring rod. Because the infiltration usually took a long time, it was important to control the gelation of the carbon precursors. RF sol, with a larger

number of phenol groups, gels faster than PF sol, which limits its usable time to 6–8 h after the precursor is freshly made. To prolong the gelation time, it is necessary to conduct the infiltration in capped vials, because oxygen from the air is known to catalyze the polymerization between phenolic compounds and formaldehyde. After aging at the designated temperatures, both precursors produced robust, dark-red polymer-silica composites, which were transformed into carbon-silica composites by treating at high temperatures under an inert atmosphere. One advantages of using silica hard templates is that the template provides continual support for the carbon framework during carbonization, preventing structural collapse. SEM images of the carbon-silica composites (Figure 4.6) show that the ordered structure remained even with the presence of carbon precursor in between the spheres.

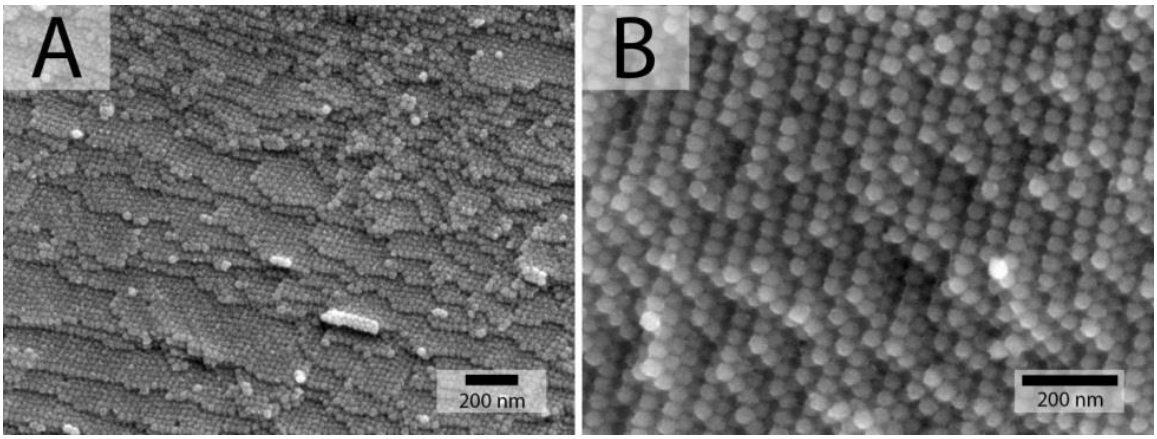

Figure 4.6 SEM images of carbon-SiO_2 composites made from A) 29.2 nm and B) 39.5 nm silica spheres.

TEM images of silica-carbon composites show similar features with the periodic structure of the silica template surrounded by the carbon phase (Figure 4.7). The carbon phase is very thin, and the spheres are in close contact, which is critical for the formation of windows to connect pores once the spheres are removed. At this stage, the spheres are already shrunk comparing to the spheres in the solution due to the condensation of silica at high temperature. As estimated from these TEM images, the shrinkage is about 2–3 nm for both sphere sizes of 29.2 and 39.5 nm.

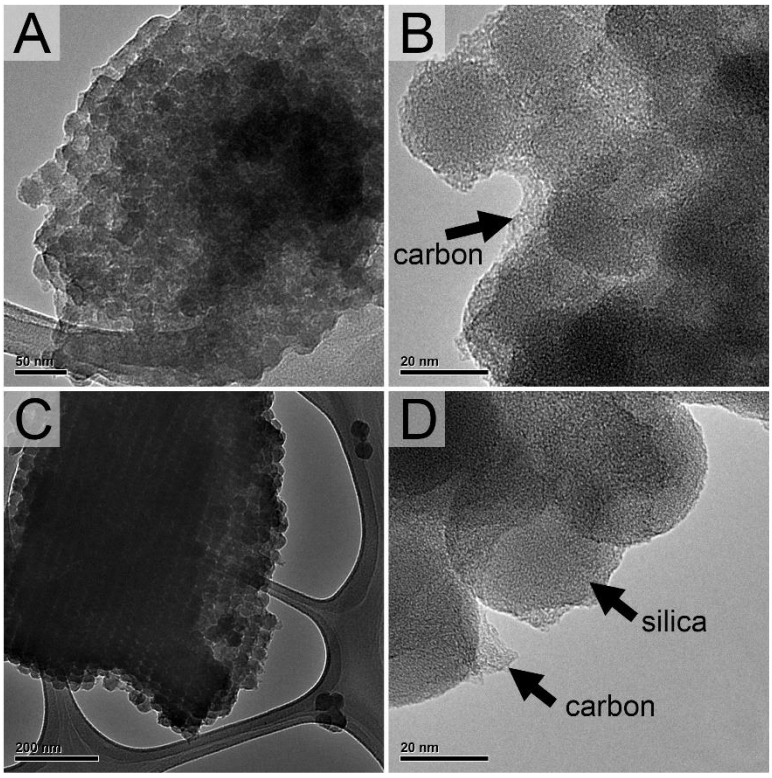

Figure 4.7 TEM images of carbon-SiO_2 composites made from (A and B) 29.2 nm, (C and D) 39.5 nm silica spheres, showing the ordered structure of the silica template and the presence of the carbon phase.

The pyrolyzed composites were hydrothermally treated with concentrated KOH at 180 °C for 48 h to remove the silica templates. After this template removal step, highly ordered mesoporous carbons were obtained (Figure 4.8). The symmetry of these ordered mesoporous carbon samples was solved by taking TEM images at multiple angles, then indexing the fast Fourier transforms (FFT) of these TEM images. Figure 4.8 shows TEM images of a carbon sample templated from 21.4 nm silica spheres, which showed different ordered patterns from different viewing angles. The FFTs of these images can be indexed to a face-centered cubic (FFC) structure with a unit cell of 19.4 nm. Other structures such as hexagonally closed pack or disordered structures can be found in different locations of the sample. However, they only occupy a very small fraction of the sample (ca. 5 %). All other carbon samples templated from silica spheres of different sizes also had FFC symmetry, which was inherited from the mother templates.

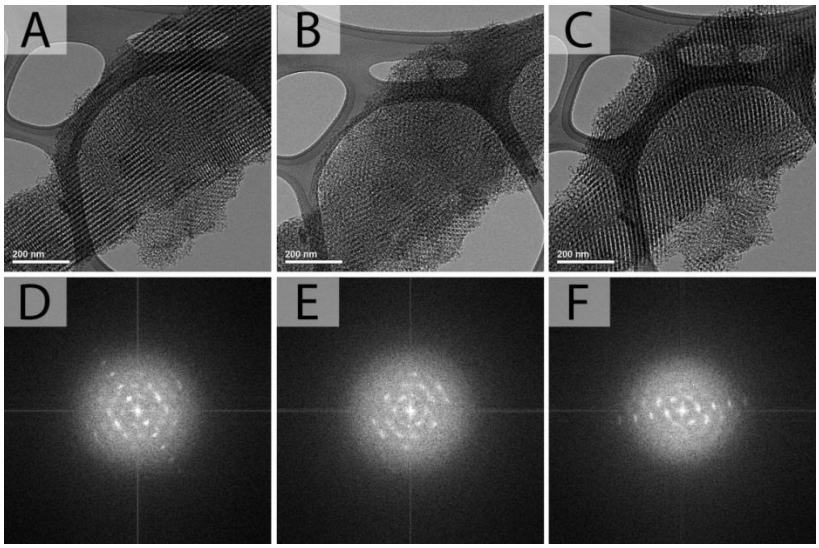

Figure 4.8 TEM images and their corresponding FFT of PF carbon templated from 20 nm silica spheres, showing ordered patterns that can be indexed to a FFC structure.

4.3.3 Characterization of 3DOm Carbons

The morphologies of 3DOm carbons prepared from PF and RF precursors are quite similar when viewed under the TEM. However, the sizes of ordered domains in PF carbons are normally bigger than those in RF carbons. All carbon samples showed ordered structures that could be indexed to a FFC geometry, except for the sample templated from the smallest spheres (9.5 nm) (Figure 4.9A and 4.10A). However, the FFT images of this sample also showed a ring pattern with a *d*-spacing close to the diameter of the templating spheres, which indicates that carbon was templated and had an ordered structure but over smaller domain sizes. The larger-sphere templates produced carbon with thicker walls and larger windows, which could be advantageous for supercapacitor materials, if the thick walls accommodate more micropores which would produce higher surface areas. It is known that micropores in PF or RF carbons are formed from the removal of water and small organic molecules during the aging and the pyrolyzing steps. RF carbons are usually less conductive than PF carbons, making them less attractive as supercapacitor materials. In this chapter, two different RF carbon samples were prepared (templated from 9.5 and 25.8 nm silica sphere) mostly to compare their performance with PF carbons. Four different PF carbons with mesopores ranging from 8 to 32 nm were prepared and extensively tested

as electrode materials for supercapacitors. The TEM images of these RF carbons and PF carbons are shown in Figure 4.9 and Figure 4.10.

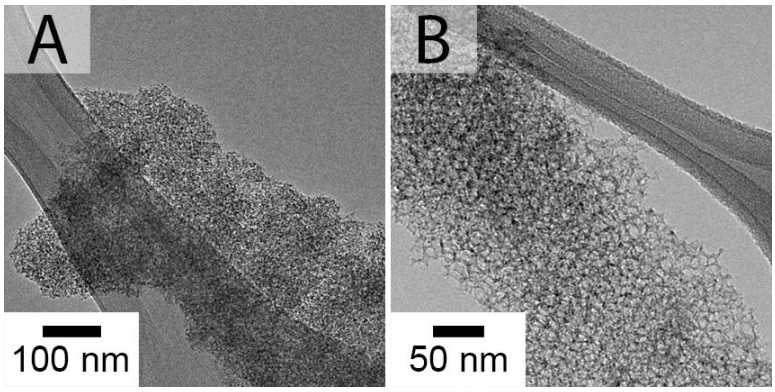

Figure 4.9 TEM images 3DOm RF carbons templated from (A) 9.5 nm and (B) 21.4 nm SiO_2 spheres.

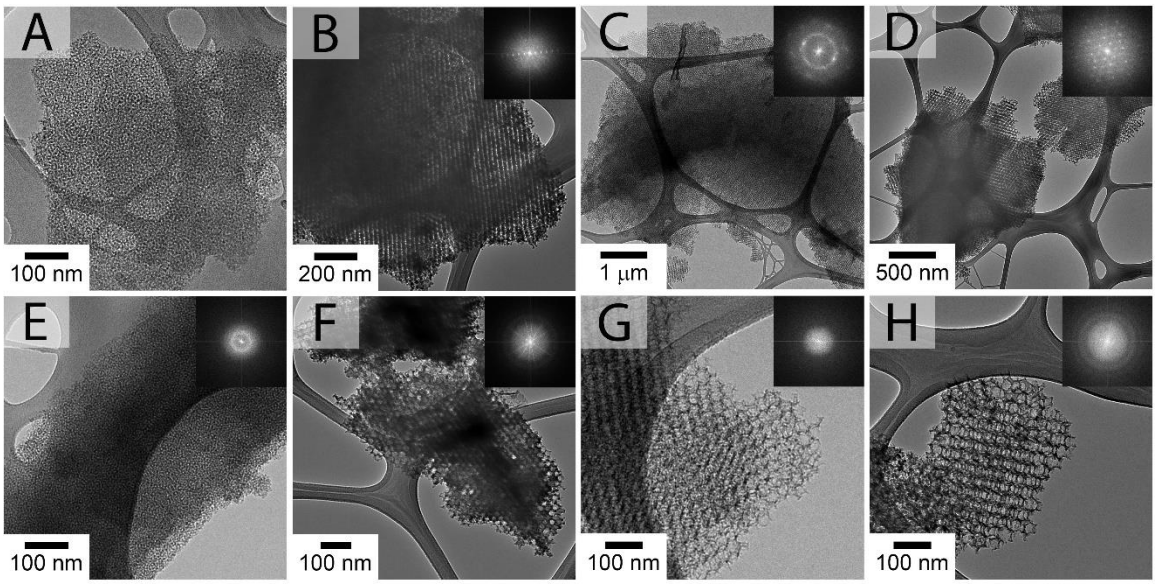

Figure 4.10 TEM images and corresponding FFTs of 3DOm PF carbons templated from: (A and E) 9.5 nm, (B and F) 21.4 nm, (C and G) 29.2 nm, and (D and H) 39.5 nm SiO_2 spheres.

Raman spectroscopy was used to characterize the extent of graphitization of the 3DOm carbons. The Raman spectra of all 3DOm carbon samples showed two prominent peaks associated with sp^2 carbon (G-band, 1597 cm^{-1}) and sp^3 carbon (D-band, 1351 cm^{-1}) (Figure 4.11). The G-band originates from the in-plane bond stretching motion of pairs of sp^2 carbon atoms, whereas the D-band involves a breathing mode of A_{1g} symmetry, which is only active in the presence of disorder.[30] The G peak shifts from 1581 cm^{-1} in graphite to

1595-1599 cm^{-1} in 3DOm carbons, which indicates that carbon prepared from RF and PF precursors contains mostly nanocrystalline graphite. The domain sizes can be estimated using the equation $(I_D)/(I_G) = (C(\lambda))/(L_a)$, where I_D, I_G are the intensities of the disordered peak and the graphitic peak, respectively, $C(\lambda = 515.5\ nm) = 4.4\ nm$, λ is the wavelength of the laser used in the Raman spectrometer, and L_a is the cluster diameter of nanocrystalline graphite.[31] The D and G peaks of PF and RF carbons are broader than those of graphite because of the additional contributions from sp^3 carbon sites present in amorphous carbonaceous materials.[30] Therefore simply fitting the spectrum with two peaks does not give an accurate value of I_D/I_G. To interpret the Raman features, the spectra were instead deconvoluted with four Gaussian peaks situated at 1190, 1351, 1518, and 1597 cm^{-1}, where the additional bands at 1190 and 1518 cm^{-1} are associated with sp^3 carbon vibrations. Figure 4.11 (left) is a typical fit of the Raman spectrum of PF carbon templated from 39.5 nm silica spheres and a plot of graphitic domain sizes vs. silica sphere sizes for all RF and PF carbons. The graphitic domain sizes of both PF and RF carbon are quite small (3.6–4 nm) which is commonly seen for carbons templated from phenol-formaldehyde based precursor. It is noteworthy that the graphitic domain sizes increase slightly with increasing size of the templating spheres (Figure 4.11, right).

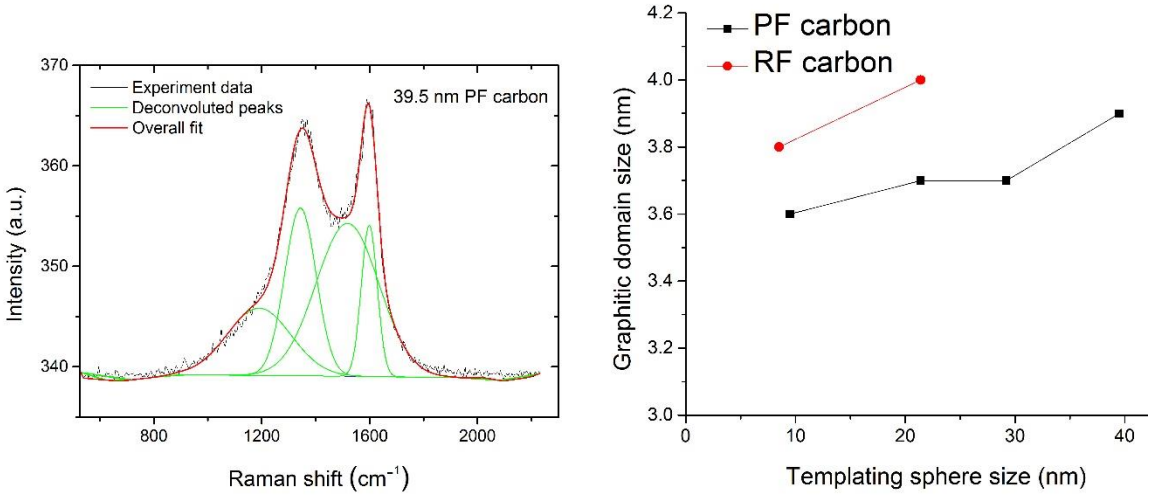

Figure 4.11 A typical Raman spectrum of 3DOm carbon and plot of the graphitic domain sizes in 3DOm RF and 3DOm PF carbons vs. the templating sphere sizes.

Nitrogen adsorption analysis was used to study the surface areas, pore volumes, and micropore volumes of the 3DOm carbon samples. All 3DOm carbons showed type IV isotherms and type H1 hystereses, with the loops created from adsorption and desorption branches being almost vertical and parallel (Figure 4.12 A). The pore size distributions estimated from the adsorption branches using a BJH model predict slightly smaller pores than the sizes of the primary silica template particles. Pore sizes of 7.2, 18.5, 23.6, and 32.6 nm were predicted for 3DOm PF carbons templated from 9.5, 21.4, 29.2, and 39.5 nm silica spheres, respectively. It should be noted that the sizes of the primary silica spheres were estimated from TEM images of the particles taken from solutions, because it is very difficult to identify the edges of these sphere in aggregated form. The actual sizes of spheres in the templates are smaller than the sizes of the primary spheres in solution and closer to the size of the templated mesopores, because they were calcined at 550 °C to remove organic components. The shrinkage of the mesopores was also caused by the removal of the supporting silica spheres. In addition, the errors when applying the BJH model, which was originally developed for cylindrical pores, to 3DOm carbons with spherical pores, may also contribute to this reduction in the reported pore sizes. The surface areas estimated using the BET equation for P/P_0 from 0.5 to 0.35 for all PF carbons are between ca. 1000 and 1650 $m^2 g^{-1}$ (Table 4.2). These values are significantly higher than the surface areas calculated for 3DOm structures with only mesopores, whose sizes were estimated from the BJH model, which strongly suggests the presence of micropores in these samples. However, the t-method failed to estimate the micropore surface area of these samples, which once again can be considered as the result of the differences between cylindrical pores and spherical pores. It is worth noting that the t-method is only applicable for samples having similar C constants in the BET equation with the standard sample (in this case is carbon). However, the C constants for standard samples are usually calculated based on cylindrical pore models, which are no longer adequate when applied to spherical pores.

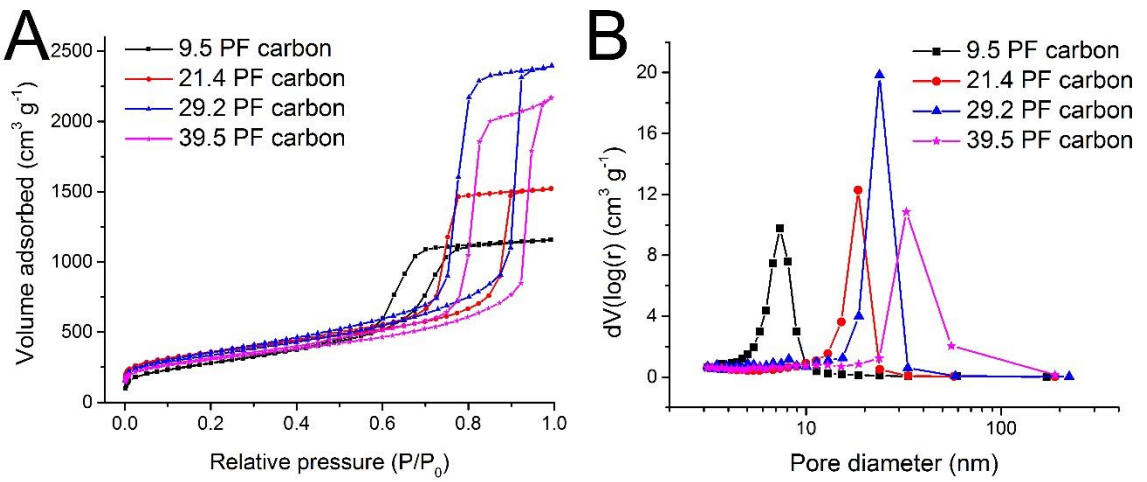

Figure 4.12 (A) Nitrogen adsorption isotherms and (B) pore size distributions of 3DOm PF carbons templated from silica spheres of different sizes.

Recently, Quantachrome developed a QSDFT model to simulate the adsorption/desorption of nitrogen in spherical pores.[32] This model seems to give accurate results (pore size distributions and surface areas) when applied to 3DOm carbons with small mesopores (< 10 nm). A pore size of 10.6 nm and a surface area of 922.7 $m^2 g^{-1}$ were estimated for 3DOm carbon templated from 9.5 nm silica spheres, which are matched to the predictions from the BJH model. However, the predictions for 3DOm carbons with medium and big mesopores (20–40 nm) are not as accurate, the predicted mesopores usually being bigger than the size of the primary silica spheres. Pore sizes of 32.7 nm and 48.8 nm were predicted for 3DOm carbons templated from 29.2 nm and 39.5 nm silica sphere correspondingly (Figure 4.13 and Table 4.2). It is possible that larger sphere templates create larger windows connecting mesopores, which makes the adsorption and desorption of nitrogen molecules from connected spherical pores similar to those in cylindrical pores. The pore diameters are normally calculated from the volume of single pores using a sphere model, which now results in an overestimate by taking two-connecting pores or multiple connecting pores into account. For instance, the QSDFT predicted bimodal pores of 35 nm and 48.8 nm for 3DOm PF carbon templated from 39.5 nm silica spheres. The actual size of the spheres after calcination is about 35 nm which was close to the prediction of the QSDFT model. The 48.8 nm mesopores are close to the value of triple connecting 35 nm pores, which have volume of $3\frac{4}{3}\pi R_1^3 = 3\frac{4}{3}\pi 35^3 = \frac{4}{3}\pi R_2^3$ and the

diameter of the pore would be ($\sqrt[3]{3} \times 35 = 50$). However, the not so accurate prediction of the big pores will not affect the predictions of this model for small mesopores and micropores because the windows connecting them are so small. The predictions of the surface area and the distribution of the surface area vs. pore size obtained by the QSDFT method are accurate and very useful to explain the capacitor properties of PF and RF carbons. According to the histograms of surface area vs. pore size for 3DOm PF carbons (Figure 4.13), small mesopores contributed mostly to the surface area of the 9.5-PF carbon, whereas the surface area in the 39.5-PF carbon originated mainly from micropores. The 21.4-PF and 29.2-PF carbon samples showed a balanced contribution from both micropores and mesopores.

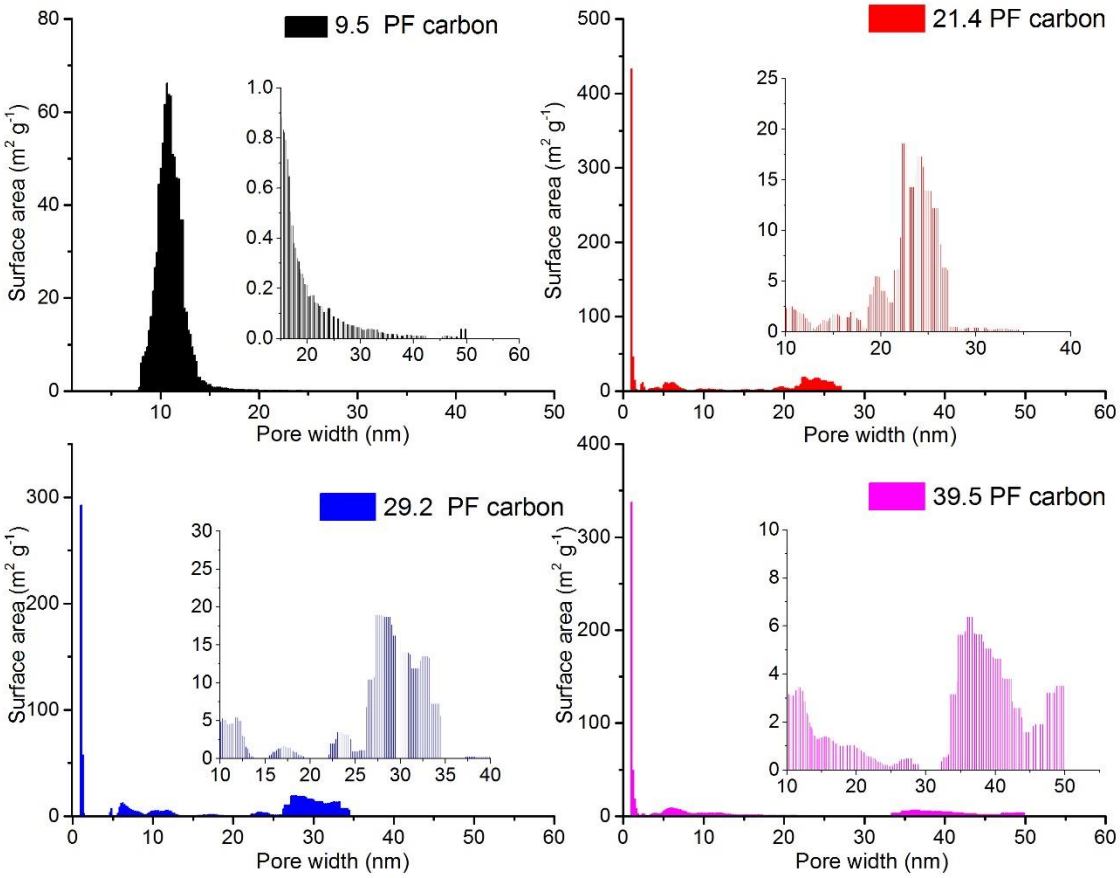

Figure 4.13 Histograms of surface area vs. pore size of 3DOm PF carbons templated from silica spheres with different sizes.

The isotherms of 3DOm RF carbons are very similar to those of 3DOm PF carbons. For samples templated from silica spheres of similar size, the predicted surface areas, pore

size distributions, and pore volumes using the same models are also very similar (Table 2). The nitrogen adsorption analysis for 3DOm RF carbons templated from bigger spheres is, however, much more difficult to perform and usually produces unusual isotherms, such as crossing of adsorption and desorption branches, non-closed loops, and unfinished desorption branches. A non-closed loop was also observed for RF carbon with bigger pores, while the other two phenomena are still under investigation.

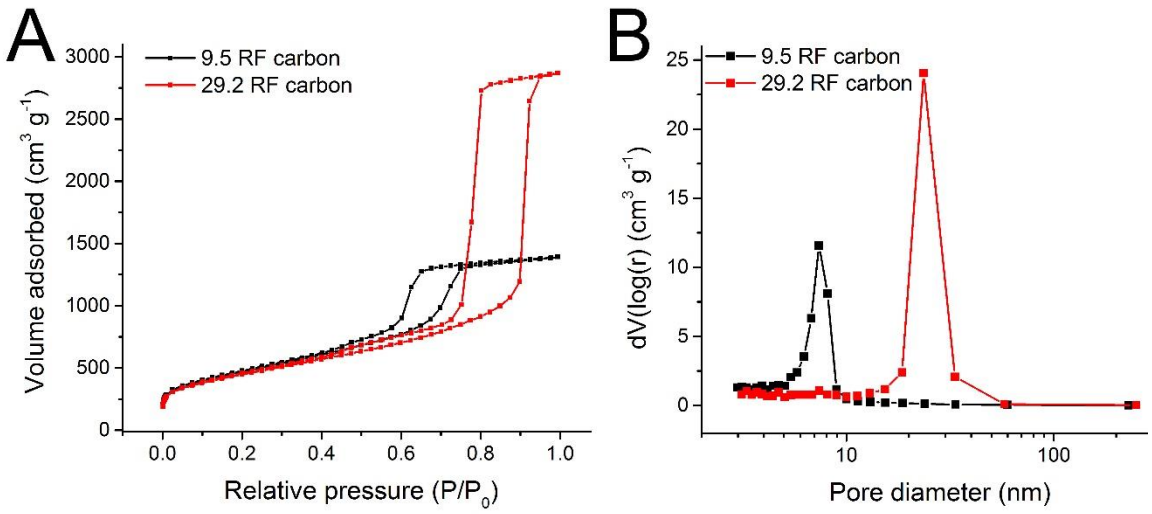

Figure 4.14 (A) Isotherms and (B) pore size distributions of 3DOm RF carbons templated from silica spheres of different sizes.

Nitrogen adsorption analysis was also performed on a commercially available activated carbon, whose electrochemical performance will be compared with 3DOm carbons. The isotherms of activated carbon are typical for microporous materials with a sharp increase of adsorbed volume at a very low pressure and a plateau over a wide range of pressure. The surface area of activated carbon is very high (1730 m^2 g^{-1}), most of which was attributed to micropores.

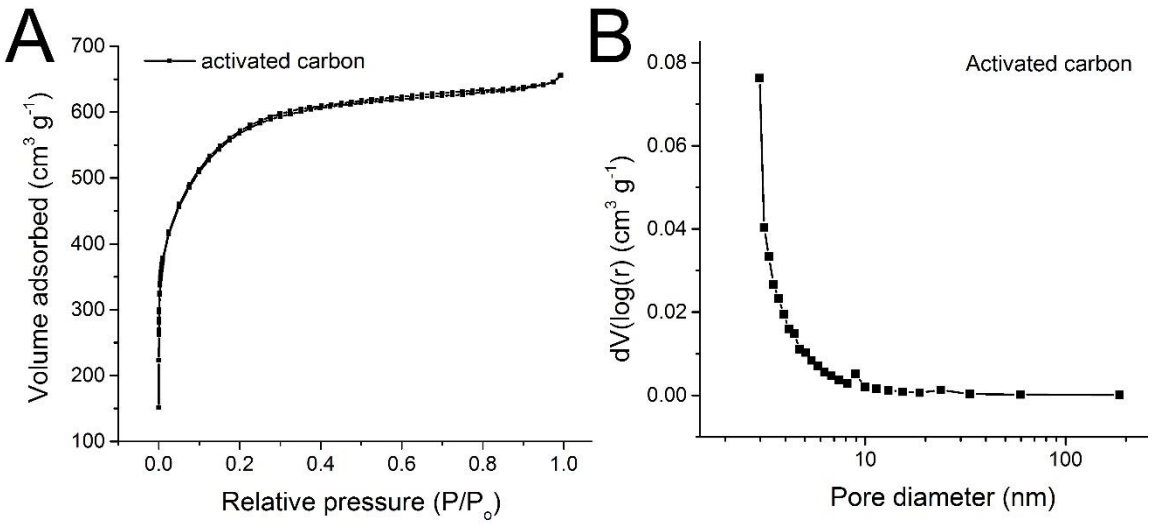

Figure 4.15 (A) isotherms and (B) pore size distribution of commercial activated carbon.

Table 4.2 Nitrogen adsorption data for 3DOm PF, 3DOm RF, and activated carbons.

Sample name	BET Surface area (m^2/g)	QSDFT Surface area (m^2/g)	BJH Pore size (nm)	BJH Pore volume (cm^3/g)
9.5 nm PF carbon	1019	922.6	7.2	1.75
21.4 nm PF carbon	1193	1172	18.5	2.01
29.2 nm PF carbon	1171	1196	23.8	3.50
39.5 nm PF carbon	1031	1004	32.6	3.08
9.5 nm RF carbon	1653	1506	7.4	1.8
29.2 nm RF carbon	1588	1414	23.6	4.08
Activated carbon	1730	1447	2.9	0.12

Before discussing the electrochemical performance of the 3DOm carbon materials, we will define our convention of naming these samples. The names should indicate the

mesopore sizes of the sample since this work aims at investigating the effects of pore size and pore structure on capacitance and rate performances of the supercapacitor. The dilemma is that mesopores of 3DOm carbons can be estimated from three different characterization techniques: TEM images of the silica template, TEM images of 3DOm carbons, and gas adsorption data. From the beginning, all sample were named after the size of the primary silica spheres that were used as the templates for the samples. However, we already discussed that the mesopores should be smaller than the size of the primary silica spheres. In fact, the gas adsorption analysis should give mesopore sizes that are close to the size of the real pores in the samples. For consistency and accuracy, we choose to name the samples based on the pore size calculated from the BJH model from the gas adsorption analysis. The samples will be named as 7.2, 18.5, 23.8, and 32.6_PF carbon and 7.4 and 23.6_RF carbon throughout the electrochemical tests below.

4.3.4 Electrochemical Performance

4.3.4.1 Cell Design.

All cells in this study were constructed using home-made cells based on symmetrical two-electrode supercapacitor designs. The cell design was similar to what has been described as the best-practice method to determine the electrode performance for supercapacitors.[33] Typically, the cell contains two aluminum caps, the top one being built with a spring-loaded tube to put pressure on the electrode once the cell is assembled. The current collectors are made of 316-stainless steel or aluminum, depending on the electrolytes used. Typically, they are 1 mm thick metal disks with the surfaces polished by superfine alumina powder (0.05 μm) to minimize the cell resistance and the capacitance contribution from the current collectors. In some cells, we used two PTFE-coated O-rings to prevent solvent evaporation and to seal the cell from air. The O-ring is more important for the cells using aqueous electrolytes or organic electrolytes that contain volatile solvents, such as acetonitrile or propylene carbonate. For cells using EMI-TFSI as an electrolyte, we did not observe any significant change in cell performance with or without the O-ring during the testing time, which is typically 2–4 days. One important component of the cell is the separator, which is used to prevent a short circuit and to allow ions to pass through. Several kinds of Celgard membranes were tested, namely 2400, 2401, 3400, and 3501,

which differ in their porosity and their wettability. For higher rate performance, a membrane with higher porosity, such as 3501, is preferred. The 3501 membrane was also coated with surfactant for better wettability with organic solvents and ionic liquid electrolytes. In this study, aluminum current collector and Celgard-3501 were used for all the tested cells.

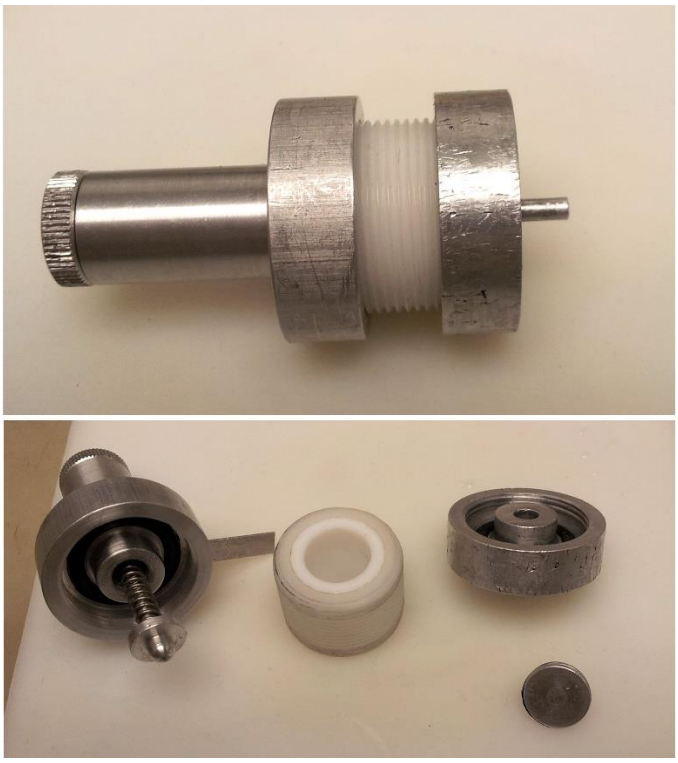

Figure 4.16 Photograph of supercapacitor cell components.

4.3.4.2 EMI-TFSI electrolyte.

EMI-TFSI is an interesting electrolyte for high energy and high power supercapacitors with a working potential up to 4.0 V and reasonable ionic conductivity at room temperature. The wide working potential of EMI-TFSI is 4–6 times higher than the typical values of aqueous electrolytes, which by theory will increase the energy density by a factor of 16 to 36. The disadvantage of using an ionic liquid electrolyte is the low ionic conductivity and small diffusion coefficients of the bigger ions making up the electrolyte, which limit the rate capability of the cell. 3DOm carbon has an ideal structure to overcome these difficulties since the mesopores are much larger than the ion sizes, and the ordered structures are expected to improve mass transport of the electrolyte inside the electrodes

significantly. Although EMI-TFSI was reported to be able to work at 4.0 V, in this study, the potential was limited to 3.5 V to prevent electrolyte decomposition due to oxidation.

4.3.4.3 Galvanostatic Tests.

The galvanostatic charge and discharge data for 3DOm PF carbons showed triangular shapes typically associated with capacitive behavior (Figure 4.17A). In most cases, the first charge cycle showed a slow increase in potential when the voltage was higher than 2.7 V, which is attributed to the irreversible oxidation of oxygen-containing functional groups on the surface of carbons. The feature gradually disappeared after the 2nd and the following cycles. All 3DOm PF carbons showed small ohmic drops (~20–50 mV), confirming the good conductivity of the carbon samples (Figure 4.17B). The specific capacitance of 3DOm PF carbons ranged from 146 to 178 F g^{-1} at a current density of 0.5 mA g^{-1}. These values are much higher than the capacitances of commercial activated carbons, which are typically less than 100 F g^{-1}.[34-36] The specific capacitance of 3DOm PF carbons is better than that of microporous carbide-derived carbons[18,37] and comparable to hierarchical porous carbide derived carbons and activated graphene.[19,20,38] The energy densities of all 3DOm carbon samples approached 250 Wh/kg (based on a capacitance of 150 F g^{-1} and a working voltage of 3.5 V). The energy density of 3DOm PF carbons is estimated to be 76 Wh/kg based on a weight ratio of 30% for the active electrode material in a packaged supercapacitor device—typical for large-scale activated carbon-based supercapacitors.

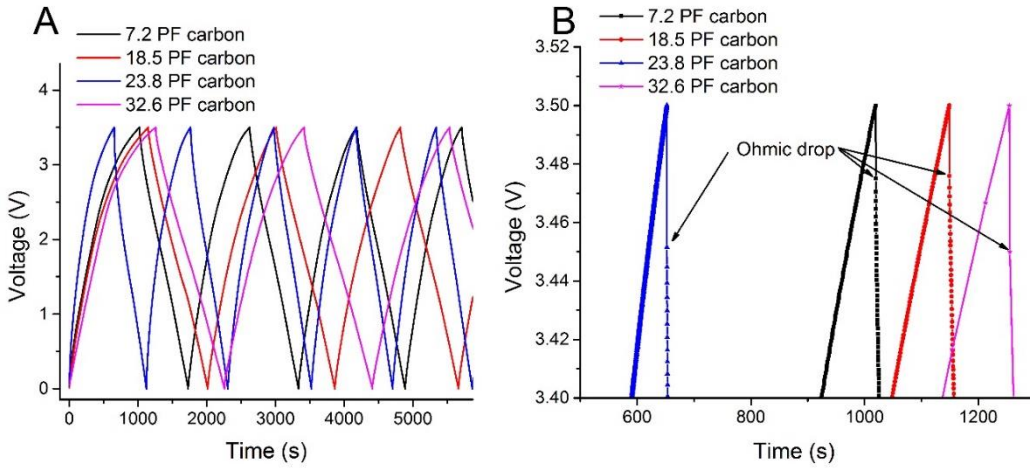

Figure 4.17 (A) Galvanostatic charge and discharge data of 3DOm PF carbons showing triangle shapes and indicating good capacitive behavior. B) The zoomed-in area at the highest potential, showing the low ohmic drops. All cells are cycled at 0.5 A g^{-1} current density.

The galvanostatic cycling data of 3DOm RF carbons showed similar features as those of 3DOm PF carbons with triangular shapes and a slow increase of the potential during the charging step at a high potential for the first few cycles. The slow increase of the voltage at high potential is more prominent in RF carbons, particularly in 3DOm RF carbon with small mesopores (7.4 nm). The ohmic drops for 3DOm RF carbons are significantly higher than those of 3DOm PF carbons. Ohmic drops of 30 and 62 mV were observed for 3DOm 7.4_RF and 3DOm 23.6_RF carbons, respectively. These features are expected since RF carbons usually have a higher oxygen content and lower conductivity than PC carbons. The capacitance values of 3DOm RF carbons are quite low (< 30 F g^{-1}) compared to those of PF carbons.

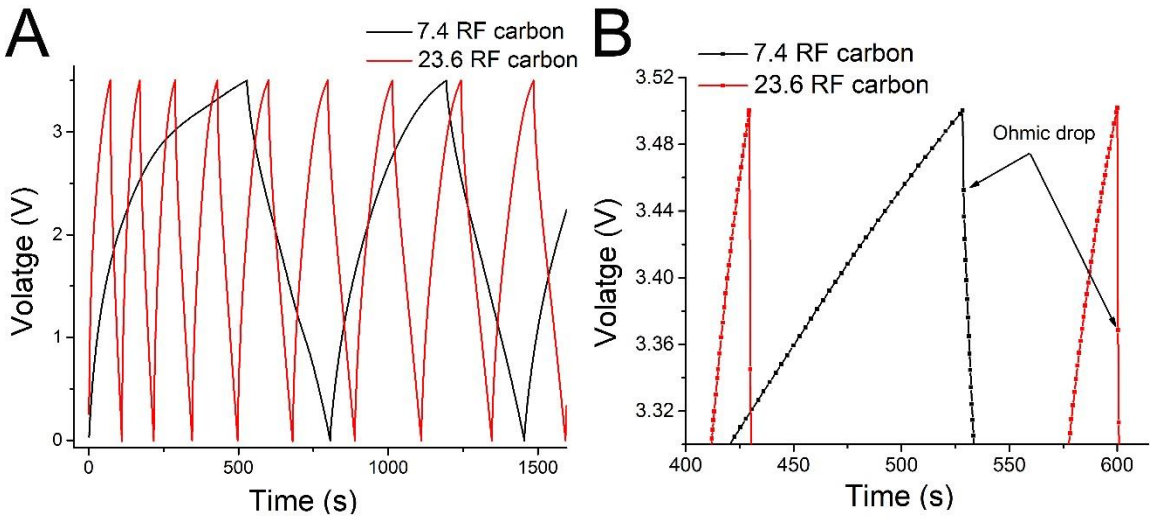

Figure 4.18 (A) Galvanostatic data of 3DOm RF carbons. (B) The zoomed-in area at the highest potential showing the ohmic drop. All cells are cycled at 0.5 A g^{-1} current density.

For the sake of comparison, galvanostatic tests were also done on commercially available activated carbon. The charge and discharge curves also formed triangular shapes characteristic of supercapacitor materials. The first and second charging curves featured a sluggish increase in potential at voltages higher than 2.5 V. The ohmic drop for this sample is about 40 mV, which is on the same magnitude with values as the PF carbon materials. The calculated specific capacitance for the activated carbon is about 155 F g^{-1}, which is comparable to the capacitance of PF carbons.

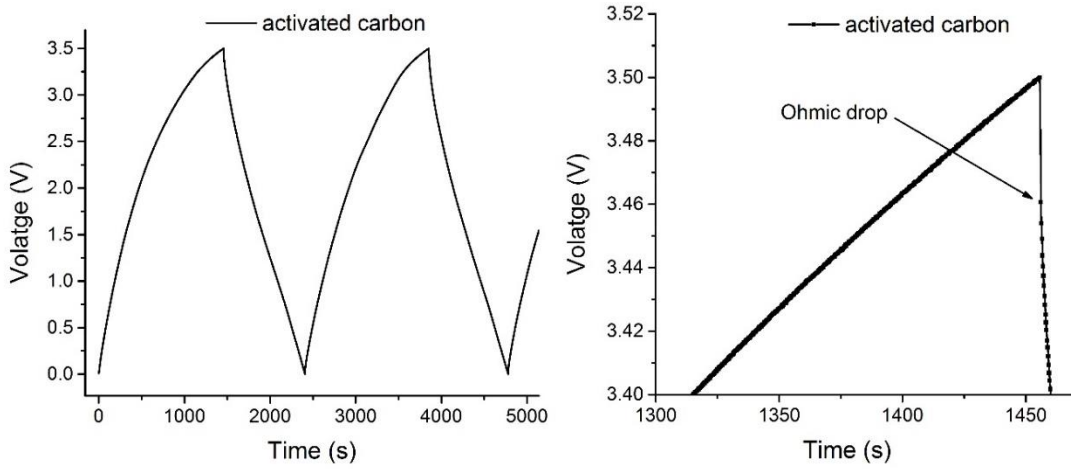

Figure 4.19 (A) Galvanostatic data of activated carbons. (B) The zoomed-in area at the highest potential, showing the ohmic drop. The cells is cycled at 0.5 A g^{-1} current density.

4.3.4.4 Electrochemical Impedance Spectroscopy Studies.

Electrochemical impedance spectroscopy (EIS) was used to study the capacitor behavior and the ion-transport kinetics within mesopores and micropores of 3DOm PF carbons. The Nyquist plots in the frequency range from 100 KHz to 10 mHz of all 3DOm PF carbons feature a sharp increase of the imaginary part of the cell impedance at low frequencies, consistent with the good capacitive behavior of these samples. For an ideal supercapacitor, the imaginary part should form a vertical line parallel to the Y-axis at low frequency and the closer to the vertical line of the imaginary part at low frequency the better capacitive behavior the sample is. The zoomed-in region in the high frequency range of the Nyquist plot shows the first intercept of the real part to be near 3 Ω for all 3DOm PF carbons. This value is typically the combined resistance of the electrolyte, the current collector, and the contact resistance between the electrode and the current collector. The suppressed semicircle in the high frequency range corresponds to a superposition of several phenomena, such as charge-transfer resistance and mass transport through mesopores and micropores in the 3DOm carbon materials. Figure 4.20B shows the frequency response of 3DOm PF carbons. The plots of specific capacitance vs. frequency in the range from 10 mHz to 100 Hz for all 3DOm PF carbons have plateaus when the frequency approaches 0.1 Hz, indicating that the response time of 3DOm carbons is typically 10 s.

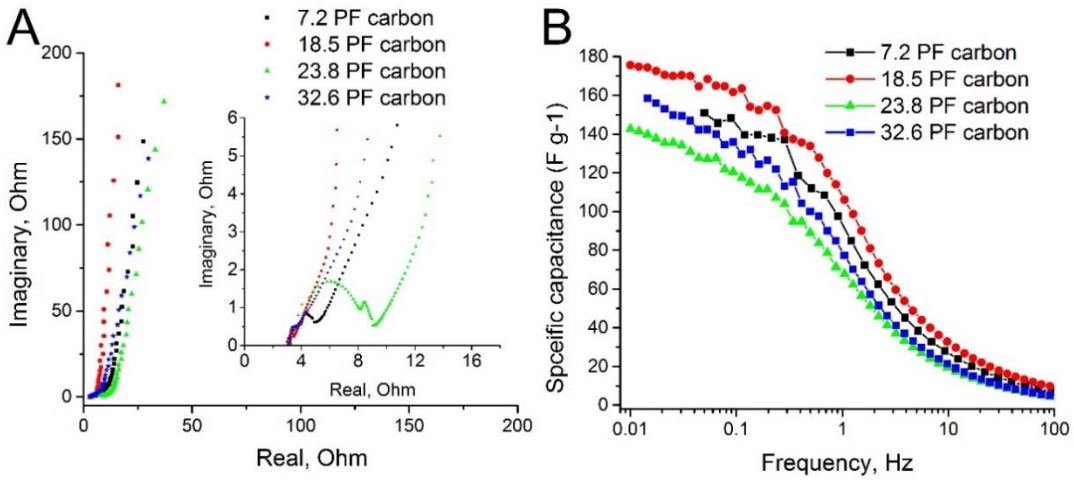

Figure 4.20 (A) Nyquist plots and (B) Frequency responses of 3DOm PF carbons with different pore sizes

4.3.4.5 Cyclic Voltammetry Studies.

Cyclic voltammetry (CV) was used to further characterize the electrochemical performance of 3DOm PF carbons. The cells were cycled between 0 and 3.5 V at different scan rates, ranging from 20 mV/s to 100 mV/s. The CVs of all 3DOm carbons showed rectangular shapes, indicating the good capacitive behavior of the samples (Figure 4.21). A sharp increase in the cathodic current at 3.2–3.5 V observed in most cases may be attributed to the oxidation of oxygen of the functional groups on the surface of carbon. This feature slowly disappeared in the second and the following cycles. It may also be related to the stability limit of the electrolyte in the presence of trace amounts of water or oxygen. We observed that this problem was less prominent if a freshly opened EMI-TFSI bottle was used. When cycled at different scan rates, 3DOm carbons showed excellent rate capabilities with the capacitance decreasing only slightly upon a five-fold increase in scan rate.

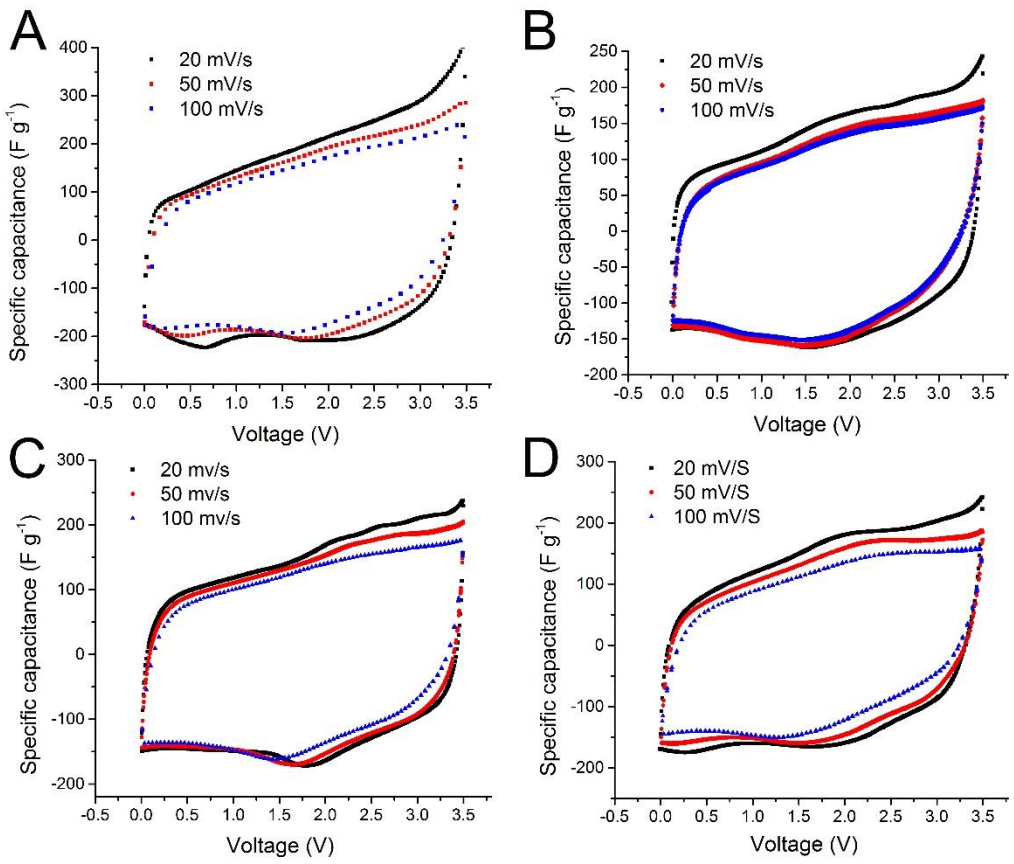

Figure 4.21 CV plots of 3DOm (A) 7.2, (B) 18.5, (C) 23.8, (D) 32.6 PF carbons, showing good capacitive behavior and excellent cyclability.

4.3.4.6 Rate Performance.

The rate performance of 3DOm RF, 3DOm PF, and activated carbons was tested by performing charge and discharge cycles at different rates, ranging from 0.5 to 25 A g^{-1}. Figure 4.22 shows a typical galvanostatic test result for 3DOm 32.6_PF carbon being charged and discharged at different rates. The characteristic triangular shape was maintained even at current density as high as 25 A g^{-1}. The ohmic drops increased at higher currents, however, the resistance of the cell calculated from different discharge current density showed a constant value of 5 Ω. This clearly showed that the cell resistance was not raised by processes such as limited ion diffusion, even at the highest current density of 25 A g^{-1}. This behavior definitely benefitted from the interconnected pore system of 3DOm carbon.

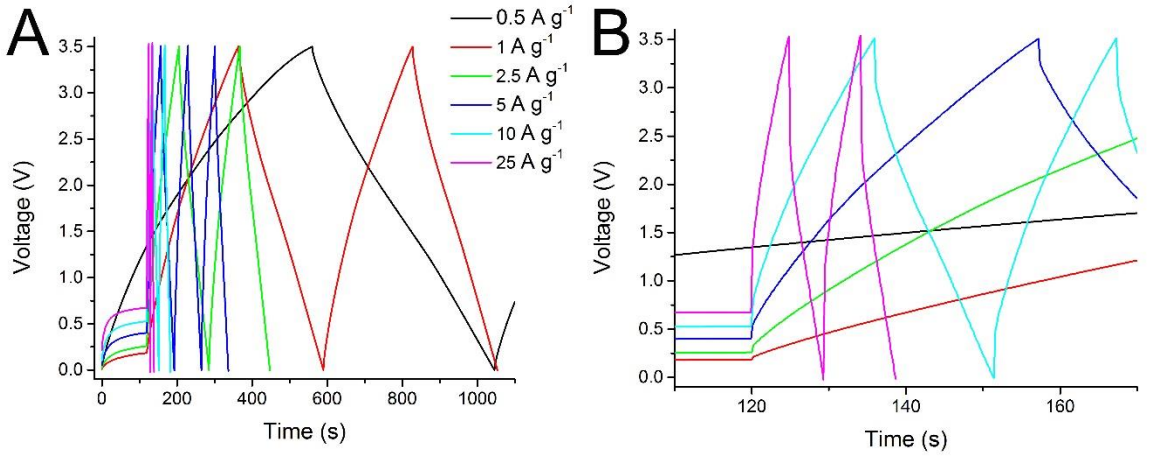

Figure 4.22 (A) Galvanostatic plot and (B) zoomed-in time range to show the test results at high charge and discharge rates for 3DOm 32.6 PF carbon at different current densities.

The rate performance of 3DOm carbons of different pore sizes is plotted in Figure 4.23. All samples showed extremely good rate performance with specific capacitance values ranging from 80 to 120 F g^{-1} at the highest current density of 25 A g^{-1}. The performance of 3DOm PF carbons is phenomenal, particularly for systems using an electrolyte with moderate conductivity such as EMI-TFSI. The rate performance of 3DOm 18.5 PF carbon is comparable to the most advanced systems based on hierarchical carbide derived carbons and activated graphene, which showed 140-170 F g^{-1} at slow rate and 100-160 F g^{-1} at high rate. [19,20,38] Even though in those reports, ionic liquids with higher ionic conductivity including EMI-BF_4 and BMIM-BF_4 were used as electrolytes, and the best sample with about 160 F g^{-1} was tested at a much smaller rate than the maximum rate used for 3DOm carbon (5.7 A g^{-1} compared to 25 A g^{-1}). All 3DOm PF carbons were able to keep more than 50 % of their capacitance when the current density was increased by a factor of 50 from 0.5 to 25 A g^{-1}. It is interesting that samples with medium-sized mesopores (18.6–23.5 nm) have better rate performance than sample with small mesopores (7.2 nm) or large mesopores (32.6 nm). Since all of these samples have the same ordered structure (cubic) and were prepared from the same precursor (PF sol), it is more likely that the mesopore sizes and the interactive roles of mesopores and micropores determine the rate performance of the material. At small charge and discharge current densities, the performance is not affected by the diffusion of ions through the pores, and all 3DOm carbon samples showed capacitance values of the same magnitude because of their similar surface areas. 3DOm

18.5 PF carbon with slightly higher surface area showed the highest capacitance of 178 F g^{-1}. The capacitance values of the other samples are about 150 F g^{-1}. At higher current densities, the diffusion of ions from the electrolyte becomes more important and affects the capacitor behavior. However, the ordered pore system of the 3DOm structure helps to limit this effect, resulting in the high capacitance at high rate. For the smallest mesopore sizes (i.e., for 7.2_PF carbon), the high rate performance is not as good as for the other PF carbons. The rate performance of the 32.6_PF carbon, the sample with the biggest mesopores and thickest walls, is however decided by both mesopores and the micropores in the walls. The capacitance contribution from the micropores is actually a significant part in this sample. Since the walls of 32.6_PF carbon are thicker than those of smaller pores, not all of micropores on the walls are accessible to the electrolyte. The samples with medium-sized mesopores have a well-balanced contribution to capacitance from both mesopores and micropores. Since the walls are not very thick in these samples, most of the micropores are easily accessible by the electrolyte. These explanations matched the predictions from the QSDFT model of surface areas vs. pore sizes of 3DOm PF carbons, which was discussed in the section on gas adsorption behavior.

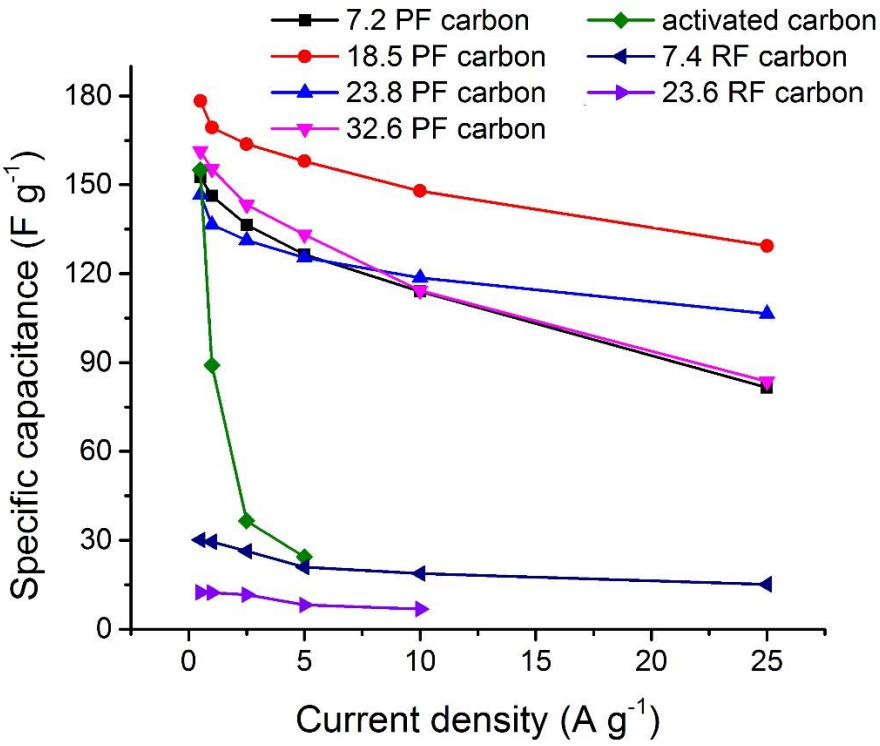

Figure 4.23 Plots comparing the rate performance 3DOm PF, 3DOm RF, and activated carbons.

3DOm RF carbons have very small capacitance values (<30 F g^{-1}) and exhibit poor rate performance. In fact, 23.6_RF carbon was not be able to maintain a high current density (> 10 A g^{-1}) due to the high resistance of the sample (Figure 4.23). Because of their poor performance, 3DOm RF carbons will not be discussed further in this chapter.

The charge and discharge profile of activated carbon at different current densities is shown in Figure 4.24. At small current densities, activated carbon showed good capacitive behavior with triangular shape and a small ohmic drop. However, at higher current densities, the triangular shape is strongly distorted by the large ohmic drop, because activated carbon contains mostly micropores with limited electrolyte accessibility, particularly at high charge and discharge current densities. The sample was also not able to maintain a current density higher than 10 A g^{-1}, and the voltage overshot the set values (< 0 V or > 3.5 V). The capacitance of activated carbon dropped quickly upon increase of current density (Figure 4.24B). This provides strong evidence for the advantage of having an ordered porous structure in 3DOm carbon that minimizes ion diffusion limitations at high current densities.

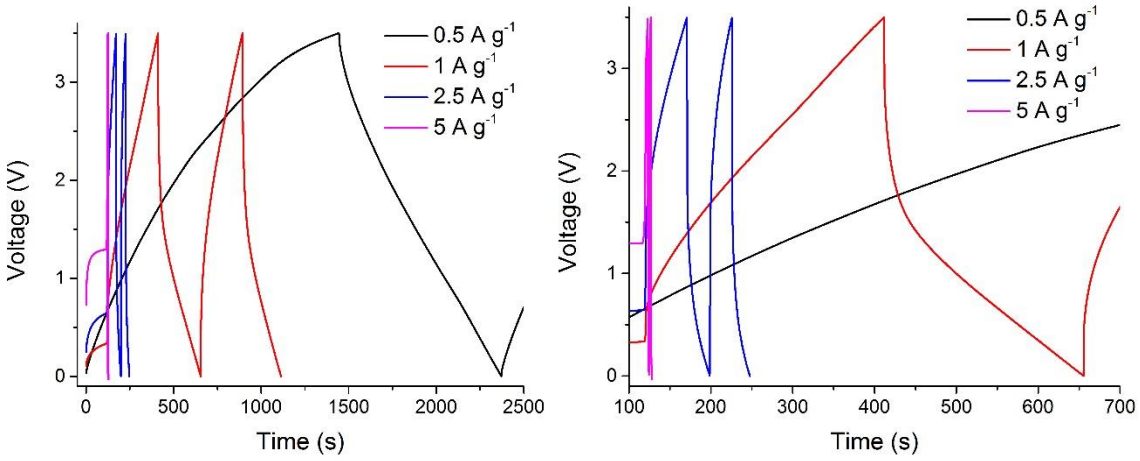

Figure 4.24 (A) Galvanostatic plot and (B) zoomed-in time range to show the test results at high charge and discharge rates for activated carbon at different current densities.

4.3.4.7 Effect of Sample Mass.

It is known that the performance of a supercapacitor cell depends strongly on the thickness of the electrodes, thicker electrode normally exhibiting poorer power capability. Therefore, depending on the targeted application of the supercapacitor cells, they are assembled with different amounts of active materials. In general, thin electrodes are used

for high power cells and thick electrodes for high energy cells.[33] Cells with both high power density and high energy density have been long-standing targets of research. However, this is difficult to achieve with activated carbon, the most common electrode material for supercapacitors, due to limited rate performance when thick electrodes are used. 3DOm carbons may provide an excellent solution to this problem because of their reasonably high capacitance and their outstanding rate performance.

To study the effect of electrode thickness on the power capability of 3DOm PF carbons, electrodes with two different loadings of active material, 1 or 6 mg/cm^2, were prepared. It is worth noting that most of the literature reports use electrodes with loadings of 1 mg/cm^2 to study electrochemical performance. This study showed that the rate performance of 3DOm PF carbon with small mesopores (7.2 nm) was strongly affected by the thickness of the electrode with a capacitance decrease of more than 50 % when the loading was increased from 1 mg/cm^2 to 6 mg/cm^2. The rate performance of 3DOm PF carbon with big mesopores (32.6 nm) decreased slightly (<20%) with the same increase of electrode loading. This clearly suggests that 3DOm carbons with large mesopores are suitable to build supercapacitor cells with combined high power and high energy density.

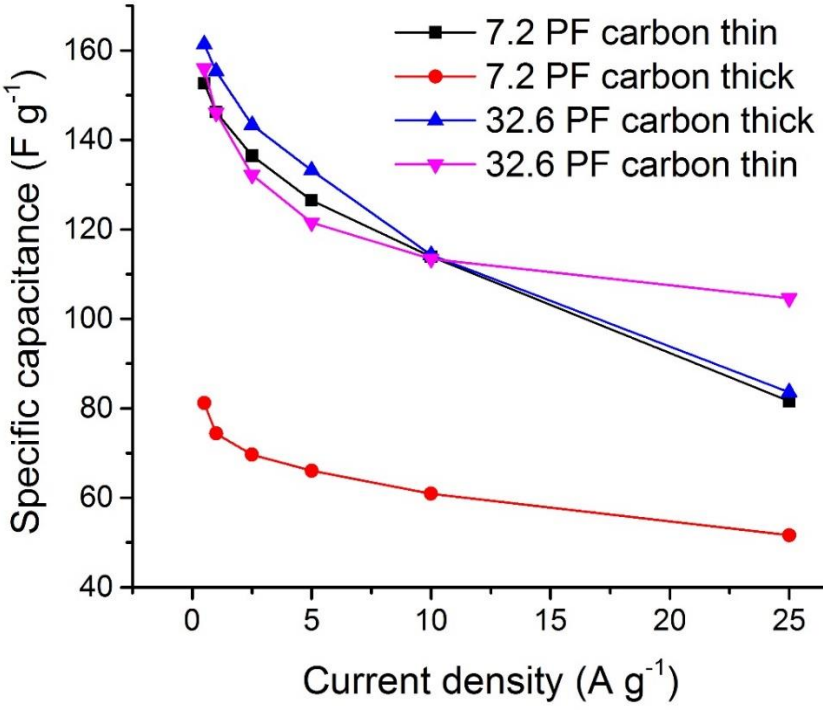

Figure 4.25 Plots comparing the rate performance of 3DOm PF carbon electrodes prepared with different mass loadings of active material.

4.4 Conclusions

3DOm carbons with ordered mesoporous structure and microporous walls are of special interest to build high energy density and high power density supercapacitor cells. The microporous walls are needed for high capacitance while the interconnected mesopore system is necessary for high power capability. In this chapter, 3DOm carbons of different mesopore sizes ranging from 7 to 32 nm were prepared through colloidal crystal templating method. First, we were able to control the size of silica spheres precisely via adjusting hydrolysis temperature and knowing the exact amount of TEOS precursor need to be added in the seeded growth method. The highly monodispersed silica spheres with the size ranging from 8-40 nm were then dried and calcined and used as templates for the synthesis of 3DOm carbons.

3DOm carbon of different mesopore sizes were successfully prepared from two different precursors (RF and PF). All samples showed ordered structures and high surface areas of 1000 – 1200 $m^2 g^{-1}$ for PF carbons and up to 1600 $m^2 g^{-1}$ for RF carbons. All of these samples were characterized by various electrochemical tests including galvanostatic, electrochemical impedance spectroscopy, and cyclic voltammetry to study their capacitive behaviors. The performances were compared to a commercial activated carbon to prove the advantages of 3DOm carbons. It is interesting that 3DOm PF carbons and 3DOm RF carbons, which have similar structure and surface areas, would perform vastly different in all electrochemical tests. In all tests, 3DOm PF carbons showed much better performances than those of RF carbons, which is ascribed to the different oxygen content and conductivity of these samples.

The best 3DOm PF carbons have shown high capacitance (178 F g^{-1} at 0.5 A g^{-1} current density) and excellent rate performance (123 F g^{-1} at 25 A g^{-1} current density). The performance of 3DOm carbons are much better than the commercial activated carbon and comparable to some of the most advanced systems reported in literature. The high energy is due to the high surface areas, which are contributed from mesopores and micropores. The excellent power capability is facilitated by the ordered, interconnected porous structure that enables efficient mass transport of the electrolyte through the active materials.

4.5 References

(1) Miller, J. R.; Burke, A. F. *The Electrochemical Society Interface* **2008**, *17*, 53.

(2) Zhai, Y.; Dou, Y.; Zhao, D.; Fulvio, P. F.; Mayes, R. T.; Dai, S. *Adv. Mater.* **2011**, *23*, 4828.

(3) Jurewicz, K.; Babeł, K.; Źiółkowski, A.; Wachowska, H. *Electrochim. Acta* **2003**, *48*, 1491.

(4) Pell, W. G.; Conway, B. E.; Marincic, N. *J. Electroanal. Chem.* **2000**, *491*, 9.

(5) Barbieri, O.; Hahn, M.; Herzog, A.; Kötz, R. *Carbon* **2005**, *43*, 1303.

(6) Shiraishi, S.; Kurihara, H.; Tsubota, H.; Oya, A.; Soneda, Y.; Yamada, Y. *Electrochem. Solid-State Lett.* **2001**, *4*, A5.

(7) Kierzek, K.; Frackowiak, E.; Lota, G.; Gryglewicz, G.; Machnikowski, J. *Electrochim. Acta* **2004**, *49*, 515.

(8) Endo, M.; Kim, Y. J.; Osawa, K.; Ishii, K.; Inoue, T.; Nomura, T.; Miyashita, N.; Dresselhaus, M. S. *Electrochem. Solid-State Lett.* **2003**, *6*, A23.

(9) Lozano-Castelló, D.; Cazorla-Amorós, D.; Linares-Solano, A.; Shiraishi, S.; Kurihara, H.; Oya, A. *Carbon* **2003**, *41*, 1765.

(10) Endo, M.; Kim, Y. J.; Ohta, H.; Ishii, K.; Inoue, T.; Hayashi, T.; Nishimura, Y.; Maeda, T.; Dresselhaus, M. S. *Carbon* **2002**, *40*, 2613.

(11) Qu, D.; Shi, H. *J. Power Sources* **1998**, *74*, 99.

(12) Jiang, Q.; Qu, M. Z.; Zhou, G. M.; Zhang, B. L.; Yu, Z. L. *Mater. Lett.* **2002**, *57*, 988.

(13) Wang, J.; Kaskel, S. *J. Mater. Chem.* **2012**, *22*, 23710.

(14) Chmiola, J.; Yushin, G.; Gogotsi, Y.; Portet, C.; Simon, P.; Taberna, P. L. *Science* **2006**, *313*, 1760.

(15) Simon, P.; Gogotsi, Y. *Nat Mater* **2008**, *7*, 845.

(16) Chmiola, J.; Largeot, C.; Taberna, P.-L.; Simon, P.; Gogotsi, Y. *Science* **2010**, *328*, 480.

(17) Daffos, B.; Taberna, P. L.; Gogotsi, Y.; Simon, P. *Fuel Cells* **2010**, *10*, 819.

(18) Largeot, C.; Portet, C.; Chmiola, J.; Taberna, P.-L.; Gogotsi, Y.; Simon, P. *J. Am. Chem. Soc.* **2008**, *130*, 2730.

(19) Liu, H.-J.; Wang, J.; Wang, C.-X.; Xia, Y.-Y. *Advanced Energy Materials* **2011**, *1*, 1101.

(20) Rose, M.; Korenblit, Y.; Kockrick, E.; Borchardt, L.; Oschatz, M.; Kaskel, S.; Yushin, G. *Small* **2011**, *7*, 1108.

(21) Yuan, C. Z.; Gao, B.; Shen, L. F.; Yang, S. D.; Hao, L.; Lu, X. J.; Zhang, F.; Zhang, L. J.; Zhang, X. G. *Nanoscale* **2011**, *3*, 529.

(22) Brun, N.; Prabaharan, S. R. S.; Surcin, C.; Morcrette, M.; Deleuze, H.; Birot, M.; Babot, O.; Achard, M.-F.; Backov, R. *J. Phys. Chem. C* **2011**, *116*, 1408.

(23) Chae, W.-S.; Gough, D. V.; Ham, S.-K.; Robinson, D. B.; Braun, P. V. *ACS. Appl. Mater. Interfaces* **2012**, *4*, 3973.

(24) Carriazo, D.; Pico, F.; Gutierrez, M. C.; Rubio, F.; Rojo, J. M.; del Monte, F. *J. Mater. Chem.* **2010**, *20*, 773.

(25) Xu, F.; Cai, R.; Zeng, Q.; Zou, C.; Wu, D.; Li, F.; Lu, X.; Liang, Y.; Fu, R. *J. Mater. Chem.* **2011**, *21*, 1970.

(26) Yang, S.-Y.; Chang, K.-H.; Tien, H.-W.; Lee, Y.-F.; Li, S.-M.; Wang, Y.-S.; Wang, J.-Y.; Ma, C.-C. M.; Hu, C.-C. *J. Mater. Chem.* **2011**, *21*, 2374.

(27) Wang, D.-W.; Li, F.; Liu, M.; Lu, G. Q.; Cheng, H.-M. *Angew. Chem.* **2008**, *120*, 379.

(28) Yokoi, T.; Sakamoto, Y.; Terasaki, O.; Kubota, Y.; Okubo, T.; Tatsumi, T. *J. Am. Chem. Soc.* **2006**, *128*, 13664.

(29) Fan, W.; Snyder, M. A.; Kumar, S.; Lee, P.-S.; Yoo, W. C.; McCormick, A. V.; Lee Penn, R.; Stein, A.; Tsapatsis, M. *Nat Mater* **2008**, *7*, 984.

(30) Ferrari, A. C.; Robertson, J. *Phys. Rev. B* **2000**, *61*, 14095.

(31) Tuinstra, F.; Koenig, J. L. *J. Chem. Phys.* **1970**, *53*, 1126.

(32) Gor, G. Y.; Thommes, M.; Cychosz, K. A.; Neimark, A. V. *Carbon* **2011**.

(33) Stoller, M. D.; Ruoff, R. S. *Energy Environ. Sci.* **2010**, *3*, 1294.

(34) Burke, A. *Electrochim. Acta* **2007**, *53*, 1083.

(35) Gamby, J.; Taberna, P. L.; Simon, P.; Fauvarque, J. F.; Chesneau, M. *J. Power Sources* **2001**, *101*, 109.

(36) Zhang, L. L.; Zhao, X. S. *Chem. Soc. Rev.* **2009**, *38*, 2520.

(37) Oschatz, M.; Kockrick, E.; Rose, M.; Borchardt, L.; Klein, N.; Senkovska, I.; Freudenberg, T.; Korenblit, Y.; Yushin, G.; Kaskel, S. *Carbon* **2010**, *48*, 3987.

(38) Zhu, Y.; Murali, S.; Stoller, M. D.; Ganesh, K. J.; Cai, W.; Ferreira, P. J.; Pirkle, A.; Wallace, R. M.; Cychosz, K. A.; Thommes, M.; Su, D.; Stach, E. A.; Ruoff, R. S. *Science* **2011**, *332*, 1537.

CHAPTER 5

Quenching Performance of Surfactant-containing and Surfactant-free Fluorophore-doped Mesoporous Silica Films for Nitroaromatic Compound Detection

Outline

Reproduced in part with permission from ref. 35.

Copyright © 2011 American Chemical Society

5.1 Introduction

Nitroaromatic compounds (NACs) are widely used in industry for the manufacture of pesticides, dyes, pharmaceuticals, and explosives. Many of them are known to cause environmental pollution and have severe effects on human health.[1] In addition, they are frequently employed as explosives in terrorist activities all around the world. Therefore, detection and quantification of NACs are of great importance in environmental pollution control and clean-up, military operations, and homeland security. Many detection methods have been developed, including fluorescence measurements,[2-6] antibody interactions,[7] ion mobility spectrometry,[8] gas chromatography coupled with mass spectrometry,[9] electrochemical analysis,[10] and surface-enhanced Raman spectroscopy.[11] Of those techniques, fluorescence sensing is among the most sensitive and cost-effective detection methods, suitable for incorporation in portable devices for on-field testing.[12]

To date, most work on fluorescence sensors for NACs has focused on conjugated polymers (CPs), utilizing their ability to amplify the sensing signal in response to interactions with NACs.[3,4,13-17] The amplifying effect of CPs was first described by Swager and co-workers in a study of the quenching capability of the compound paraquat toward the fluorescence of cyclophane-derivatized poly(phenylene ethynylenes).[18] The polymer showed up to 66-fold enhancements in quenching, resulting from its delocalized electronic structure. The amplification is due to energy migration throughout the structure when a quencher molecule binds to any chain of the polymer. In that study, a cyclophane was integrated into the polymer backbone to enhance the binding of the quencher to the polymer by forming a stable complex with paraquat. The sensing performance of CPs improves with longer radiation lifetimes and greater mobility of electrons in the polymer. In the solid state (thin films or particles), neighboring chains of CPs tend to assemble into parallel patterns, forming excimers (self-quenching) due to strong π-π interactions. These excimers can act as traps, blocking the migration of electrons and reducing the sensing performance. To prevent excimer formation and to increase the diffusion of analytes inside the polymer

films, robust three-dimensional scaffolds such as pentiptycene, triphenylene, and dibenzochrysene have been added into the polymer backbone.[6,19] Recently, systems based on polysilanes, polymetalloles, and molecular imprinting of CPs have been developed for NAC detection, and showed improved selectivity and detection limits toward these analytes.[20-22] The sensing performance of CP films depends strongly on the thickness and the organization of the polymer chains inside the films.[23] Porous, thin films of CPs with high analyte diffusivity are preferred. However, photobleaching of thin CP films limits their usable lifetimes. In addition, because of the low quantum yield, relatively thick CP films are usually required to create measurable fluorescence intensity. Limitations of thick CP films include poor molecular organization with weak intermolecular interactions that result in slow sensing times.

Small fluorescence molecules offer another effective way to detect NACs at lower cost and with simpler syntheses compared to CPs. Differences between polymer-based and small-molecule-based detection include the physical mechanism of fluorophore quenching and the absence of excitation migration in the small molecules. In principle, a single quencher molecule can quench a number of polymer molecules via excitation migration and interaction between neighboring polymer chains. These effects are absent in small-fluorophore sensors, lowering their sensitivity and detection limit. However, the greatest advantage of using a small-fluorophore sensor is the ability to incorporate the fluorophore in a matrix that can enhance binding and/or introduce excitation migration. In addition, the matrix can protect the fluorophore from photobleaching and excimer formation.[24-26]

Mesoporous silica is an ideal host for carrying fluorescence compounds because of its large surface area and its excellent thermal, chemical, and mechanical stability. Porphyrin- or 2,7-diazapyrene or CP-functionalized mesoporous silica has been used for NAC detection and showed high quenching performance, good chemical resistance, and strong photostability.[27-32] The fast fluorescence quenching was attributed to the high surface area of the mesostructure, which increased the accessibility of analyte to the fluorophore attached to the silica surface. Excimer formation in these host-guest structures was limited since the fluorophore was dispersed over such a large surface area. Fluorophore-bridged mesoporous silica is usually prepared using surfactants as templates. In most cases, silica precursors such as R-Si(OC_2H_5)$_3$ and R-Si(OCH_3)$_3$, in which R- is a fluorophore

substituent, are mixed with a surfactant in ethanol, THF, or water and then spin coated or dip coated onto transparent substrates to form thin films. Afterwards, the surfactant is removed by thermal treatment or solvent extraction to obtain fluorophore-functionalized mesoporous silica films. To support the formation of a mesostructure, common silica precursors, such as tetraethyl orthosilicate (TEOS) or tetramethyl orthosilicate (TMOS), are added alongside the organo-silicate precursors. Another way to produce fluorophore-bridged mesoporous silica films is to fabricate surfactant-free mesoporous silica films first and then attach fluorophores to the mesopore walls. Both of these methods target surfactant-free thin films with fluorophores covalently bonded to silica surfaces. Considering the added free pore volume, one would expect that analyte diffusivity is better in surfactant-free films than in those still containing the surfactant, although it would also depend on the hydrophobicity/hydrophilicity of the surface. However, diffusion of analytes in the films is not always the most important factor, as the films are usually very thin with thickness values from tens of nanometers to less than 200 nm. Other important factors affecting the quenching performance of a thin film sensor include the binding constant of the analytes to the fluorophore, and the electron transfer rate between the quencher and fluorophore.

Both NACs and organic fluorophores are often hydrophobic, so they can easily interact with each other through van der Waals or dipole-dipole forces. In fluorophore-doped silica films, the interactions also depend on other film components. These silica surfaces are quite hydrophilic because, owing to the presence of the thermally labile, organic fluorophores, they are not usually treated at high temperatures that induce a higher level of condensation. Consequently, they contain a large fraction of surface hydroxyl groups. Therefore, hydrophobic NACs do not interact strongly with silica surfaces that contain organic fluorophores. However, the inclusion of surfactants that attract NACs in the film can improve the binding NACs with fluorophores. Chen et al. studied the effect of surfactants on the quenching performance of an anionic conjugated polymer (MPS-PPV) toward various small quenchers.[33] They found that an ionic surfactant amplified the quenching performance of MPS-PPV toward charged quenchers, whereas nonionic surfactants worked better for neutral species such as DNT and TNT. The down side of keeping the surfactant in the film is the slow diffusion of NACs through the surfactant environment.

However, with very thin films, this problem can be mitigated. Stevens et al. were able to observe fluorescence quenching by methanol in mesoporous silica films that still contained the surfactant Pluronic P123 together with meso-tetrakis(4-sulfonatophenyl)porphyrin and coumarin 481.[34] Furthermore, because of the different thermal expansion of silica walls and surfactant cores, a mild heat treatment can open up the film structure. Such an annealing step can also remove solvent trapped inside the film, creating more space for NAC diffusion.

In the work described in this chapter, several phenol-substituted pyrene compounds were synthesized and tested for NAC detection, both in solution and in thin films of mesoporous silica. Several kinds of films were fabricated and used to study quenching with DNT in the gas phase.[35] First, surfactant-containing mesoporous silica thin films doped with these fluorophores were prepared. The amphiphilic surfactant P123 was used to improve the binding of DNT to the film. Two types of surfactant-free mesoporous silica films were prepared, including fluorophore-impregnated films and fluorophore-bridged films. The former were prepared by immersing surfactant-removed films in the fluorophore solution. The latter were prepared by first synthesizing an organo-silica precursor by coupling a phenol-substituted pyrene fluorophore with 3-triethoxysilylpropyl isocyanate. The organo-silica precursor was then used to prepare mesoporous films, which were treated with hot ethanol to remove the surfactant. Both, the film structure and the film components were found to affect the quenching performance. Fluorophore-bridged mesoporous silica thin films showed the best quenching performance with 43% quenching after 5 s and 88% quenching after 60 s, which is one of the fastest and highest efficiency responses reported in literature. Films prepared by a simple one-pot synthesis containing an inexpensive surfactant also showed very good quenching performance with 39% quenching after 60 s and 94% after 405 s.

5.2 Experimental Section

5.2.1 Materials.

Pyrene (98%), DNT (97%), and palladium tetrakistriphenylphosphine (99%) were purchased from Aldrich; 4-methoxy phenylboronic acid (98%) was purchased from

Combi-block; all other chemical reagents and solvents were purchased from Sigma-Aldrich and used without further purification.

5.2.2 Preparation of fluorophore.

1,3,6,8-Tetrabromopyrene: Bromine (35 g) was added dropwise into a solution of pyrene (10 g) in nitrobenzene (80 mL) and mechanically stirred for 6 h at 120 °C to obtain a pale-green precipitate. The product was filtered and washed with copious amounts of nitrobenzene and dichloromethane (DCM), then dried at 120 °C under vacuum before further use.

1,3,6,8-Tetrakis(4-methoxyphenyl)pyrene (TKMPP): TKMPP was prepared according to established procedures using the Suzuki coupling reaction.[36-38] 1,3,6,8-tetrabromopyrene (2.85 g), 4-methyoxybenzeneboronic acid (5 g), palladium tetrakistriphenylphosphine (0.1 g), and potassium carbonate (6 g) were added to 50 mL dry dioxane and stirred at 85 °C for 120 h under nitrogen. The reaction mixture was poured into a mixture of concentrated HCl and ice (25 wt% HCl) and extracted with DCM. The solution was then dried over magnesium sulfate and recrystallized from toluene to give 2.62 g of TKMPP, a bright yellow powder (yield: 76%). ^{1}H NMR (300 MHz, C_6D_6): δ = 8.37 (s, 4H, CH), 8.12 (s, 2H, CH), 7.52 (m, 8H, CH), 6.93 (m, 8H, CH), 3.36 (s, 12H, CH_3); UV-vis (DCM): $\lambda_{max}(\varepsilon)$ = 393 nm.

1,3,6,8-Tetrakis(4-hydroxyphenyl)pyrene (TKHPP): TKMPP (3 g) was added to 100 mL of concentrated HBr solution and stirred at room temperature for 3 h. *N*-Methyl-*N*,*N*-dioctyloctan-1-ammonium chloride (Aliquat 336) (5 g) was added to the mixture and stirred at 130 °C for 24 h. The reaction mixture was then poured into water (1 L) in a 3 L separator funnel. DCM (300 ml) was added to the solution and shaken well to extract the product into the organic phase. The organic phase was dried over $MgSO_4$ and concentrated before being crystallized from propanol solution. The obtained precipitate was washed with water and kept in the dark for further use (yield: 65%). ^{1}H NMR (300 MHz, DMF-d_7): δ = 8.25 (s, 2H, CH), 7.96 (s, 4H, CH), 7.61 (d, 8H, CH), 7.12 (d, 8H, CH), 3.59 (s, 4H).

1,3,6,8-Tetrakis[4-(3-triethoxysilylpropylaminocarbonyloxy)phenyl]pyrene (TKSPP): A mixture of 3-triethoxysilylpropyl isocyanate (0.8 g), TKHPP (0.3 g), triethylamine (5

mL), and DCM (50 mL) was stirred at room temperature for 24 h and then refluxed for 6 h. Solvent was removed from the reaction mixture by rotary evaporation. The residue was dissolved in toluene and filtered to remove any insoluble material. Recrystallization in toluene/hexane was repeated twice, and the precipitate was collected by suction filtration and dried under reduced pressure (yield: 58%). ^{1}H NMR (500 MHz, $CDCl_3$) δ = 8.18 (s, 4H), 7.98 (s, 2H), 7.64 (d, 8H), 7.30 (d, 8H), 5.45 (t, 4H), 3.87 (q, 24H), 3.33 (m, 8H), 1.74 (m, 8H), 1.26 (t, 36H), and 0.73 (t, 8H) ppm.

5.2.3 Preparation of thin-film sensors.

Silica–surfactant–fluorophore composite films with different mesostructures were prepared by spin-coating mixtures of TEOS, P123 surfactant, and TKMPP in a mixture of ethanol (EtOH) and tetrahydrofuran (THF) on a quartz substrate. The substrates were pre-cleaned by sonication with EtOH for 15 min, then dried at 110 °C. After spin-coating, the films were dried at room temperature for 24 h before carrying out the fluorescence quenching experiments. To enhance the stability of the silica framework, some films were annealed at 100 °C for 24 h.

5.2.3.1 Composite films with wormlike mesopores.

TEOS (0.4 g), P123 (0.24 g), TKMPP (0.5 mL of saturated TKMPP in a mixture of EtOH and THF (50–50 wt%)), and HCl (80 μL) were added to 8.5 mL of EtOH:THF (50–50 wt%) and stirred overnight. The precursor solution was spin-coated at 4500 rpm for 30 s on a quartz substrate to produce films with wormlike structures.

5.2.3.2 2D-hexagonal composite films.

TEOS (2.6 g), HCl (1.35 g of 0.04 wt% solution), TKMPP (0.5 mL of saturated TKMPP in a mixture of EtOH and THF (50–50 wt%)) was mixed with 3 g of EtOH and stirred for 15 min. In another vial, P123 (0.7 g) was dissolved in EtOH (2 g) and stirred. The two solutions were then mixed and stirred for another 3 h. The precursor was spin-coated at 3000 rpm for 45 s to prepare 2D-hexagonal composite films.

5.2.3.3 3D-hexagonal composite films.

TEOS (2.6 g), HCl (1.35 g of 0.04 wt% solution), TKMPP (0.5 mL of saturated TKMPP in a mixture of EtOH and THF (50–50 wt%)) was mixed with 3 g of EtOH and stirred for 15 min. In another vial, P123 (0.35 g) was dissolved in EtOH (2 g) and stirred. The two solutions were then mixed and stirred for 15 min. The precursor was spin-coated at 3000 rpm for 45 s to prepare 3D-hexagonal composite films.

5.2.3.4 TKMPP-impregnated, surfactant-free mesoporous silica films.

Each of the mesoporous silica films prepared as above (with TKMPP dopants) were first aged at 100 °C for 24 h to strengthen the silica framework, then calcined in air at 450 °C for 6 h (ramp rate: 5 ˚C/min) to remove the surfactant. The surfactant-free films were then immersed multiple times in TKMPP solution in DCM, each time for 30 s, to refill mesopores with fluorophore molecules.

5.2.3.5 TKSPP-bridged mesoporous silica films.

TKSPP-bridged mesoporous silica films with different mesoporous structures were prepared in a manner similar to the preparation of the non-calcined, doped films above. The only difference was that TKMPP was replaced with TKSPP, the fluorophore concentration in the precursor solutions being 10^{-6} M. The spin-cast films were then annealed at 100 °C for 24 h and immersed in hot ethanol to remove surfactant.

5.2.4 Characterization.

Transmission electron microscopy (TEM) was carried out with a Technai T12 microscope operating at 120 kV with emission currents ranging from 7 to 12 μA. Samples were prepared by first stripping the mesostructured films off the substrates and then dispersing them into EtOH and sonicating for 5 min. Thermogravimetric (TG) analysis and differential scanning calorimetry (DSC) were performed on a Netzsch model STA 409 instrument. Fourier transform infrared (FTIR) spectroscopy was carried out using a Nicolet Magna-IR 760 spectrometer. Samples for FTIR spectroscopy were prepared as thin pellets by mixing and pressing powdered samples with optical grade KBr. Fluorescence spectra were collected with a PTI Quantamaster fluorimeter (London, Ontario, Canada) at room

temperature. Quenching experiments were performed by placing the films in a sealed 20-mL vial containing 2 g of DNT for a fixed time. Glass wool was used to prevent direct contact between the film and DNT. The film was then placed in a quartz cuvette with four clear sides, and the fluorescence intensity was measured immediately. To examine quenching effects of potential interferents (Minute Maid 100% apple juice, perfume (Axe® deodorant body spray Kilo), benzene, toluene, and ethanol), glass wool was wetted with the liquid interferent. The wetted glass wool was then placed on the bottom of a vial, followed by another piece of dry glass wool and subsequently the as-synthesized film with wormlike mesopores. The vial was sealed for specific times, followed by immediate measurements of the fluorescence intensity. Geometry optimization and energy calculations were performed using the Gaussian 09 computational package that automatically assigns the proper atomic radii.

5.3 Results And Discussion

5.3.1 Fluorophore preparation.

Pyrene is a well-studied molecule for fluorescent probes and fluorescent sensors because of its high quantum yield and long lifetime. The use of pyrene itself is limited because of its tendency to form π-aggregates/excimers at high concentrations or in the solid state.[36] One way to prevent aggregation and formation of excimers is to substitute hydrogen with bulkier groups, which introduces greater steric hindrance. For NAC sensors, electron donating substitution groups are of interest because of their ability to enhance the electron density of the pyrene core, facilitating the electron transfer process to electron-deficient compounds (NACs). The sensing performance of pyrene for NACs could be further improved with conjugated substitution groups, which act as excitation migration pathways when interacting with NACs. For these reasons, the X-shaped phenyl-substituted pyrene is of great interest for NAC sensors. In addition, the compounds usually show strong emission, excellent quantum yields, and photobleaching resistance, which are ideal properties for fluorescence sensors.

The synthesis of an X-shaped pyrene followed an established method and is outlined in Scheme 5.1.[36-39] TKMPP was synthesized via the Suzuki coupling reaction between

tetrabromopyrene and 4-methoxybenzeneboronic acid. It was then used as the precursor for TKHPP, which was further reacted with 3-triethoxysilylpropyl isocyanate to obtain the organo-silicon precursor TKSPP used in the preparation of fluorophore-bridged mesoporous silica.

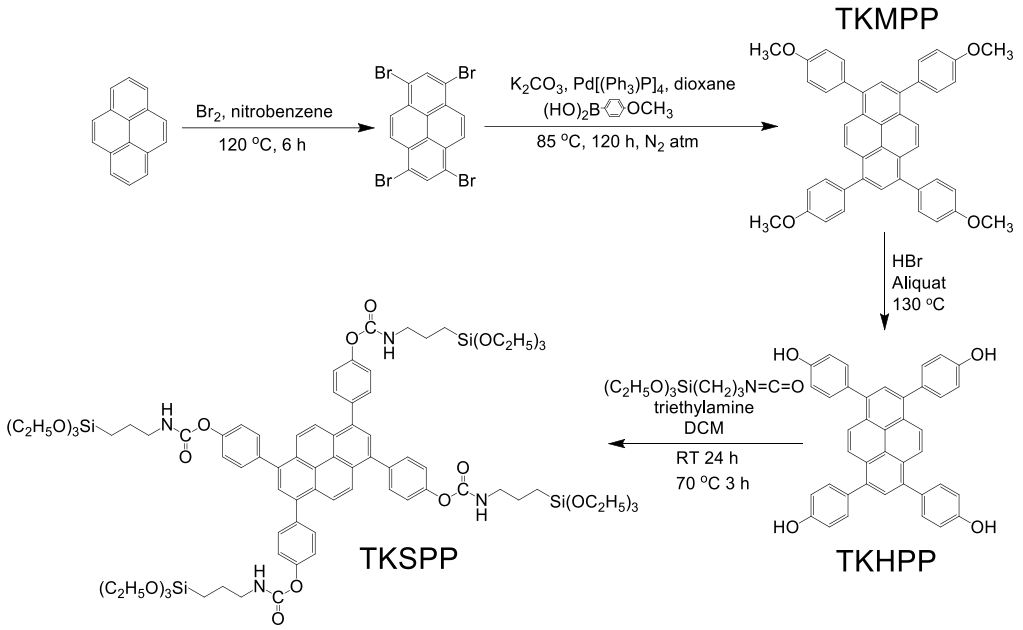

Scheme 5.1 Synthesis scheme for the preparation of TKMPP, TKHPP and TKSPP.

A geometry optimization of TKMPP was performed using molecular-mechanics calculations with a universal force field. The result showed that the four methoxyphenyl arms are not planar with the pyrene core, with torsion angles varying from 45° to 62°, and that the longest molecular dimension is about 2 nm (Figure 5.1A). The large torsion angles result from the strong steric repulsion between the hydrogen atoms of the phenyl groups and those of the pyrene core. This structure limits the tendency of TKMPP to form excimers in the solid state. Absorption and emission spectra of TKMPP were computed using density-functional theory at the B3LYP/6-311G* level, showing that the HOMO and LUMO of TKMPP are at -4.9 and -1.7 eV, respectively (Figure 5.1B). These energy levels are close to the experimental values from absorption spectra of TKMPP in DCM in Figure 5.2. The energy levels also overlap closely with the energy spectrum of DNT, thereby permitting electron transfer between the two species.

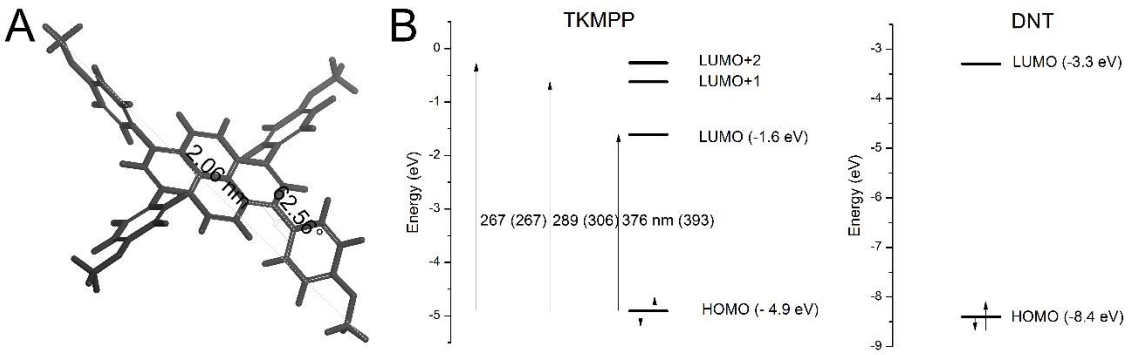

Figure 9Figure 5.1. (A) Optimized geometry of 1,3,6,8-tetrakis(methoxyphenyl)pyrene. (B) Energy diagram of TKMPP (left) and DNT (right), calculated by density-functional theory at the B3LYP/6-311G* level. Computed values are shown in parentheses, experimental values without parentheses.

5.3.2 Solution study.

TKMPP is quite nonpolar and easily dissolved in solvents such as DCM, toluene, and benzene. In good solvents such as these, TKMPP molecules are solvated and remain as discrete molecules. It is important to study TKMPP in that state because such a study can give information about the absorption and emission of single molecules, as well as the binding and quenching constants between TKMPP and analytes. We chose DCM as the solvent for all of the following studies to avoid any possible electron transfer between TKMPP and an aromatic solvent. The UV-vis spectrum of TKMPP in DCM shows three peaks at 393, 306, and 267 nm, corresponding to HOMO to LUMO, LUMO+1 and LUMO+2 transitions, respectively (Figure 5.2). It is interesting that the fluorescence emission spectrum of TKMPP only shows one peak at 432 nm, independent of the excitation wavelength. This results from the balance between conformational effects and electronic effects, in which any extra energy resulting from excitation at shorter wavelengths is used to change the conformation of the four bulky groups.[37]

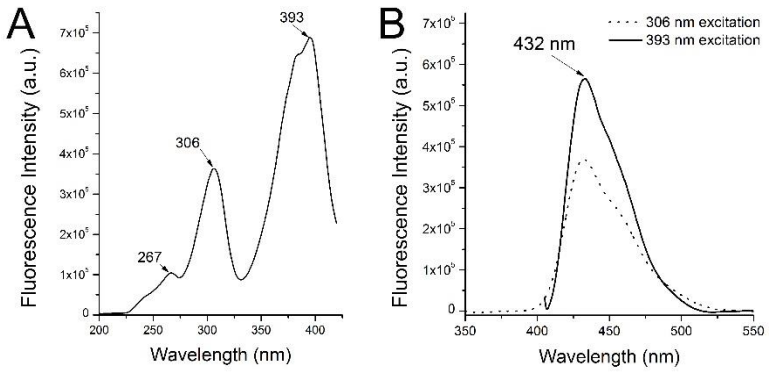

Figure 5.2 UV-vis absorption (left) and emission spectra (right) of TKMPP in DCM.

The fluorescence quenching properties of TKMPP in DCM were studied by examining the steady-state fluorescence intensity changes in response to three different electron-deficient aromatic compounds: 2,4-dinitrotoluene (DNT), nitrobenzene (NB), and 1,3-dinitrobenzene (DNB). Upon adding quenchers, the fluorescence intensity of TKMPP solution decreased quickly, demonstrating the efficiency of the quenching process. The emission spectra of TKMPP show similar features with or without quenchers, with only one peak at 432 nm and a shoulder at longer wavelengths. No new emission band was observed even at very high quencher concentrations (Figure 5.3), indicating that no new fluorescent compound was formed during the quenching experiment. For all three NACs, the relative fluorescence intensity plotted against quencher concentration followed nearly straight lines with slight curvature at high quencher concentration, indicating that a static-quenching mechanism was involved. The binding constants of TKMPP with DNT, DNB, and NB can be calculated by fitting the quenching data to the Stern-Volmer equation (Eq. 1).

$$\frac{F_o}{F} = 1 + K_s[Q] \qquad (1)$$

Here, Fo and F are the fluorescence intensities in the absence and presence of the quencher, respectively, Ks denotes the static quenching constant, and [Q] is the quencher concentration. The calculated static quenching constants are 2195, 1062, and 1652 M-1 for DNT, DNB, and NB, respectively, indicating that among these analytes, TKMPP binds most strongly with DNT (Ks = 2195 M-1). This result suggests that discrete TKMPP molecules interact well with these NACs and possibly also with other NACs that have

overlapping energy levels. For this behavior to apply in the solid state, it is crucial that TKMPP must stay present as isolated molecules that are approachable by analytes.

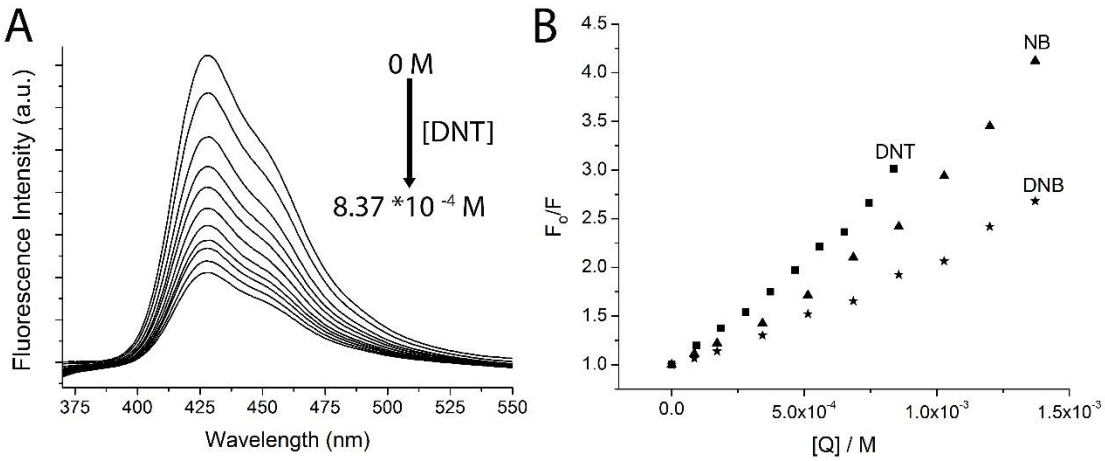

Figure 5.3 A) Fluorescence quenching of TKMPP by DNT and B) Stern-Volmer plot of TKMPP in DCM in response to DNT, DNB, and NB.

5.3.3 Quenching test on filter paper.

A rapid test was performed using filter paper as a substrate to study the quenching performance of TKMPP in the solid state. First, a few drops of TKMPP in DCM were placed onto a filter paper and then dried to deposit the fluorophore on the substrate. A bright blue emission was observed when the filter paper was irradiated with a UV-lamp (λ_{ex} = 366 nm, Figure 5.4B). The paper was then placed in a sealed vial containing 2 g of solid DNT covered with cotton to prevent direct contact. After 3 minutes exposure to DNT-containing air, the paper was irradiated by the UV-lamp again and only showed a very dim blue emission (Figure 5.4C), which indicates that the emission of solid TKMPP was effectively quenched by DNT in the gas phase.

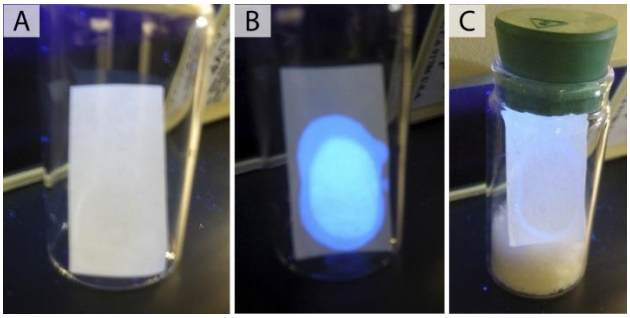

Figure 5.4 Photographs of (A) filter paper, (B) TKMPP on filter paper, and (C) TKMPP on filter paper immersed in DNT-containing vial for 3 minutes. All samples were irradiated with a UV-lamp at 366 nm.

5.3.4 Fluorophore-doped, surfactant-containing mesoporous silica thin films.

In the solid state, where molecules are close to each other and not protected by solvation, pyrene-based fluorophores are usually packed to form excimers due to the strong π-π interactions between pyrene cores. Even though with TKMPP, this tendency is limited by the presence of the four bulky substituents, it is necessary to distribute the fluorophore in porous, inert media to keep them separated. To achieve this, we chose to distribute TKMPP in mesoporous silica, which provides a robust, high-surface-area framework. TKMPP-doped P123-containing mesoporous silica thin films were prepared by spin-coating solutions of TKMPP-P123-TEOS in ethanol or in a mixed solvent of ethanol and THF on quartz substrates. Three different target film structures (2D-hexagonal, 3D-hexagonal, and wormlike) were prepared to study the effect of film morphology on the quenching performance toward DNT in the gas phase. The mesostructure of the films was formed by the so-called evaporation-induced self-assembly (EISA) mechanism. In this process, surfactant molecules form micelles, which upon solvent evaporation assemble into different liquid-crystalline mesostructures, such as hexagonal, cubic, and lamellar phases. Inorganic precursors and other components in the solution are incorporated into these mesophases through electrostatic interactions, van der Waals forces, hydrogen bonding, or covalent bonding. In the fluorescent composite film, the final position of the luminescence compounds depends on the interactions between silica, surfactant molecules, and the fluorophore. The placement of luminescent molecules in silica-surfactant composite films can be controlled by using different surfactants (anionic, cationic, amphiphilic) and choosing luminescent compounds with different functional groups.[40-43] Zink and co-

workers were able to place luminescent compounds in three distinct regions: the silica framework, the hydrophobic cores of the surfactant micelles, and the ionic interface containing the charged headgroups of the ionic surfactant and their counterions.[40,41] For a fluorescence sensor, the luminescent compounds must be placed in regions that are easily approachable by the analyte, ensuring good quenching performance. The hydrophilic (silica surface) and charged (surfactant heads) regions are not suitable because the targeted analyte (DNT) is hydrophobic. Placing the fluorophore inside the silica framework is even worse as it would not be accessible by the analyte. The surfaces of hydrophobic cores are better positions compared to the regions mentioned above. To achieve this placement, we used the block copolymer P123 with polyethyleneoxide (PEO) and polypropyleneoxide (PPO) as a template for mesostructured films. In ethanolic solution, P123 forms micelles with hydrophobic cores composed of PPO blocks and hydrophilic arms composed of PEO blocks. The hydrophobic fluorophore (TKMPP) is more likely to be distributed on the surface and inside the hydrophobic cores composed of PPO blocks. In the following sections, the film morphologies and film compositions are discussed on the basis of TEM, SEM, FTIR, and TGA-DSC data. The films were then used to test their quenching performance toward DNT in the gas phase.

5.3.4.1 Film morphologies.

SEM was used to investigate the surface textures and to estimate the film thicknesses. It is interesting that films with wormlike mesopores have a very textured surface, whereas films with 2D-hexagonal and 3D-hexagonal mesopores give relatively smooth surfaces (Figure 5.5). As the diffusion of analyte into thin films mostly goes through the top surface via defects (cracks, holes), films with mesopores are expected to have better diffusion capability than the films with 2D, and 3D-hexagonal mesopores.

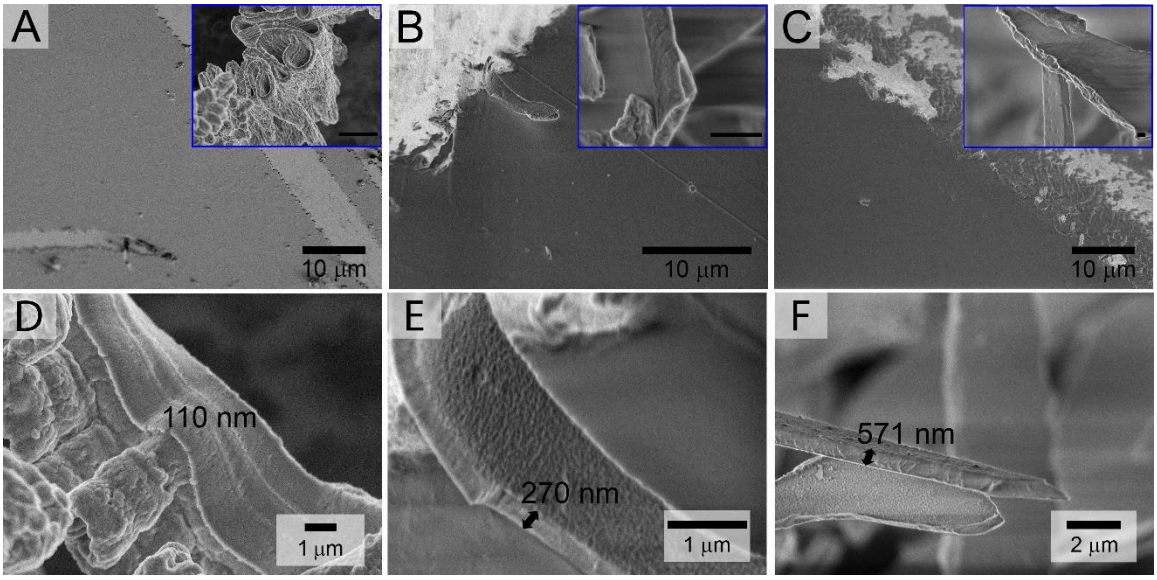

Figure 5.5 SEM images of the surfaces of unannealed films with (A) and (D) wormlike mesopores, (B) and (E) 2D-hexagonal mesopores, and (C) and (F) 3D-hexagonal mesopores. Some regions were scratched for thickness measurements, revealing the silicon substrate (lighter areas). The darker areas are the film surfaces. Insets are zoomed-in images of the corresponding films that had been peeled off the surface, showing the roughness of the film surfaces in more detail. Scale bars for the inset images are 500 nm. (D), (E), and (F) are used to estimate the thicknesses of the films.

TEM was used to investigate the morphologies of the films. Figure 5.6 shows the morphologies of TKMPP-doped mesoporous silica thin films before heat treatment at 100 °C for 24 h. The contrast in the TEM images between the silica phase (darker) and organic phases (including the P123 surfactant and the TKMPP fluorophore, lighter) can give an idea about how the components are arranged in the films. Films with wormlike mesopores (Figure 5.6 A) are characterized by interconnected, disordered pores distributed throughout the film, providing an efficient structure for analyte transport through the organic phase. Estimated pore sizes, wall thicknesses, and film thicknesses are summarized in Table 5.1.

The films with 2D-hexagonal mesopores are characterized by long channels when viewed perpendicular to the [001] direction (Figure 5.6 B), and hexagonally closed-pack circles when viewed along the [001] direction (not shown). The long channels in 2D-hexagonal films are typically oriented parallel to the surface of the substrate, which impedes diffusion of analyte molecules through the film and decreases the quenching efficiency. Because the pieces of film were scraped off the substrate for the preparation of

TEM samples, we cannot confirm how the channels were actually oriented on the substrate. However, the poor quenching performance of 2D-hexagonal films with DNT (see below) is consistent with channels oriented parallel to the substrate in the as-synthesized samples.

Table 5.1 Fluorophore content and dimensions of unannealed films.

type of film	**fluorophore concentration[a] (M)(nm)**	**film thickness[b] (nm)**	**pore diameter[c] (nm)**	**wall thickness[c]**
wormlike	2.5×10^{-4}	110	4.3±0.4	5.7±0.6
2D-hexagonal	5.4×10^{-5}	270	3.3±0.2	5.0±0.2
3D-hexagonal	1.5×10^{-4}	571	4.2±0.4	5.8±0.4
TKSPP-bridged, surfactant removed	7.0×10^{-5}	270	4.6±0.4	5.7±0.5

[a] The concentration of fluorophores in each film was determined by extracting TKMPP from the films into DCM solution, then determining the amount of TKMPP in the extracted solutions using a fluorescence calibration curve from standard TKMPP solutions, and dividing by the estimated volume of the film.

[b] Estimated from SEM images (Figure 5.5).

[c] Estimated from multiple TEM images.

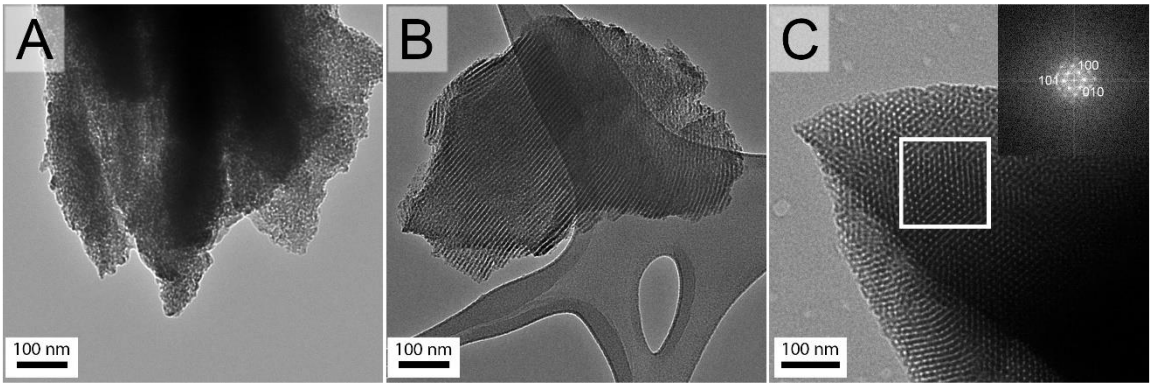

Figure 5.6 TEM images of unannealed films with (A) wormlike, (B) 2D-hexagonal, and (C) 3D-hexagonal mesopores. The inset in (C) is a fast-Fourier-transform (FFT) pattern of the area inside the square.

The mesostructure of the 3D-hexagonal films was solved by indexing FFT patterns of a few TEM images. The inset in Figure 5.6C is the FFT pattern of the selected area and shows a perfect 6-fold symmetry that originates either from (111) planes of a cubic system or (100) planes of a hexagonal system. We tried to solve the FFT patterns of various views (Figure 5.7) with both cubic and hexagonal systems, but only the 3D-hexagonal system satisfied all conditions. Hence, the unit cell parameters were calculated to be $a = b = 11.6$ nm and $c = 20.03$ nm with space group $P6_3/mmc$.

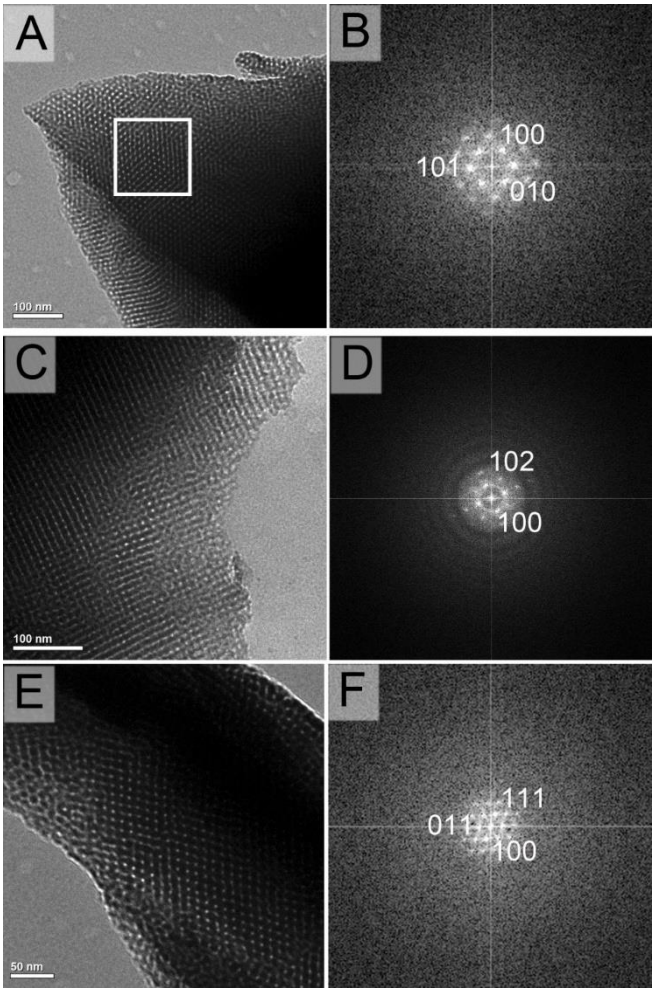

Figure 5.7 TEM images and FFT patterns of unannealed 3D-hexagonal films. Three different sample regions are shown in (A), (C), and (E), with corresponding FFT patterns in (B), (D), and (F), respectively.

5.3.4.2 Film composition.

The organic and inorganic components of the films were investigated by performing thermogravimetric (TG) analysis and IR spectroscopy on powder samples stripped from the films. TG analysis was carried out in air, ramping at a rate of 5 °C/min from room temperature to 800 °C. The data for films with wormlike, 2D-hexagonal, and 3D-hexagonal mesopores (Figure 5.8) showed that all volatile or combustible components were removed when the temperature reached 450 °C. These include P123 surfactant, TKMPP fluorophore, trapped solvents (water, THF, and ethanol), and water from condensation of the silica framework. The fraction of water from silica condensation is expected to be

relatively small, as the silica framework was pre-condensed, using hydrochloric acid as a catalyst. Films with wormlike mesopores showed a total weight loss of 74.3%, whereas the weight losses for 2D-hexagonal and 3D-hexagonal films were 53.6% and 43.3%, respectively. The order of these weight losses matched that of the ratios of P123 to TEOS in the film precursors, the highest ratio corresponding to the films with wormlike mesopores and the lowest ratio to the 3D-hexagonal films. The fluorophore concentrations in the films varied between 5.4×10^{-5} and 2.5×10^{-4} M, depending on the film type (Table 1). These concentrations were slightly smaller than the fluorophore concentrations calculated of the films containing only SiO_2, P123, and TKMPP as calculated on the basis of the concentrations of their precursors, the difference being due to the presence of solvent molecules in the films, such as H_2O, EtOH, and THF.

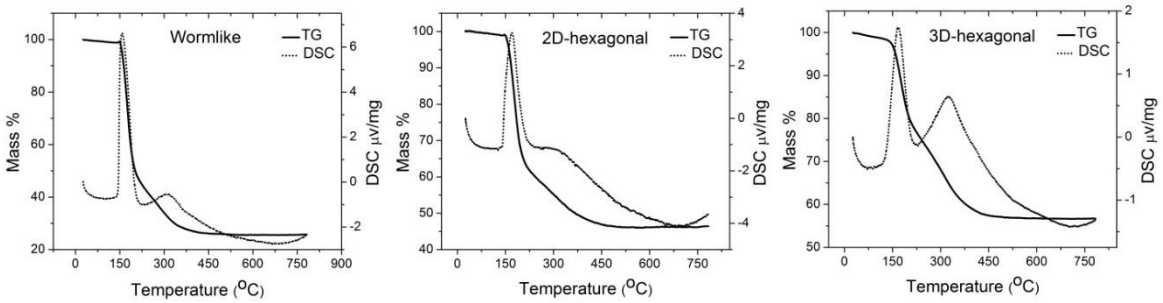

Figure 5.8 Thermogravimetric analysis and differential scanning calorimetry traces of films with wormlike, 2D-hexagonal, and 3D-hexagonal mesopores.

FTIR spectra of the films are shown in Figure 5.9. Because the amount of fluorophore in these samples was very small, all absorption peaks could be assigned to SiO_2 and P123 phases. The broad band from 3600 to 3372 cm^{-1} is due to O–H stretching vibrations (H-bonded), the sharp peak at 2972 cm^{-1} is assigned to the antisymmetric C–H stretch of CH_3 in P123, the group of peaks from 2933 to 2865 cm^{-1} to symmetric C–H stretches of CH_3 and CH_2 in P123, the band at 1637 cm^{-1} corresponds to the scissor bending vibration of molecular water, the peak at 1375 cm^{-1} to the CH_3 symmetric deformation, 1350 cm^{-1} CH_2 wag, 1079 cm^{-1} Si–O–Si stretch, 948 cm^{-1} Si–O stretch, 800 cm^{-1} Si–O bending, and 453 cm^{-1} the Si–O out of plane mode.

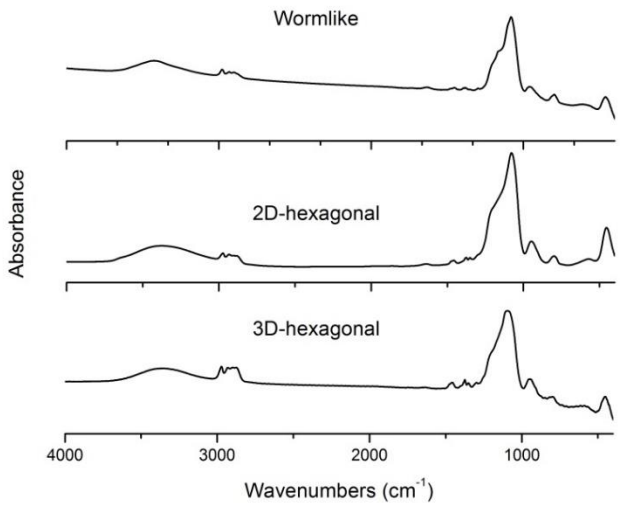

Figure 5.9 FTIR spectra of films with wormlike, 2D-hexagonal, and 3D-hexagonal mesopores.

5.3.4.3 Quenching studies of as-synthesized films.

The sensing performance of air-dried, as-synthesized films toward DNT in the gas phase was tested by fluorescence spectroscopy. The fluorescence spectra of TKMPP-doped, mesoporous silica thin films with wormlike structure showed a peak at 425 nm with a shoulder at 453 nm, and the peak position did not change, even after very long interaction time with DNT vapor (i.e., when the intensity of the emission peak become very low). This behavior persisted even after films had been stored for long periods of time. In fact, some films with wormlike mesopores, that were kept at room temperature and exposed to ambient light for three months, were able to perform as well as the freshly made films when interacting with DNT. The emission peak of the fluorophore in the solid material was blue-shifted by 7 nm compared to the peak in solution (the peak occurs at 432 nm in DCM solution), which can be attributed to the reduction of the rotational degree of freedom of the external rings as a result of steric interactions, leading to the requirement for more energy to rotate to the state at which the fluorophore can be excited.[37] The wormlike film showed excellent quenching properties toward DNT vapor, 39% during the first 45 s and 94% after 405 s (Figure 5.10A and Table 2), comparable to the performance of many CP-based sensors reported in the literature (Table 3; a more extensive table is provided in the Supporting Information, Table S1). The fast reaction can be ascribed to the interconnected

pore system, which facilitates the diffusion of DNT through the mesochannel system, and also to the role of the silica and surfactant phases in preventing self-quenching of the encapsulated fluorophore molecules. The high quenching efficiency is due to the strong binding of the fluorophore with DNT, which was further improved by the inclusion of P123 surfactant in the films. Interestingly, despite the presence of P123, the diffusion of DNT in the film is quite fast, as indicated by the fact that 80% of the fluorophore emission is quenched in the first 150 s.

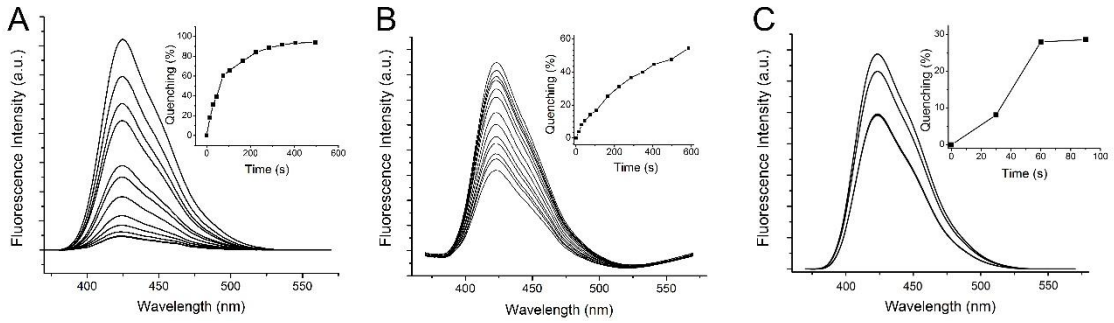

Figure 5.10 Fluorescence spectra and quenching graphs (insets) of silica films with (A) wormlike, (B) 2D-hexagonal, and (C) 3D-hexagonal mesopores, all containing TKMPP, upon contacting DNT vapor.

Table 5.2 Quenching efficiency of the mesostructured silica films.

	% reduction (in parentheses: quenching time/s)			
type of film	**wormlike**	**2D-hexagonal**	**3D-hexagonal[a]**	**cubic[a]**
as-synthesized, TKMPP-doped, containing P123	18 (15) 39 (45) 94 (405)	4 (15) 9 (45) 52 (405)	28 (90)	NA
annealed, TKMPP-doped, containing P123	40 (15) 68 (45) 95 (405)	20 (15) 38 (45) 80 (405)	<4 (30) 30 (200) 60 (580)	NA
TKMPP-impregnated	49 (60) 63 (180)	55 (75) 55 (180)	16 (75) 27 (225)	NA
TKSPP-bridged, containing P123	8.5 (30) 46 (150)	3 (30) 6 (90)	NA	2 (30) 4 (90)
TKSPP-bridged, surfactant removed	43 (5) 72 (30) 94 (120)	3 (5) 14 (30) 46 (120)	NA	0 (5) 1 (30) 2 (600)

[a] NA = not applicable as the film does not have that structure

Table 5.3. Comparison of quenching efficiencies of representative nitroaromatic sensors.

fluorophore	**sensor form**	**quenching efficiency/% (in parentheses: quenching time/s)**	**quencher**	**reference**
tetrakis(4-methoxyphenyl)porphyrin	nanofibrous film	38 (2400)	DNT	[44]
9,10-bis[trimethylsilylethynyl]anthracene	drop-cast film	18 (300); 40 (420)	4-nitrotoluene	[45]
thiophene-based polymer (P3TzdHT2)	30 nm polymer film	89 (300)	DNT	[46]
9,10-bis(1,3-dicarboxyphenyl-5-ethynyl)anthracene	thin film	77 (35); 96 (110)	nitrobenzene	[47]
phenothiazine-based oligomers	spin-cast film (30 nm)	60 (300); 76 (600)	DNT	[48]
		32 (300); 47 (600)	TNT	
stilbene-functionalized (S)-binaphthyl	self-assembled film	72 (600)	TNT	[49]
		91 (600)	DNT	
π-conjugated phenylene–ethynylene diimine	thin film	40 (600)	TNT	[2]
		82 (600)	DNT	
conjugated polymer (CP)-coated on optic fiber tip	thin film	48 (25); 60 (35)	DNT	[13]
CP	fibrous film	40 (600); 70 (3600)	DNT	[3]
oligo(diphenylsilane)	self-assembled monolayer	55 (10); 82 (30); 91 (100)	TNT	[4]

Table 5.3. Continued

fluorophore	sensor form	quenching efficiency/% (in parentheses: quenching time/s)	quencher	reference
C1609 dye-bridged 3DOM SiO_2	3DOM film	10 (600)	TNT	[50]
		36 (600)	DNT	
CP-based on 1,2-diiminocyclohexane unit	spin-cast film	80 (900)	DNT	[51]
poly(1-pyrenylmethylmaleimide-*alt*-1-alkene)	drop-cast film	80 (159)	3,5-dinitrobenzonitrile	[52]
porphyrin-doped bimodal porous silica film	thin film	50 (10); 97 (120)	TNT	[53]
oligopyrene	thin film	50 (10); 75 (30)	TNT	[17]
polycyclic aromatics	self-assembled monolayer	22 (60); 80 (600)	TNT	[54]
porphyrin-bridged mesoporous silica	thin film	27 (10); 65 (1200)	TNT	[28]
alkoxycarbonyl-substituted, carbazole-cornered, arylene-ethynylene tetracycle	spin-cast film	83 (60)	TNT	[55]
		90 (60)	DNT	
cadmium porphyrin-doped mesoporous silica	spin-cast film	56 (10)	TNT	[56]
poly(iptycenebutadiynylene)	spin-cast film	75 (30)	DNT	[57]
polystyrene functionalized with *N*-substituted-4-amino-1,8-naphthalimide	spin-cast film	45 (60); 82 (600)	DNT	[58]
poly[1-phenyl-2-(4-trimethylsilylphenyl)ethyne	spin-cast film (7 nm)	37 (60); 90 (1200)	DNT	[59]
pentiptycene-containing CP	2.5 nm film	50 (30); 75 (60)	TNT	[6]

The fluorescence spectrum of TKMPP-doped 2D-hexagonal and 3D-hexagonal mesoporous silica thin films also showed a peak at 424 nm, blue shifted by 8 nm compared to the emission of TKMPP in DCM solution. The quenching performance of these films was not as good as that of the films with wormlike mesopores (Table 2). The poorer performance of 2D-hexagonal films is attributed to the long channels that lie parallel to the substrate, slowing down the diffusion of DNT through the film. The weaker response of films with of 3D-hexagonal mesopores may be an indication of limited interconnectivity between pores and may also be due to the greater film thickness (571 nm). With only 28% of quenching after 90 s, it appears that only fluorophores on the surface and close to the surface of the 3D-hexagonal film were able to interact with the analytes.

A film with wormlike mesopores (with better performance than films with 2D- and 3D-hexagonal mesopores) was selected to investigate the effects of thickness on quenching performance. The thickness of the film was controlled by the numbers of coatings on the substrate. SEM was used to investigate the morphology and to estimate the thicknesses of these films. It is interesting that the thicknesses the films do not linearly increase with the number of coatings. The reason is the first layer containing surfactant and TEOS has higher affinity to the precursor than the bare quartz substrate, which results in thicker films for the following coating. All films feature rugged surfaces, which benefit diffusion of analyte molecules into the film. Therefore the quenching rates of these films depend mostly on their thicknesses. The study showed that an eight-fold increase in thickness only caused a slight decrease in the quenching rate (Figure 5.11)

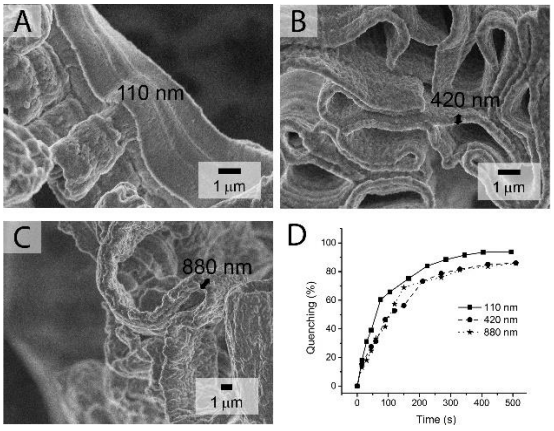

Figure 5.11 (A), (B), and (C) are SEM images of films with wormlike mesopores of different thicknesses; (D) quenching plot those films.

It is interesting to note that films prepared without the silica source (TEOS) but under otherwise identical conditions as those used for the films with wormlike, 2D-hexagonal, or 3D-hexagonal mesopores also exhibited rapid quenching responses to DNT vapor (Figure 5.12). In these films, the P123 surfactant also prevents aggregation of TKMPP fluorophores while maintaining access to DNT molecules. However, the response of the silica-free films was not as stable and reproducible as that of the mesostructured films with silica, and their mechanical robustness was also much lower.

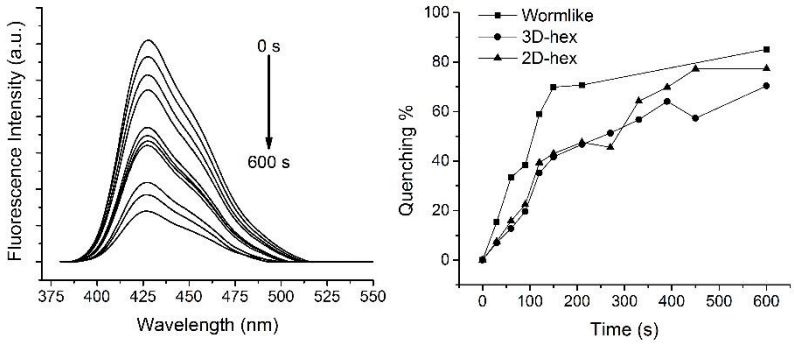

Figure 5.12 (Left) Fluorescence spectra of a control film exposed to DNT vapor. The control film was prepared using the procedure for 2D-hexagonal films but leaving out the silica source. (Right) Quenching plots for control films exposed to DNT vapor. These films were prepared using the procedures for films with wormlike, 2D-hexagonal, and 3D-hexagonal mesopores but leaving out the silica source.

To examine the effects of interferents on fluorescence quenching, the TKMPP-doped films were exposed to vapors of benzene, toluene, apple juice, ethanol, and perfume. None of these interferents affected the fluorescence intensity by more than 10% within 120 s of exposure time (Figure 5.13).

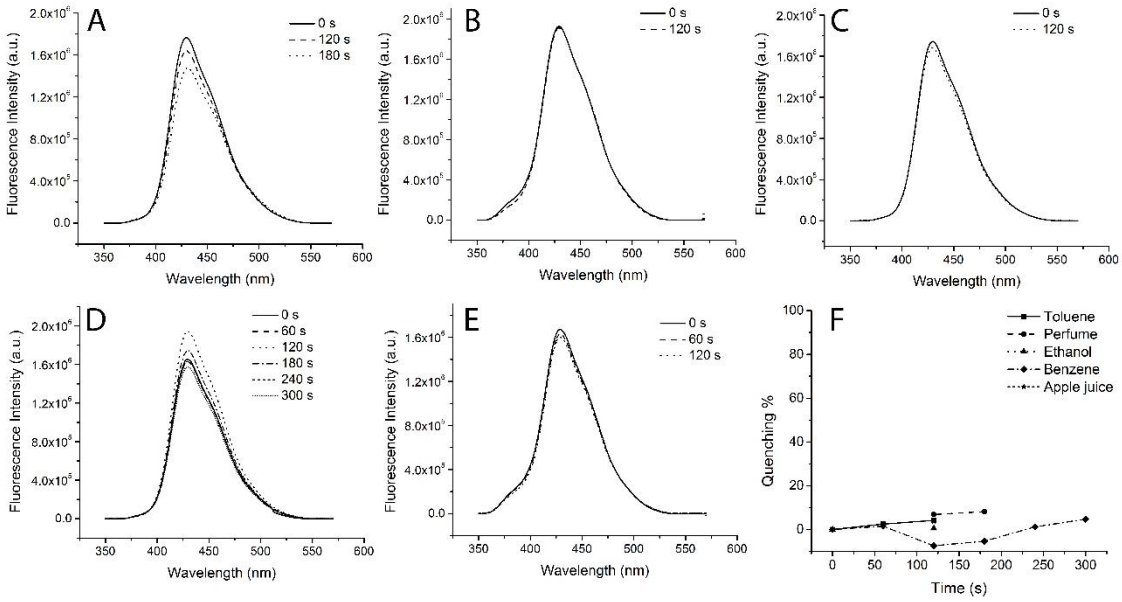

Figure 5.13 Fluorescence spectra of TKMPP-doped films (as synthesized) with wormlike mesopore structure upon exposure to (A) perfume, (B) ethanol, (C) apple juice, (D) benzene, and (E) toluene vapors. All these interferents caused less than 10% fluorescence intensity changes over 120 s of exposure.

5.3.5 Annealed films.

Films with wormlike, 2D-hexagonal, and 3D-hexagonal mesostructures were subsequently annealed (100 ˚C, 24 h, in air) to (a) strengthen the silica framework to stabilize the film sensor for long storage times and work at high humidity, and (b) remove solvent trapped inside the film and the micelles, leaving more space for DNT to diffuse through.

TG traces of the annealed films, shown in Figure 5.14, reveal weight losses of 69% for films with wormlike mesopores, 35% for 2D-hexagonal, and 32% for 3D-hexagonal films when 600 ˚C was reached. Compared to unannealed films, the organic content of heat-treated films is about 13% less for 2D-hexagonal and 3D-hexagonal films, and only 5% less for films with wormlike mesopores. These differences are attributed to the loss of trapped solvents during the heat treatment step. Because 3D-hexagonal films performed poorly, as discussed in the previous section, they were not investigated further.

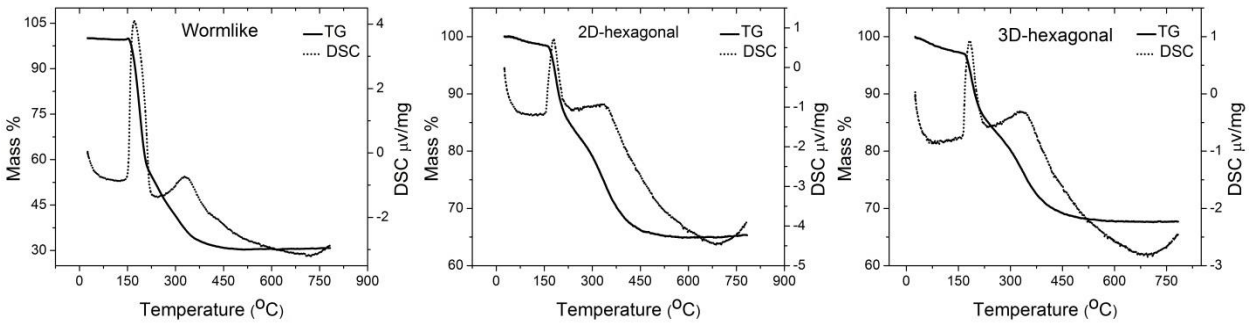

Figure 5.14 Thermogravimetric analysis and differential scanning calorimetry traces of annealed films with wormlike, 2D-hexagonal, and 3D-hexagonal mesopores.

TEM images of the annealed, wormlike and 2D-hexagonal films show the same mesostructure as the films before treatment (Figure 5.15), which indicates that treatment did not cause the collapse of the silica framework, and the films stayed intact.

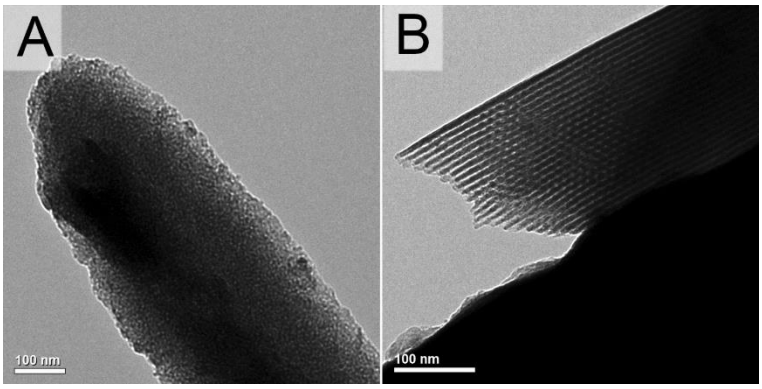

Figure 10Figure 5.15. TEM images of films with (A) wormlike and (B) 2D-hexagonal mesopores after annealing at 100 °C for 24 h.

Fluorescence spectra of the annealed films showed similar features with an emission peak at 425 nm for the films with wormlike mesopores and at 424 nm for the 2D-hexagonal films. However, the initial intensity of emission from both films decreased significantly after the heat treatment (by 29% for films with wormlike mesopores and by 82% for 2D-hexagonal films). Although the absolute intensity may vary from film to film due to an uneven distribution of fluorophore molecules over the films, the phenomenon of decreasing fluorescence intensity was observed for more than 10 samples and was ascribed to the

change of the environment around fluorophore after heat treatment. It is possible that during annealing, micelles were melted and captured some TKMPP molecules on the surfaces. When cooled to room temperature, the micelles changed back to the gel form, increasing the steric hindrance experienced by the encapsulated luminescent molecules. An intensity decrease due to loss of fluorophore molecules by evaporation or oxidation is less likely, considering that the melting point of TKMPP is about 260 °C.[37] To check the hypothesis of quenching due to shrinking micelles, we investigated the excitation of the fluorophore both in DCM solution (λ_{em} = 432 nm) and in thin films (λ_{em} = 425 nm). Figure 5.16 shows the excitation spectra of TKMPP in solution and in as-synthesized and heat-treated films with wormlike mesopores. Excitation peaks occur at 267 and 306 nm in solution and are shifted to 245 and 304 nm, respectively, in the thin films. These blue-shifts are attributed to the decreased freedom of the fluorophore in the film compared to the solution. In addition, the intensity ratio of the first peak to the second peak (λ_{ex} = 267 nm to λ_{ex} = 306 nm for the solution and λ_{ex} = 245 nm to λ_{ex} = 304 nm for the thin film) changes significantly. In solution, the fluorophores enjoy more freedom and can be excited at longer wavelengths, whereas in the solid state, a large fraction of fluorophores can only be excited at shorter wavelengths. When these films are annealed, the fraction of the fluorophore excited at shorter wavelengths increases significantly (Figure 5.16), which indicates further loss of freedom for fluorophores. Changes in the ratios of the peaks at 245 and at 304 nm were also observed for 2D- and 3D-hexagonal films (Figure 5.17).

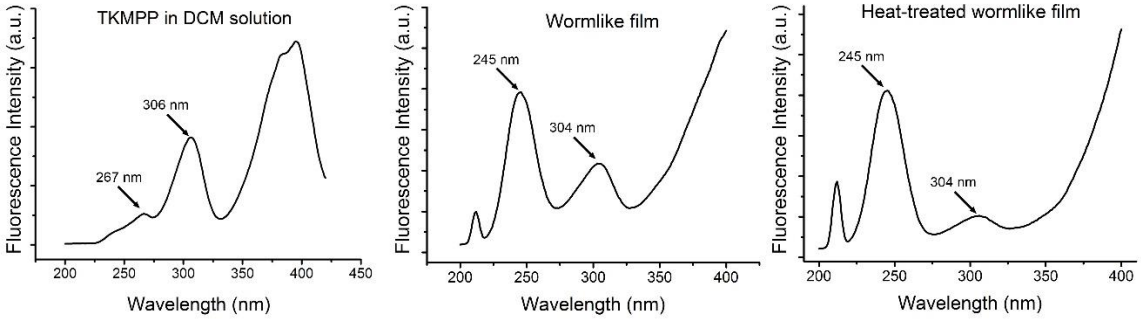

Figure 5.16 Excitation scans of TKMPP in DCM solution (λem = 432 nm), of as-synthesized (λem = 425 nm), and annealed (λem = 425 nm) films with wormlike mesopores. After heat treatment, the intensity ratios between the first and the second peak of the the wormlike films changed.

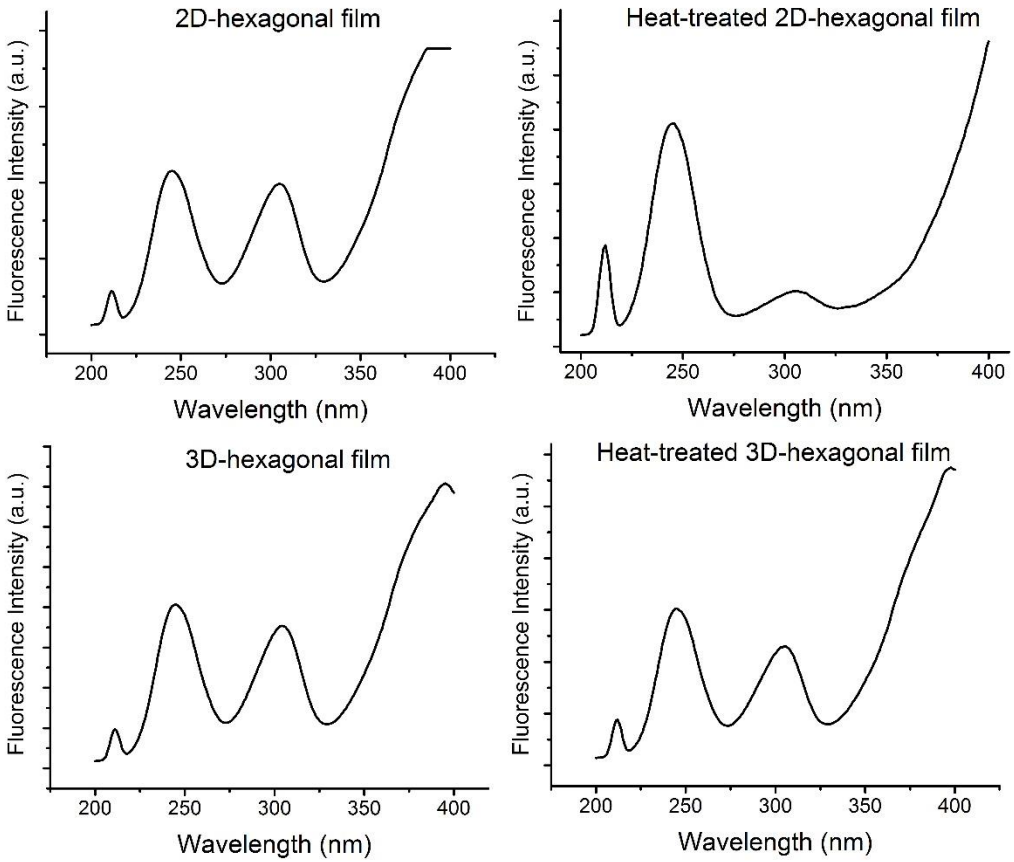

Figure 5.17 Excitation scans of TKMPP in 2D- and 3D-hexagonal films (λem = 425 nm), and heat-treated 2D- and 3D-hexagonal films (λem = 425 nm). After heat treatment, the intensity ratios between the first and the second peak of these films change.

Another interesting observation is that the fluorescence of annealed films was quenched much faster compared to as-synthesized films (Figure 5.18). For films with wormlike mesopores, it only took 15 s for 40% quenching, while the corresponding time for the as-synthesized films was 45 s (Table 5.2). The performance of the 2D-hexagonal films was also better after heat treatment. The improvements in the quenching performance may be attributed to the decrease in initial intensity (perhaps due to oxygen quenching), which means fewer fluorophore molecules needed to be quenched, while the number of DNT molecules in the vapor phase was the same for the two experiments.

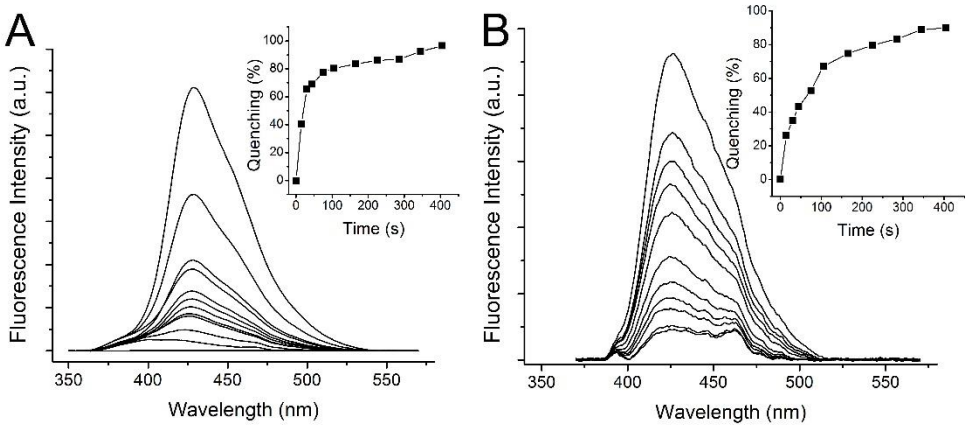

Figure 5.18 Fluorescence spectra and quenching graph (inset) of (A) TKMPP-doped films with wormlike mesopores; (B) TKMPP-doped 2D-hexagonal films upon exposure to DNT vapor. Both films had been heated at 100 °C for 24 h.

5.3.6 TKMPP-impregnated, surfactant-free mesoporous silica films.

To determine the influence of the surfactant on the sensor response, surfactant-free films were prepared. In one method, P123 surfactant was removed from the mesoporous silica thin films by calcination at 550 °C for 6 h in air. The calcined films were then immersed in a TKMPP solution in DCM to load the mesoporous silica with the fluorophore. FTIR spectra of all calcined films showed similar features and did not contain any peaks from surfactants or solvents; only peaks from the silica phase were present (Figure 5.19).

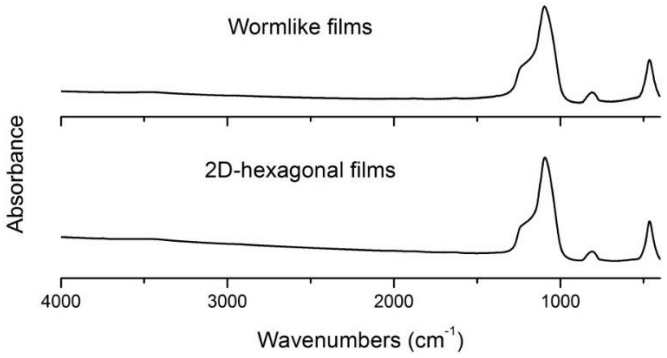

Figure 5.19 FTIR spectra of calcined films with wormlike and 2D-hexagonal mesopores showed only peaks attributable to a silica phase.

The morphologies of the calcined films were investigated by TEM (Figure 5.20). After calcination, films with wormlike mesopores still maintained their structure, whereas the long channels featured in 2D-hexagonal films and the order of 3D-hexagonal films almost disappeared.

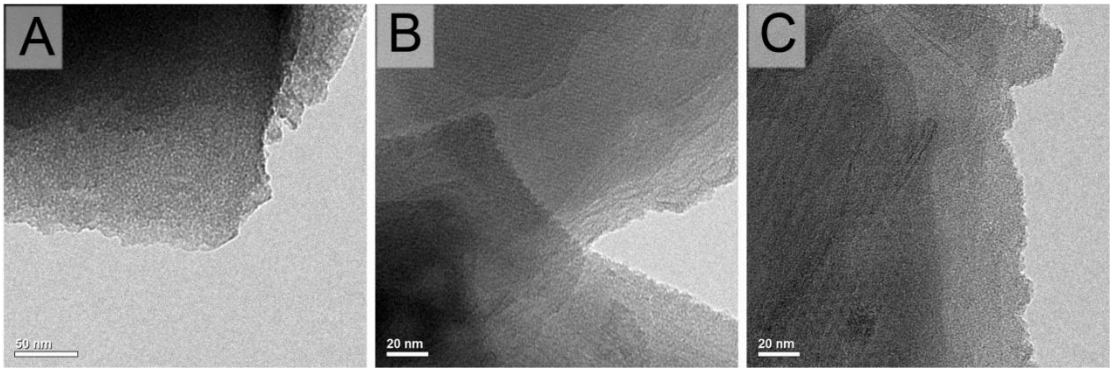

Figure 5.20 TEM images of films calcined at 550 °C for 6 h in air with (A) wormlike, (B) 2D-hexagonal, and (C) 3D-hexagonal mesopores.

The quenching performance of the impregnated films toward DNT is shown in Figure 5.21. The emission peak of the wormlike film is much broader than the corresponding peaks for the 2D- and 3D-hexagonal films, indicating a higher level of excimer formation. The formation of excimers in the impregnated films is unavoidable, particularly on external surfaces, where the fluorophores are not separated by silica walls. All films showed slow quenching rates and low quenching efficiencies with less than 65% of fluorophore being quenched after 180 s exposure to a DNT atmosphere. The quenching behavior of 2D- and 3D-hexagonal impregnated films was similar, although the 2D-hexagonal films showed a little faster and more efficient quenching. Only 27% of the fluorophore emission in the 3D-hexagonal films was quenched after 225 s, while the value for 2D-hexagonal films was 55% after 75 s (Figure 5.21). All films approached 80% of quenching after being left overnight in a vial containing DNT. The quenching rates of these films were much slower than those of the surfactant-containing films with wormlike mesopores described in the previous sections.

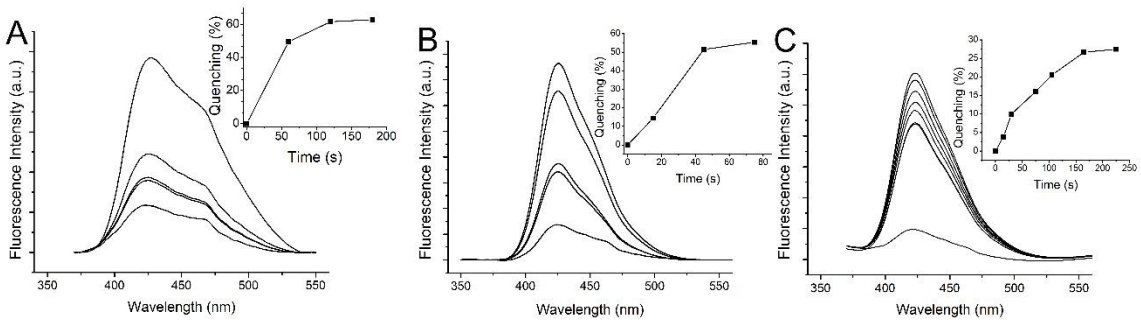

Figure 5.21 Fluorescence spectra and quenching graph (inset) of TKMPP-doped (A) wormlike film, (B) 2D-hexagonal films, and (C) 3D-hexagonal films upon exposure to DNT vapor after surfactant removal.

5.3.7 TKSPP-bridged mesoporous silica films.

In a second method to prepare surfactant-free films, TKSPP was used as silica precursor together with TEOS to prepare mesostructured films ("TKSPP-bridged films"). Surfactant was then etched out by hot ethanol extraction at 60 °C for 24 h. Although the recipes used for the preparation of TKSPP-bridged mesoporous silica films were the same as for the TKMPP-doped films, the obtained structures were quite different. After surfactant extraction in hot ethanol, the targeted wormlike film also showed random pores, but less contrast was observed between silica phase and pore space, and the pore sizes were smaller (Figure 5.22), which may slow down the diffusion of DNT molecules in these samples. The targeted 2D-hexagonal films were successfully synthesized. All samples featured long, parallel channel arrays. In contrast, the synthesis targeting TKSPP-bridged 3D-hexagonal films did not produce hexagonal symmetry but films with cubic pore symmetry instead. It is interesting that such a small content of TKSPP (10-6 M) compared to TEOS (1.24 M) in the precursor changed the mesostructure of the obtained films.

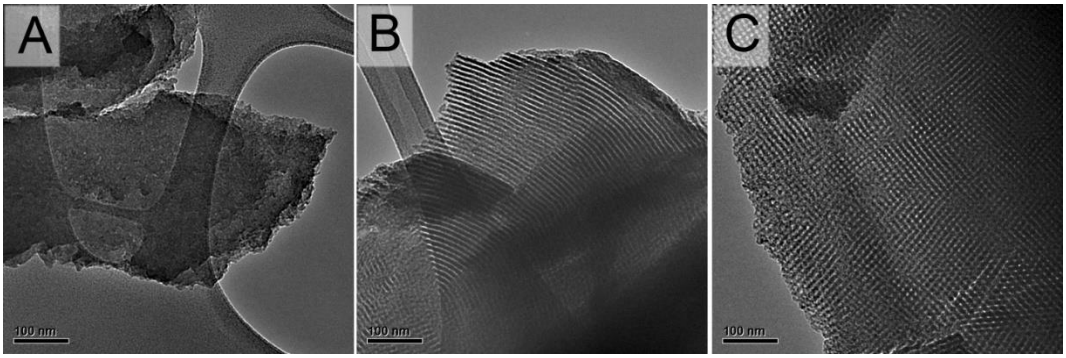

Figure 5.22 TEM images of TKSPP-bridged (A) wormlike; (B) 2D-hexagonal; (C) cubic mesoporous silica films after extraction of the surfactant.

Before surfactant removal, all TKSPP-bridged films showed a relatively poor performance (Figure 5.23). The quenching performance of surfactant-free TKSPP-bridged cubic mesoporous silica films was also very poor, with less than 2% of the fluorophore quenched after 120 s exposure. This suggests that the pores (< 6.1±0.5 nm as estimated from TEM images), which were surrounded by relatively thick walls, were not well interconnected in this material.

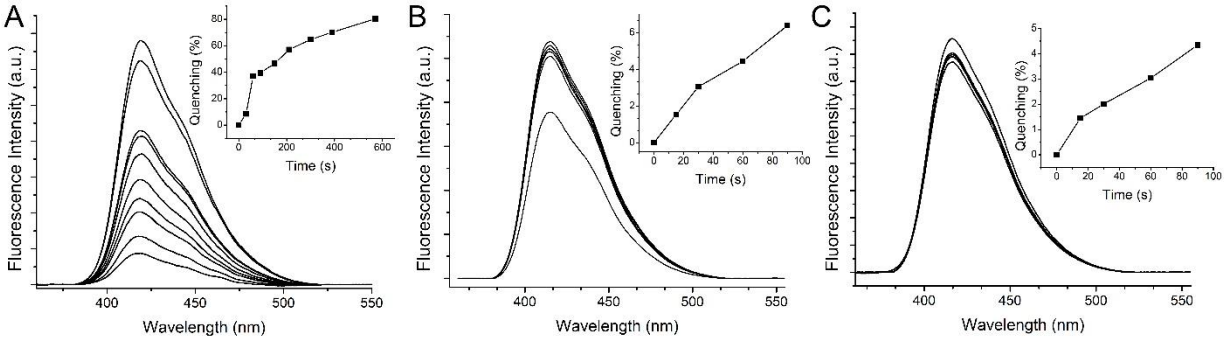

Figure 5.23 Fluorescence spectra and quenching graphs (insets) of surfactant-containing, TKSPP-bridged films with (A) wormlike, (B) 2D-hexagonal, and (C) cubic mesostructure, upon exposure to DNT vapor.

However, surfactant-free films with 2D-hexagonal or wormlike mesopores exhibited very fast quenching rates toward DNT (Figure 5.24). TKSPP-bridged 2D-hexagonal mesoporous silica films (40% quenching after 90 s and 78% quenching after 660 s of exposure) and films with wormlike pores (43% quenching in the first 5 s exposure to DNT

atmosphere, 88% after 60 s, and 99% after overnight exposure) showed even better quenching rates and quenching efficiencies than their TKMPP-doped analogs (Table 2). The high rate performance of the surfactant-free films is attributed to the faster diffusion of DNT molecules inside these films. By comparison with published data summarized in Tables 3 and S1, TKSPP-bridged mesoporous silica thin films with wormlike mesopores are among the fastest and most effective sensors for DNT, even faster than some CPs and comparable to other porphyrin-doped mesoporous silica thin films.

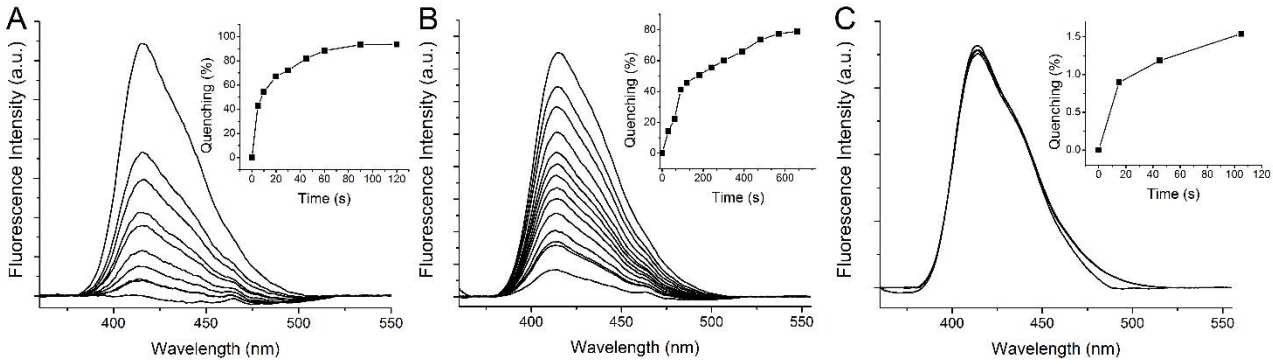

Figure 5.24 Fluorescence spectra and quenching graph (inset) of TKSPP-bridged (A) wormlike film; (B) 2D-hexagonal film; (C) cubic film upon exposure to DNT vapor after surfactant removal.

5.4 Conclusions

We have described the preparation of 1,3,6,8-phenyl substituted pyrene compounds and of various films including TKMPP doped- and TKSPP-bridged mesoporous silica thin films. The fluorophore and fluorophore-containing films were tested as sensors for DNT on the basis of fluorescence quenching rates and efficiencies. In solution, TKMPP showed good interactions with DNT with a large quenching constant (K_s = 2195 M^{-1}), indicating that it is an efficient sensing compound for DNT and possibly other NACs. The sensing performance of the films toward DNT in the gas phase was found to depend on both film structure and film composition. Surfactant-free, TKSPP-bridged films with wormlike mesopores showed the best performance, comparable to the most advanced fluorescence sensors based on conjugated polymers. Surfactant-containing, TKMPP-doped mesoporous silica films were also effectively and quickly quenched by DNT with detection limits on

the order of 10^{-8} M or better. These films can be prepared in a simple, one-pot synthesis, which is an advantage over the multi-step preparation of TKSPP-bridged films. For a set of films (i.e., surfactant-containing or surfactant-free) with various mesopore architectures, the wormlike structure gave the best performance, whereas 2D-hexagonal mesostructures with long diffusion channels usually showed poorer performance. All films exhibited long-term storage stability and good resistance to photobleaching by ambient light, facilitated by the protection provided by the silica framework. We believe that owing to their easy, fast, and cheap syntheses, the sensing films are good candidates for incorporation in portable sensing devices. The high quenching efficiency and stability of the films offer potentially useful chemosensory materials for rapid detection of explosives.

5.5 References

(1) Lotufo, G. R.; Farrar, J. D.; Inouye, L. S.; Bridges, T. S.; Ringelberg, D. B. *Environ. Toxicol. Chem.* **2001**, *20*, 1762.

(2) Caron, T.; Guillemot, M.; Montméat, P.; Veignal, F.; Perraut, F.; Prené, P.; Serein-Spirau, F. *Talanta* **2010**, *81*, 543.

(3) Long, Y.; Chen, H.; Yang, Y.; Wang, H.; Yang, Y.; Li, N.; Li, K.; Pei, J.; Liu, F. *Macromolecules* **2009**, *42*, 6501.

(4) He, G.; Zhang, G.; Lü, F.; Fang, Y. *Chem. Mater.* **2009**, *21*, 1494.

(5) Díaz Aguilar, A.; Forzani, E. S.; Leright, M.; Tsow, F.; Cagan, A.; Iglesias, R. A.; Nagahara, L. A.; Amlani, I.; Tsui, R.; Tao, N. J. *Nano Lett.* **2009**, *10*, 380.

(6) Yang, J.-S.; Swager, T. M. *J. Am. Chem. Soc.* **1998**, *120*, 5321.

(7) Goldman, E. R.; Medintz, I. L.; Whitley, J. L.; Hayhurst, A.; Clapp, A. R.; Uyeda, H. T.; Deschamps, J. R.; Lassman, M. E.; Mattoussi, H. *J. Am. Chem. Soc.* **2005**, *127*, 6744.

(8) Ewing, R. G.; Atkinson, D. A.; Eiceman, G. A.; Ewing, G. J. *Talanta* **2001**, *54*, 515.

(9) Yinon, J. *Forensic and environmental detection of explosives*; John Wiley & Sons Chichester, 1999.

(10) Fierke, M. A.; Olson, E. J.; Bühlmann, P.; Stein, A. *ACS. Appl. Mater. Interfaces* **2012**, *4*, 4731.

(11) Sylvia, J. M.; Janni, J. A.; Klein, J. D.; Spencer, K. M. *Anal. Chem.* **2000**, *72*, 5834.

(12) Krausa, M.; Reznev, A. A.; North Atlantic Treaty Organization. Scientific Affairs Division. *Vapour and trace detection of explosives for anti-terrorism purposes*; Kluwer Academic: Dordrecht ; London, 2004.

(13) Nguyen, H. H.; Li, X.; Wang, N.; Wang, Z. Y.; Ma, J.; Bock, W. J.; Ma, D. *Macromolecules* **2009**, *42*, 921.

(14) Li, Z.; Dong, Y. Q.; Lam, J. W. Y.; Sun, J.; Qin, A.; Häußler, M.; Dong, Y. P.; Sung, H. H. Y.; Williams, I. D.; Kwok, H. S.; Tang, B. Z. *Adv. Funct. Mater.* **2009**, *19*, 905.

(15) Zhu, D.; He, Q.; Cao, H.; Cheng, J.; Feng, S.; Xu, Y.; Lin, T. *Appl. Phys. Lett.* **2008**, *93*, 261909.

(16) Narayanan, A.; Varnavski, O. P.; Swager, T. M.; Goodson, T. *J. Phys. Chem. C* **2008**, *112*, 881.

(17) Bai, H.; Li, C.; Shi, G. *Sens. Actuators B Chem.* **2008**, *130*, 777.

(18) Zhou, Q.; Swager, T. M. *J. Am. Chem. Soc.* **1995**, *117*, 7017.

(19) Yamaguchi, S.; Swager, T. M. *J. Am. Chem. Soc.* **2001**, *123*, 12087.

(20) Sohn, H.; Calhoun, R. M.; Sailor, M. J.; Trogler, W. C. *Angew. Chem. Int. Ed.* **2001**, *40*, 2104.

(21) Sohn, H.; Sailor, M. J.; Magde, D.; Trogler, W. C. *J. Am. Chem. Soc.* **2003**, *125*, 3821.

(22) Sanchez, J. C.; DiPasquale, A. G.; Rheingold, A. L.; Trogler, W. C. *Chem. Mater.* **2007**, *19*, 6459.

(23) Wang, Z.; Wang, Z. Y.; Ma, J.; Bock, W. J.; Ma, D. *Polymer* **2010**, *51*, 842.

(24) Angelos, S.; Johansson, E.; Stoddart, J. F.; Zink, J. I. *Adv. Funct. Mater.* **2007**, *17*, 2261.

(25) Hunks, W. J.; Ozin, G. A. *J. Mater. Chem.* **2005**, *15*, 3716.

(26) Germain, M. E.; Knapp, M. J. *Chem. Soc. Rev.* **2009**, *38*, 2543.

(27) Johnson-White, B.; Zeinali, M.; Shaffer, K. M.; Patterson, C. H.; Charles, P. T.; Markowitz, M. A. *Biosens. Bioelectron.* **2007**, *22*, 1154.

(28) Tao, S.; Li, G. *Colloid. Polym. Sci.* **2007**, *285*, 721.

(29) Gao, D.; Wang, Z.; Liu, B.; Ni, L.; Wu, M.; Zhang, Z. *Anal. Chem.* **2008**, *80*, 8545.

(30) Feng, J.; Li, Y.; Yang, M. *Sens. Actuators B Chem.* **2010**, *145*, 438.

(31) Liu, F.; Zhang, L.-J.; Xiao, J.-H.; Hu, J.; Liu, H.-L. *Front. Mater. Sci. China* **2010**, *4*, 158.

(32) Balkus Jr, K. J.; Pisklak, T. J.; Hundt, G.; Sibert, J.; Zhang, Y. *Microporous Mesoporous Mater.* **2008**, *112*, 1.

(33) Chen, L.; McBranch, D.; Wang, R.; Whitten, D. *Chem. Phys. Lett.* **2000**, *330*, 27.

(34) Stevens, N.; Akins, D. L. *Sens. Actuators B Chem.* **2007**, *123*, 59.

(35) Vu, A.; Phillips, J.; Buhlmann, P.; Stein, A. *Chem. Mater.* **2013**.

(36) Hu, J.-y.; Era, M.; Elsegood, M. R. J.; Yamato, T. *Eur. J. Org. Chem.* **2010**, *2010*, 72.

(37) de Halleux, V.; Calbert, J.-P.; Brocorens, P.; Cornil, J.; Declercq, J.-P.; Brédas, J.-L.; Geerts, Y. *Adv. Funct. Mater.* **2004**, *14*, 649.

(38) Vollmann, H.; Becker, H.; Corell, M.; Streeck, H. *Justus Liebig's Annalen der Chemie* **1937**, *531*, 1.

(39) Mizoshita, N.; Goto, Y.; Maegawa, Y.; Tani, T.; Inagaki, S. *Chem. Mater.* **2010**, *22*, 2548.

(40) Hernandez, R.; Franville, A.-C.; Minoofar, P.; Dunn, B.; Zink, J. I. *J. Am. Chem. Soc.* **2001**, *123*, 1248.

(41) Minoofar, P. N.; Hernandez, R.; Chia, S.; Dunn, B.; Zink, J. I.; Franville, A.-C. *J. Am. Chem. Soc.* **2002**, *124*, 14388.

(42) Yamaguchi, A.; Amino, Y.; Shima, K.; Suzuki, S.; Yamashita, T.; Teramae, N. *J. Phys. Chem. B* **2006**, *110*, 3910.

(43) Wark, M.; Ganschow, M.; Rohlfing, Y.; Schulz-Ekloff, G.; Woehrle, D. *Stud. Surf. Sci. Catal.* **2001**, *135*, 3292.

(44) Yang, Y.; Wang, H.; Su, K.; Long, Y.; Peng, Z.; Li, N.; Liu, F. *J. Mater. Chem.* **2011**, *21*, 11895.

(45) Shanmugaraju, S.; Joshi, S. A.; Mukherjee, P. S. *J. Mater. Chem.* **2011**, *21*, 9130.

(46) Nagarjuna, G.; Kumar, A.; Kokil, A.; Jadhav, K. G.; Yurt, S.; Kumar, J.; Venkataraman, D. *J. Mater. Chem.* **2011**, *21*, 16597.

(47) Gole, B.; Shanmugaraju, S.; Bar Arun, K.; Mukherjee Partha, S. *Chem. Commun.* **2011**, *47*, 10046.

(48) Zhang, X.; Qiu, X.; Lu, R.; Zhou, H.; Xue, P.; Liu, X. *Talanta* **2010**, *82*, 1943.

(49) Vijayakumar, C.; Tobin, G.; Schmitt, W.; Kim, M.-J.; Takeuchi, M. *Chem. Commun.* **2010**, *46*, 874.

(50) Fang, Q.; Geng, J.; Liu, B.; Gao, D.; Li, F.; Wang, Z.; Guan, G.; Zhang, Z. *Chem. Eur. J.* **2009**, *15*, 11507.

(51) Clavaguera, S.; Dautel, O. J.; Hairault, L.; Methivier, C.; Montmeat, P.; Pasquinet, E.; Pradier, C.-M.; Serein-Spirau, F.; Wakim, S.; Veignal, F.; Moreau, J. J. E.; Lere-Porte, J.-P. *J. Polym. Sci., Part A Polym. Chem.* **2009**, *47*, 4141.

(52) Burattini, S.; Colquhoun, H. M.; Greenland, B. W.; Hayes, W.; Wade, M. *Macromol. Rapid Commun.* **2009**, *30*, 459.

(53) Tao, S.; Yin, J.; Li, G. *J. Mater. Chem.* **2008**, *18*, 4872.

(54) Zhang, S.; Lue, F.; Gao, L.; Ding, L.; Fang, Y. *Langmuir* **2007**, *23*, 1584.

(55) Naddo, T.; Che, Y.; Zhang, W.; Balakrishnan, K.; Yang, X.; Yen, M.; Zhao, J.; Moore, J. S.; Zang, L. *J. Am. Chem. Soc.* **2007**, *129*, 6978.

(56) Tao, S.; Li, G.; Zhu, H. *J. Mater. Chem.* **2006**, *16*, 4521.

(57) Zhao, D.; Swager, T. M. *Macromolecules* **2005**, *38*, 9377.

(58) Le Barny, P. L.; Obert, E. T.; Soyer, F.; Malval, J. P.; Leray, I.; Lemaitre, N.; Pansu, R.; Simic, V.; Doyle, H.; Redmond, G.; Loiseaux, B. *Proc. SPIE-Int. Soc. Opt. Eng.* **2005**, *5990*, 59900S/1.

(59) Liu, Y.; Mills, R. C.; Boncella, J. M.; Schanze, K. S. *Langmuir* **2001**, *17*, 7452.

CHAPTER 6

Summary and Outlook

Outline

6.1 Summary of The Thesis Results

6.2 Outlook

6.1 Summary of Thesis Results

This thesis has demonstrated the successful design, fabrication, and testing of nanostructured and nanoporous materials for energy storage and sensing applications.

In chapter 2, monolithic, three-dimensionally ordered macroporous and mesoporous (3DOM/m) $LiFePO_4$/C composites were synthesized by a multiconstituent, dual templating method. In which, F127 surfactant was used as template for the mesopores and PMMA colloidal crystal was used as template for the macropores. The ordered porous structure was obtained by controlling the crystallization of $LiFePO_4$ by applying a multiple steps heating procedure, which minimized the collapse of the macroporous framework upon the removal of the surfactant and the colloidal crystal templates. Monolithic composite pieces of $LiFePO_4$ dispersed in a carbon phase around an interconnected network of ordered macropores were obtained. The composite walls themselves contained micropores or small mesopores. The carbon phase enhanced the electrical conductivity of the cathode and maintained $LiFePO_4$ as a highly dispersed phase during the synthesis and during electrochemical cycling. The obtained $LiFePO_4$/C composites showed high capacity and good rate performance, which are potential to applications such as power sources for EVs and HEVs.

In chapter 3, spherical $Li_3Fe_2(PO_4)_3$ particles and $LiFePO_4$ spheres embedded in carbon matrix were prepared and tested as high volumetric energy density electrode materials for LIBs. Spherical $Li_3Fe_2(PO_4)_3$ particles were fabricated by calcining $LiFePO_4$/C

composites, which were prepared in chapter 2, in the air at different temperatures. The $LiFePO_4$ spheres embedded in carbon matrix was prepared by coating LFP-carbon precursor onto quartz substrates then applying a series of heat treatments. Both electrode materials showed high volumetric energy density capacity since uniform spherical particles can be packed with higher efficiency than randomly shaped particles.

In chapter 4, Three-dimensionally ordered mesoporous (3DOm) carbons with well-defined geometry, three-dimensionally interconnected pore structure, and tunable pore size in the range from 8 to 40 nm were fabricated using colloidal crystal templating method. To achieve precise control over the pore sizes in the carbon products, parameters were established for direct syntheses or seed growth of monodisperse silica nanospheres with specific sizes, using L-lysine-assisted hydrolysis of silicon alkoxide precursors. Porous carbons were then templated from these materials using phenol–formaldehyde (PF) or resorcinol–formaldehyde (RF) precursors. These carbon electrodes can simultaneously provide high energy densities and high power densities in EDLCs using the ionic liquid EMI-TFSI with wide operative potential window as an electrolyte. The optimal pore sizes (21-29 nm) were identified that provided a large interface between the electrode and the electrolyte while maintaining good ion transport through the relatively viscous electrolyte.

In chapter 5, various surfactant-templated, mesoporous silica thin films containing a phenyl-substituted pyrene fluorophore were prepared and tested as sensors for the nitroaromatic compound 2,4-dinitrotoluene (DNT). The effects of materials parameters on quenching efficiency were evaluated, including the influence of mesopore architecture (wormlike, cubic, or hexagonal mesopores), presence or absence of the templating surfactant in the mesopores, and mode of fluorophore incorporation (doping, impregnating, grafting). Among films with similar components, films with wormlike mesopore architecture exhibited a better quenching performance than those with 2D-hexagonal or 3D-hexagonal mesopore structure. Surfactant-free, fluorophore-bridged films with wormlike mesopores showed the best quenching performance (43% after 5 s and 88% after 60 s), which compares favorably with state-of-the-art sensors based on fluorescent conjugated polymers. Surfactant-containing, fluorophore-doped films with wormlike mesopores were also effectively quenched by DNT, with 39% quenching after 45 s and

94% of quenching after 405 s. It is notable that the surfactant blocks the diffusion of DNT only slightly while it enhances the binding of DNT to the film, boosting the quenching performance.

6.2 Outlook

Nanostructured and nanoporous electrode materials with the high surface area, short diffusion path, and high surface to volume ratio have been transforming the lithium ion battery and supercapacitor technologies.[1-15] The 21st century will witness the revolution in the energy storage field utilizing nano-sized electrode materials. However, it is difficult to predict which technologies will first be available to practical applications such as EVs and HEVs considering the broad research on nanometarials for energy storage application nowadays. In the future, LIBs will continue to attract great attention because of their many advantages including high energy density, high power, and good cyclability. Further improvement of LIBs will focus on improving the capacity (for large scale energy storage) and rate performance (for transportation).[9,16-18] Electrode materials that can accept more than one lithium ion per transition metal and electrode materials that have different charge storage mechanisms such as conversion electrodes, are potential candidates to enhance capacity of LIBs.[19-23] The performances of these special electrodes can benefit from using nanosized materials resulting from their small sizes and their high surface areas. Most often, the charge storing/releasing processes in these kinds of electrodes are forbidden in the bulk counterparts. Nanoporous electrode materials particularly the ones with ordered pore system are of special interests for high power applications. On the anode side, research will focus on electrode materials with extremely high capacity (Si, Sn, SnO_2, alloys, and conversion anode).[4,24-28] The biggest problem of these anode materials is the pulverization during the charge/discharge processes leading to poor cyclability. To this aspect, nanomaterials have been showing significant improvement in the mechanical stability that can sustain the volume changes. EDLC is also holding a bright future for applications that need extremely high power rate and long life cycle. Carbonaceous materials with hierarchically porous structures and high conductivity that can simultaneously supply high energy density and high power density is of great interest.

6.3 References

(1) Yang, Y.; McDowell, M. T.; Jackson, A.; Cha, J. J.; Hong, S. S.; Cui, Y. *Nano Lett* **2010**, *10*, 1486.

(2) Wang, W.; Kumta, P. N. *ACS Nano* **2010**, *4*, 2233.

(3) Wang, Y.; Cao, G. *Adv. Mater.* **2008**, *20*, 2251.

(4) Szczech, J. R.; Jin, S. *Energy Environ. Sci.* **2011**, *4*, 56.

(5) Sotiropoulou, S.; Sierra-Sastre, Y.; Mark, S. S.; Batt, C. A. *Chem. Mater.* **2008**, *20*, 821.

(6) Rakhi, R. B.; Chen, W.; Cha, D.; Alshareef, H. N. *Adv. Energy Mater.* **2012**, *2*, 381.

(7) slides, C. R.; Martin, C. R. *Adv. Mater.* **2005**, *17*, 125

(8) Djenizian, T.; Hanzu, I.; Knauth, P. *J. Mater. Chem.* **2011**, *21*, 9925.

(9) Arico, A. S.; Bruce, P.; Scrosati, B.; Tarascon, J.-M.; van Schalkwijk, W. *Nat. Mater.* **2005**, *4*, 366.

(10) Manthiram, A.; Murugan, A. V.; Sarkar, A.; Muraliganth, T. *Energy Environ. Sci.* **2008**, *1*, 621.

(11) Myung, S.-T.; Takahashi, N.; Komaba, S.; Yoon, C. S.; Sun, Y.-K.; Amine, K.; Yashiro, H. *Adv. Funct. Mater.* **2011**, *21*, 3231.

(12) Guo, Y.-G.; Hu, J.-S.; Wan, L.-J. *Adv. Mater.* **2008**, *20*, 2878.

(13) Derrien, G.; Hassoun, J.; Panero, S.; Scrosati, B. *Adv. Mater.* **2007**, *19*, 2336.

(14) Balaya, P.; Saravanan, K.; Hariharan, S.; Ramar, V.; Lee, H. S.; Kuezma, M.; Devaraj, S.; Nagaraju, D. H.; Ananthanarayanan, K.; Mason, C. W. *Proceedings of SPIE* **2011**, *8035*, 803503/1.

(15) Balaya, P. *Energy Environ. Sci.* **2008**, *1*, 645.

(16) Tarascon, J.-M. *Philosophical Transactions of the Royal Society A: Mathematical, Physical and Engineering Sciences* **2010**, *368*, 3227.

(17) Yuan, L.-X.; Wang, Z.-H.; Zhang, W.-X.; Hu, X.-L.; Chen, J.-T.; Huang, Y.-H.; Goodenough, J. B. *Energy Environ. Sci.* **2011**, *4*, 269.

(18) Goodenough, J. B.; Kim, Y. *Chem. Mater.* **2010**, *22*, 587.

(19) Sun, B.; Horvat, J.; Kim, H. S.; Kim, W.-S.; Ahn, J.; Wang, G. *J. Phys. Chem. C* **2010**, *114*, 18753.

(20) Li, Y.; Tan, B.; Wu, Y. *Nano Lett.* **2007**, *8*, 265.

(21) Balaya, P.; Li, H.; Kienle, L.; Maier, J. *Adv. Funct. Mater.* **2003**, *13*, 621

(22) Croy, J. R.; Kim, D.; Balasubramanian, M.; Gallagher, K.; Kang, S.-H.; Thackeray, M. M. *J. Electrochem. Soc.* **2012**, *159*, A781.

(23) Morcrette, M.; Rozier, P.; Dupont, L.; Mugnier, E.; Sannier, L.; Galy, J.; Tarascon, J.-M. *Nat. Mater.* **2003**, *2*, 775

(24) Jia, H.; Gao, P.; Yang, J.; Wang, J.; Nuli, Y.; Yang, Z. *Adv. Energy Mater.* **2011**, *1*, 1036.

(25) Esmanski, A.; Ozin, G. A. *Adv. Funct. Mater.* **2009**, *19*, 1999.

(26) Park, M.-H.; Kim, M. G.; Joo, J.; Kim, K.; Kim, J.; Ahn, S.; Cui, Y.; Cho, J. *Nano Lett.* **2009**, *9*, 3844.

(27) Yao, Y.; McDowell, M. T.; Ryu, I.; Wu, H.; Liu, N.; Hu, L.; Nix, W. D.; Cui, Y. *Nano Lett.* **2011**, *11*, 2949.

(28) Qu, Y.; Zhou, H.; Duan, X. *Nanoscale* **2011**, *3*, 4060.

Reference List

Chapter 1

(1) Yang, Z.; Zhang, J.; Kintner-Meyer, M. C. W.; Lu, X.; Choi, D.; Lemmon, J. P.; Liu, J. *Chem. Rev.* **2011**, *111*, 3577.

(2) Axsen, J.; Kurani, K. S.; Burke, A. *Transport Policy* **2010**, *17*, 173.

(3) Goodenough, J. B.; Kim, Y. *Chem. Mater.* **2010**, *22*, 587.

(4) Tarascon, J. M.; Armand, M. *Nature* **2001**, *414*, 359.

(5) Winter, M.; Brodd, R. J. *Chem. Rev.* **2004**, *104*, 4245.

(6) Rakhi, R. B.; Chen, W.; Cha, D.; Alshareef, H. N. *Advanced Energy Materials* **2012**, *2*, 381.

(7) Myung, S.-T.; Takahashi, N.; Komaba, S.; Yoon, C. S.; Sun, Y.-K.; Amine, K.; Yashiro, H. *Adv. Funct. Mater.* **2011**, *21*, 3231.

(8) Arico, A. S.; Bruce, P.; Scrosati, B.; Tarascon, J.-M.; van Schalkwijk, W. *Nat. Mater.* **2005**, *4*, 366.

(9) Huggins, R. A. 2009.

(10) Levi, M. D.; Aurbach, D. *J. Phys. Chem. B* **1997**, *101*, 4641.

(11) Simon, P.; Gogotsi, Y. *Nat Mater* **2008**, *7*, 845.

(12) Ji, X. L.; Lee, K. T.; Nazar, L. F. *Nat. Mater.* **2009**, *8*, 500.

(13) Lytle, J. C.; Wallace, J. M.; Sassin, M. B.; Barrow, A. J.; Long, J. W.; Dysart, J. L.; Renninger, C. H.; Saunders, M. P.; Brandell, N. L.; Rolison, D. R. *Energ. Environ. Sci.* **2011**, *4*, 1913.

(14) Ren, X.; Zhang, S. S.; Tran, D. T.; Read, J. *J. Mater. Chem.* **2011**, *21*, 10118.

(15) Conway, B. *Electrochemical supercapacitors: scientific fundamentals and technological applications (POD)*; Kluwer Academic/plenum. New York, 1999.

(16) Becker, H. I. In *United State Patent Office*; Company, G. E., Ed.; General Electric Company: USA, 1957; Vol. 2800616.

(17) Miller, J. *Battery+ Energy Storage Technology* **2007**, 61.

(18) Miller, J. R.; Burke, A. F. *The Electrochemical Society Interface* **2008**, *17*, 53.

(19) Zhi, M.; Xiang, C.; Li, J.; Li, M.; Wu, N. *Nanoscale* **2013**, *5*, 72.

(20) Shukla, A. K.; Prem Kumar, T. *Wiley Interdisciplinary Reviews: Energy and Environment* **2013**, *2*, 14.

(21) Zhai, Y.; Dou, Y.; Zhao, D.; Fulvio, P. F.; Mayes, R. T.; Dai, S. *Adv. Mater.* **2011**, *23*, 4828.

(22) Yuan, C. Z.; Gao, B.; Shen, L. F.; Yang, S. D.; Hao, L.; Lu, X. J.; Zhang, F.; Zhang, L. J.; Zhang, X. G. *Nanoscale* **2011**, *3*, 529.

(23) Oschatz, M.; Kockrick, E.; Rose, M.; Borchardt, L.; Klein, N.; Senkovska, I.; Freudenberg, T.; Korenblit, Y.; Yushin, G.; Kaskel, S. *Carbon* **2010**, *48*, 3987.

(24) Portet, C.; Lillo-Rodenas, M. A.; Linares-Solano, A.; Gogotsi, Y. *Phys. Chem. Chem. Phys.* **2009**, *11*, 4943.

(25) Chmiola, J.; Largeot, C.; Taberna, P.-L.; Simon, P.; Gogotsi, Y. *Science* **2010**, *328*, 480.

(26) Rose, M.; Korenblit, Y.; Kockrick, E.; Borchardt, L.; Oschatz, M.; Kaskel, S.; Yushin, G. *Small* **2011**, *7*, 1108.

(27) Liu, H.-J.; Wang, J.; Wang, C.-X.; Xia, Y.-Y. *Advanced Energy Materials* **2011**, *1*, 1101.

(28) Lotufo, G. R.; Farrar, J. D.; Inouye, L. S.; Bridges, T. S.; Ringelberg, D. B. *Environ. Toxicol. Chem.* **2001**, *20*, 1762.

(29) Krausa, M.; Reznev, A. A.; North Atlantic Treaty Organization. Scientific Affairs Division. *Vapour and trace detection of explosives for anti-terrorism purposes*; Kluwer Academic: Dordrecht ; London, 2004.

(30) Caron, T.; Guillemot, M.; Montméat, P.; Veignal, F.; Perraut, F.; Prené, P.; Serein-Spirau, F. *Talanta* **2010**, *81*, 543.

(31) Nguyen, H. H.; Li, X.; Wang, N.; Wang, Z. Y.; Ma, J.; Bock, W. J.; Ma, D. *Macromolecules* **2009**, *42*, 921.

(32) Long, Y.; Chen, H.; Yang, Y.; Wang, H.; Yang, Y.; Li, N.; Li, K.; Pei, J.; Liu, F. *Macromolecules* **2009**, *42*, 6501.

(33) Li, Z.; Dong, Y. Q.; Lam, J. W. Y.; Sun, J.; Qin, A.; Häußler, M.; Dong, Y. P.; Sung, H. H. Y.; Williams, I. D.; Kwok, H. S.; Tang, B. Z. *Adv. Funct. Mater.* **2009**, *19*, 905.

(34) He, G.; Zhang, G.; Lü, F.; Fang, Y. *Chem. Mater.* **2009**, *21*, 1494.

(35) Zhu, D.; He, Q.; Cao, H.; Cheng, J.; Feng, S.; Xu, Y.; Lin, T. *Appl. Phys. Lett.* **2008**, *93*, 261909.

(36) Narayanan, A.; Varnavski, O. P.; Swager, T. M.; Goodson, T. *J. Phys. Chem. C* **2008**, *112*, 881.

(37) Bai, H.; Li, C.; Shi, G. *Sens. Actuators B Chem.* **2008**, *130*, 777.

(38) Wang, Z.; Wang, Z. Y.; Ma, J.; Bock, W. J.; Ma, D. *Polymer* **2010**, *51*, 842.

(39) Angelos, S.; Johansson, E.; Stoddart, J. F.; Zink, J. I. *Adv. Funct. Mater.* **2007**, *17*, 2261.

(40) Hunks, W. J.; Ozin, G. A. *J. Mater. Chem.* **2005**, *15*, 3716.

(41) Germain, M. E.; Knapp, M. J. *Chem. Soc. Rev.* **2009**, *38*, 2543.

(42) Vu, A.; Qian, Y.; Stein, A. *Advanced Energy Materials* **2012**, *2*, 1056.

(43) Di Renzo, F.; Galarneau, A.; Trens, P.; Fajula, F. *Handbook of Porous Solids* **2002**, *3*, 1311.

(44) Hatton, B.; Landskron, K.; Whitnall, W.; Perovic, D.; Ozin, G. A. *Acc Chem Res* **2005**, *38*, 305.

(45) Wan, Y.; Shi, Y.; Zhao, D. *Chemical communications (Cambridge, England)* **2007**, 897.

(46) Kleitz, F. In *Handbook of Heterogeneous Catalysis (2nd Ed.)*; Ertl, G., Ed. 2008; Vol. 1, p 178.

(47) El-Safty, S. A. *J. Porous Mater.* **2011**, *18*, 259.

(48) Edler, K. J. In *Porous Materials*; Bruce, D. W., O'Hare, D., Walton, R. I., Eds.; Wiley: Chichester, 2011, p 69.

(49) Lu, Y.; Ganguli, R.; Drewien, C. A.; Anderson, M. T.; Brinker, C. J.; Gong, W.; Guo, Y.; Soyez, H.; Dunn, B.; Huang, M. H.; Zink, J. I. *Nature* **1997**, *389*, 364.

(50) Grosso, D.; Cagnol, F.; de A. A. Soler-Illia, G. J.; Crepaldi, E. L.; Amenitsch, H.; Brunet-Bruenau, A.; Bourgeois, A.; Sanchez, C. *Adv. Funct. Mater.* **2004**, *14*, 309.

(51) Das, S. K.; Darmakolla, S.; Bhattacharyya, A. J. *J. Mater. Chem.* **2010**, *20*, 1600.

(52) Saravanan, K.; Ananthanarayanan, K.; Balaya, P. *Energy Environ. Sci.* **2010**, *3*, 939.

(53) Wang, D.; Choi, D.; Yang, Z.; Viswanathan, V. V.; Nie, Z.; Wang, C.; Song, Y.; Zhang, J.-G.; Liu, J. *Chem. Mater.* **2008**, *20*, 3435.

(54) S. Zhu, H. Z., T. Miyoshi, M. Hibino, I. Honma, M. Ichihara, *Adv. Mater.* **2004**, *16*, 2012.

(55) Shiva, K.; Asokan, S.; Bhattacharyya, A. J. *Nanoscale* **2011**, *3*, 1501.

(56) Guerra, E. M.; Cestarolli, D. T.; Oliveira, H. P. *J. Sol-Gel Sci. Technol.* **2010**, *54*, 93.

(57) Nara, H.; Fukuhara, Y.; Takai, A.; Komatsu, M.; Mukaibo, H.; Yamauchi, Y.; Momma, T.; Kuroda, K.; Osaka, T. *Chem. Lett.* **2008**, *37*, 142.

(58) Whitehead, A. H.; Elliott, J. M.; Coleman, N. R. B.; Bartlett, P. N.; Attard, G. S.; Owen, J. R. *Proc. Electrochem. Soc.* **1999**, *98-16*, 128.

(59) Brezesinski, K.; Haetge, J.; Wang, J.; Mascotto, S.; Reitz, C.; Rein, A.; Tolbert, S. H.; Perlich, J.; Dunn, B.; Brezesinski, T. *Small* **2011**, *7*, 407.

(60) Wang, Y.; Smarsly, B. M.; Djerdj, I. *Chem. Mater.* **2010**, *22*, 6624.

(61) Haetge, J.; Hartmann, P.; Brezesinski, K.; Janek, J.; Brezesinski, T. *Chem. Mater.* **2011**, *23*, 4384.

(62) Krins, N.; Bass, J. D.; Grosso, D.; Henrist, C.; Delaigle, R.; Gaigneaux, E. M.; Cloots, R.; Vertruyen, B. n. d.; Sanchez, C. m. *Chem. Mater.* **2011**, *23*, 4124.

(63) Schroden, R. C.; Stein, A. In *Colloids and Colloid Assemblies: Synthesis, Modification, Organization and Utilization of Colloid Particles*; Caruso, F., Ed.; Wiley-VCH: Weinheim, 2004, p 465.

(64) Stein, A.; Li, F.; Denny, N. R. *Chem. Mater.* **2008**, *20*, 649.

(65) Sakamoto, J. S.; Dunn, B. *J. Mater. Chem.* **2002**, *12*, 2859.

(66) Dong, W.; Sakamoto, J. S.; Dunn, B. *Sci. Tech. Adv. Mater.* **2003**, *4*, 3.

(67) Yan, H.; Sokolov, S.; Lytle, J. C.; Stein, A.; Zhang, F.; Smyrl, W. H. *J. Electrochem. Soc.* **2003**, *150*, A1102.

(68) Tonti, D.; Torralvo, M. J.; Enciso, E.; Sobrados, I.; Sanz, J. *Chem. Mater.* **2008**, *20*, 4783.

(69) Yan, H.; Blanford, C. F.; Holland, B. T.; Smyrl, W. H.; Stein, A. *Chem. Mater.* **2000**, *12*, 1134.

(70) Ergang, N. S.; Lytle, J. C.; Yan, H.; Stein, A. *J. Electrochem. Soc.* **2005**, *152*, A1989.

(71) Eftekhari, A. *Solid State Ionics* **2003**, *161*, 41.

(72) Doherty, C. M.; Caruso, R. A.; Smarsly, B. M.; Drummond, C. J. *Chem. Mater.* **2009**, *21*, 2895.

(73) Cui, W.; Liu, H.; Wang, C.; Xia, Y. *Electrochem. Commun.* **2008**, *10*, 1587.

(74) Kavan, L.; Zukalova, M.; Kalbac, M.; Graetzel, M. *J. Electrochem. Soc.* **2004**, *151*, A1301.

(75) Yamada, H.; Yamato, T.; Moriguchi, I.; Kudo, T. *Solid State Ionics* **2004**, *175*, 195.

(76) Bing, Z.; Yuan, Y.; Wang, Y.; Fu, Z.-W. *Electrochem. Solid-State Lett.* **2006**, *9*, A101.

(77) Jusic, A. *Lijecnicki vjesnik* **1992**, *114*, 166.

(78) Woo, S.-W.; Dokko, K.; Kanamura, K. *Electrochim. Acta* **2007**, *53*, 79.

(79) Li, Z. H.; Zhao, T. P.; Zhan, X. Y.; Gao, D. S.; Xiao, Q. Z.; Lei, G. T. *Electrochim. Acta* **2010**, *55*, 4594.

(80) Lytle, J. C.; Yan, H.; Ergang, N.; Smyrl, W. H.; Stein, A. *J. Mater. Chem.* **2004**, *14*, 1616.

(81) Kotobuki, M.; Isshiki, Y.; Munakata, H.; Kanamura, K. *Electrochim. Acta* **2010**, *55*, 6892.

(82) Wu, M.-S.; Lin, Y.-P. *Electrochim. Acta* **2011**, *56*, 2068.

(83) Sommer, R.; Schaller, H. *Molecular & general genetics : MGG* **1979**, *168*, 331.

(84) Polarz, S.; Antonietti, M. *Chem. Commun.* **2002**, 2593.

(85) Yang, H.; Zhao, D. *J. Mater. Chem.* **2005**.

(86) Lu, a.-H.; Schüth, F. *Adv. Mater.* **2006**, *18*, 1793.

(87) Lu, A.-H.; Zhao, D.; Wan, Y. *Nanocasting - A Versatile Strategy for Creating Nanostructured Porous Materials*; RSC Publishing: Cambridge, UK, 2009.

(88) Wang, G.; Liu, H.; Horvat, J.; Wang, B.; Qiao, S.; Park, J.; Ahn, H. *Chem. Eur. J.* **2010**, *16*, 11020.

(89) Liu, H.; Wang, G.; Liu, J.; Qiao, S.; Ahn, H. *J. Mater. Chem.* **2011**, *21*, 3046.

(90) Liu, H.; Du, X.; Xing, X.; Wang, G.; Qiao, S. Z. *Chemical communications (Cambridge, England)* **2012**, *48*, 865.

(91) Cheng, M.-Y.; Hwang, B.-J. *J. Power Sources* **2010**, *195*, 4977.

(92) Kleitz, F.; Choi, S. H.; Ryoo, R. *Chemical communications (Cambridge, England)* **2003**, 2136.

(93) Kim, T.-W.; Kleitz, F.; Paul, B.; Ryoo, R. *J. Am. Chem. Soc.* **2005**, *127*, 7601.

(94) Zhao, D.; Feng, J.; Huo, Q.; Melosh, N.; Fredrickson, G. H.; Chmelka, B. F.; Stucky, G. D. *Science* **1998**, *279*, 548.

(95) Zhao, D.; Huo, Q.; Feng, J.; Chmelka, B. F.; Stucky, G. D. *J. Am. Chem. Soc.* **1998**, *120*, 6024.

(96) Ren, Y.; Hardwick, L. J.; Bruce, P. G. *Angew. Chem. Int. Ed.* **2010**, *49*, 2570.

(97) Kim, H.; Cho, J. *Nano Lett.* **2008**, *8*, 3688.

(98) Luo, J.-Y.; Zhang, J.-J.; Xia, Y.-Y. *Chem. Mater.* **2006**, *18*, 5618.

(99) Jiao, F.; Bruce, P. G. *Adv. Mater.* **2007**, *19*, 657.

(100) Ren, Y.; Armstrong, A. R.; Jiao, F.; Bruce, P. G. *J. Am. Chem. Soc.* **2009**, *132*, 996.

(101) Lim, S.; Yoon, C. S.; Cho, J. *Chem. Mater.* **2008**, *20*, 4560.

(102) Feng Jiao, J. B., Adrian H. Hill, Peter G. Bruce, *Angew. Chem. Int. Ed.* **2008**, *47*, 9711.

(103) Dupont, L.; Laruelle, S.; Grugeon, S.; Dickinson, C.; Zhou, W.; Tarascon, J. M. *J. Power Sources* **2008**, *175*, 502.

(104) Shaju, K. M.; Jiao, F.; Debart, A.; Bruce, P. G. *Phys. Chem. Chem. Phys.* **2007**, *9*, 1837.

(105) Yue, W.; Xu, X.; Irvine, J. T. S.; Attidekou, P. S.; Liu, C.; He, H.; Zhao, D.; Zhou, W. *Chem. Mater.* **2009**, *21*, 2540.

(106) Kim, H.; Cho, J. *J. Mater. Chem.* **2008**, *18*, 771.

(107) Yoon, S.; Jo, C.; Noh, S. Y.; Lee, C. W.; Song, J. H.; Lee, J. *Phys Chem Chem Phys* **2011**, *13*, 11060.

(108) Shi, Y.; Guo, B.; Corr, S. A.; Shi, Q.; Hu, Y.-S.; Heier, K. R.; Chen, L.; Seshadri, R.; Stucky, G. D. *Nano Lett.* **2009**, *9*, 4215.

(109) Yue, W.; Randorn, C.; Attidekou, P. S.; Su, Z.; Irvine, J. T. S.; Zhou, W. *Adv. Funct. Mater.* **2009**, *19*, 2826.

(110) Fang, X.; Yu, X.; Liao, S.; Shi, Y.; Hu, Y.-S.; Wang, Z.; Stucky, G. D.; Chen, L. *Micropor. Mesopor. Mater.* **2012**, *151*, 418.

(111) Shon, J. K.; Kim, H.; Kong, S. S.; Hwang, S. H.; Han, T. H.; Kim, J. M.; Pak, C.; Doo, S.; Chang, H. *J. Mater. Chem.* **2009**, *19*, 6727.

(112) Ke, F.-S.; Huang, L.; Wei, H.-B.; Cai, J.-S.; Fan, X.-Y.; Yang, F.-Z.; Sun, S.-G. *J. Power Sources* **2007**, *170*, 450.

(113) Kim, J. M.; Huh, Y. S.; Han, Y.-K.; Cho, M. S.; Kim, H. J. *Electrochem. Comm.* **2012**, *14*, 32.

(114) Ha, H.-W.; Kim, T. W.; Choy, J.-H.; Hwang, S.-J. *J. Phys. Chem. C* **2009**, *113*, 21941.

(115) Lee, K.-H.; Song, S.-W. *ACS. Appl. Mater. Interfaces* **2011**, *3*, 3697.

(116) Qu, B.; Zhang, M.; Lei, D.; Zeng, Y.; Chen, Y.; Chen, L.; Li, Q.; Wang, Y.; Wang, T. *Nanoscale* **2011**, *3*, 3646.

(117) Li, H.; He, P.; Wang, Y.; Hosono, E.; Zhou, H. *J. Mater. Chem.* **2011**, *21*, 10999.

(118) Sakamoto, J. S.; Dunn, B. *J. Electrochem. Soc.* **2002**, *149*, A26.

(119) Wang, J.; Zhou, Y.; Hu, Y.; O'Hayre, R.; Shao, Z. *J. Phys. Chem. C* **2011**, *115*, 2529.

(120) Zhang, F.; Zhang, Y.; Song, S.; Zhang, H. *J. Power Sources* **2011**, *196*, 8618.

(121) Demir-Cakan, R.; Hu, Y.-S.; Antonietti, M.; Maier, J.; Titirici, M.-M. *Chem. Mater.* **2008**, *20*, 1227.

(122) Shaju, K. M.; Bruce, P. G. *Adv. Mater.* **2006**, *18*, 2330.

(123) Pechini, M. P. *U. S. Patent* **1967**, No. 3.

(124) Li, Y.; Li, J. *J. Phys. Chem. C* **2008**, *112*, 14216.

(125) Kotobuki, M.; Okada, N.; Kanamura, K. *Chem. Commun.* **2011**, *47*, 6144.

(126) Woo, S.-W.; Okada, N.; Kotobuki, M.; Sasajima, K.; Munakata, H.; Kajihara, K.; Kanamura, K. *Electrochim. Acta* **2010**, *55*, 8030.

(127) Heinroth, F.; Münzer, S.; Feldhoff, A.; Passinger, S.; Cheng, W.; Reinhardt, C.; Chichkov, B.; Behrens, P. *Journal of Materials Science* **2009**, *44*, 6490.

(128) Wang, K.; Wei, M.; Morris, M. A.; Zhou, H.; Holmes, J. D. *Adv. Mater.* **2007**, *19*, 3016.

(129) Martin, C. R. *Science* **1994**, *266*, 1961.

(130) Li, N.; Martin, C. R. *J. Electrochem. Soc.* **2001**, *148*, A164.

(131) Sides, C. R.; Croce, F.; Young, V. Y.; Martin, C. R.; Scrosati, B. *Electrochem. Solid-St. Lett.* **2005**, *8*, A484.

(132) Zhang, R.; Dai, H.; Du, Y.; Zhang, L.; Deng, J.; Xia, Y.; Zhao, Z.; Meng, X.; Liu, Y. *Inorg. Chem.* **2011**, *50*, 2534.

(133) Wang, Z.; Li, F.; Ergang, N. S.; Stein, A. *Chem. Mater.* **2006**, *18*, 5543.

(134) Wang, Z.; Stein, A. *Chem. Mater.* **2008**, *20*, 1029.

(135) Wang, Z.; Kiesel, E. R.; Stein, A. *J. Mater. Chem.* **2008**, *18*, 2194.

(136) Wang, Z.; Li, F.; Ergang, N. S.; Stein, A. *Carbon* **2008**, *46*, 1702.

(137) Wang, Z.; Fierke, M. A.; Stein, A. *J. Electrochem. Soc.* **2008**, *155(9)*, A658.

Chapter 2

(1) Padhi, A. K.; Nanjundaswamy, K. S.; Goodenough, J. B. *J. Electrochem. Soc.* **1997**, *144*, 1188.

(2) Tarascon, J. M.; Armand, M. *Nature* **2001**, *414*, 359.

(3) Manthiram, A. *J. Phys. Chem. Lett.* **2011**, 176.

(4) Nishimura, S.-I.; Kobayashi, G.; Ohoyama, K.; Kanno, R.; Yashima, M.; Yamada, A. *Nat. Mater.* **2008**, *7*, 707.

(5) Huggins, R. A. 2009.

(6) Chung, S.-Y.; Bloking, J. T.; Chiang, Y.-M. *Nat. Mater.* **2002**, *1*, 123.

(7) Meethong, N.; Kao, Y.-H.; Speakman, S. A.; Chiang, Y.-M. *Adv. Funct. Mater.* **2009**, *19*, 1060.

(8) Kang, B.; Ceder, G. *Nature* **2009**, *458*, 190.

(9) Hu, Y.-S.; Guo, Y.-G.; Dominko, R.; Gaberscek, M.; Jamnik, J.; Maier, J. *Adv. Mater.* **2007**, *19*, 1963

(10) Huang, H.; Yin, S. C.; Nazar, L. F. *Electrochem. Solid-State Lett.* **2001**, *4*, A170.

(11) Konarova, M.; Taniguchi, I. *Mater. Res. Bull.* **2008**, *43*, 3305.

(12) Murugan, A. V.; Muraliganth, T.; Ferreira, P. J.; Manthiram, A. *Inorg. Chem.* **2009**, *48*, 946.

(13) Kim, M. G.; Cho, J. *Adv. Funct. Mater.* **2009**, *19*, 1497.

(14) Muraliganth, T.; Murugan, A. V.; Manthiram, A. *J. Mater. Chem.* **2008**, *18*, 5661.

(15) Gaberscek, M.; Kuzma, M.; Jamnik, J. *Phys. Chem. Chem. Phys.* **2007**, *9*, 1815.

(16) Long, J. W.; Sassin, M. B.; Fischer, A. E.; Rolison, D. R.; Mansour, A. N.; Johnson, V. S.; Stallworth, P. E.; Greenbaum, S. G. *J. Phys. Chem. C* **2009**, *113*, 17595.

(17) Baxter, J.; Bian, Z.; Chen, G.; Danielson, D.; Dresselhaus, M. S.; Fedorov, A. G.; Fisher, T. S.; Jones, C. W.; Maginn, E.; Kortshagen, U.; Manthiram, A.; Nozik, A.;

Rolison, D. R.; Sands, T.; Shi, L.; Sholl, D.; Wu, Y. *Energy Environ. Sci.* **2009**, *2*, 559.

(18) Wang, Z.; Kiesel, E. R.; Stein, A. *J. Mater. Chem.* **2008**, *18*, 2194.

(19) Wang, Z.; Fierke, M. A.; Stein, A. *J. Electrochem. Soc.* **2008**, *155(9)*, A658.

(20) Woo, S.-W.; Dokko, K.; Nakano, H.; Kanamura, K. *J. Mater. Chem.* **2008**, *18*, 1674.

(21) Su, F.; Zeng, J.; Bai, P.; Lv, L.; Guo, P.-Z.; Sun, H.; Li, H. L.; Yu, J.; Lee, J. Y.; Zhao, X. S. *Ind. Eng. Chem. Res.* **2007**, *46*, 9097.

(22) Lu, A.-H.; Schmidt, W.; Spliethoff, B.; Schuth, F. *Adv. Mater.* **2003**, *15*, 1602

(23) Fan, J.; Wang, T.; Yu, C.; Tu, B.; Jiang, Z.; Zhao, D. *Adv. Mater.* **2004**, *16*, 1432

(24) Zhang, W.-M.; Hu, J.-S.; Guo, Y.-G.; Zheng, S.-F.; Zhong, L.-S.; Song, W.-G.; Wan, L.-J. *Adv. Mater.* **2008**, *20*, 1160.

(25) Wang, Z. Y.; Ergang, N. S.; Al-Daous, M. A.; Stein, A. *Chem. Mater.* **2005**, *17*, 6805.

(26) Cao, F. F.; Wu, X. L.; Xin, S.; Guo, Y. G.; Wan, L. J. *J. Phys. Chem. C* **2010**, *114*, 10308.

(27) Tirado, J. L.; Santamaría, R.; Ortiz, G. F.; Menéndez, R.; Lavela, P.; Jiménez-Mateos, J. M.; Gómez García, F. J.; Concheso, A.; Alcántara, R. *Carbon* **2007**, *45*, 1396.

(28) Monnier, A.; Schuth, F.; Huo, Q.; Kumar, D.; Margolese, D.; Maxwell, R. S.; Stucky, G. D.; Krishnamurty, M.; Petroff, P.; Firouzi, A.; Janicke, M.; Chmelka, B. F. *Science* **1993**, *261*, 1299.

(29) Yang, P.; Zhao, D.; Margolese, D. I.; Chmelka, B. F.; Stucky, G. D. *Chem. Mater.* **1999**, *11*, 2813.

(30) Yang, P.; Zhao, D.; Margolese, D. I.; Chmelka, B. F.; Stucky, G. D. *Nature* **1998**, *396*, 152.

(31) Dominko, R.; Bele, M.; Goupil, J.-M.; Gaberscek, M.; Hanzel, D.; Arcon, I.; Jamnik, J. *Chem. Mater.* **2007**, *19*, 2960.

(32) Lim, S.; Yoon, C. S.; Cho, J. *Chem. Mater.* **2008**, *20*, 4560.

(33) Luo, J.-y.; Wang, Y.-g.; Xiong, H.-m.; Xia, Y.-y. *Chem. Mater.* **2007**, *19*, 4791.

(34) Doherty, C. M.; Caruso, R. A.; Smarsly, B. M.; Drummond, C. J. *Chem. Mater.* **2009**, *21*, 2895.

(35) Doherty, C. M.; Caruso, R. A.; Drummond, C. J. *Energy Environ. Sci.* **2010**, *3*, 813.

(36) Wang, G.; Liu, H.; Liu, J.; Qiao, S.; Lu, G. M.; Munro, P.; Ahn, H. *Adv. Mater.* **2010**, *22*, 4944.

(37) Doherty, C. M.; Caruso, R. A.; Smarsly, B. M.; Adelhelm, P.; Drummond, C. J. *Chem. Mater.* **2009**, *21*, 5300.

(38) Liu, R.; Shi, Y.; Wan, Y.; Meng, Y.; Zhang, F.; Gu, D.; Chen, Z.; Tu, B.; Zhao, D. *J. Am. Chem. Soc.* **2006**, *128*, 11652.

(39) Kang, Y.-S.; Lee, H. I.; Zhang, Y.; Han, Y. J.; Yie, J. E.; Stucky, G. D.; Kim, J. M. *Chem. Commun.* **2004**, 1524.

(40) Vu, A.; Stein, A. *Chem. Mater.* **2011**, *23*, 3237.

(41) Li, F.; Wang, Z.; Ergang, N. S.; Fyfe, C. A.; Stein, A. *Langmuir* **2007**, *23*, 3996.

(42) Meng, Y.; Gu, D.; Zhang, F.; Shi, Y.; Yang, H.; Li, Z.; Yu, C.; Tu, B.; Zhao, D. *Angew. Chem. Int. Ed.* **2005**, *44*, 7053.

(43) Schroden, R. C.; Al-Daous, M.; Sokolov, S.; Melde, B. J.; Lytle, J. C.; Stein, A.; Carbajo, M. C.; Fernández, J. T.; Rodríguez, E. E. *J. Mater. Chem.* **2002**, *12*, 3261.

(44) Van Der Pauw, L. J. *Philips Tech. Rev.* **1958/59**, *20*, 220.

(45) Ellis, B. L.; Makahnouk, W. R. M.; Makimura, Y.; Toghill, K.; Nazar, L. F. *Nat. Mater.* **2007**, *6*, 749.

(46) Dong, A.; Ren, N.; Tang, Y.; Wang, Y.; Zhang, Y.; Hua, W.; Gao, Z. *J. Am. Chem. Soc.* **2003**, *125*, 4976.

(47) Li, D.; Zhou, H.; Honma, I. *Nat. Mater.* **2004**, *3*, 65.

(48) Song, M.-S.; Kim, D.-Y.; Kang, Y.-M.; Kim, Y.-I.; Lee, J.-Y.; Kwon, H.-S. *J. Power Sources* **2008**, *180*, 546.

(49) Ferrari, A. C.; Robertson, J. *Phys. Rev. B* **2000**, *61*, 14095.

(50) Doeff, M. M.; Hu, Y.; McLarnon, F.; Kostecki, R. *Electrochem. Solid-State Lett.* **2003**, *6*, A207.

(51) Tuinstra, F.; Koenig, J. L. *J. Chem. Phys.* **1970**, *53*, 1126.

(52) Ergang, N. S.; Fierke, M. A.; Wang, Z.; Smyrl, W. H.; Stein, A. *J. Electrochem. Soc.* **2007**, *154*, A1135.

(53) Wang, Z.; Li, F.; Ergang, N. S.; Stein, A. *Chem. Mater.* **2006**, *18*, 5543.

(54) Wang, Z.; Li, F.; Ergang, N. S.; Stein, A. *ECS Trans.* **2008**, *6*, 199.

(55) Wang, Z.; Stein, A. *Chem. Mater.* **2008**, *20*, 1029.

(56) J.R.Dahn *Phys. Rev. B* **1991**, *44*, 9170.

(57) Ergang, N. S.; Lytle, J. C.; Lee, K. T.; Oh, S. M.; Smyrl, W. H.; Stein, A. *Adv. Mater.* **2006**, *18*, 1750.

Chapter 3

(1) Axsen, J.; Kurani, K. S.; Burke, A. *Transport Policy* **2010**, *17*, 173.

(2) Goodenough, J. B.; Kim, Y. *Chem. Mater.* **2010**, *22*, 587.

(3) Yuan, L.-X.; Wang, Z.-H.; Zhang, W.-X.; Hu, X.-L.; Chen, J.-T.; Huang, Y.-H.; Goodenough, J. B. *Energy Environ. Sci.* **2011**, *4*, 269.

(4) Delacourt, C.; Poizot, P.; Tarascon, J.-M.; Masquelier, C. *Nat Mater* **2005**, *4*, 254.

(5) Delmas, C.; Maccario, M.; Croguennec, L.; Le Cras, F.; Weill, F. *Nat Mater* **2008**, *7*, 665.

(6) Kang, B.; Ceder, G. *Nature* **2009**, *458*, 190.

(7) Nishimura, S.-I.; Kobayashi, G.; Ohoyama, K.; Kanno, R.; Yashima, M.; Yamada, A. *Nat. Mater.* **2008**, *7*, 707.

(8) Chen, Z.; Dahn, J. *J. Electrochem. Soc.* **2002**, *149*, A1184.

(9) Dominko, R.; Bele, M.; Gaberscek, M.; Remskar, M.; Hanzel, D.; Pejovnik, S.; Jamnik, J. *J. Electrochem. Soc.* **2005**, *152*, A607.

(10) Hu, Y. S.; Guo, Y. G.; Dominko, R.; Gaberscek, M.; Jamnik, J.; Maier, J. *Adv. Mater.* **2007**, *19*, 1963.

(11) Chung, S.-Y.; Bloking, J. T.; Chiang, Y.-M. *Nat. Mater.* **2002**, *1*, 123.

(12) Vu, A.; Stein, A. *Chem. Mater.* **2011**, *23*, 3237.

(13) Doherty, C. M.; Caruso, R. A.; Smarsly, B. M.; Adelhelm, P.; Drummond, C. J. *Chem. Mater.* **2009**, *21*, 5300.

(14) Doherty, C. M.; Caruso, R. A.; Smarsly, B. M.; Drummond, C. J. *Chem. Mater.* **2009**, *21*, 2895.

(15) Badot, J. C.; Ligneel, É.; Dubrunfaut, O.; Guyomard, D.; Lestriez, B. *Adv. Funct. Mater.* **2009**, *19*, 2749.

(16) Sun, C.; Rajasekhara, S.; Goodenough, J. B.; Zhou, F. *J. Am. Chem. Soc.* **2011**, *133*, 2132.

(17) Liu, J.; Conry, T. E.; Song, X.; Doeff, M. M.; Richardson, T. J. *Energy Environ. Sci.* **2011**, *4*, 885.

(18) Lee, M. H.; Kim, J. Y.; Song, H. K. *Chem. Commun.* **2010**, *46*, 6795.

(19) Wang, Y.; Hosono, E.; Wang, K.; Zhou, H. *Angew. Chem. Int. Ed.* **2008**, *47*, 7461.

(20) Liu, Y.; Liu, D.; Zhang, Q.; Yu, D.; Liu, J.; Cao, G. *Electrochim. Acta* **2010**, *56*, 2559.

(21) Wang, K.; Cai, R.; Yuan, T.; Yu, X.; Ran, R.; Shao, Z. *Electrochim. Acta* **2009**, *54*, 2861.

(22) Zhi, X.; Liang, G.; Wang, L.; Ou, X.; Gao, L.; Jie, X. *J. Alloys Compd.* **2010**, *503*, 370.

(23) Cho, Y.-D.; Fey, G. T.-K.; Kao, H.-M. *J. Power Sources* **2009**, *189*, 256.

(24) Lin, Y.; Gao, M. X.; Zhu, D.; Liu, Y. F.; Pan, H. G. *J. Power Sources* **2008**, *184*, 444.

(25) Sato, M.; Tajimi, S.; Okawa, H.; Uematsu, K.; Toda, K. *Solid State Ionics* **2002**, *152-153*, 247.

(26) S. Zhu, H. Z., T. Miyoshi, M. Hibino, I. Honma, M. Ichihara, *Adv. Mater.* **2004**, *16*, 2012.

(27) Ferrari, A. C.; Robertson, J. *Phys. Rev. B* **2000**, *61*, 14095.

(28) Doeff, M. M.; Hu, Y.; McLarnon, F.; Kostecki, R. *Electrochem. Solid-State Lett.* **2003**, *6*, A207.

(29) Tuinstra, F.; Koenig, J. L. *J. Chem. Phys.* **1970**, *53*, 1126.

(30) Sevilla, M.; Fuertes, A. B. *Carbon* **2006**, *44*, 468.

(31) Padhi, A. K.; Nanjundaswamy, K. S.; Goodenough, J. B. *J. Electrochem. Soc.* **1997**, *144*, 1188.

(32) Masquelier, C.; Padhi, A. K.; Nanjundaswamy, K. S.; Goodenough, J. B. *J. Solid State Chem.* **1998**, *135*, 228.

(33) Wu, X.-L.; Jiang, L.-Y.; Cao, F.-F.; Guo, Y.-G.; Wan, L.-J. *Adv. Mater.* **2009**, *21*, 2710.

(34) Maier, J. *Nat Mater* **2005**, *4*, 805.

(35) Balaya, P.; Li, H.; Kienle, L.; Maier, J. *Adv. Funct. Mater.* **2003**, *13*, 621.

(36) Jamnik, J.; Maier, J. *Phys. Chem. Chem. Phys.* **2003**, *5*, 5215.

Chapter 4

(1) Miller, J. R.; Burke, A. F. *The Electrochemical Society Interface* **2008**, *17*, 53.

(2) Zhai, Y.; Dou, Y.; Zhao, D.; Fulvio, P. F.; Mayes, R. T.; Dai, S. *Adv. Mater.* **2011**, *23*, 4828.

(3) Jurewicz, K.; Babeł, K.; Źiółkowski, A.; Wachowska, H. *Electrochim. Acta* **2003**, *48*, 1491.

(4) Pell, W. G.; Conway, B. E.; Marincic, N. *J. Electroanal. Chem.* **2000**, *491*, 9.

(5) Barbieri, O.; Hahn, M.; Herzog, A.; Kötz, R. *Carbon* **2005**, *43*, 1303.

(6) Shiraishi, S.; Kurihara, H.; Tsubota, H.; Oya, A.; Soneda, Y.; Yamada, Y. *Electrochem. Solid-State Lett.* **2001**, *4*, A5.

(7) Kierzek, K.; Frackowiak, E.; Lota, G.; Gryglewicz, G.; Machnikowski, J. *Electrochim. Acta* **2004**, *49*, 515.

(8) Endo, M.; Kim, Y. J.; Osawa, K.; Ishii, K.; Inoue, T.; Nomura, T.; Miyashita, N.; Dresselhaus, M. S. *Electrochem. Solid-State Lett.* **2003**, *6*, A23.

(9) Lozano-Castelló, D.; Cazorla-Amorós, D.; Linares-Solano, A.; Shiraishi, S.; Kurihara, H.; Oya, A. *Carbon* **2003**, *41*, 1765.

(10) Endo, M.; Kim, Y. J.; Ohta, H.; Ishii, K.; Inoue, T.; Hayashi, T.; Nishimura, Y.; Maeda, T.; Dresselhaus, M. S. *Carbon* **2002**, *40*, 2613.

(11) Qu, D.; Shi, H. *J. Power Sources* **1998**, *74*, 99.

(12) Jiang, Q.; Qu, M. Z.; Zhou, G. M.; Zhang, B. L.; Yu, Z. L. *Mater. Lett.* **2002**, *57*, 988.

(13) Wang, J.; Kaskel, S. *J. Mater. Chem.* **2012**, *22*, 23710.

(14) Chmiola, J.; Yushin, G.; Gogotsi, Y.; Portet, C.; Simon, P.; Taberna, P. L. *Science* **2006**, *313*, 1760.

(15) Simon, P.; Gogotsi, Y. *Nat Mater* **2008**, *7*, 845.

(16) Chmiola, J.; Largeot, C.; Taberna, P.-L.; Simon, P.; Gogotsi, Y. *Science* **2010**, *328*, 480.

(17) Daffos, B.; Taberna, P. L.; Gogotsi, Y.; Simon, P. *Fuel Cells* **2010**, *10*, 819.

(18) Largeot, C.; Portet, C.; Chmiola, J.; Taberna, P.-L.; Gogotsi, Y.; Simon, P. *J. Am. Chem. Soc.* **2008**, *130*, 2730.

(19) Liu, H.-J.; Wang, J.; Wang, C.-X.; Xia, Y.-Y. *Advanced Energy Materials* **2011**, *1*, 1101.

(20) Rose, M.; Korenblit, Y.; Kockrick, E.; Borchardt, L.; Oschatz, M.; Kaskel, S.; Yushin, G. *Small* **2011**, *7*, 1108.

(21) Yuan, C. Z.; Gao, B.; Shen, L. F.; Yang, S. D.; Hao, L.; Lu, X. J.; Zhang, F.; Zhang, L. J.; Zhang, X. G. *Nanoscale* **2011**, *3*, 529.

(22) Brun, N.; Prabaharan, S. R. S.; Surcin, C.; Morcrette, M.; Deleuze, H.; Birot, M.; Babot, O.; Achard, M.-F.; Backov, R. *J. Phys. Chem. C* **2011**, *116*, 1408.

(23) Chae, W.-S.; Gough, D. V.; Ham, S.-K.; Robinson, D. B.; Braun, P. V. *ACS. Appl. Mater. Interfaces* **2012**, *4*, 3973.

(24) Carriazo, D.; Pico, F.; Gutierrez, M. C.; Rubio, F.; Rojo, J. M.; del Monte, F. *J. Mater. Chem.* **2010**, *20*, 773.

(25) Xu, F.; Cai, R.; Zeng, Q.; Zou, C.; Wu, D.; Li, F.; Lu, X.; Liang, Y.; Fu, R. *J. Mater. Chem.* **2011**, *21*, 1970.

(26) Yang, S.-Y.; Chang, K.-H.; Tien, H.-W.; Lee, Y.-F.; Li, S.-M.; Wang, Y.-S.; Wang, J.-Y.; Ma, C.-C. M.; Hu, C.-C. *J. Mater. Chem.* **2011**, *21*, 2374.

(27) Wang, D.-W.; Li, F.; Liu, M.; Lu, G. Q.; Cheng, H.-M. *Angew. Chem.* **2008**, *120*, 379.

(28) Yokoi, T.; Sakamoto, Y.; Terasaki, O.; Kubota, Y.; Okubo, T.; Tatsumi, T. *J. Am. Chem. Soc.* **2006**, *128*, 13664.

(29) Fan, W.; Snyder, M. A.; Kumar, S.; Lee, P.-S.; Yoo, W. C.; McCormick, A. V.; Lee Penn, R.; Stein, A.; Tsapatsis, M. *Nat Mater* **2008**, *7*, 984.

(30) Ferrari, A. C.; Robertson, J. *Phys. Rev. B* **2000**, *61*, 14095.

(31) Tuinstra, F.; Koenig, J. L. *J. Chem. Phys.* **1970**, *53*, 1126.

(32) Gor, G. Y.; Thommes, M.; Cychosz, K. A.; Neimark, A. V. *Carbon* **2011**.

(33) Stoller, M. D.; Ruoff, R. S. *Energy Environ. Sci.* **2010**, *3*, 1294.

(34) Burke, A. *Electrochim. Acta* **2007**, *53*, 1083.

(35) Gamby, J.; Taberna, P. L.; Simon, P.; Fauvarque, J. F.; Chesneau, M. *J. Power Sources* **2001**, *101*, 109.

(36) Zhang, L. L.; Zhao, X. S. *Chem. Soc. Rev.* **2009**, *38*, 2520.

(37) Oschatz, M.; Kockrick, E.; Rose, M.; Borchardt, L.; Klein, N.; Senkovska, I.; Freudenberg, T.; Korenblit, Y.; Yushin, G.; Kaskel, S. *Carbon* **2010**, *48*, 3987.

(38) Zhu, Y.; Murali, S.; Stoller, M. D.; Ganesh, K. J.; Cai, W.; Ferreira, P. J.; Pirkle, A.; Wallace, R. M.; Cychosz, K. A.; Thommes, M.; Su, D.; Stach, E. A.; Ruoff, R. S. *Science* **2011**, *332*, 1537.

Chapter 5

(1) Lotufo, G. R.; Farrar, J. D.; Inouye, L. S.; Bridges, T. S.; Ringelberg, D. B. *Environ. Toxicol. Chem.* **2001**, *20*, 1762.

(2) Caron, T.; Guillemot, M.; Montméat, P.; Veignal, F.; Perraut, F.; Prené, P.; Serein-Spirau, F. *Talanta* **2010**, *81*, 543.

(3) Long, Y.; Chen, H.; Yang, Y.; Wang, H.; Yang, Y.; Li, N.; Li, K.; Pei, J.; Liu, F. *Macromolecules* **2009**, *42*, 6501.

(4) He, G.; Zhang, G.; Lü, F.; Fang, Y. *Chem. Mater.* **2009**, *21*, 1494.

(5) Díaz Aguilar, A.; Forzani, E. S.; Leright, M.; Tsow, F.; Cagan, A.; Iglesias, R. A.; Nagahara, L. A.; Amlani, I.; Tsui, R.; Tao, N. J. *Nano Lett.* **2009**, *10*, 380.

(6) Yang, J.-S.; Swager, T. M. *J. Am. Chem. Soc.* **1998**, *120*, 5321.

(7) Goldman, E. R.; Medintz, I. L.; Whitley, J. L.; Hayhurst, A.; Clapp, A. R.; Uyeda, H. T.; Deschamps, J. R.; Lassman, M. E.; Mattoussi, H. *J. Am. Chem. Soc.* **2005**, *127*, 6744.

(8) Ewing, R. G.; Atkinson, D. A.; Eiceman, G. A.; Ewing, G. J. *Talanta* **2001**, *54*, 515.

(9) Yinon, J. *Forensic and environmental detection of explosives*; John Wiley & Sons Chichester, 1999.

(10) Fierke, M. A.; Olson, E. J.; Bühlmann, P.; Stein, A. *ACS. Appl. Mater. Interfaces* **2012**, *4*, 4731.

(11) Sylvia, J. M.; Janni, J. A.; Klein, J. D.; Spencer, K. M. *Anal. Chem.* **2000**, *72*, 5834.

(12) Krausa, M.; Reznev, A. A.; North Atlantic Treaty Organization. Scientific Affairs Division. *Vapour and trace detection of explosives for anti-terrorism purposes*; Kluwer Academic: Dordrecht ; London, 2004.

(13) Nguyen, H. H.; Li, X.; Wang, N.; Wang, Z. Y.; Ma, J.; Bock, W. J.; Ma, D. *Macromolecules* **2009**, *42*, 921.

(14) Li, Z.; Dong, Y. Q.; Lam, J. W. Y.; Sun, J.; Qin, A.; Häußler, M.; Dong, Y. P.; Sung, H. H. Y.; Williams, I. D.; Kwok, H. S.; Tang, B. Z. *Adv. Funct. Mater.* **2009**, *19*, 905.

(15) Zhu, D.; He, Q.; Cao, H.; Cheng, J.; Feng, S.; Xu, Y.; Lin, T. *Appl. Phys. Lett.* **2008**, *93*, 261909.

(16) Narayanan, A.; Varnavski, O. P.; Swager, T. M.; Goodson, T. *J. Phys. Chem. C* **2008**, *112*, 881.

(17) Bai, H.; Li, C.; Shi, G. *Sens. Actuators B Chem.* **2008**, *130*, 777.

(18) Zhou, Q.; Swager, T. M. *J. Am. Chem. Soc.* **1995**, *117*, 7017.

(19) Yamaguchi, S.; Swager, T. M. *J. Am. Chem. Soc.* **2001**, *123*, 12087.

(20) Sohn, H.; Calhoun, R. M.; Sailor, M. J.; Trogler, W. C. *Angew. Chem. Int. Ed.* **2001**, *40*, 2104.

(21) Sohn, H.; Sailor, M. J.; Magde, D.; Trogler, W. C. *J. Am. Chem. Soc.* **2003**, *125*, 3821.

(22) Sanchez, J. C.; DiPasquale, A. G.; Rheingold, A. L.; Trogler, W. C. *Chem. Mater.* **2007**, *19*, 6459.

(23) Wang, Z.; Wang, Z. Y.; Ma, J.; Bock, W. J.; Ma, D. *Polymer* **2010**, *51*, 842.

(24) Angelos, S.; Johansson, E.; Stoddart, J. F.; Zink, J. I. *Adv. Funct. Mater.* **2007**, *17*, 2261.

(25) Hunks, W. J.; Ozin, G. A. *J. Mater. Chem.* **2005**, *15*, 3716.

(26) Germain, M. E.; Knapp, M. J. *Chem. Soc. Rev.* **2009**, *38*, 2543.

(27) Johnson-White, B.; Zeinali, M.; Shaffer, K. M.; Patterson, C. H.; Charles, P. T.; Markowitz, M. A. *Biosens. Bioelectron.* **2007**, *22*, 1154.

(28) Tao, S.; Li, G. *Colloid. Polym. Sci.* **2007**, *285*, 721.

(29) Gao, D.; Wang, Z.; Liu, B.; Ni, L.; Wu, M.; Zhang, Z. *Anal. Chem.* **2008**, *80*, 8545.

(30) Feng, J.; Li, Y.; Yang, M. *Sens. Actuators B Chem.* **2010**, *145*, 438.

(31) Liu, F.; Zhang, L.-J.; Xiao, J.-H.; Hu, J.; Liu, H.-L. *Front. Mater. Sci. China* **2010**, *4*, 158.

(32) Balkus Jr, K. J.; Pisklak, T. J.; Hundt, G.; Sibert, J.; Zhang, Y. *Microporous Mesoporous Mater.* **2008**, *112*, 1.

(33) Chen, L.; McBranch, D.; Wang, R.; Whitten, D. *Chem. Phys. Lett.* **2000**, *330*, 27.

(34) Stevens, N.; Akins, D. L. *Sens. Actuators B Chem.* **2007**, *123*, 59.

(35) Vu, A.; Phillips, J.; Buhlmann, P.; Stein, A. *Chem. Mater.* **2013**.

(36) Hu, J.-y.; Era, M.; Elsegood, M. R. J.; Yamato, T. *Eur. J. Org. Chem.* **2010**, *2010*, 72.

(37) de Halleux, V.; Calbert, J.-P.; Brocorens, P.; Cornil, J.; Declercq, J.-P.; Brédas, J.-L.; Geerts, Y. *Adv. Funct. Mater.* **2004**, *14*, 649.

(38) Vollmann, H.; Becker, H.; Corell, M.; Streeck, H. *Justus Liebig's Annalen der Chemie* **1937**, *531*, 1.

(39) Mizoshita, N.; Goto, Y.; Maegawa, Y.; Tani, T.; Inagaki, S. *Chem. Mater.* **2010**, *22*, 2548.

(40) Hernandez, R.; Franville, A.-C.; Minoofar, P.; Dunn, B.; Zink, J. I. *J. Am. Chem. Soc.* **2001**, *123*, 1248.

(41) Minoofar, P. N.; Hernandez, R.; Chia, S.; Dunn, B.; Zink, J. I.; Franville, A.-C. *J. Am. Chem. Soc.* **2002**, *124*, 14388.

(42) Yamaguchi, A.; Amino, Y.; Shima, K.; Suzuki, S.; Yamashita, T.; Teramae, N. *J. Phys. Chem. B* **2006**, *110*, 3910.

(43) Wark, M.; Ganschow, M.; Rohlfing, Y.; Schulz-Ekloff, G.; Woehrle, D. *Stud. Surf. Sci. Catal.* **2001**, *135*, 3292.

(44) Yang, Y.; Wang, H.; Su, K.; Long, Y.; Peng, Z.; Li, N.; Liu, F. *J. Mater. Chem.* **2011**, *21*, 11895.

(45) Shanmugaraju, S.; Joshi, S. A.; Mukherjee, P. S. *J. Mater. Chem.* **2011**, *21*, 9130.

(46) Nagarjuna, G.; Kumar, A.; Kokil, A.; Jadhav, K. G.; Yurt, S.; Kumar, J.; Venkataraman, D. *J. Mater. Chem.* **2011**, *21*, 16597.

(47) Gole, B.; Shanmugaraju, S.; Bar Arun, K.; Mukherjee Partha, S. *Chem. Commun.* **2011**, *47*, 10046.

(48) Zhang, X.; Qiu, X.; Lu, R.; Zhou, H.; Xue, P.; Liu, X. *Talanta* **2010**, *82*, 1943.

(49) Vijayakumar, C.; Tobin, G.; Schmitt, W.; Kim, M.-J.; Takeuchi, M. *Chem. Commun.* **2010**, *46*, 874.

(50) Fang, Q.; Geng, J.; Liu, B.; Gao, D.; Li, F.; Wang, Z.; Guan, G.; Zhang, Z. *Chem. Eur. J.* **2009**, *15*, 11507.

(51) Clavaguera, S.; Dautel, O. J.; Hairault, L.; Methivier, C.; Montmeat, P.; Pasquinet, E.; Pradier, C.-M.; Serein-Spirau, F.; Wakim, S.; Veignal, F.; Moreau, J. J. E.; Lere-Porte, J.-P. *J. Polym. Sci., Part A Polym. Chem.* **2009**, *47*, 4141.

(52) Burattini, S.; Colquhoun, H. M.; Greenland, B. W.; Hayes, W.; Wade, M. *Macromol. Rapid Commun.* **2009**, *30*, 459.

(53) Tao, S.; Yin, J.; Li, G. *J. Mater. Chem.* **2008**, *18*, 4872.

(54) Zhang, S.; Lue, F.; Gao, L.; Ding, L.; Fang, Y. *Langmuir* **2007**, *23*, 1584.

(55) Naddo, T.; Che, Y.; Zhang, W.; Balakrishnan, K.; Yang, X.; Yen, M.; Zhao, J.; Moore, J. S.; Zang, L. *J. Am. Chem. Soc.* **2007**, *129*, 6978.

(56) Tao, S.; Li, G.; Zhu, H. *J. Mater. Chem.* **2006**, *16*, 4521.

(57) Zhao, D.; Swager, T. M. *Macromolecules* **2005**, *38*, 9377.

(58) Le Barny, P. L.; Obert, E. T.; Soyer, F.; Malval, J. P.; Leray, I.; Lemaitre, N.; Pansu, R.; Simic, V.; Doyle, H.; Redmond, G.; Loiseaux, B. *Proc. SPIE-Int. Soc. Opt. Eng.* **2005**, *5990*, 59900S/1.

(59) Liu, Y.; Mills, R. C.; Boncella, J. M.; Schanze, K. S. *Langmuir* **2001**, *17*, 7452.

Chapter 6

(1) Yang, Y.; McDowell, M. T.; Jackson, A.; Cha, J. J.; Hong, S. S.; Cui, Y. *Nano Lett* **2010**, *10*, 1486.

(2) Wang, W.; Kumta, P. N. *ACS Nano* **2010**, *4*, 2233.

(3) Wang, Y.; Cao, G. *Adv. Mater.* **2008**, *20*, 2251.

(4) Szczech, J. R.; Jin, S. *Energy Environ. Sci.* **2011**, *4*, 56.

(5) Sotiropoulou, S.; Sierra-Sastre, Y.; Mark, S. S.; Batt, C. A. *Chem. Mater.* **2008**, *20*, 821.

(6) Rakhi, R. B.; Chen, W.; Cha, D.; Alshareef, H. N. *Adv. Energy Mater.* **2012**, *2*, 381.

(7) slides, C. R.; Martin, C. R. *Adv. Mater.* **2005**, *17*, 125

(8) Djenizian, T.; Hanzu, I.; Knauth, P. *J. Mater. Chem.* **2011**, *21*, 9925.

(9) Arico, A. S.; Bruce, P.; Scrosati, B.; Tarascon, J.-M.; van Schalkwijk, W. *Nat. Mater.* **2005**, *4*, 366.

(10) Manthiram, A.; Murugan, A. V.; Sarkar, A.; Muraliganth, T. *Energy Environ. Sci.* **2008**, *1*, 621.

(11) Myung, S.-T.; Takahashi, N.; Komaba, S.; Yoon, C. S.; Sun, Y.-K.; Amine, K.; Yashiro, H. *Adv. Funct. Mater.* **2011**, *21*, 3231.

(12) Guo, Y.-G.; Hu, J.-S.; Wan, L.-J. *Adv. Mater.* **2008**, *20*, 2878.

(13) Derrien, G.; Hassoun, J.; Panero, S.; Scrosati, B. *Adv. Mater.* **2007**, *19*, 2336.

(14) Balaya, P.; Saravanan, K.; Hariharan, S.; Ramar, V.; Lee, H. S.; Kuezma, M.; Devaraj, S.; Nagaraju, D. H.; Ananthanarayanan, K.; Mason, C. W. *Proceedings of SPIE* **2011**, *8035*, 803503/1.

(15) Balaya, P. *Energy Environ. Sci.* **2008**, *1*, 645.

(16) Tarascon, J.-M. *Philosophical Transactions of the Royal Society A: Mathematical, Physical and Engineering Sciences* **2010**, *368*, 3227.

(17) Yuan, L.-X.; Wang, Z.-H.; Zhang, W.-X.; Hu, X.-L.; Chen, J.-T.; Huang, Y.-H.; Goodenough, J. B. *Energy Environ. Sci.* **2011**, *4*, 269.

(18) Goodenough, J. B.; Kim, Y. *Chem. Mater.* **2010**, *22*, 587.

(19) Sun, B.; Horvat, J.; Kim, H. S.; Kim, W.-S.; Ahn, J.; Wang, G. *J. Phys. Chem. C* **2010**, *114*, 18753.

(20) Li, Y.; Tan, B.; Wu, Y. *Nano Lett.* **2007**, *8*, 265.

(21) Balaya, P.; Li, H.; Kienle, L.; Maier, J. *Adv. Funct. Mater.* **2003**, *13*, 621

(22) Croy, J. R.; Kim, D.; Balasubramanian, M.; Gallagher, K.; Kang, S.-H.; Thackeray, M. M. *J. Electrochem. Soc.* **2012**, *159*, A781.

(23) Morcrette, M.; Rozier, P.; Dupont, L.; Mugnier, E.; Sannier, L.; Galy, J.; Tarascon, J.-M. *Nat. Mater.* **2003**, *2*, 775

(24) Jia, H.; Gao, P.; Yang, J.; Wang, J.; Nuli, Y.; Yang, Z. *Adv. Energy Mater.* **2011**, *1*, 1036.

(25) Esmanski, A.; Ozin, G. A. *Adv. Funct. Mater.* **2009**, *19*, 1999.

(26) Park, M.-H.; Kim, M. G.; Joo, J.; Kim, K.; Kim, J.; Ahn, S.; Cui, Y.; Cho, J. *Nano Lett.* **2009**, *9*, 3844.

(27) Yao, Y.; McDowell, M. T.; Ryu, I.; Wu, H.; Liu, N.; Hu, L.; Nix, W. D.; Cui, Y. *Nano Lett.* **2011**, *11*, 2949.

(28) Qu, Y.; Zhou, H.; Duan, X. *Nanoscale* **2011**, *3*, 4060.